Design and fabrication of miniaturised electroanalytical systems

Thesis presented by

Neus Godino Amado

to apply for the degree of Doctor of Electronic Engineering at

Universitat Autònoma de Barcelona

UAB
Universitat Autònoma de Barcelona

CNM
Centre Nacional de Microelectrònica   IMB

CSIC

Bellaterra, March 2010

- -

Dr. Francisco Javier del Campo García, Ramon y Cajal at Instituto de Microelectrónica de Barcelona IMB-CNM (CSIC), and Dr. Francesc Xavier Muñoz Pascual, Researcher Professor at Instituto de Microelectrónica de Barcelona IMB-CNM (CSIC), certify that the thesis entitled: DESIGN AND FABRICATION OF MINIATURISED ELECTROANALYTICAL SYSTEMS was carried out under their supervision within IMB-CNM.

In witness whereof for the Departament d'Enginyeria Electrònica of Universitat Autònoma de Barcelona, they hereby sign this present certification.

Bellaterra, March 2010

Fco. Javier del Campo García   Francesc Xavier Muñoz Pascual

- -

Acknowledgments

Once achieved the important step of writing a thesis, it is time to thank all the people who have helped me finishing "my work". There are so many kinds of helps, and all of you helped me at some point, in some way.

Primer vull agraïr el suport rebut durant aquests anys pels meus dos directors de tesi, Francesc Xavier Muñoz i Javier del Campo. Gràcies, Paco, per la teva confiança i per donar-me l'oportunitat de treballar en aquest petit (o ja no tant petit!) grup del CNM. Gracias, Javier, por tu paciencia, por tu apoyo durante todo este tiempo, por todas tus lecciones de electroquímica, por todas tus buenas ideas y por escucharme en todo momento. I would really like to thank Dr. Detlef Snakenborg, Dr. Mikkel F. Hansen, Professor Jenny Emnéus and Professor Jörg P. Kutter, for their kind hosting, for their good advises, the extraordinary help and obviously, for giving me the chance to work in such a nice and productive environment during my stay at DTU-Nanotech.

Al grup de Microbiologia Mediambiental de la UAB de Barcelona i al grup de Nanotecnologia del IMB-CNM per la seva col·laboració en dos dels articles inclosos en aquesta tesi. I would also like to thank Professor Richard G. Compton for his help in understanding the nanoelectrodes behaviour and Professor Leif Nyholm for encouraging me with my simulations.

Als meus companys del CNM amb els que he compartit reunions de grup, extensió 1313, racó al laboratori, taula a l'hora de dinar, cafès al matí a 0ºC, correccions lingüístiques, fonts de xocolata, festes de sant joan, cursos de doctorat i les grans jornades pre-docs!. Afortunadamente, la comunidad francesa no pudo combatir mi ineptitud para aprender francés, sino estos agradecimientos parecerían un panfleto de la ONU. Gracias por no enseñarme francés! To the international community in Copenhagen for making my spring Danish stays so great and for the guitar lessons, for the olives, for the sushi, for the brunches, for the parties, for the shouts, for the nice trips, for the jokes in the corridor, for the jokes in the labs, for the jokes in the office, for so many laughs… and for not wearing socks, tigre!. A l'Olga per compartir amb mi molt més que els seus $45m^2$.

Als IMNOV, per tants bons menjars, tants viatges freaks, tants crits en converses emmascarades, tants concerts de Divide i Wenceslao, tantes bones estones a les Voltes, al Born, a Poblenou, a Poble Sec i, fins i tot, a Sants-L'Hospitalet. A les nenes dansaires per a apendre a moure el ventre i gaudir amb mi dels impagables moments a la terrasseta a ple hivern. A en Màrius, i a tota la família Belles, pel seu suport, els seus ànims, els seus savis consells i pel temps meravellós que he compartit amb tots ells.

A mi familia, mis padres, mi hermana y Dídac, por el apoyo incondicional en todo momento, su cariño, su afecto y, aunque a veces no lo aprecie suficiente, su sinceridad.

So finally, turning up to the most international language, which is not catalan (really?), just say that all of you together transformed "my work" in "our work". I hope you enjoyed as much as me meeting each other on the road. Thanks!

Contents

CHAPTER 8 : Rotary microvalve

ANNEX 1: Study of electrode kinetics

ANNEX 2: Wall effect in channel microelectrodes

ANNEX 3: Estimation of flow rate from experimental data

ANNEX 4: Papers included in this thesis

Nomenclature, units and abbreviations

Summary of the nomenclature:

α	Charge transfer coefficient	
A	Electrode area	m^2
c	Concentration	$kg \cdot m^{-3}$
δ	Diffusion layer thickness	m
D	Diffusion coefficient	$m^2 \cdot s^{-1}$
e^-	Electron	
E	Electrode potential	V
$E^{o'}$	Formal potential	V
E_{eq}	Equilibrium potential	V
E_f	Initial potential	V
E_i	Final potential	V
F	Faraday constant	$C \cdot mol^{-1}$
η	Viscosity	$kg \cdot m^{-1} \cdot s^{-1}$
h	Half of the height of the microchannel	
I	Current	A
I_p	Peak current	A
I_o	Limiting current	A
j	Current density	$A \cdot m^{-2}$
j_o	Exchange current flux	$A \cdot m^{-2}$
K_m	Half saturation coefficient	$mol \cdot m^{-3}$
k_f	Reduction electron kinetic transfer constant	$m \cdot s^{-1}$
k_b	Oxidation electron kinetic transfer constant	$m \cdot s^{-1}$
k_o or k_s	Standard heterogenous rate constant	$m \cdot s^{-1}$
n	Number of exchanged electrons	
[O]	Oxidised specie concentration	$mol \cdot m^{-3}$
ρ	Density	$kg \cdot m^{-3}$
p	Pressure	Pa
Q	Flow rate	$m^3 \cdot s^{-1}$
q	Charge	C
R	Universal gas constant	$J \cdot K^{-1} \cdot mol^{-1}$
[R]	Reduced specie concentration	$mol \cdot m^{-3}$
r_o	Electrode radius	m
s	Solubility	$mol \cdot m^{-3}$
T	Temperature	K
T_g	Transition temperature	K
t	Time	s

υ	Potential scan rate	$V \cdot s^{-1}$
$\vec{v}$	Velocity	$m \cdot s^{-1}$
ξ	Overpotential	V
w	Band microelectrode width	
x_e	Band microelectrode length	

Summary of units:

A		Ampere
Å	10^{-10}m	Angstrom
C	A·s	Coulomb
g		gram
h		hour
J	$kg \cdot m^2 \cdot s^{-2}$	Joule
K		Kelvin
kg		kilogram
L		liter
m		meter
M	$mol \cdot L^{-1}$	Molar
min		minute
mol		$6.023 \cdot 10^{23}$ units
N	$kg \cdot m \cdot s^{-2}$	Newton
s		second
Pa	$kg \cdot m^{-1} \cdot s^{-2}$	Pascal
V		Volt
Ω		Ohm

Summary of abbreviations:

AFM	Atomic Force Microscope
β-GAL	β-galactosidase
CAD	Computer Aided Design
CAM	Computer Aided Machinning
CE	Counter Electrode
CNC	Computer Numerical Control
CNM	Centro Nacional de Microelectrónica
CNT	Carbon nanotubes
COC	Copolymers
COP	Cycloolefin polymers
CV	Cyclic Voltammetry
CVD	Chemical Vapour Deposition
DMF	N,N-Dimethylformamide
DOF	Degree of freedom
DTU	Technical University of Denmark
EBL	Electron Beam Lithography
ELISA	Enzyme-Linked ImmunoSorbent Assay
FEM	Finite Element Method
HOMO	Highest Occupied Molecular Orbital
IC	Integrated Circuit
ID	Inner Diameter
IDA	Interdigitated Array Microelectrodes
IMB	Instituto de Microelectrónica de Barcelona
ITO	Indium Tin Oxide
IUPAC	Internation Union of Pure and Applied Chemistry
LPCVD	Low Pressure Chemical Vapour Deposition
LUMO	Lowest Unoccupied Molecular Orbital
μTAS	MicroTotal Analysis Systems
MEMS	Micro Electro Mechanical Systems
OD	Outer Diameter
PAP	p-aminophenol
PAPGP	4-aminophenyl-β-D-galactopiranoside
PCB	Printed Circuit Board
PC	Polycarbonate
PDE	Partial Differential Equation
PDMS	Polydymethylsiloxane
PECVD	Plasma Enhanced Chemical Vapour Deposition
PMMA	Polymethyl metracrylate

PVC	Polyvinyl chloride
PVD	Physical Vapour Deposition
RE	Reference electrode
Re	Reynolds Number
RIE	Reactive Ion Etching
RSD	Residual Standard Deviation
UAB	Universitat Autònoma de Barcelona
UV	Ultraviolet
WE	Working Electrode

Abstract

Miniaturisation is without any question more than a simple reduction of dimensions. In this thesis, we focus on the miniaturisation of devices for electroanalysis based on amperometric detection. From the detector point of view, the most accepted definition of a microelectrode is that it is an electrode which size is smaller than the diffusion layer thickness. In that case, radial diffusion becomes an important contribution to the global current. From the integration point of view, reduction of device dimensions and integration in microfluidic devices bring about several advantages such as: portability, reliability, reduction of sample and reagent consumption and automation of chemical analysis.

This thesis focuses on two objectives: study and optimisation of the detection using finite element methods and integration of the detector in such microfluidic devices.

First, simulations of the most typical amperometric detection techniques using macro- and microelectrode were done to deeply understand the fundamentals of the detection. Once we were able to model the basic techniques, these were applied to real devices. The first modelled device was a previously developed microrespirometer. Using simulation we were able to obtain biofilm metabolic information for this quite complex system. It required knowledge of all the parameters related to the fate of oxygen across the different parts of the microrespirometer. Later, all the knowledge gained in the simulation of microelectrodes was applied to the simulation of arrays of nanoelectrodes, which are a natural step in dimension reduction. In that case, using three dimensional models we were able to describe the mass transport at the nanoscale behaviour, which differs from the "micro", as the previous mentioned radial diffusion becomes even more important.

In the last part of the thesis, we integrated the microelectrodes in microfluidic devices. In such devices, we combined both the use of magnetic beads and electrochemical detection to fabricate a microdevices able to perform a wide range of bioassays. The microdevices were fabricated using polymer fast prototyping techniques. Te main objective was to build a versatile device which was easy to use in the laboratory for any bioassay as well as easy to modify depending on the applications demands. Moreover, the microdevice was further improved including a microvalve. Such active component allows us to minimise one of the most recalcitrant problems in electrochemistry, and which is electrode fouling. It also allows performing some biofunctionalising process within the device as the detection chamber is kept separated from the rest of the microdevice. The challenge of that integration was still to use fast prototyping techniques and the same materials to preserve all the flexibility features of the previous microdevice.

Resumen

La miniaturización de dispositivos es sin duda un proceso más complejo que la simple reducción de sus dimensiones. Esta tesis se centra en la miniturización de dispositivos de electroanálisis basados en detección amperométrica. Desde el punto de vista de la detección, la definición más aceptada de microelectrodo lo define como un electrodo que posee una de sus dimensiones inferior al tamaño de la capa de difusión. En estos casos, la contribución de la difusión radial en el perímetro del microelectrodo tiene un peso muy importante en el valor de la corriente global. Desde el punto de vista de la integración, la reducción del tamaño de los dispositivos y su integración en sistemas microfluídicos conlleva una serie de ventajas como: portabilidad, fiabilidad, reducción de consumo del volumen de muestra y reactivos, así como la automatización del análisis.

Esta tesis se ha centrado en dos objetivos fundamentales: el estudio y la optimación de la detección utilizando modelos basados en elementos finitos, así como la integración de los detectores en sistemas microfluídicos.

Primero se realizaron modelos sobre técnicas amperométricas básicas simulando tanto el caso de macroelectrodo como microelectrodo. Una vez capaces de simular dichas técnicas, estos modelos fueron aplicados a la predicción del comportamiento de dispositivos reales. El primer dispositivo modelado fue un microrespirómetro. Utilizando simulaciones, hemos sido capaces de extraer información metabólica del *biofilm* en este complicado sistema, siendo necesario el cálculo de parámetros de transporte del oxígeno a través de las diferentes capas de materiales que componían el dispositivo. Más tarde, el conocimiento acumulado en el modelado de matrices de microelectrodos fue aplicado al modelado de nanoelectrodos, los cuales son un paso natural en el proceso de miniaturización. En este caso, fueron necesarios modelos tridimensionales para describir el proceso de transporte de materia, ya que la contribución de la difusión radial, previamente mencionada, es aún más importante y hace imposible la reducción de los modelos a dos dimensiones.

En la última parte de la tesis, se integraron microelectrodos en sistemas microfluídicos. En esos dispositivos, combinamos el uso de partículas magnéticas con detección electroquímica desarrollando dispositivos aplicables a un amplio rango de bioensayos. Los dispositivos fueron fabricados utilizando técnicas de prototipado rápido en polímeros. El objetivo era crear un sistema versátil que fuera de fácil manejo en el laboratorio, así como de fácil modificación, pudiendo ser modificado en función de las demandas de las diferentes aplicaciones. Más tarde, el sistema microfluídico fue mejorado incluyendo una microválvula. Gracias al uso de este componente activo es posible minimizar uno de los problemas más importantes en electroquímica, como es el deterioro de la superficie de los electrodos. Además, es posible integrar y realizar procesos de biofuncionalización en el mismo dispositivo, ya que la cámara de detección se mantiene en todo momento independiente al resto del sistema. Uno de los retos de la integración de dicha válvula fue su fabricación utilizando los mismos materiales y los mismos procesos de prototipado que el resto del microdispositivo.

Resum

La miniaturització de dispositius és sens dubte un procés més complex que la simple reducció de les seves mides. Aquesta tesi es centra en la miniaturització de dispositius d'electroanàlisis basats en detecció amperomètrica. Des del punt de vista de la detecció, la definició més acceptada de microelèctrode el defineix com un elèctrode pel qual una de les seves dimensions és inferior a la capa de difusió. En aquests cassos, la contribució de la difusió radial al perímetre del microelèctrode té un pes molt important en el valor del corrent global. Des del punt de vista de la integració, la reducció de la mida dels dispositius i la seva integració en sistemes microfluídics comporta una sèrie d'avantatges com: portabilitat, fiabilitats, reducció del consum de volum de la mostra i de reactius, així com l'automatització de l'anàlisi.

Aquesta tesi s'ha centrat en dos objectius fonamentals: l'estudi i l'optimització de la detecció utilitzant models basats en elements finits, així com la integració dels detectors en sistemes microfluídics.

Primer es van realitzar models sobre tècniques amperomètriques bàsiques, simulant tant el cas de macroelèctrode com el de microelèctrode. Una vegada capaços de modelar aquestes tècniques, els models van ser aplicats a la predicció del comportament de dispositius reals. El primer dispositiu modelat va ser un microrespiròmetre. Utilitzant simulacions, hem estat capaços d'extreure informació metabòlica d'un *biofilm* en aquest complicat sistema, on va ser necessari el càlcul de paràmetres de transport de l'oxigen a través de les diferents capes de materials que composaven el mateix. Més tard, el coneixement acumulat en el modelatge de matrius de microelèctrodes va ser aplicat al modelatge de matrius de nanoelèctrodes, els quals són un pas natural en el procés de miniaturització. En aquest cas, van ser necessaris models en tres dimensions per tal de descriure el procés de transport de matèria, ja que la contribució de la difusió radial, prèviament mencionada, és encara més important i fa impossible la reducció dels models a dues dimensions.

A l'última part de la tesi, es van integrar microelèctrodes en sistemes microfluídics. En aquests dispositius es van combinar l'ús de partícules magnètiques amb detecció electroquímica, sent possible desenvolupar dispositius aplicables a un ampli rang de bioassajos. Els dispositius van ser fabricats utilitzant tècniques de prototipatge ràpid en polímers. L'objectiu era crear un sistema versàtil de fàcil ús al laboratori, així com de fàcil modificació, que pugui ser modificat en funció de les demandes de les diferents aplicacions. Aquest sistema va ser posteriorment optimitzat incloent una microvàlvula. Gràcies a l'ús d'aquest component actiu és possible minimitzar un dels problemes més importants en l'electroquímica, com és el deteriorament de la superfície dels elèctrodes. A més a més, és possible integrar i realitzar processos de biofuncionalització en el mateix dispositiu, ja que la càmera de detecció es manté en tot moment independent de la resta del sistema. Un dels reptes de l'esmentada integració d'aquesta vàlvula va ser la seva fabricació utilitzant els mateixos materials i els mateixos processos de prototipatge que la resta del microdispositiu.

CHAPTER 1:

Motivation and Objectives

The objective of this thesis is the design and fabrication of miniaturised analytical systems applied to Electroanalysis. The advantages of electroanalysis compared with other conventional analytical techniques, such as spectrophotommetric or chromatographic methods, rely mainly on the relative simplicity and lower cost of the instrumentation required. However, Electroanalytical techniques beyond potentiometric ion selective electrodes are seldom used in the analytical laboratory, mainly because of the lesser sensitivity and more limited throughput of commercially available systems.

Since the early nineties, miniaturisation has been an important topic in analytical chemistry, including Electroanalysis. Thus, the availability of photolithographic techniques enabled the fabrication of microelectrode arrays in different materials, geometries, and devices which would otherwise be impossible. Microelectrodes and their arrays provide significant sensitivity enhancements and respond faster than conventional electrodes, which has brought them an increasing popularity among analytical chemists. More recent advances in materials science have brought about new photocurable and elastomeric materials which, combined with conventional microfabrication and nanofabrication techniques, have made possible the integration of microfluidic components and their use in more advanced miniaturised analytical systems.

On top of microfabrication techniques, numerical simulations are another important tool both for the design engineer and for the practising electrochemist. To the design engineer, simulations are important as a prediction tool, because they allow saving unnecessary trial and error fabrication cycles that are also time consuming and expensive. To the electrochemist, simulations allow the interpretation of experimental data and the understanding of underlying physical phenomena.

In this thesis, we will use simulation to study electrochemical processes of analytical interest at microelectrodes, focusing on the effect of mass transport to devices of different geometries and spatial arrangement. Simulations have been at the base of new designs, but they have also been use to characterise those new devices and to validate certain measurements. In the context of this thesis, miniaturisation is not just a reduction of the detectors (electrodes), but it also means the integration of such microelectrodes in microfluidic systems. Integration of microelectrodes in lab on a chip device is a challenging process which opens new and interesting ways of detection.

So the objective of the thesis, which is the design and fabrication of miniaturised electroanalytical systems, can be said to have two clear dimensions:

1. **Use of numerical simulations in design and validation, and**

2. **Combination of microfabrication and rapid prototyping techniques in fabrication.**

Use of numerical simulations in design and validation

Simulations are a fundamental tool to understand physical complex problems described by partial differential equations that cannot be solved analytically. The solution of such equation systems is even more complicated when more than one phenomena act simultaneously. In our case, we will use simulations throughout this thesis to:

- *Predict the response of future designs and optimise detection*. Simulations can show us trends and uncover the main parameters affecting the response of a given system, leading to better future design. Electrode geometry may be designed and modified considering the optimum configuration for the desired application. Moreover, sensitivity can be improved by analysing the best way to perform such detection depending on the measurement conditions.

- *Validate systems*: Simulations can be used as a validation tool for experimental results. Once the measurements are performed, it is always necessary to have patterns or theoretical expressions to validate experimental results. Using simulations we can validate such results, and confirm the correct functioning of the devices, and help identify possible causes of failure. Moreover, simulations can be use to extract intrinsic information of the devices, as how the different features affect to the detection.

Combination of microfabrication and rapid prototyping techniques in fabrication

The main goal of this thesis is the fabrication of a lab on a chip device based on electrochemical detection, so we need to integrate microelectrodes in microfludic devices. The main advantages of such microdevices are their portability, reliability and the reduction of sample and reagent consumption. These are enough reasons to focus our effort to fabricate such microdevices, but from the detection point of view, integrating microelectrodes in microfludics devices allows us to perform electrochemical detection in different ways, using hydrodynamics, and to increase sensitivity and reproducibility.

Figure 1-1 schematises a generic approach to develop microdevices, and that has been applied in this thesis. The idea of fabricating a new microdevice is always born from a new concept, a new application or the need to solve existing problem. The first step is to define how this device will be: geometry, material and different components. This first step is ideally followed by simulations, because theoretical studies can give us fundamental information about how this device will behave and if such behaviour meets our demands. Simulations afford the first decision point in the development process before moving on to fabrication. Once the fabrication is finished, we need to validate the real behaviour of our devices making calibration measurements. At that point, simulations play again an important role, as in most cases, there are not theoretical expressions to validate the experimental results and the only way is the corroboration with modelled ones. After all of these checks and validations, the microdevice is ready to reach the last level and become a new integral part of the laboratory.
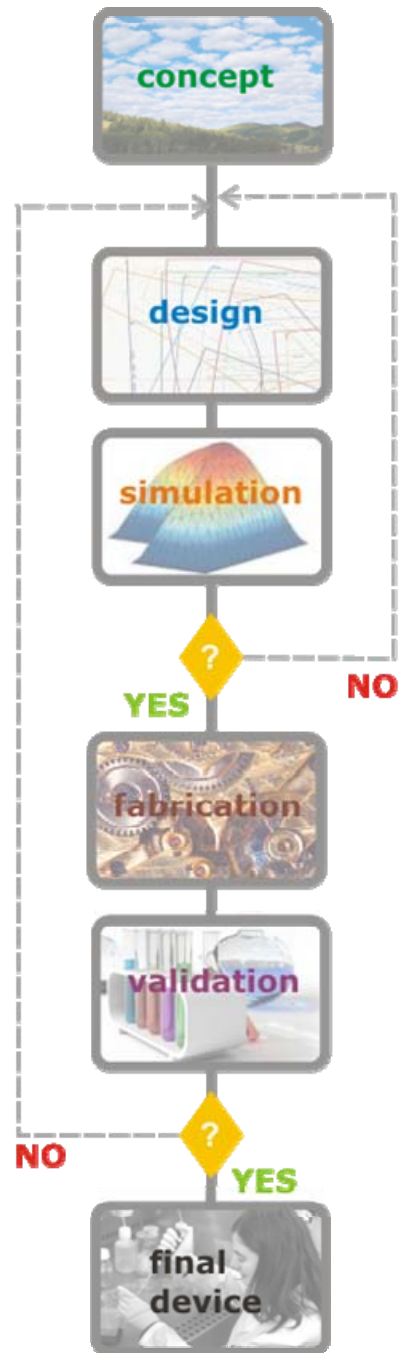

Figure 1-1: Diagrammatic representation of the most important steps in the design and fabrication of a microdevice.

CHAPTER 2: Introduction

This thesis focuses on the design, fabrication and application of minituarised electroanalytical systems. This chapter contains a brief overview of the different aspects related to the development of the work. First there is an introduction to the fundamentals of electrochemistry, where the most important concepts related to electron transfer, mass transport and electrochemical techniques are detailed. Then, a brief explanation of microelectrodes and their special behaviour is given. The last two parts of the introduction provide an overview on two important topics: the integration of the electrochemical sensors in microfluidic platform, and design and simulation, where the most important works on the simulation of microelectrodes under different conditions are highlighted.

2.1 Fundamentals of electrochemistry

Electrochemistry studies heterogeneous electron transfer processes, most commonly between an electrode and species in solution [1]. It can be said that, electrochemistry studies the relation between interfacial chemical changes and electrical phenomena. These may be either chemical reactions brought about by the passage of electric current -or the application of a given electrode potential- in electroanalytical and synthetic applications, or the generation of electrical energy from chemical reactions in batteries and fuel cells [2]. The electrode-solution interface is by and large the most common types of electrochemical system, but electrochemistry is also possible across gas-liquid and liquid-liquid interfaces [3, 4]. Metals (Au, Pt, Ir, Cu, Hg and amalgams), semimetals (Glassy carbon, graphite and other carbon allotropes) and semiconductors (Si, ITO, certain carbon nanotubes) are the most frequent electrode materials [5], which choice should depend on the application –although it often boils down to availability of materials-. The liquid phase may be aqueous or not, but in all cases it should contain an electroactive species and, ideally, an inert supporting electrolyte to increase its conductivity and avoid the effects of migration on the current.

The rate of electrochemical processes may be controlled by three distinct phenomena: electrode kinetics, mass transport and homogeneous chemical reactions, as showed in Figure 2-1. The following sections provide an overview of electrode kinetics and mass transport. A general treatment of how homogenous chemical reactions affect electrochemical processes has been deliberately left out of this chapter, although a biochemical reaction will be also involved in some of the applications done in this work but it will be particularly defined in Chapter 7.
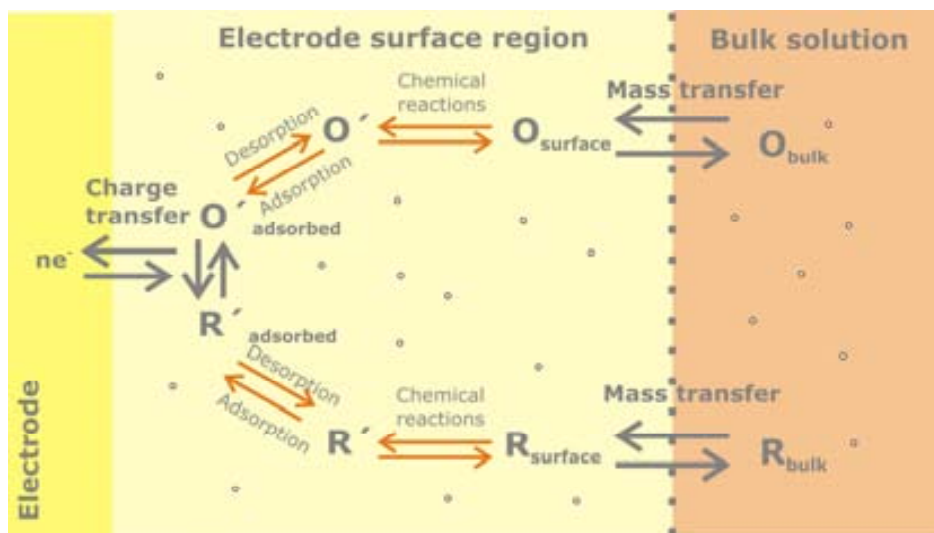
Figure 2-1: Pathway of the different processes that can be involved in a redox reaction at an electrode interface

The work presented in this thesis focuses on electroanalytical applications using microfabricated metal electrodes and aqueous solutions.

Electrochemical processes are typically represented as reduction equations such as:

$$O + ne^- \rightleftharpoons R \qquad (2.1)$$

where O is an oxidised species, n is the number of electrons, e^-, involved and R is the reduced species of the redox couple. Assuming the case of a metal electrode, with a high density of electronic states forming its conduction bands, the average energy of its electrons is located around the Fermi level, E_F. This energy level can be modified applying an external potential and allowing the injection or subtraction of electrons from the conductor [2]. Figure 2-2 shows a diagram of the oxidation and reduction processes. The energy level at the conductor (E_F), the receptor orbital, called LUMO (Lowest Unoccupied Molecular Orbital) [6] and donor orbital, called HOMO (Highest Occupied Molecular Orbital) are also shown.
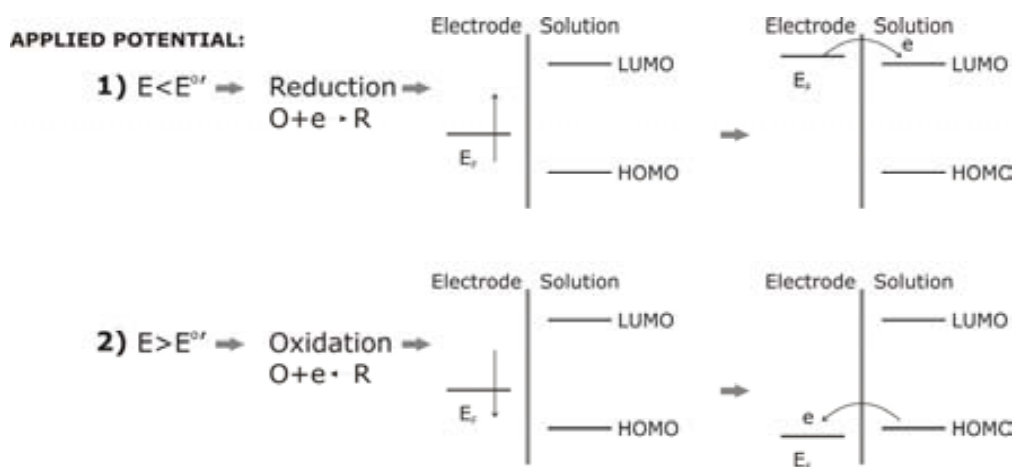
Figure 2-2: Diagramatic scheme of electron transfer and energy levels for: 1) reduction and 2) oxidation processes

To maintain the principle of electroneutrality in the solution, electrochemical processes require at least two electrodes to proceed, so that the electrons injected at the cathode may be extracted at the anode [2]. The sign convention for the current used in this thesis follows IUPAC's (International Union of Pure and Applied Chemistry) recommendations, so that positive currents correspond to oxidations – the electrode acts as electron sink-, and negative currents to reduction processes –the electrode acts as electron source-.

The relation between potential, E, and the relative concentrations of the electroactive species, [O] and [R], at the electrode surface is described by Nernst's equation:

$$E = E^{o'} + \frac{2.3RT}{nF} \log \frac{\left[O_{electrode}\right]}{\left[R_{electrode}\right]} \tag{2.2}$$

where $E^{o'}$ is the formal potential of the redox couple at the equilibrium, R is the ideal gas constant (8.314 J K^{-1} mol^{-1}), F is the Faraday constant (96485 C·mol^{-1}), n is the number of exchanged electrons and T is the temperature in Kelvin.

2.1.1 Electrode kinetics

In this thesis we assume heterogeneous electron transfer to be described by Butler - Volmer's kinetic model [2], which will be described in this subsection. In the following redox reaction:

$$O + ne^{-} \underset{k_b}{\overset{k_f}{\rightleftharpoons}} R$$
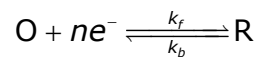
where k_f and k_b are the electron kinetic transfer constants for the reduction and for the oxidation, respectively. The reaction velocity is defined as mass change per unit of time and area ($mol·m^2·s^{-1}$). Both reduction (V_f) and oxidation rates (V_b) are first order, so they depend linearly on concentration, as:

$$V_f = k_f \left[O\right] \tag{2.3}$$

$$V_b = k_b \left[O\right] \tag{2.4}$$

The observed current can be defined as the difference between the cathodic current flux (reduction) and the anodic current flux (oxidation):

$$j = nF\left(V_f - V_b\right) = nF\left(k_f \left[O\right] - k_b \left[R\right]\right) \tag{2.5}$$

The effect of applying an external potential on the kinetic electron transfer constant (k_f and k_b) is explained by changes in the Gibbs free energy barrier [2]. All chemical reactions need to overcome an energetic barrier to take place: the standard free energy of activation $\Delta G^{\ddagger}$ [7]. The point in the reaction pathway where the energy is maximum is known as transition state or activated complex [6, 7], as depicted in Figure 2-3. The kinetic constants can be expressed in Arrhenius form:

$$k_f = A_f e^{-\Delta G_c^{\ddagger}/RT} \tag{2.6}$$

$$k_b = A_b e^{-\Delta G_a^{\ddagger}/RT} \tag{2.7}$$

where A_f and A_b are frequency factors related to the number of effective collisions between reactive molecules or, in electrochemical processes, between electroactive species and the electrode. When the energy of the electrons in the electrode changes as a result of an applied potential, the activation free energy barrier of the chemical reaction shifts, and the electrochemical process is effectively controlled. Thus, an increment in $\Delta G^{\ddagger}$ means a reduction in the kinetic constant of the reaction. At equilibrium, and assuming charge transfer coefficients of 0.5, the activation energies at the cathode and at the anode must be the same $\Delta G_{0a}^{\ddagger} = \Delta G_{0c}^{\ddagger}$, and the probability of the electron transfer is the same in both directions.

Outside equilibrium, when an external potential is applied, the energy level of the electrons at the electrode is modified and one of the reactions (oxidation or reduction) is favoured. If the potential is changed ΔE, the relative energy of the electrons at the electrodes changes as $-nF\Delta E = -nF(E-E^{o'})$ [2] and the curve corresponding to the state $O+ne^-$ departs from this energy change. Figure 2-3 shows the effect on ΔG due to negative and positive increments of ΔE. For instance, if $\Delta E > 0$ $\Delta G_{a}^{\ddagger}$ decreases respect $\Delta G_{0a}^{\ddagger}$ and the oxidation $R \rightleftharpoons O + ne^-$ is more probable. The free activation energy can therefore be described as:

$$\Delta G_{a}^{\ddagger} = \Delta G_{0a}^{\ddagger} - \left(1-\alpha\right)nF\left(E - E^{o'}\right) \tag{2.8}$$

$$\Delta G_{c}^{\ddagger} = \Delta G_{0c}^{\ddagger} + \alpha nF\left(E - E^{o'}\right) \tag{2.9}$$

where α is the charge transfer coefficient. This coefficient is related to the symmetry of the energy barrier, and takes a value between 0 and 1. For metal electrodes and outer-sphere electron transfer processes, the value of the coefficient is close to 0.5 [8]. This means that the activation complex is halfway between both states (reagents and products).
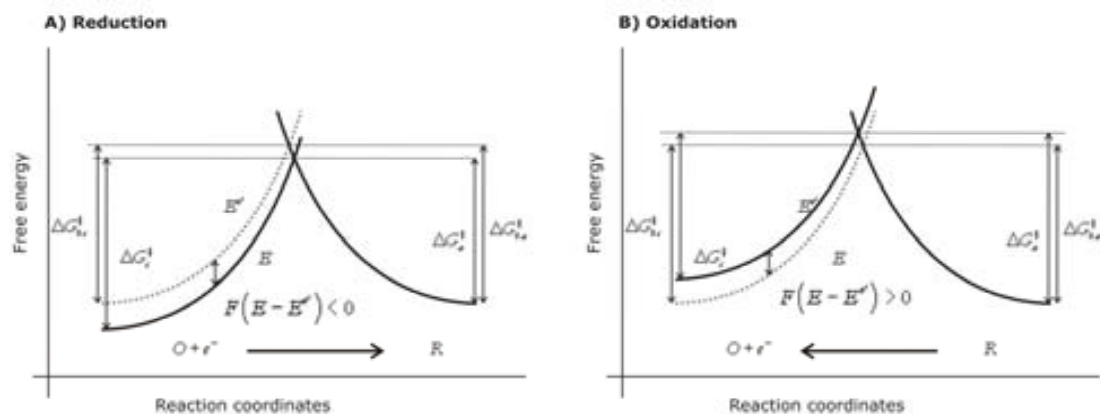

Figure 2-3: Potential change on the standard free energies of activation for A) reduction and B) oxidation.

Hence, considering equations (2.8) and (2.9), the kinetic constants can be described as:

$$k_f = k_f^o e^{-\alpha nF\left(E-E^{o'}\right)/RT} \tag{2.10}$$

$$k_b = k_b^o e^{(1-\alpha)nF\left(E-E^{o'}\right)/RT} \tag{2.11}$$

where:

$$k_f^o = A_f e^{-\Delta G_{0c}^{\ddagger}/RT} \tag{2.12}$$

$$k_b^o = A_b e^{-\Delta G_{0a}^{\ddagger}/RT} \tag{2.13}$$

At equilibrium, $k_f^o = k_b^o = k^o$. k^o or k_s is known as the standard heterogeneous rate constant, and the reversibility of the electron transfer step is related to it. Electron transfer is said to be reversible when $k_s \to \infty$ and irreversible when $k_s \to 0$. The value for k_s depends on properties of the solution and the electrode material. Generally, k_s has values between 1 and 10^{-5} cm·s^{-1} [2, 7]. Considering equations (2.10), (2.11) and the definition of standard rate, the current flux (equation (2.5)) can be related to the applied potential as:

$$j = nFk^o\left([O]e^{-\alpha\frac{nF}{RT}\left(E-E^{o'}\right)} - [R]e^{(1-\alpha)\frac{nF}{RT}\left(E-E^{o'}\right)}\right) \tag{2.14}$$

At the equilibrium, the total net current is zero, which means that:

$$nFk^o[O]e^{-\alpha\frac{nF}{RT}\left(E-E^{o'}\right)} = nFk^o[R]e^{(1-\alpha)\frac{nF}{RT}\left(E-E^{o'}\right)} \tag{2.15}$$

The potential at the electrode is related to the concentrations of the electroactive species $\left([O]_o, [R]_o\right)$ through the Nernst equation:

$$E_{eq} = E^{o'} + \frac{RT}{nF}\ln\frac{[O]_o}{[R]_o} \tag{2.16}$$

Therefore, it is possible to define an exchange current flux, j_o, such that:

$$j_o = nFk^o[O]_o^{1-\alpha}[R]_o^{\alpha} \tag{2.17}$$

If equation (2.14) is described using the definition of the exchange current j_o, the current flux can now be defined in terms of the equilibrium potential, E_{eq}, which makes the concept of overpotential, ξ, easier to grasp:

$$\eta = E - E_{eq} \tag{2.18}$$

So, the current flux can be finally defined as:

$$j = j_o\left(\frac{[O]}{[O]_o}e^{-\alpha\frac{nF}{RT}\xi} - \frac{[R]}{[R]_o}e^{(1-\alpha)\frac{nF}{RT}\xi}\right) \tag{2.19}$$

This expression is the well known Butler and Volmer model. Note that such definition of a heterogeneous electron transfer is based on macroscopic concepts from classic thermodynamics [2]. Therefore it cannot be used in molecular studies relating the electron structure of the electroactive species or the electrode material, in contrast to Marcus' theory [9, 10]. Marcus' model, later expanded by Hush [11, 12], is a microscopic theory which

considers two terms in the standard free energy of activation. One is related to bond length and angle changes in the molecule due to electron transfer, and the other is related to the reorganisation of the solvent molecules around the molecule. However, in all the theoretical studies developed in this work it was not necessary to use microscopic theory and electron transfers has been treated according to the Butler - Volmer model throughout the thesis.

2.1.2 Mass transfer

Mass transfer refers to the movement of matter between the electrode surface and the solution bulk. In the absence of homogeneous chemical reactions and given sufficiently fast electron transfer rates, then mass transport controls the current. Depending on its nature, mass transfer is divided into diffusion, convection and migration [8].

$$\vec{j}_{mass} = \vec{j}_{diffusion} + \vec{j}_{convection} + \vec{j}_{migration} \tag{2.20}$$

Diffusion

Diffusion is the microscopic and random movement of species in a concentration gradient [8], from regions of higher concentration to regions of lower concentration. Fick's laws mathematically describe the mass flux and the concentration of material as a function of position and time [2]. The flux of a species $c(x,y,z)$, defined as the number of moles passing through a certain position per unit time and area, is:

$$\vec{j}_{diffusion} = -D\nabla c \tag{2.21}$$

Equation (2.21) is known as Fick's first law, and the proportionality factor D is known as diffusion coefficient. Fick's second law describes the concentration changes over time, and is mathematically described as:

$$\frac{\partial c}{\partial t} = D\nabla^2 c \tag{2.22}$$

Due to viscous forces the velocity of the fluid is always zero next to a solid surface [13], and diffusion is always the transport mode governing the final approach of electroactive species to an electrode surface [14]. This is of paramount importance in all electroanalytical measurements where mass transport is the limiting process, as the current density is simply the diffusional flux normal to the electrode surface:

$$i = nFj_{diffusion} = -nFD\frac{\partial\left[c\left(x,t\right)\right]}{\partial x}\bigg|_{x=electrode} \tag{2.23}$$

where n, F, j, D and c take their usual meanings. (Note: in this case, x coordinate means the perpendicular coordinate to the electrode surface)

Convection

There are two forms of convection: natural convection and forced convection. Natural or free convection is the macroscopic movement of layers of fluid due to temperature, pressure or density gradients [15]. Forced convection occurs when the movement is due to the application of external forces. Mathematically, convective mass transfer is described by:

$$\vec{j}_{convection} = c \cdot \vec{v} \tag{2.24}$$

where $\vec{v}$ represents to the fluid velocity. There are different ways to induce such external forces in microsystems, based on different physical phenomena. The most common are mechanical or electroosmotic pumps, capillarity forces, and even centripetal forces [15]. The fluidic systems presented in this thesis use a syringe pump to set the fluid in motion, so it is always a pressure driven flow.

Migration

Last, migration is the microscopic movement of charged particles under the influence of an electric field [2]. The application of an electric potential, ϕ, between two electrodes establishes an electric field that drives the movement of ions or other charged species in the solution. Migrational flux is mathematically described as:

$$\vec{j}_{migration} = -\frac{zF}{RT} Dc \cdot \nabla \phi \tag{2.25}$$

Where z is the charge of the ions c(x,y,z). In most electroanalytical experiments migration can be neglected if a moderately high concentration of inert electrolyte (support electrolyte) is used [2]. It is good practice to use a supporting electrolyte concentration at least 100 times greater than that of the electroactive species under study. Then the charge in the solution can be safely assumed to be transported by the supporting electrolyte components [16], and the contribution of migration to the overall current can be neglected.

2.2 Voltammetric techniques at microelectrodes

The sections above have described how the concentration of electroactive species are related to electric current and potential. The following sections focus on voltammetric techniques and microelectrodes, a special type of electrodes that present several advantages to the electroanalytical chemist. Potentiometric, or zero current techniques, are not considered in the present thesis, although they are very useful electrochemical techniques. The reader interested in potentiometric measurements is kindly pointed to the following texts [17, 18].

2.2.1 Voltammetric techniques

Voltammetric techniques study the current resulting from the application of a potential wave function to the working electrode, usually with respect to a reference electrode different from the auxiliary or counter electrode. It was mentioned above that the current can be related to the presence of electroactive species in the solution, but it also depends on the potential function applied. The techniques range in complexity and they can be as simple as a potential step in chronoamperometry, where the current is simply measured as a function of time, or as complicated as differential pulse voltammetry, where a series of pulses is superimposed over a potential staircase, and the current is sampled at very specific times to eliminate the effects of capacitive currents and other sources of background current.

The three voltammetric techniques used in this thesis are potential step chronoamperometry, linear sweep and cyclic voltammetry. These techniques will be more thoroughly described in Chapter 4, but they will be briefly described here for convenience.
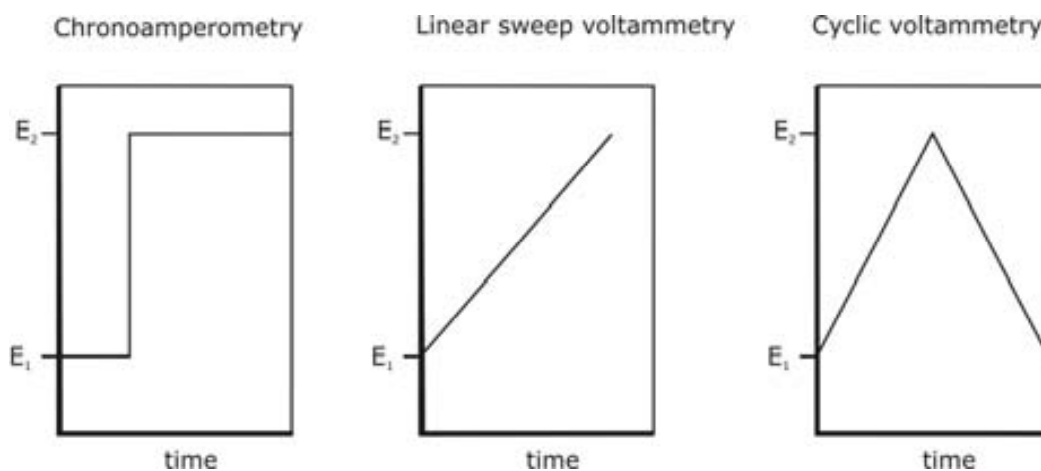
Figure 2-4: Diagramms of the potential functions applied in chronoamperometry, linear sweep voltammetry and cyclic voltammetry.

Chronoamperometry: this technique measures the transient current response to a potential jump. The potential is stepped from a value where no redox reaction occurs to a potential at which the electrochemical reaction takes place (Figure 2-4A). A large initial current is recorded which decays rapidly as a result of a growing diffusion layer and decreasing concentration gradient near the electrode.

Linear sweep voltammetry: this technique consists on applying a linear potential sweep, from an initial potential, E_i, to a final potential value, E_f (Figure 2-4B). It is good practice to set the initial potential at a value where no redox reaction occurs and sweep it towards the potential region where the electrochemical reaction

of interest takes place. The linear swept rate is known as scan rate and the current is represented as a function of potential versus the reference electrode.

Cyclic voltammetry: the potential is swept as in linear sweep voltammetry, but in this case there are at least two ramps, forward and backward sweeps, resulting in a triangular wave (Figure 2-4C).

2.3 Microelectrodes and their advantages

To the unaware, microelectrodes are simply electrodes presenting at least one dimension under 25μm [2, 8]. However, this rather over simplifying definition is misleading, as what defines a microelectrode is not only its size, but also the relation between this and the size of its diffusion layer. Christian Amatore offered a more general definition of microelectrodes in [14]. The definition of microelectrode also involves a consideration of the diffusion layer size and shape. Microelectrodes are characterised by the importance of radial diffusion vis-à-vis planar diffusion. In this game, the diffusion coefficient of electroactive species and the duration of the experiment are critical, and the same electrode displaying microelectrode behaviour in an aqueous solution may show macroelectrode behaviour inside an ionic liquid [19], even if it has a dimension below 25 microns.

These special features of microelectrodes lead to several advantages compared with macroelectrodes [20], and make electrode miniaturisation an extremely valuable approach to electroanalysis. Some of the advantages due to the small geometric features of microelectrodes are that:
- They can be used in high resistivity media because, due to their low Faradaic currents, they suffer from very small ohmic (iR) drops.
- They also display lower background currents, which are proportional to electrode area.
- They are in general more sensitive because they experience much higher current densities than macroelectrodes.
- They can be used in the study of fast electron transfer and homogeneous kinetics processes because, in addition to the previous advantages, they respond very fast to concentration changes.
- They can be used in small samples.
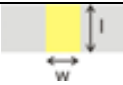
Disk microelectrodes are the most common but other configurations have also been studied. These are band, hemisphere and sphere microelectrodes. Although disks and bands are the two microelectrode geometries used in this thesis, Table 2-1 summarises the different

configurations found in the literature, showing the critical dimension for each configuration and the expressions describing their respective limiting currents [2].

As it was mentioned above, radial diffusion allows microelectrodes to achieve a stationary current. Microbands are an exception because, due to their geometry, quasi-stationary state is achieved and the current decreases slightly with time [2]. The combination of microelectrodes leads to the next topic, which is microelectrode arrays.

Table 2-1: Common microelectrode types, with their critical dimensional, steady state current expression and shape.

Configuration	Dimension	Limiting current		Shape
Band	w:width l:length	$nFl[R]_o 2\pi D_R / \ln(64\, D_R\, t/w^2)$	Quasi-stationary	
Disk	r_o:radius	$4nF\, D_R[R]_o r_o$	Stationary	
Hemisphere	r_o:radius	$2\pi nF\, D_R[R]_o r_o$	Stationary	
Sphere	r_o:radius	$4\pi nF\, D_R[R]_o r_o$	Stationary	

Microelectrode arrays are used because the currents measured by single microelectrodes are frequently too small or difficult to measure (for instance due to the presence of electrical noise). Microelectrode arrays are sets of microelectrodes working together either independently or in parallel. In this thesis we have only used arrays of microelectrodes working in parallel. Microelectrode arrays keep most of the advantages mentioned above for a single electrode and highly increase the value of the measured current. The one advantage of single microelectrodes that microelectrode arrays do not share is reduced ohmic drop. In the case of microelectrode arrays, because the current is amplified N times, the product iR is consequently N times bigger than at a microelectrode. In some cases, it could even be larger than for a macroelectrode of the same area as occupied by the array. This has important consequences, for example, in continuous electroanalysis or in electrosynthesis in microreactors. Barring this, microelectrode arrays add a much larger current to the advantages afforded by microelectrodes. An important configuration is the well known interdigitated microelectrode [21, 22]. These are sets of band microelectrodes, and when there is no interaction between them the quasi-stationary current value showed in Table 2-1 can be used. In this work, the electrode configuration used for stagnant application is the disk microelectrode array and the disk nanoelectrode array. They consist on arrays of arranged disk electrodes. In hydrodynamics conditions, the configuration used is the microband which is more the simplest and most favourable configuration to use in such conditions.

2.3.1 Electrochemical experiments

One of the most popular electrochemical experimental set-up for voltammetric measurements is shown in Figure 2-5. It consists of 3 electrodes and a potentiostat. The three electrodes are the working electrode (WE), the counter electrode (CE) and the reference electrode (RE). A potentiostat is an electronic system that applies the corresponding external potential to the electrodes. The current is measured between working and counter electrode and, but as in every electronic circuit, it is necessary to have a potential reference. In a voltammetric cell the potential is applied between working (or counter) electrode and the reference electrode which is where the applied external potential is referenced [16].The main characteristics of a good reference electrode are [16] that:

- Its equilibrium potential is known.
- The chemical composition of the electrode and the solution directly in contact with it are constant.
- It must achieve thermodynamic equilibrium quickly.

Moreover, no observable current should go through the reference electrode or it should be neglibible, otherwise it could modify the concentrations involved at the equilibrium and vary the potential. One of the most common reference electrode is the Ag/AgCl electrode [2]. It is based on the equilibrium between a chlorinised Ag electrode and KCl solution known concentration. In some cases, this KCl solution also contains AgCl to provide the system further stability. The most reliable reference electrode is calomel, although its use is not allowed at certain applications due to the presence of mercury.

The measured electric current passes between working and counter electrodes through the solution. The counter electrode must be larger than the working electrode so that it does not limit the processes occurring at the working electrode. At the same time, counter and working electrodes must be sufficiently separated to ensure that the processes at the counter electrode do not interfere with those taking place at the working electrode.
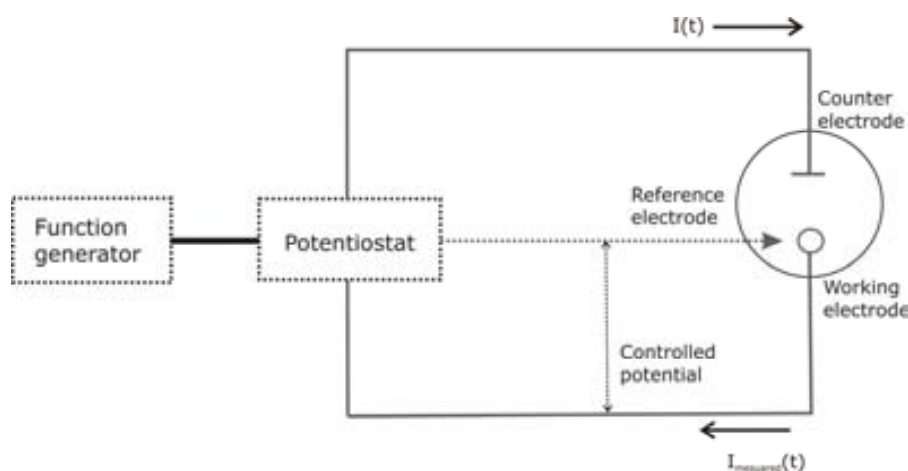

Figure 2-5: Diagrammatic representation of an electrochemical cell. It consists on three electrodes (working, counter and reference) connected to a potentiostat.

In the next section a briefly overview about microfluidics is given. Microelectrodes can be placed in microfluidic devices to take advantages of their sensitivity and rapidity of response.The voltammetric techniques explained so far and the basic cell configuration can be both used under hydrodynamic conditions.

2.4 Microfluidics and lab on a chip

This section contains two parts, fundamentals of microfluidics and an overview of lab on a chip system. The interest of lab on a chip devices lies in the analytical limitations of conventional approaches to meet all the requirements that many applications demand. Moreover, since the lab on a chip concept rests on a reduction of dimension of the device, it clearly means several advantages as: portability, reliability, reduction of sample and reagent consumption and automation of chemical analysis [23-27]. However, handling such small liquid volumes lead to a different hydrodynamic behaviour comparing to the "macro-scale".

2.4.1 Fundamentals of microfluidics

Microfluidics is the science and technology of systems that process or manipulate small (10^{-9} to 10^{-18} litres) amounts of fluids, using channels with dimensions of tens to hundreds of micrometres [27] (*sic*). However from the fluidic point of view, miniaturisation does not simply mean a reduction of dimensions. The importance of forces at work changes as the size of channels decreases. For instance, at the micro scale inertial forces are not nearly as important as viscosity or pressure differences because depth inside the channel can be neglected. As a consequence of the importance of viscous force in microfluidics, the flow regime is laminar and turbulence is almost inexistent or just a very local phenomenon [15]. Laminar flow is defined when a fluid flows in parallel layers without disruption between the layers.

The main advantage of laminar flow is its predictability, but on the other hand the lack of turbulence makes mixing more difficult. Another characteristic of microfluidic devices is that diffusion becomes a fundamental mechanism for mass transport, and mixing in these systems occurs mainly by diffusion [28]. Finally, as the surface to volume ratio increases with decreasing channel dimensions, new effects due to the interaction between the surface and the liquid may affect the liquid movement significantly [29].

The equations that define fluid dynamics are summarised below, and specific particularities of fluid dynamics at the microscale are included. Fluid dynamics describe *flow*, or the movement of fluid [30]. The fundamental variable describing the kinematics of a fluid is its velocity $\vec{v}(x, y, z, t)$ and the two limiting cases are:

- *stationary flow*: when the velocity is time-independent $\dfrac{\partial \vec{v}}{\partial t} = 0$

- *uniform flow*: when the velocity is position-independent $\nabla \vec{v} = 0$

From the conservation of mass it is possible to deduce the *continuity equation*, described by:

$$\frac{\partial \rho}{\partial t} + \nabla \cdot (\rho \vec{v}) = 0 \tag{2.26}$$

where ρ is the density of the fluid.

An *incompressible flow* is defined as a fluid which density is constant regardless of time and position. In this case, the continuity equation is defined as:

$$\nabla \cdot \vec{v} = 0 \tag{2.27}$$

Application of Newton's second law to the particles composing the fluid leads to the Navier-Stokes equation [31]. It is the hydrodynamics movement equation and in general terms can be defined as:

$$\rho \left(\frac{\partial \vec{v}}{\partial t} + \vec{v} \cdot (\nabla \vec{v}) \right) = \sum_j f_j \tag{2.28}$$

where f_j are the external forces per unit volume. Considering the most common external forces, Navier-Stokes' equation for an incomprenssible fluid is:

$$\rho \left(\frac{\partial \vec{v}}{\partial t} + (\vec{v} \cdot \nabla) \vec{v} \right) = -\nabla p + \eta \nabla^2 \vec{v} + \rho \vec{g} + \rho_{el} \vec{E} \tag{2.29}$$

The first term on the right corresponds to the hydraulic force, the second term is the viscous force where η is the fluid viscosity, the third term is gravitational force and the last term is the electric force where ρ_{el} is the electric charge density. The latter is only important when intense electric fields are applied, as in the case of electrophoresis [32].

As the surface-to-volume ratio is much higher in microsystems, other forces gain importance, such as capillary forces [33]. Capillarity basically depends on *surface tension*, γ, and the *contact angle*, Θ, between the liquid and the surfaces. The surface tension of a liquid is defined as the work needed to bring enough molecules from inside the liquid volume to the surface to form a new unit area. The contact angle is the parameter characterizing the curvature of a liquid surface in contact with two other phases. However, the microfluidic channels built during this thesis were sufficiently large to neglect capillary and surface tension forces. Further information about such phenomena can be found in [28, 29].

From the normalisation of equation (2.29) it is possible to define non-dimensional parameters connecting the different terms. One of the most important non-dimensional parameters is the Reynolds number, Re. The Reynolds number relates the viscous force with the inertial term, $\vec{v} \cdot (\nabla \vec{v})$, and it is described as:

$$\text{Re} = \frac{\rho V_o L_o}{\eta} \tag{2.30}$$

where V_o is the average velocity of the moving liquid and L_o is the typical length scale. Mechanically, the viscous forces can be defined as the friction of the fluid with the walls of the channel, therefore the higher surface to volume ratio the larger friction to liquid motion. Experimentally, Reynolds numbers higher than 2300 corresponds to turbulent flow*s* where inertial forces are dominant and, conversely, Reynolds numbers under 2000 correspond to

laminar flow regime [15]. The typical length scales in microsystems are of the order of micrometers result in very low Reynolds numbers and, consequently, mainly laminar flow regimes.

2.4.2 Lab on a chip overview

Since the first works of Manz and Harrison [34-36] in the early nineties, µTAS (micrototal analysis systems, later named lab on a chip) have excited the interest of many researchers due to their high degree of integration, portability, minimal reagent consumption, high performance, and speed [23-27]. Microfluidic chips are versatile systems; they can be used in a wide range of scientific fields like biomedical and pharmaceutical analysis, clinical diagnostics, environmental monitoring and forensic investigations. This section looks over the general history of the field, its applications, materials and microfluidic components. Particularly, we focus on lab on a chip devices based on electrochemical detection which is the technique used in this thesis.

There is a large volume of work in the bibliography describing electrochemical detection in lab on a chip [37-41], although fluorescence has been the most popular and traditional detection method to date [37, 38, 42-44]. Electrochemistry offers the possibility to detect a wide range of analytes, a high degree of portability using quite inexpensive and low power consumption devices compared with other detection techniques, and very high compatibility with microfabrication techniques [37, 39, 45]. For that reason, electrochemical lab on a chip are a good opportunity for on-site real-time applications and real sample applications as Escarpa and co-workers described recently [46]. Although electrochemistry can be used for other functions like on chip pumping, sample clean-up or preconcentration, we will focus on electrochemical detectors mainly using amperometry as it is the detection performed during this thesis.

All analytical measurements have to deal with two important parameters: sensitivity and selectivity. Lab on a chip devices can deal with extremely small volumes, which poses both important advantages and disadvantages [39, 45]. Small volumes mean reagents cost reduction and improvement in detection speed, but it also means low signal levels. At this point, electrochemical detection is a good option because electrochemical reactions are based on surface reactions on electrode, so electrochemical sensors can be miniaturised without losing performance [39]. Moreover, different signal amplification strategies can be used to increase sensitivity, an example of which will be described in Chapter 7. There a simple switching between flow rates highly amplify the final signal.

Selectivity can be achieved using specific enzymes or antibody/antigen systems [44], however separation techniques have been highly related to lab a on chip since its origin. In that case the sample is injected, and its different components are sequentially detected after being separated [43]. The most popular separation techniques are electrophoresis and chromatography [43, 47-49]. Chromatography can be used to separated charged and un-

charged molecules and it is based on the physicochemical differences of the different components and their different affinity towards a solid immobilised phase [43]. On the other hand, electrophoresis uses an electric field to separate charged molecules according to their charge-to-mass ratios in a liquid phase or gel [48]. Moreover electrokinetic flow offers other advantages [37] like a flat velocity profile instead of the parabolic one obtained by pressure-driven flow, which means less band broadening, and easier control of the flow at different microchannels using a few electrodes. Althoug electrophoresis is not used in this thesis, we recomend some good reviews and books [43, 47-54].

Due to the previous advantages, electrochemistry has become one of the most important alternatives to optical detection. The most important drawbacks of using electrochemistry for detection in lab on a chip applications are similar to its limitations in conventional measurements [39]. Mainly, it is the necessity for electroactive analytes and the problems related to fouling the electrodes. This second drawback was taken into account to design the microdevices presented in this thesis. Furthermore, the basic motivation of the integration of a microvalve in our system is based on the idea of keeping the electrodes in the best conditions, as will be described in Chapter 8.

Immunoassays and magnetic beads

Immunoassay has become one of the most popular methods for the detection of a wide range of small molecules. The advantages of lab on chip become even more important in the case of immunoassays. For instance, biological reagents are expensive, so using small and accurate volumes drastically reduce the total experimental cost. Moreover, miniaturisation leads to a reduction of the diffusion distance and an increase of the surface to volume ratio, which enhances antigen-antibody binding reactions [55]. Immunoassays can be classified in homogenous/heterogeneous and competitive/noncompetitive assays. Heterogeneous assays involve a solid support on which the antibody is immobilised, while homogenous assays take place in the solution phase. On the other hand, in a competitive assay the target analyte competes, with a labelled analyte, for a limited number of binding sites, so the signal decreases as the labelled analyte is displaced, whereas for a noncompetitive assay, such the sandwich immunoassay represented in Figure 2-6, the signal is proportional to the target analyte concentration.

Labels play an important role in immunoassays, as in most cases, they are used as more than a simple marker. For example, enzymes can catalyze the conversion of a substrate into a detectable product, amplifying the final signal and increasing sensitivity [55]. Moreover, for electrochemical detection where electroactive species are required, the use of enzymatic labels is fundamental to catalyze a reaction fielding in an electroactive product. Zhang *et. al.* [56] presented a microsystem, were platinum electrodes are fabricated on glass and covered by a polydimethylsiloxane (PDMS) layer, for the detection of tumor markers, carcinoembryonic antigen (CEA) and alpha-fetoprotein (AFT). Both antigens are incubated

with two enzyme labelled antibodies in a non-competitive assay. The samples are injected into the microdevice, separated by electrophoresis and detected amperometrically.

In Chatrathi *et. al.* work [57], they immovilised antibody over gold surface electrode based on the covalent attached between the gold surface and thiolated antibodies. They use such immobilisation for the detection, performing a sandwich immoassay, of Staphylococcal enterotoxin B, which is an enterotoxin produced by *Staphylococcous aureus* and causing the most common foodborne illnesses. Krylov *et. al.* [58] presented an interesting enzymatic assay for the detection of antioxidant measuring the concentration of superoxide and hydrogen peroxide after mixing with an antioxidant solution. Both, superoxide and hydrogen peroxide are generated using an immobilised enzyme, xanthine oxidase. So, the assay consist on injecting a buffer solution through the enzymatic chamber where both substances are generated thanks to the catalytic enzyme reaction, later the generated product is mixed with an antioxidant solution and finally detected amperometrically at the electrodes.

Multinanalyte assays reduce the sample volumes and the cost compared to parallel assay. Wilson *et. a*l [59] described a multianalyte immunoassay based on amperometric detection. It basically consists on several iridium electrodes where specific antibodies were immobilises by adsorption, so each electrode is able to detect one specific analyte according to the antibody. The immunoassay is a sandwich assay where the last antibody is marked with an enzyme (alkaline phosphatase). The distance between electrodes must be large enough to avoid cross-talk interference between neighbouring electrodes.
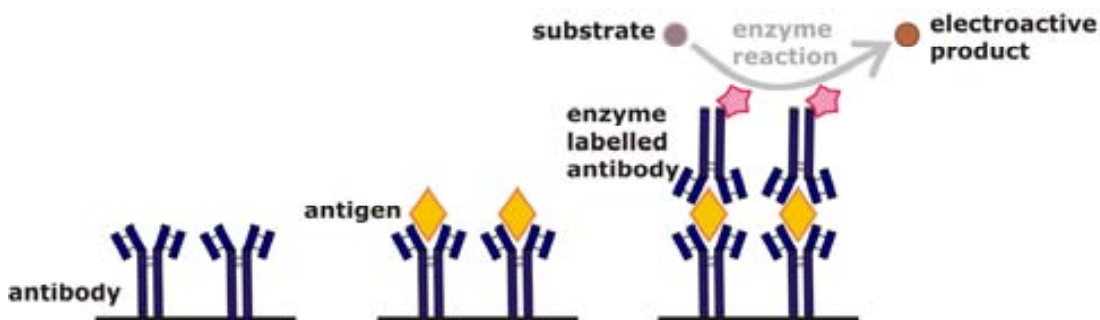
Figure 2-6: Diagrammatic representation of a sandwich immunoassay. The product of the label enzyme reaction must be electroactive in an electrochemical immunoassay.

One important type of heterogenous assay use microbeads as a solid support [55, 60, 61] for the antibodies instead of the electrode surface. Microbeads are very useful in bioassay. They highly increase the surface area in small volumes, they reduce incubation time and, as they often contain an iron core, they can be easily captured and moved around with the aid of a magnet. The incorporation of magnetic particles is an important aspect of lab-on-a-chip devices because of the flexibility they offer [61-63]. In electrochemical biosensors, where the bio-recognition element is typically linked to the electrode surface using magnetic beads allows keeping the electrodes clean and active longer. Moreover, any biomolecule can be virtually immobilised on their surface following conventional chemical approaches. Suitably modified magnetic particles can be used to pre-concentrate a sample, they can then be

driven towards the detector, where the assay may be finished after performing yhe necessary intermediate steps. Using magnetic beads, the same electrodes may be used for the detection of different analytes and they may also last longer because fouling and passivation may be prevented. Magnetic particles and amperometry have been successfully combined for (bio)electroanalytical purposes [64-69]. Ahn and co- workers [64] developed a general biochemical system for biomolecules detection using magnetic beads. The electrochemical sensor, interdigitated gold microelectrodes made on silicon, and the microfluidic platform, made of glass, where fabricated independently and bonded together. The system is composed of five input channels where the needed reagents for the sandwich immunoassays are contained and injected sequentially. The magnetic beads are captured due to the magnetic field created by an electromagnet. Later, they optimised the previous system reducing the material cost and simplifying the fabrication process [65]. For that purpose, a chip containing the interdigitated electodes is placed on a polymer microfluidic deviced fabricated by injection molding (see Figure 2-7). Moreover, a magnetic bead separator was fabricated. It consists on 100x50 array electroplated permalloy square patterns. Using an external permament magnet, the magnetic field is concentrated between the permalloy patterns creating a high magnetic field gradient between them and attraping and spreading the magnetic beads for the whole surface occupied by the permalloy pattern array. Merkoçi *et. al*. [69] described, an amperometric lab on a chip for the detection of a carbofuran using magnetic beads. In that work, the detection was based on the enzymatic inhibition due to the ability of the toxic compound to attach to the active site of the enzyme and inhibit its activity. They used glass microfabricated chip and a plexigas holder to house the chip and the fluidic reservoirs. Heineman *et. al.* [70] demonstrated the great potential of nanointerdigitated electrodes, due to their high sensitivity, to perform bioassays. For that purpose, 10μL of a solution containing the biofunctionalised magnetic beads was directed placed on the electrodes. The bioassay consists on a sandwich assay, so the presence of the target bacteriophage was indirectly detected by amperometry.
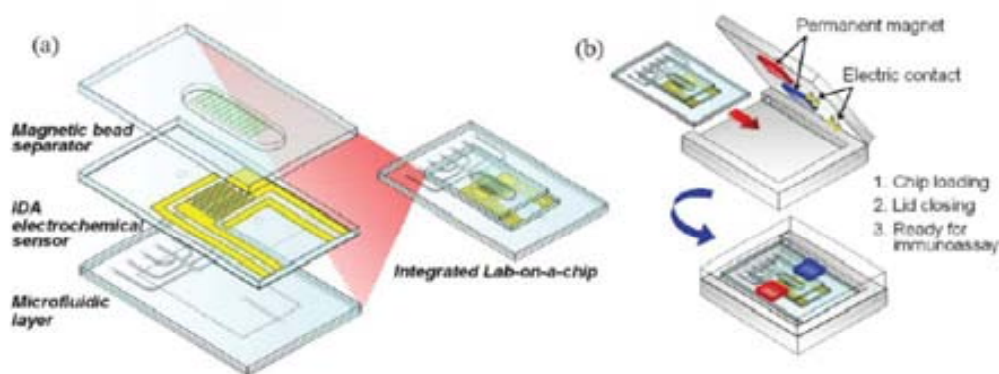

Figure 2-7: Representation of the polymer lab on a chip system presented by Ahn *et. al*. [65] (a)Magnetic bead separator, detection and microfluidic features layers are showed, they are all bonded together (b) The lab on a chip is closed on a external structure where electric contacts and permanent magnets are hosted. Reproduced with permission of the RSC.

Materials

This subsection contains two main parts related to the fabrication of the microfluidic devices and the electrodes, respectively.

The materials used to fabricate the microfluidic devices highly depend on the application but they mainly are fabricated of glass, silicon and polymers. Early works in microfluidics were mainly based on microfabrication technologies [34-36] so the most common materials were silicon, glass or even quartz. This was a natural transition as all the knowledge about patterning, etching and bonding was transferred from the micro electro mechanical systems (MEMS) to lab on a chip. However, the use of polymers has increased exponentially during the last decade [23, 71-73], paving the way to a vast new range of possibilities. Some polymer techniques can even be used outside a cleanroom environment, which drastically reduces time and cost of development. Such reduction and the possibility of mass production using techniques like hot embossing or injection molding lead to disposable polymer devices, which are required in clinical assays to eliminate the risk of contamination [72]. Furthermore, some of these polymers are permeable to oxygen and carbon dioxide, one demanded characteristic in biological applications like, for example, cell growth.

There are different classifications of polymers. One of the most popular is based on their different response to thermal treatment [74]. In that case, polymers can be divided in thermosets (also called duroplastic materials) or thermoplastics. The criterion of demarcation there is whether or not they are affected by curing process involving irreversible chemical reactions that change the linkage between molecules in the polymer chains. Additionally, one of the most important physical parameters describing polymers is their glass transition temperature (T_g) [74]. For temperatures above the glass transition the polymer becomes flexible, soft, and easy to deform, while for temperatures below T_g behaves pretty much like a rigid, solid amorphous glass [72]. A brief definition of both kind of polymers is:

> *Duroplastic materials* can be liquid or solid at room temperature and as the temperature increases or they are radiated the polymer chains start to cross-link. This process is normally called curing. This is the way to create hard and inflexible structures with them. The curing process is irreversible, and instead of melting, duroplastic materials descompose at high temperature. Therefore, T_g is high and close to the decomposition temperature.

> *Thermoplastic materials* are mouldable around T_g when their softness changes. Since this is not a curing process, so modified parts can be reshaped by reheating the material. The most typical thermoplastic are: polymethyl methacrylate (PMMA), polycarbonate (PC), cycloolefin polymers (COP) or copolymers (COC).
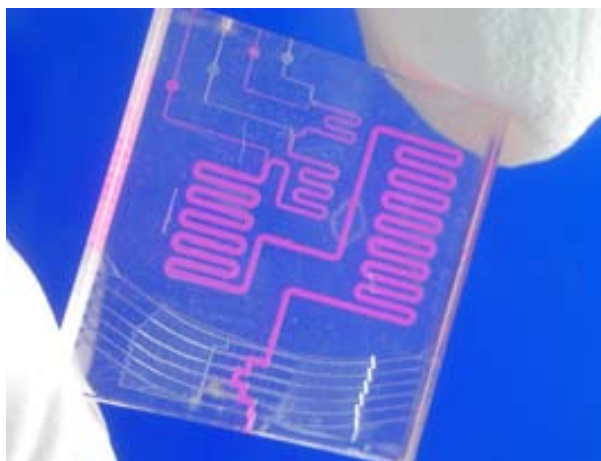
Figure 2-8: Picture of a polymer microdevice fabricated in PMMA and SU8 for the detection ammonia (Berthelot reaction) by absorbance. Picture cortesy of Dr. Detlef Snakenborg.

Related to microelectrode fabrication, platinum and gold are probably the most commonly used electrode materials [5, 75] due to their wide potential window for electrochemical measurements and their suitability for biological applications. On the other hand, silicon and glass are the most common material used as substrate in microtechnology. However, other materials can be uses either to fabricate the microelectrodes or as substrates. The Microsystems and BioMEMS group of the University of Cincinnati, led by Professor Chong H. Ahn has published numerous works using different electrode materials and substrates. They described a phosphate sensor [76] consisting of cobalt microelectrodes integrated in a microfluidic channel. A Co layer is deposited over an Au layer using standard microfabrication technology. They also fabricated a Bismuth electrode [77] for the detection of Pb(II) and Cd (II) inside a microfluidic device. Microelectrodes are defined over a cylic olefin copolymer (COC). In [78], Ahn and co- workers used nanoinjection molding to fabricate gold electrodes on COC. First, a master mold for the injection molding is fabricated and subsequently used to define the electrode patterns on the polymer structure. Once the patterns are defined as cavities, a gold layer is deposited. After several etching steps, the metal outside the cavities is removed and the electrodes are defined. The main advantage of this technology is that the lithography step is reduced just to the nanoinjection process. In [79, 80], Ahn's group fabricated a flexible biosensor on a spirally rolled microtube to facilitate packaging and simplify integration as a clinical tool. Gold electrodes were first fabricated on a flexible layer (Kapton film) and then rolled spirally making tubes of different diameters. They fabricated glucose electrodes and demonstrated their feasibility for cardiovascular characterisation. Later, these workers used a similar approach to fabricate a lab on a chip, working as smart catheter, capable of continuously monitoring multiple physiological and metabolic parameters in traumatic brain injured patients [81].

Wilson *et. al*. [59] used an iridium oxide electrode to perform a multianalyte immonoassay. Iridum oxide has several advantages for immunoassay as its 3D matrix, where proteins can be easily immobilised with a high degree of transport for water, protons and other ions as

well as due to its conductive behaviour. Seo *et. al.* [82] fabricated in their work embedded inlaid gold microelectrodes in a plastic substrate (polyethylene terephthalate, PET). The fabrication is based on an alternative lithographic method using a novel imprinting procedure.

Screen printing is a serigraphic technique widely used in electrochemistry to fabricate electrodes [83-85]. Screen printed electrodes are produced by printing different inks on plastic or ceramic substrates. The composition of the ink determines the selectivity and sensitivity of the microelectrodes [85]. Bejarano *et. al.* [86] fabricated 3D patterns using screen printing to design microelectrodes and microchannels at the same time. Using such technology they avoided working in a clean room, and combining different materials in the fabrication of the microfluidic devices, which can be a complicated process.

This subsection about materials can be not closed without mentioning the increasing use of nanomaterials in electrochemistry [49]. Carbon nanotubes, nanoparticles and nanowires are the most popular nanomaterials used for electrochemical detection nowadays. The main advantages using these nanomaterials for electrochemical detection are: increase of sensitivity, lower limits of detection and higher versatility, as they can be used in a wide range of assays [37, 49]. Carbon nanotubes (CNT) have had a deep impact on a wide range of applications and fields due its high conductivity. In particular, they are very useful in electrochemical applications because of their high surface area and rigid structure [87], but their description and use beyond the scope of the present thesis.

Components

The integration of microfluidic components such as microvalves or micropumps, is one of the most challenging tasks of minituarisation [88]. Fabricating an ideal valve means zero leakage, zero consumption, zero dead volume and infinite pressure capability [89]. However, as it is not possible to achieve all these features at the same time, trade-offs are required so that the valve configuration must suit the final application. So, it is important to highlight that there is a wide diversity of microvalves considering their design, material and actuation [88] because they mainly depend on the application, as well as the conditions where they are going to be used or how often they are going to be swtiched [89].

Valves are classified in passive, when they actuate by themselves, or active, when they need an external actuator. The most popular active microvalves consist in mechanical moving parts, mainly actuated by magnetic, electric, piezoelectric or thermal actuators, or non-mechanical moving parts, based on electrochemical, phase change or rheological materials. One example is the microfluidic large scale integration (LSI) presented by Quake's group [26, 90, 91]. The basis of its operation relies on the mechanical flexibility of the polymer used for the fabrication [90], polydimethylsiloxane (PDMS). Using air pressure or vacumm in an additional pneumatic channel, the microfluidic PDMS microchannel can be open or collapsed, so the fluid can pass freely or be stopped. Another example of active valve, closer to the microvalve developed during this thesis, is the rotary microvalve

presented by Yin *et. al.*[92], who integrated a packed column within a small valve in a fully automated chromatographic system for peptide analysis. The whole device is fabricated in polyamide films using laser ablation. The rotary valve is mounted and clamped on the polyamide chip aligning the valves ports with the ports defined on the chip.

Passive valves are based on the pressure gradient across the fluidic channel. The most common types of passive valves are: cantilever, disc and membrane types [88, 93]. They are parallel to the substrate, whose motion under forward pressure allows the flow then and block under reverse, so they are widely used to fabricate micropumps [88]. Generally, micropumps consist of a pump chamber with two microvalves, one at the inlet and the other one at the outlet. The displacement of the pump chamber, due to an actuator, combined with the valves movement lead to fluid pumping [89]. For reader's interested in micropumps we recommend the following works [94-96].

2.5 Simulation overview

The simulations performed during this thesis consisted in the solution of the mass transport equations to microelectrodes of different geometries under different environments. All cases fall in one of two categories: stationary or hydrodynamic conditions.

- Stationary cases involve the simulation of diffusion at disk microelectrodes, either in isolation or grouped in arrays, and nanoelectrode arrays.
- Hydrodynamic simulations, on the other hand, address diffusion at microband electrodes placed inside microfluidic channels.

Simulations are used at the design stage but also to aid in the interpretation of experimental results, where they have led to the realisation of important insights. Simulation is an essential tool to study and predict mass transport using microelectrodes. An overview of simulations performed by several authors in stagnant and under hydrodynamic conditions is presented in this section.

2.5.1 Microelectrodes in a stagnant solution

The simplest case that we modelled corresponds to a microdisk electrode oxidising or reducing an electroactive species in a quiescent solution. Mass transport from the bulk to the microelectrode surface is mathematically described by Fick's laws [2], and the partial differential equations need to be solved in combination with the right boundary conditions [2]. However, while it is possible to reach the expression for its steady state current analytically, the transient description of the current is a numerical solution consisting on a mathematical series [97]. The first expression describing the transient behaviour of the current at a microelectrode was presented by Aoki and Osteryoung [98, 99]. It is a numerical solution based on a parameter defined as: $\tau = 4Dt / r^2$ where D is the diffusion coefficient of the

electroactive species, *t* is time and *r* is the radius of the microdisk. The solution has two regions with two different solutions depending on the value of τ. Shoup and Szabo [100] presented a solution of just one expression for all values of τ, with an error smaller than 0.6%. In addition to this, there are some other later approximations, defined by Rajendran [101] or Mahon and Oldham [102], among others.

The first models of mass transfer using a microdisk compared their simulated results with the theoretical approximations previously mentioned [97]. One of the first model was presented by Flanagan and Marcoux [103]. Later, Heinze [104] built a model based on an algorithm of finite differences to describe the diffusional stationary process at a microdisk.

One of the major difficulties to simulate the mass transport at a microelectrode is the singularity found at the microelectrode perimeter, because the boundary conditions there change abruptly. While the condition on the outer points is of no-mass-flux because the microelectrode is surrounded by an insulator [97], there is a flux condition inside the electrode boundary, as it is showed in Figure 2-9. Moreover, the concentration profile over the microelectrode is not flat, as in the case of a macroelectrode, but hemispherical. Hence the distribution of current across the surface of the microelectrode is not uniform, the current density being much larger at the perimeter. One way to avoid the singularity, used by Amatore [105, 106], is to apply conformal projections. In those works, they present solutions for the stationary and transient cases using the Hopscotch algorithm based on finite differences [107]. Amatore and Svir [108] reduced the problem of the singularity using two discretisation domains, one closer to the electrode, where the intervals are smaller, and another one further from the electrode, with longer intervals. Gavaghan [109-114] built his models using cylindrical coordinates. The domain is also discretised so that the intervals are smaller in the zones near the discontinuity, and uses both finite elements [109, 114] and finite differences [110-113]. Girault [115] also developed a discretisation algorithm of the two-dimensional domain so that the intervals are smaller in the points where the gradient of concentration is higher.
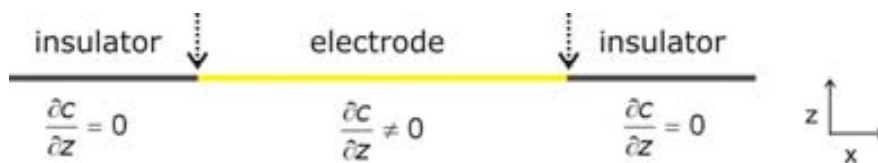
Figure 2-9: Diagrammatic scheme of an inlaid microelectrode embedded in an insulator layer. There is only mass flux through the electrode, so at the points marked by the arrows there is a concentration gradient singularity.

2.5.2 Microelectrode arrays

As the current supplied by a single microelectrode is quite small, it is normally useful to amplify the measured signal using a microelectrode array [116]. Here the microelectrodes

are mainly distributed either in cubic or hexagonal arrangement [117-120] but they can also be random ensembles [117, 121].

The solution of the mass transport problem at microelectrode arrays is more complex than for single microelectrodes. It is now necessary to consider the distance between microelectrodes in the array and the interaction between them. For short measurement times, the diffusion layer around each microelectrode is small enough and the interaction between microelectrodes can be neglected. In this case, each microelectrode in the array behaves independently from each other (see Figure 2-10A). As time elapses, the diffusion layers of neighbouring microelectrodes can overlap [117, 119, 122] (see Figure 2-10B).This interaction between microelectrodes is reflected in the measured current as they are not independent. Gueshi *et al.* [118] solved the partial differential equations numerically and Rellet *et al.* [120] used finite difference to solve the system proposed by Gueshi, but neither approach was very accurate. Shoup and Szabo [107] solved the system using a Hopscotch algorithm [123], and more recently, Girault *et al.* [116, 119] defined a three-dimensional model to establish some design guidelines. In this case, simulations have become the only way to achieve an accurate determination of the current at these rather complex devices [121]. The difficulty of finding a universal guideline to define microelectode arrays remains on the fact that the diffusion overlapping depends on different design parameters, as microdisk radius and the intercenter distance, as well as experimental parameters, as diffusion coefficient and scan rate [124]. Compton *et al*. [117, 122] used a two-dimensional approach known as the diffusion domain approach, based on an strategy first described by Amatore [125]. Such approximation consists on dividing the whole array in diffusionally independent and highly symmetric unit cells. This approximation is widely explained in Chapter 4, as it is an fundamental tool to model the micro- and nanodisk arrays used in this work.
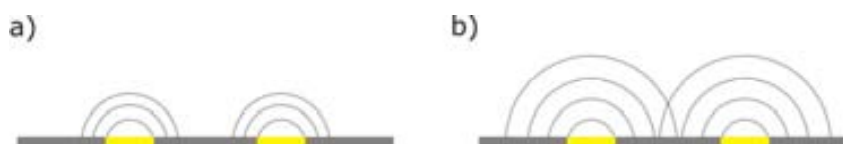
Figure 2-10: Representation ot concentration profiles at neighbouring disk microelectrodes. At short times (case a)), there is no interaction between neighbouring diffusion layers and each microdisk behaves like an independent microelectrode. At long times (case b)) neighbouring diffusion layer overlapped and affect the measured current.

In this thesis COMSOL Multiphysics (COMSOLAB, Sweeden), a commercial software package, was used to solve the mass transport problems and simulate the voltammetric response of microelectrodes. This software is based on the finite element method. Our main objective is not the development of mathematical models, but rather to understand the phenomena underpinning electrochemical detection and the application of this knowledge to the design and fabrication of new devices. The discontinuity problem mentioned above was overcome by the use of more elements in the domain regions where the concentration

gradients are steeper. Moreover, as the disk microelectrode arrays were well simulated during this thesis, this led us to a further step which was the simulation of nanodisk arrays (Chapter 6). Although there were some works about the design and fabrication of nanoelectrodes [126-132], there were no theoretical studies as those perfomed for microdisks arrays to establish some design guidelines explaining how the different parameters affect diffusional mass transport.

2.5.3 Microelectrodes under hydrodynamic conditions

Electrochemical detection in fluidic systems allows the continuous monitoring of the current or the study of mechanistical processes in which heterogeneous electron transfer is involved [133]. Channel electrodes are defined as electrodes placed on one of the channel walls over which the electrolyte solution flows [8]. Ideally, the reference electrode must be as close as possible to the working electrode [2, 134]. However, if the reference electrode can not be placed in the same channel, then at least it must be in direct contact with the solution flowing through it [133]. The most popular geometry for microelectrodes in fluidic channels is the microband [135-137]. In this thesis, microband channel electrodes were integrated in a microfluidic device as it will be described in Chapter 7. In order to characterise and validate the experimental current, different hydrodynamic models were solved. Each of these models has it own pecularities, but they all share the fact that microband electrodes were located in a long, straight channel of rectangular section. For the hydrodymamic case, where both mass and momentum transfer affect, modelling is even more necessary and it is almost the only way to find an approximate solution.

Levich [13] solved the partial differential equations that define mass transport close to the walls in a fluidic channel of cylindrical cross section when the velocity profile is stationary. From this approximation it is possible to deduce a theoretical expression for the transport-limited current measured by a macroelectrode placed in a fluidic channel. Based on Levich's theory, Compton *et al.* [136] described the theory for band microelectrodes inside a microchannel where Levich's conditions can be considered. Considering a known velocity profile, they demonstrated that microelectrode response depends on such flow velocity. For high flow velocities, the measured current can be described according to Levich's prediction [13]. However, for lower fluid velocities the measured currents are higher due to the contribution of radial diffusion at the edge of the microelectrodes. They solved the mass transport using a Hopscotch algorithm based on finite differences. More recently, Compton *et al.* [138] presented a study of the velocity profile of the microelectrodes placed at the inlet of a channel where the parabolic profile is still not achieved. They predicted the profile through electrochemical mesuarements.

Among other authors, Adrien C. Fisher has used different discretisation techniques, based on finite element methods and finite differences, to study microelectrodes placed in microfluidic channels. For instance, he used finite elements to model the stationary current for a macroelectrode and for a microelectrode in a channel [137]. While diffusional transport

is three-dimensional, the convective term is just one-dimensional in the direction of movement. An electrochemical microreactor is described in [139] considering different channel widths. In that work, it was demonstrated that even in spite of the possible effect of the walls to the measured current, the current depends on flow rate as Levich's prediction. These results were later validated with a three dimensional model [140]. The influence of the channel walls on the measured current has been studied more recently in [141]. Futhermore, an even more realistic model is described in [142] where the effect of the ohmic drop across the microfluidic channel is also taken into account.

Other authors like C. Amatore or H.H. Girault have also studied the behaviour of microelectrodes under hydrodynamic conditions. Amatore *et al.* [135] uses a conformal projection, previously used in [105, 106], in order to solve the mass transport, by diffusion and convection, for a band microelectrode in a microfluidic channel. Furthermore, they used the results obtained in that work to define a method to build the hydrodynamic velocity profile [143-145] in rectangular cross section channels. In those works, they compared the experimental current values with the modelled ones to build, indirectly, the velocity profile developed in the microchannel. This allowed them to study changes in the velocity profile due to different material slip properties or wall roughness. Later, they presented simulations and experimental results that describe mass transport under steady state flow at channel microband electrodes for a single electrode [146] and for dual electrode configuration [147]. In [146] simulations performed using COMSOL Multyphisics described the steady state amperometric response of the microband related to channel geometry and flow velocities. Girault *et al.* [148] described a model to solve the mass transport and the fluid movement considering recessed and protruding microelectrodes.

2.6 Summary

We have first introduced the fundamental concepts of electrochemistry and microelectrodes which are essential to understand the electrochemical detection developed during this thesis. They will be further used to build our theoretical models. We also have presented overviews of lab on a chip and simulation of microelectrodes. With the simulation overview, we aim to contextualise our work and demonstrate the necessity of simulation as fundamental validation tool for most of real cases. In the lab on a chip review, we have explained the advantages of the integration concept as well as the most relevant applications and materials, related to the applications developed during this thesis.

2.7 References

[1] Brett, C.M.A. and A.M.O. Brett, *Electroanalysis*. Oxford Chemistry Primers. Vol. 64. 1998: Oxford Science Press.

[2] Allen J. Bard, L.R.F., *ELECTROCHEMICAL METHODS. Fundamentals and Applications*. 2nd ed. 2001, New York: John Wiley & sons.

[3] Banks, C.E., T.J. Davies, R.G. Evans, G. Hignett, A.J. Wain, N.S. Lawrence, J.D. Wadhawan, F. Marken, and R.G. Compton, *Electrochemistry of immobilised redox droplets: Concepts and applications.* Physical Chemistry Chemical Physics, 2003. 5(19): p. 4053-4069.

[4] Campbell, J.A. and H.H. Girault, *Steady state current for ion transfer reactions at a micro liquid/liquid interface.* Journal of Electroanalytical Chemistry, 1989. 266(2): p. 465-469.

[5] Ordeig, O., J. Del Campo, F.X. Muñoz, C.E. Banks, and R.G. Compton, *Electroanalysis utilizing amperometric microdisk electrode arrays.* Electroanalysis, 2007. 19(19-20): p. 1973-1986.

[6] Atkins, P.W., *Química física*. 1999: Omega.

[7] Scholz, F., ed. *Electroanalytical Methods: Guide to Experiments and Applications*. 2002, Springer.

[8] Wang, J., *Analytical Electrochemistry*. Second Edition ed. 2000: Wiley-VCH.

[9] Marcus, R.A., *Theory of Oxidation-Reduction Reactions Involving Electron Transfer .1.* Journal of Chemical Physics, 1956. 24(5): p. 966-978.

[10] Marcus, R.A., *Electron Transfer at Electrodes and in Solution - Comparison of Theory and Experiment.* Electrochimica Acta, 1968. 13(5): p. 995-&.

[11] Hush, N.S., *Adiabatic Rate Processes at Electrodes .1. Energy-Charge Relationships.* Journal of Chemical Physics, 1958. 28(5): p. 962-972.

[12] Hush, N.S., *Homogeneous and Heterogeneous Optical and Thermal Electron Transfer.* Electrochimica Acta, 1968. 13(5): p. 1005-&.

[13] Levich, V.G., *Physicochemical Hydrodynamics*. 1962, Englewood Cliffs, N. J.: Prentice-Hall, Inc.

[14] Amatore, C., *Electrochemistry at ultramicroelectrodes*, in *Phyical Electrochemistry. Principles, methods and applications*, I. Rubinstein, Editor, Marcel Dekker, Inc.

[15] Kutter, J.P. and H. Klank, *Microfluidics-Theoretical Aspect*, in *Microsystem Engineering of Lab-on-a-Chip Devices*, O. Geschke, H. Klank, and P. Telleman, Editors. 2004, Wiley-VCH.

[16] Compton, R.G. and G.H.W. Sanders, *Electrode Potentials*. Oxford Chemistry Primers. Vol. 41. 1996: Oxford Science Press.

[17] Amman, D., *Ion-Selective Microelectrodes: Principles, Design and Application*. 1986, Berlin: Springer-Verlag.

[18] Cattrall, R.W., *Chemical Sensors*. 1997, New York: Oxford University Press.

[19] Kawano, R. and M. Watanabe, *Equilibrium potentials and charge transport of an I-/I3- redox couple in an ionic liquid.* Chemical Communications, 2003. 9(3): p. 330-331.

[20] Wu, Q.H., K.M. Lee, and C.C. Liu, *Development of Chemical Sensors Using Microfabrication and Micromachining Techniques.* Sensors and Actuators B-Chemical, 1993. 13(1-3): p. 1-6.

[21] Aoki, K., M. Morita, O. Niwa, and H. Tabei, *Quantitative analysis of reversible diffusion-controlled currents of redox soluble species at interdigitated array electrodes under steady-state conditions.* Journal of Electroanalytical Chemistry, 1988. 256(2): p. 269-282.

[22] Aoki, K. and M. Tanaka, *Time-dependence of diffusion-controlled currents of a soluble redox couple at interdigitated microarray electrodes.* Journal of Electroanalytical Chemistry, 1989. 266(1): p. 11-20.

[23] Duffy, D.C., J.C. McDonald, O.J.A. Schueller, and G.M. Whitesides, *Rapid prototyping of microfluidic systems in poly(dimethylsiloxane).* Analytical Chemistry, 1998. 70(23): p. 4974-4984.

[24] McDonald, J.C., D.C. Duffy, J.R. Anderson, D.T. Chiu, H. Wu, O.J.A. Schueller, and G.M. Whitesides, *Fabrication of microfluidic systems in poly(dimethylsiloxane).* Electrophoresis, 2000. 21(1): p. 27-40.

[25] Squires, T.M. and S.R. Quake, *Microfluidics: Fluid physics at the nanoliter scale.* Reviews of Modern Physics, 2005. 77(3): p. 977-1026.

[26] Unger, M.A., H.P. Chou, T. Thorsen, A. Scherer, and S.R. Quake, *Monolithic microfabricated valves and pumps by multilayer soft lithography.* Science, 2000. 288(5463): p. 113-116.

[27] Whitesides, G.M., *The origins and the future of microfluidics.* Nature, 2006. 442(7101): p. 368-373.

[28] Stone, H.A., A.D. Stroock, and A. Ajdari, *Engineering flows in small devices: Microfluidics toward a lab-on-a-chip*, in *Annual Review of Fluid Mechanics*. 2004. p. 381-411.

[29] Yang, L.J., T.J. Yao, and Y.C. Tai, *The marching velocity of the capillary meniscus in a microchannel.* Journal of Micromechanics and Microengineering, 2004. 14(2): p. 220-225.

[30] Acheson, D.J., *Elementary fluid dynamics.* Oxford applied mathematics and computing science. 2005, Oxford: Oxford University Press.

[31] Bruus, H., *Theoretical microfluidics*, in *MIC-Department of Micro and Nanotechnology*. 2004, Technical University of Denmark.

[32] Kutter, J.O.P., *Current developments in electrophoretic and chromatographic separation methods on microfabricated devices.* TrAC - Trends in Analytical Chemistry, 2000. 19(6): p. 352-363.

[33] Tabeling, P., *Introduction to microfluidics*. 2005, Oxford: Oxford University Press.

[34] Harrison, D.J., K. Fluri, K. Seiler, Z. Fan, C.S. Effenhauser, and A. Manz, *Micromachining a miniaturized capillary electrophoresis-based chemical analysis system on a chip.* Science, 1993. 261(5123): p. 895-897.

[35] Harrison, D.J., A. Manz, Z. Fan, H. Lüdi, and H.M. Widmer, *Capillary electrophoresis and sample injection systems integrated on a planar glass chip.* Analytical Chemistry, 1992. 64(17): p. 1926-1932.

[36] Manz, A., D.J. Harrison, E.M.J. Verpoorte, J.C. Fettinger, A. Paulus, H. Ludi, and H.M. Widmer, *Planar chips technology for miniaturization and integration of separation techniques into monitoring systems. Capillary electrophoresis on a chip.* Journal of Chromatography, 1992. 593(1-2): p. 253-258.

[37] Crevillén, A.G., M. Pumera, M.C. González, and A. Escarpa, *Towards lab-on-a-chip approaches in real analytical domains based on microfluidic chips/electrochemical multi-walled carbon nanotube platforms.* Lab on a Chip - Miniaturisation for Chemistry and Biology, 2009. 9(2): p. 346-353.

[38] Dittrich, P.S., K. Tachikawa, and A. Manz, *Micro total analysis systems. Latest advancements and trends.* Analytical Chemistry, 2006. 78(12): p. 3887-3907.

[39] Nyholm, L., *Electrochemical techniques for lab-on-a-chip applications.* Analyst, 2005. 130(5): p. 599-605.

[40] Sassa, F., K. Morimoto, W. Satoh, and H. Suzuki, *Electrochemical techniques for microfluidic applications.* Electrophoresis, 2008. 29(9): p. 1787-1800.

[41] West, J., M. Becker, S. Tombrink, and A. Manz, *Micro Total Analysis Systems: Latest Achievements.* Analytical Chemistry, 2008. 80(12): p. 4403-4419.

[42] Hubner, J., K.B. Mogensen, A.M. Jorgensen, P. Friis, P. Telleman, and J.P. Kutter, *Integrated optical measurement system for fluorescence spectroscopy in microfluidic channels.* Review of Scientific Instruments, 2001. 72(1 I): p. 229-233.

[43] Kutter, J.P. and Y. Fintschenko, eds. *Separation methods in microanalytical systems*. 2006, CRC press, Taylor & Francis group.

[44] Van Den Berg, A. and P. Bergveld, *Labs-on-a-Chip: Origin, highlights and future perspectives - On the occasion of the 10th µTAS conference.* Lab on a Chip - Miniaturisation for Chemistry and Biology, 2006. 6(10): p. 1266-1273.

[45] Ríos, A., A. Escarpa, M.C. González, and A.G. Crevillén, *Challenges of analytical microsystems.* TrAC - Trends in Analytical Chemistry, 2006. 25(5): p. 467-479.

[46] Crevillén, A.G., M. Hervás, M.A. López, M.C. González, and A. Escarpa, *Real sample analysis on microfluidic devices.* Talanta, 2007. 74(3): p. 342-357.

[47] Escarpa, A., M.C. González, M.A.L. Gil, A.G. Crevillén, M. Hervás, and M. García, *Microchips for CE: Breakthroughs in real-world food analysis.* Electrophoresis, 2008. 29(24): p. 4852-4861.

[48] Kutter, J.P. and O. Geschke, *Analytical Chemistry on Microsystems*, in *Microsystem Engineering of Lab-on-a-Chip Devices*, O. Geschke, H. Klank, and P. Telleman, Editors. 2004, Wiley-VCH.

[49] Pumera, M. and A. Escarpa, *Nanomaterials as electrochemical detectors in microfluidics and CE: Fundamentals, designs, and applications.* Electrophoresis, 2009. 30(19): p. 3315-3323.

[50] Du, Y. and E. Wang, *Capillary electrophoresis and microchip capillary electrophoresis with electrochemical and electrochemiluminescence detection.* Journal of Separation Science, 2007. 30(6): p. 875-890.

[51] Escarpa, A., M.C. González, A.G. Crevillén, and A.J. Blasco, *CE microchips: An opened gate to food analysis.* Electrophoresis, 2007. 28(6): p. 1002-1011.

[52] Holcomb, R.E., J.R. Kraly, and C.S. Henry, *Electrode array detector for microchip capillary electrophoresis.* Analyst, 2009. 134(3): p. 486-492.

[53] Matysik, F.M., *Advances in amperometric and conductometric detection in capillary and chip-based electrophoresis.* Microchimica Acta, 2008. 160(1-2): p. 1-14.

[54] Trojanowicz, M., *Recent developments in electrochemical flow detections-A review. Part I. Flow analysis and capillary electrophoresis.* Analytica Chimica Acta, 2009. 653(1): p. 36-58.

[55] Bange, A., H.B. Halsall, and W.R. Heineman, *Microfluidic immunosensor systems.* Biosensors and Bioelectronics, 2005. 20(12): p. 2488-2503.

[56] Zhang, S., W. Cao, J. Li, and M. Su, *MCE enzyme immunoassay for carcinoembryonic antigen and alpha-fetoprotein using electrochemical detection.* Electrophoresis, 2009. 30(19): p. 3427-3435.

[57] Chatrathi, M.P., J. Wang, and G.E. Collins, *Sandwich electrochemical immunoassay for the detection of Staphylococcal enterotoxin B based on immobilized thiolated antibodies.* Biosensors and Bioelectronics, 2007. 22(12): p. 2932-2938.

[58] Krylov, A.V., H. Adamzig, A.D. Walter, B. Löchel, E. Kurth, O. Pulz, J. Szeponik, F. Wegerich, and F. Lisdat, *Parallel generation and detection of superoxide and hydrogen peroxide in a fluidic chip.* Sensors and Actuators, B: Chemical, 2006. 119(1): p. 118-126.

[59] Wilson, M.S. and W. Nie, *Electrochemical multianalyte immunoassays using an array-based sensor.* Analytical Chemistry, 2006. 78(8): p. 2507-2513.

[60] Choi, J.-W., *Fabrication of micromachined magnetic particle separator for bioseparation in microfluidic systmes*, in *Microfluidic techniques: Reviews and protocols*, S.D. Minteer, Editor. 2006, Humana press.

[61] Verpoorte, E., *Beads and chips: new recipes for analysis.* Lab. Chip., 2003. 3: p. 60N.

[62] Gijs, M.A.M., *Magnetic bead handling on-chip: New opportunities for analytical applications.* Microfluidics and Nanofluidics, 2004. 1(1): p. 22-40.

[63] Thomas, J.H., S.K. Kim, P.J. Hesketh, H.B. Halsall, and W.R. Heineman, *Microbead-based electrochemical immunoassay with interdigitated array electrodes.* Analytical Biochemistry, 2004. 328: p. 113-122.

[64] Choi, J.W., K.W. Oh, J.H. Thomas, W.R. Heineman, H.B. Halsall, J.H. Nevin, A.J. Helmicki, H.T. Henderson, and C.H. Ahn, *An integrated microfluidic biochemical detection system for protein analysis with magnetic bead-based sampling capabilities.* Lab on a Chip - Miniaturisation for Chemistry and Biology, 2002. 2(1): p. 27-30.

[65] Do, J. and C.H. Ahn, *A polymer lab-on-a-chip for magnetic immunoassay with on-chip sampling and detection capabilities.* Lab on a Chip - Miniaturisation for Chemistry and Biology, 2008. 8(4): p. 542-549.

[66] Farrell, S., N.J. Ronkainen-Matsuno, H.B. Halsall, and W.R. Heineman, *Bead-based immunoassays with microelectrode detection.* Analytical and Bioanalytical Chemistry, 2004. 379(3): p. 358-367.

[67] Gabig-Ciminska, M., A. Holmgren, H. Andresen, K. Bundvig Barken, M. Wümpelmann, J. Albers, R. Hintsche, A. Breitenstein, P. Neubauer, M. Los, A. Czyz, G. Wegrzyn, G. Silfversparre, B. Jürgen, T. Schweder, and S.O. Enfors, *Electric chips for rapid detection and quantification of nucleic acids.* Biosensors and Bioelectronics, 2004. 19(6): p. 537-546.

[68] Goral, V.N., N.V. Zaytseva, and A.J. Baeumner, *Electrochemical microfluidic biosensor for the detection of nucleic acid sequences.* Lab on a Chip - Miniaturisation for Chemistry and Biology, 2006. 6(3): p. 414-421.

[69] Llopis, X., M. Pumera, S. Alegret, and A. Merkoçi, *Lab-on-a-chip for ultrasensitive detection of carbofuran by enzymatic inhibition with replacement of enzyme using magnetic beads.* Lab on a Chip - Miniaturisation for Chemistry and Biology, 2009. 9(9): p. 213-218.

[70] Bange, A., J. Tu, X. Zhu, C. Ahn, H.B. Halsall, and W.R. Heineman, *Electrochemical detection of MS2 phage using a bead-based immunoassay and a NanoIDA.* Electroanalysis, 2007. 19(21): p. 2202-2207.

[71] Becker, H. and C. Gärtner, *Polymer microfabrication methods for microfluidic analytical applications.* Electrophoresis, 2000. 21(1): p. 12-26.

[72] Becker, H. and C. Gärtner, *Polymer microfabrication technologies for microfluidic systems.* Analytical and Bioanalytical Chemistry, 2008. 390(1): p. 89-111.

[73] Becker, H. and L.E. Locascio, *Polymer microfluidic devices.* Talanta, 2002. 56(2): p. 267-287.

[74] Nicholson, J.W., *The chemistry of polymers.* 2006: RSC Publishing.

[75] Streeter, I., N. Fietkau, J. Del Campo, R. Mas, F.X. Muñoz, and R.G. Compton, *Voltammetry at regular microband electrode arrays: Theory and experiment.* Journal of Physical Chemistry C, 2007. 111(32): p. 12058-12066.

[76] Zou, Z., J. Han, A. Jang, P.L. Bishop, and C.H. Ahn, *A disposable on-chip phosphate sensor with planar cobalt microelectrodes on polymer substrate.* Biosensors and Bioelectronics, 2007. 22(9-10): p. 1902-1907.

[77] Zou, Z., A. Jang, E. MacKnight, P.M. Wu, J. Do, P.L. Bishop, and C.H. Ahn, *Environmentally friendly disposable sensors with microfabricated on-chip planar bismuth electrode for in situ heavy metal ions measurement.* Sensors and Actuators, B: Chemical, 2008. 134(1): p. 18-24.

[78] Rust, M.J., J. Do, H.L. Se, and C.H. Ahn, *Nanoinjection lithography for submicrometer electrodes on polymer substrates.* IEEE Transactions on Nanotechnology, 2007. 6(4): p. 460-464.

[79] Li, C., J. Han, and C.H. Ahn, *Flexible biosensors on spirally rolled micro tube for cardiovascular in vivo monitoring.* Biosensors and Bioelectronics, 2007. 22(9-10): p. 1988-1993.

[80] Li, C., P.M. Wu, J. Han, and C.H. Ahn, *A flexible polymer tube lab-chip integrated with microsensors for smart microcatheter.* Biomedical Microdevices, 2008. 10(5): p. 671-679.

[81] Li, C., P.M. Wu, W. Jung, C.H. Ahn, L.A. Shutter, and R.K. Narayan, *A novel lab-on-a-tube for multimodality neuromonitoring of patients with traumatic brain injury (TBI).* Lab on a Chip - Miniaturisation for Chemistry and Biology, 2009. 9(14): p. 1988-1990.

[82] Seo, J.H., P.L. Leow, S.H. Cho, H.W. Lim, J.Y. Kim, B.A. Patel, J.G. Park, and D. O'Hare, *Development of inlaid electrodes for whole column electrochemical detection in HPLC.* Lab on a Chip - Miniaturisation for Chemistry and Biology, 2009. 9(15): p. 2238-2244.

[83] Albareda-Sirvent, M., A. Merkoçi, and S. Alegret, *Configurations used in the design of screen-printed enzymatic biosensors. A review.* Sensors and Actuators, B: Chemical, 2000. 69(1): p. 153-163.

[84] Honeychurch, K.C. and J.P. Hart, *Screen-printed electrochemical sensors for monitoring metal pollutants.* TrAC - Trends in Analytical Chemistry, 2003. 22(7-8): p. 456-469.

[85] Renedo, O.D., M.A. Alonso-Lomillo, and M.J.A. MartÃnez, *Recent developments in the field of screen-printed electrodes and their related applications.* Talanta, 2007. 73(2): p. 202-219.

[86] Bejarano, D., P. Lozano, D. Mata, S. Cito, M. Constantí, and I. Katakis, *Screen printing as a holistic manufacturing method for multifunctional microsystems and microreactors.* Journal of Micromechanics and Microengineering, 2009. 19(11).

[87] Pumera, M., *The electrochemistry of carbon nanotubes: Fundamentals and applications.* Chemistry - A European Journal, 2009. 15(20): p. 4970-4978.

[88] Oh, K.W. and C.H. Ahn, *A review of microvalves.* Journal of Micromechanics and Microengineering, 2006. 16(5).

[89] Kutter, J.P., K.B. Mogensen, H. Klank, and O. Geschke, *Microfluidics-Components*, in *Microsystem Engineering of Lab-on-a-Chip Devices*, O. Geschke, H. Klank, and P. Telleman, Editors. 2004, Wiley-VCH.

[90] Melin, J. and S.R. Quake, *Microfluidic large-scale integration: The evolution of design rules for biological automation*, in *Annual Review of Biophysics and Biomolecular Structure*. 2007. p. 213-231.

[91] Thorsen, T., S.J. Maerkl, and S.R. Quake, *Microfluidic large-scale integration.* Science, 2002. 298(5593): p. 580-584.

[92] Yin, H., K. Killeen, R. Brennen, D. Sobek, M. Werlich, and T. Van De Goor, *Microfluidic chip for peptide analysis with an integrated HPLC column, sample enrichment column, and nanoelectrospray tip.* Analytical Chemistry, 2005. 77(2): p. 527-533.

[93] Bien, D.C.S., S.J.N. Mitchell, and H.S. Gamble, *Fabrication and characterization of a micromachined passive valve.* Journal of Micromechanics and Microengineering, 2003. 13(5): p. 557-562.

[94] Iverson, B.D. and S.V. Garimella, *Recent advances in microscale pumping technologies: A review and evaluation.* Microfluidics and Nanofluidics, 2008. 5(2): p. 145-174.

[95] Laser, D.J. and J.G. Santiago, *A review of micropumps.* Journal of Micromechanics and Microengineering, 2004. 14(6).

[96] Woias, P., *Micropumps - Past, progress and future prospects.* Sensors and Actuators, B: Chemical, 2005. 105(1): p. 28-38.

[97] Britz, D., K. Poulsen, and J. Strutwolf, *Reference values of the diffusion-limited current at a microdisk electrode.* Electrochimica Acta, 2004. 50(1): p. 107-113.

[98] Aoki, K. and J. Osteryoung, *Diffusion-controlled current at the stationary finite disk electrode: Theory.* Journal of Electroanalytical Chemistry, 1981. 122: p. 19-35.

[99] Aoki, K. and J. Osteryoung, *Formulation of the diffusion-controlled current at very small stationary disk electrodes.* Journal of Electroanalytical Chemistry, 1984. 160(1-2): p. 335-339.

[100] Shoup, D. and A. Szabo, *Chronoamperometric current at finite disk electrodes.* Journal of Electroanalytical Chemistry, 1982. 140(2): p. 237-245.

[101] Rajendran, L. and M.V. Sangaranarayanan, *A 2-Point Pade-Approximation for the Non-Steady-State Chronoamperometric Current at Ultramicrodisc Electrodes.* Journal of Electroanalytical Chemistry, 1995. 392(1-2): p. 75-78.

[102] Mahon, P.J. and K.B. Oldham, *The transient current at the disk electrode under diffusion control: a new determination by the Cope-Tallman method.* Electrochimica Acta, 2004. 49(28): p. 5041-5048.

[103] Flanagan, J.B. and L. Marcoux, *Digital Simulation of Edge Effects at Planar Disk Electrodes.* Journal of Physical Chemistry, 1973. 77(8): p. 1051-1055.

[104] Heinze, J., *Diffusion processes at finite (micro) disk electrodes solved by digital simulation.* Journal of Electroanalytical Chemistry, 1981. 124(1-2): p. 73-86.

[105] Amatore, C.A. and B. Fosset, *Space Variables Well Fitted for the Study of Steady-State and near-Steady-State Diffusion at a Microdisk.* Journal of Electroanalytical Chemistry, 1992. 328(1-2): p. 21-32.

[106] Michael, A.C., R.M. Wightman, and C.A. Amatore, *Microdisk Electrodes .1. Digital-Simulation with a Conformal-Map.* Journal of Electroanalytical Chemistry, 1989. 267(1-2): p. 33-45.

[107] Shoup, D. and A. Szabo, *Hopscotch - an Algorithm for the Numerical-Solution of Electrochemical Problems.* Journal of Electroanalytical Chemistry, 1984. 160(1-2): p. 1-17.

[108] Amatore, C. and I. Svir, *A new and powerful approach for simulation of diffusion at microelectrodes based on overlapping sub-domains: application to chronoamperometry at the microdisk.* Journal of Electroanalytical Chemistry, 2003. 557: p. 75-90.

[109] Galceran, J., D.J. Gavaghan, and J.S. Rollett, *2-Dimensional Implementation of the Finite-Element Method with Singularity Correction for Diffusion-Limited Current at an Unshielded Disc Electrode.* Journal of Electroanalytical Chemistry, 1995. 394(1-2): p. 17-28.

[110] Gavaghan, D.J., *An exponentially expanding mesh ideally suited to the fast and efficient simulation of diffusion processes at microdisc electrodes. 1. Derivation of the mesh.* Journal of Electroanalytical Chemistry, 1998. 456(1-2): p. 1-12.

[111] Gavaghan, D.J., *An exponentially expanding mesh ideally suited to the fast and efficient simulation of diffusion processes at microdisc electrodes. 2. Application to chronoamperometry.* Journal of Electroanalytical Chemistry, 1998. 456(1-2): p. 13-23.

[112] Gavaghan, D.J., *An exponentially expanding mesh ideally suited to the fast and efficient simulation of diffusion processes at microdisc electrodes. 3. Application to voltammetry.* Journal of Electroanalytical Chemistry, 1998. 456(1-2): p. 25-35.

[113] Gavaghan, D.J. and J.S. Rollett, *Correction of Boundary Singularities in Numerical-Simulation of Time-Dependent Diffusion-Processes at Unshielded Disk Electrodes.* Journal of Electroanalytical Chemistry, 1990. 295(1-2): p. 1-14.

[114] Harriman, K., D.J. Gavaghan, P. Houston, and E. Suli, *Adaptive finite element simulation of currents at microelectrodes to a guaranteed accuracy. Theory.* Electrochemistry Communications, 2000. 2(3): p. 157-162.

[115] Taylor, G., H.H. Girault, and J. McAleer, *Digital-Simulation of Charge-Transfer to an Ultramicrodisc Interface.* Journal of Electroanalytical Chemistry, 1990. 293(1-2): p. 19-44.

[116] Beriet, C., R. Ferrigno, and H.H. Girault, *Simulation of the chronoamperometric response of a regular array of micro-disc electrodes.* Journal of Electroanalytical Chemistry, 2000. 486(1): p. 56-64.

[117] Davies, T.J. and R.G. Compton, *The cyclic and linear sweep voltammetry of regular and random arrays of microdisc electrodes: Theory.* Journal of Electroanalytical Chemistry, 2005. 585(1): p. 63-82.

[118] Gueshi, T., K. Tokuda, and H. Matsuda, *Voltammetry at partially covered electrodes: Part I. Chronopotentiometry and chronoamperometry at model electrodes.* Journal of Electroanalytical Chemistry, 1978. 89(2): p. 247-260.

[119] Lee, H.J., C. Beriet, R. Ferrigno, and H.H. Girault, *Cyclic voltammetry at a regular microdisc electrode array.* Journal of Electroanalytical Chemistry, 2001. 502(1-2): p. 138-145.

[120] Reller, H., F. Kirowa-Eisner, and E. Gileadi, *Ensembles of microelectrodes : A digital-simulation.* Journal of Electroanalytical Chemistry, 1982. 138(1): p. 65-77.

[121] Fletcher, S. and M.D. Horne, *Random assemblies of microelectrodes (RAM (TM) electrodes) for electrochemical studies.* Electrochemistry Communications, 1999. 1(10): p. 502-512.

[122] Davies, T.J., S. Ward-Jones, C.E. Banks, J. del Campo, R. Mas, F.X. Munoz, and R.G. Compton, *The cyclic and linear sweep voltammetry of regular arrays of microdisc electrodes: Fitting of experimental data.* Journal of Electroanalytical Chemistry, 2005. 585(1): p. 51-62.

[123] Gourlay, A.R. and G.R. McGuire, *General Hopscotch Algorithm for the Numerical Solution of Partial Differential Equations.* IMA Journal of Applied Mathematics, 1971. 7: p. 216-227.

[124] Guo, J. and E. Lindner, *Cyclic voltammograms at coplanar and shallow recessed microdisk electrode arrays: Guidelines for design and experiment.* Analytical Chemistry, 2009. 81(1): p. 130-138.

[125] Amatore, C., J.M. Saveant, and D. Tessier, *Charge transfer at partially blocked surfaces: A model for the case of microscopic active and inactive sites.* Journal of Electroanalytical Chemistry, 1983. 147(1-2): p. 39-51.

[126] Arrigan, D.W.M., *Nanoelectrodes, nanoelectrode arrays and their applications.* Analyst, 2004. 129(12): p. 1157-1165.

[127] Compton, R.G., G.G. Wildgoose, N.V. Rees, I. Streeter, and R. Baron, *Design, fabrication, characterisation and application of nanoelectrode arrays.* Chemical Physics Letters, 2008. 459: p. 1-17.

[128] Lanyon, Y.H. and D.W.M. Arrigan, *Recessed nanoband electrodes fabricated by focused ion beam milling.* Sensors and Actuators, B: Chemical, 2007. 121(1): p. 341-347.

[129] Lanyon, Y.H., G. De Marzi, Y.E. Watson, A.J. Quinn, J.P. Gleeson, G. Redmond, and D.W.M. Arrigan, *Fabrication of nanopore array electrodes by focused ion beam milling.* Analytical Chemistry, 2007. 79(8): p. 3048-3055.

[130] Murray, R.W., *Nanoelectrochemistry: Metal nanoparticles, nanoelectrodes, and nanopores.* Chemical Reviews, 2008. 108(7): p. 2688-2720.

[131] Zhang, B., Y. Zhang, and H.S. White, *The nanopore electrode.* Analytical Chemistry, 2004. 76: p. 6229-6238.

[132] Zhang, B., Y. Zhang, and H.S. White, *Steady-State Voltammetric Response of the nanopore Electrode.* Analytical Chemistry, 2006. 78(477-483).

[133] Cooper, J.A. and R.G. Compton, *Channel electrodes - A review.* Electroanalysis, 1998. 10(3): p. 141-155.

[134] Harrar, J.E. and I. Shain, *Electrode Potential Gradients and Cell Design in Controlled Potential Electrolysis Experiments.* Anal. Chem., 1966. 38(9): p. 1148-1158.

[135] Amatore, C., A. Oleinick, and I. Svir, *Simulation of diffusion-convection processes in microfluidic channels equipped with double band microelectrode assemblies: approach through quasi-conformal mapping.* Electrochemistry Communications, 2004. 6(11): p. 1123-1130.

[136] Compton, R.G., A.C. Fisher, R.G. Wellington, P.J. Dobson, and P.A. Leigh, *Hydrodynamic Voltammetry with Microelectrodes - Channel Microband Electrodes - Theory and Experiment.* Journal of Physical Chemistry, 1993. 97(40): p. 10410-10415.

[137] Stevens, N.P.C. and A.C. Fisher, *Finite element simulations in electrochemistry .2. Hydrodynamic voltammetry.* Journal of Physical Chemistry B, 1997. 101(41): p. 8259-8263.

[138] Thompson, M. and R.G. Compton, *Voltammetric monitoring of transient hydrodynamic flow profiles in microfluidic flow cells.* Analytical Chemistry, 2007. 79(2): p. 626-631.

[139] Yunus, K. and A.C. Fisher, *Voltammetry under microfluidic control, a flow cell aproach.* Electroanalysis, 2003. 15(22): p. 1782-1786.

[140] Henley, I.E., K. Yunus, and A.C. Fisher, *Voltammetry under microfluidic control: Computer-aided design development and application of novel microelectrochemical reactors.* Journal of Physical Chemistry B, 2003. 107(16): p. 3878-3884.

[141] Matthews, S.M., G.Q. Du, and A.C. Fisher, *Microfluidic voltammetry: simulation of the chronoamperometric response of microband electrodes sited within microreactors.* Journal of Solid State Electrochemistry, 2006. 10(10): p. 817-825.

[142] Henley, I. and A. Fisher, *Computational electrochemistry: A model to studying ohmic distortion of voltammetry in multiple working electrode, microfluidic devices, an adaptive FEM approach.* Electroanalysis, 2005. 17(3): p. 255-262.

[143] Amatore, C., O.V. Klymenko, and I. Svir, *In situ and online monitoring of hydrodynamic flow profiles in microfluidic channels based upon microelectrochemistry: Optimization of electrode locations.* Chemphyschem, 2006. 7(2): p. 482-487.

[144] Amatore, C., A. Oleinick, O.V. Klymenko, and I. Svir, *In situ and online monitoring of hydrodynamic flow profiles in microfluidic channels based upon microelectrochemistry: Concept, theory, and validation.* Chemphyschem, 2005. 6(8): p. 1581-1589.

[145] Klymenko, O.V., A.I. Oleinick, C. Amatore, and I. Svir, *Reconstruction of hydrodynamic flow profiles in a rectangular channel using electrochemical methods of analysis.* Electrochimica Acta, 2007. 53(3 SPEC. ISS.): p. 1100-1106.

[146] Amatore, C., N. Da Mota, C. Sella, and L. Thouin, *Theory and experiments of transport at channel microband electrodes under laminar flows. 1. Steady-state regimes at a single electrode.* Analytical Chemistry, 2007. 79(22): p. 8502-8510.

[147] Amatore, C., N. Da Mota, C. Lemmer, C. Pebay, C. Sella, and L. Thouin, *Theory and experiments of transport at channel microband electrodes under laminar flows. 2. Electrochemical regimes at double microband assemblies under steady state.* Analytical Chemistry, 2008. 80(24): p. 9483-9490.

[148] Ferrigno, R., P.F. Brevet, and H.H. Girault, *Finite element simulation of the amperometric response of recessed and protruding microband electrodes in flow channels.* Journal of Electroanalytical Chemistry, 1997. 430(1-2): p. 235-242.

CHAPTER 3: Materials and methods

This chapter contains different aspects related to the experimental part of this thesis. First, there is a brief overview of the fabrication methods used. The first section is related to the fabrication of the detector. In this work microelectrodes were designed and fabricated for electroanalysis purposes. In the fabrication of such electrodes, standard micro/nano technology processes were used, so a brief overview of the general micro/nanotechnology techniques is presented. Later, an overview of polymer fabrication using rapid prototyping method is introduced, including a mention to polymer bonding. They both are used in the fabrication of the polymeric holder for the microfluidic devices. The following two sections are related to microfluidic and electrical interconnection, which despite being critical are often overlooked. Finally, at the end of the section there is a list of the instrumentation and the reagents used for the different electrochemical measurements performed during this thesis.

3.1 Fabrication of microelectrodes using micro/nano technologies

Micro/nano fabrication techniques have introduced enormous advantages in the fabrication of chemical sensors at the micro scale [1-3], such as miniaturisation, reduction of the sample volumes needed for the measurements, reduction of the fabrication costs and an increment of the response speed. These advantages, mainly miniaturisation, lead to the integration of microelectrode in microfluidics devices, also called lab on chip or μ-TAS (micro total analysis systems) [4-6]. Electroanalysis has become one of the most popular techniques for such devices due to its ease of integration [7, 8].

We describe some standard micro/nano fabrication processes in the following subsections. They are mainly related to the fabrication of the electrodes used in this thesis which are disk microelectrode arrays, disk nanoelectrode arrays and microbands, all of them made of gold. In the fabrication of every electroanalytical device there are mainly four fundamental steps, such as: oxidation, deposition, lithography and etching [9]. Such steps can be combined to achieve high complexity microdevices.

3.1.1 Oxidation

Oxidation is the process used to obtain thin layers of silicon dioxide (SiO_2) with a homogenous thickness and high quality, in a temperature range from 900 to 1200 ºC [10]. It is possible to differentiate between *dry oxidation* and *wet oxidation*. In a dry oxidation

process, silicon is oxidised in an atmosphere containing oxygen (O_2), while in wet oxidation process such atmosphere contains water (H_2O). Oxide growth rate is higher for wet oxidation process but the oxide obtained has less quality. Silicon is also oxidised at room temperature, such oxide is known as native oxide and it has a thickness around 20 Å.
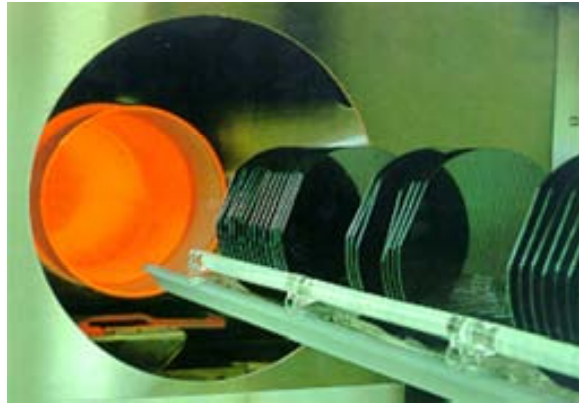

Figure 3-1: Picture of silicon wafers in an oxidation oven

3.1.2 Deposition

Deposition is the creation of a thin layer of a certain material [11]. The properties of the layer, as adhesion or stress, are related to the technique used. Two of the most common techniques are: *chemical vapour deposition* (CVD) and *physical vapour deposition* (PVD). Chemical vapour deposition includes deposition techniques with a chemical reaction at the substrate surface [12]. These processes take place at a high temperature, in most cases over 300ºC in a controlled gas atmosphere. Two of the most popular chemical depositions at vapour phase are: LPCVD (*low pressure* CVD) and PECVD (*plasma enhanced* CVD) [10]. LPCVD is achieved at low pressure (0.1-1 torr). The substrate is kept at high temperature, between 550-900ºC, depending on the material to deposit [11]. Several wafers can be processed at the same time and conformality is excellent. In PECVD, a radiofrequency source is use to generate plasma which contains highly reactive species and the substrate is kept between 150-350ºC.

Material deposited by physical vapour deposition (PVD) is transported from the material source to the substrate, both placed in the same chamber, by evaporation or by inert ionic sputtering [13]. In *evaporation*, the target material is heated to high temperatures to generate a vapour. Such vapour is condensed on the substrate surface creating a thin layer of the desired material. Several techniques are used to heat the target, the most popular are: heating the target due to the high currents passing through closer coils and *e- beam evaporation* which consists on heating the surface material due to the sputtering of an electron beam.Evaporation is achieved in a vacuum chamber with a pressure lower than 10^{-4} Pa in order to avoid contamination of the deposited layer [12]. In a deposition by *sputtering of inert ions*, the target material is physically sputtered by positive argon, although it is also

possible to use other inert gases as xenon [13]. As a result of the sputtering, the atoms of the material, individually or forming groups, are taken out from the target surface and deposited on the wafer. In this thesis, metals like Titanium, Niquel and Gold while oxide and nitride layer were deposited by PECVD.

3.1.3 Lithography

The most popular lithographic techniques are *photolithography*, *electron beam* (e-beam) lithography or *X-ray* lithography. In this section, we focus on photolithography and e-beam lithography because both techniques were used during this thesis.

Photolithography is a lithographic technique where ultraviolet light is used to transfer patterns to a photo-sensitive polymer deposited on a wafer. To coat the wafer with the resist, a certain volume of polymer is poured at the centre and spun over the entire surface. The thickness of the resist is controlled by the resist viscosity, spinning speed and the contact angle between the resist and the surface. Two-dimensional geometric patterns are drawn on the mask made of glass or quartz, typically with a layer of chrome of around 100nm. UV-light passes through the bright patterns of the mask and irradiated the resist. Depending on the response to the UV light, it is possible to differentiate between positive and negative photoresists [11]. If the photoresist is positive, the solubility of the irradiated areas changes and they are removed in the developing process. On the other hand, for negative photoresist the ultraviolet light polymerises the irradiated areas and the non irradiated areas are removed in the developing process.

After the ultraviolet exposition, wafer and polymer are heated during 20-30 minutes at 120-180ºC to improve the adhesion of the transferred patterns [11]. Finally, as it was mentioned, a developing process is needed. In this last step, photoresist areas, which are not adhered, are removed using developer solvents.

Electron beam lithography (EBL) is the most used nanostructure fabrication method [14], it was used in this work to define an array of nanodisks. Basically, it consists on exposing an electron sensitive resist to an electron beam. The resolution achieved using EBL is higher than photolithographic resolution. Electron beam causes smaller diffraction than UV light, due to its much smaller wavelength, and smaller patterns can be defined. However, it is a more expensive process because vacuum is needed as electrons are charged particles. It is possible to use both positive and negative resists. One popular positive resist is polymethyl methacrilate (PMMA). It was one of the first resist used, and even today it is one of the most common [14].

Figure 3-2: Photolithography are at IMB-CNM clean room.

3.1.4 Etching

Etching can be defined as a selective removal of material. The most important parameters in any etching process are the selectivity and the directionality of the attack [15]. One of the main challenges is to remove one material without affecting other materials on the wafer [12]. In most of the cases, a resist is used as an etching mask. Selectivity is directly related to etch rate. One material is selective to an etching when it is removed at higher rate than other materials present, under the same conditions. Directionality is related to the profile of the removed material under the mask. It can be isotropic or anisotropic. In an isotropic etching, the material is removed at the same rate in all directions and rounded profiles are obtained. For anisotropic etchings, the profile is sharper because there are directions in the material where the etching is faster.

Etching techniques are classified in dry and wet. Wet etching consists on immersing the substrate in a chemical reagent, under controlled conditions of concentration, time and temperature. Wet etching is usually isotropic and less selective than dry etchings [15]. However, wet etching can also be anistropic where the etching rate depends on the cristolographic direction, for example silicon etching by potassium hydroxide (KOH).

Dry etching uses ionised plasma, and allows the definition of smaller patterns than wet etching because it tends to be anisotropic [16]. One of the most popular dry etching methods is the well known *reactive ion etching* (RIE) [16]. In this process, both chemical and physical processes are at play. Reactive species react at the substrate surface after it has been activated by the collisions of the plasma ions. It is a highly directional etching, in which the vertical etching rate is higher than the etching at the walls.

Figure 3-3: Etching baths at IMB-CNM clean room

3.2 Rapid prototyping

Multidisciplinarity is one of the hallmarks of micro-total analysis systems (μTAS) or lab on a chip devices. It is possible to find applications in a very wide range of scientific fields such as [5, 17-19]. Minituarisation of devices can lead to many advantages, as reduction in reagent and analyte consumption, shorter time of analysis and lower manufacturing costs [20].

In this section we will focus on rapid prototyping techniques such as soft lithography and milling micromachining. These techniques share their flexibility and ease to adapt to design and fabrications changes, to achieve a rapid prototype. If only a few numbers of devices are required or if the final design mainly depends on the application or its results, it is critical to have a prototype in a short period of time to perform rapid tests in the lab. These techniques allow the user to have final devices within hours and to easily modify their features depending on the application constraints. These were the main objectives of the microfluidic devices developed during this thesis. First, due to the flexibility of those techniques it is possible to integrate different parts just modifying the design and fabricating the whole device again or adding them as external modules. Finally, they are in general inexpensive techniques, as they can be implmemented outside a cleanroom environment. Rapid prototyping techniques also simplify the fabrication of active components, such as pumps and valves, using elastomeric rather than rigid materials [21-25].

Another popular rapid prototyping technique is CO_2-laser ablation [23, 26-29]. Although this technique is beyond the scope of this thesis, it mainly consists on material removal by radiation. On of the most important advantages of this technique is the possibility to define structures in a very short time (a few minutes) [30]. However, sometimes there are small bumps of resolidified material on the edges of the structure, and the structure is not as smooth as when using other techniques [29]. The presence and the shapes of such bumps

depend on the material. It can be a main drawback because these bumps make bonding processes more difficult. Moreover, laser ablation requires of constant recalibrations in order to quantify how the different adjustable parameters affect in the definition of the microstructures. It leads to a loss of precission compared with other techniques.

3.2.1 Soft lithography (Replica molding)

The name of soft lithography comes from the idea of an alternative to standard photolithographic methods. The most important characteristic, which actually defines the name, is the use of an elastomer, a polymer with elastic properties [31], as a stamp, mold or mask [32, 33]. Soft lithography can be applied to a wide range of techniques such us microcontact printing (μCP), replica molding (REM) or microtransfer molding (μTM) [32]. Moreover, it is possible to pattern a lot of different molecules and materials as: self assembled monolayers (SAMs), unsensitised polymers (for example: epoxy, polymethyl methacrylate (PMMA) or polyvinyl chloride (PVC)), conducting polymers, sol-gel materials and organic and inorganic salts, amongst others. Such flexibility turns soft lithography is one of the most popular techniques to fabricate polymer devices [34, 35].

In this thesis, we will focus on replica molding using soft lithography so we will use the elastomer for the rapid replication of previously defined patterns. The technique consists in pouring the pre-polymer over a master. Such master is a mold which contains on its surface the negative image of the desired patterns [32]. Afterwards, the polymer is cured and peeled of from the master, having the patterns transferred. Some advantages of using elastomers in replica molding are the possibilites to make conformal contact with surface over large areas, to pattern non-planar surfaces and to release the cured elastomer easily from the master. Soft lithography is an inexpensive technique and quite easy to learn and apply, so it can be used by a wide range of users from different scientific fields. Moreover, the stamp can be used many times over since it is not exposed to high pressures or high temperatures [27].

The concept of rapid prototyping in replica molding with soft lithography lies in the possibility to use other rapid prototyping techniques to define the master, e.g.: micromilling, laser ablation or a printed transparency for photolithographic methods [36]. It drastically reduces time and cost. These masters basically consist on photoresist patterns defined on a silicon wafer or patterns directly defined on a polymer layer. The main drawback of this kind of rapid prototyping is resolution limit of the techniques used to fabricate the master. For example, using a transparency as a mask leads to a resolution around 25 μm [20]. Obviously, if it is necessary to transfer lower patterns it is possible to use photolithographic steps (chrome photomask) or other lithographic methods [11, 14] to define the master. In that case, maybe the whole process is not absolutely considered as rapid prototyping, but still keeps all the advantages of replica molding itself.

Elastomers, such as polydimethylsiloxane (PDMS), polyurethanes or polymides [32], are the basic materials used for replica molding in soft lithography. Compared with silicon or glass, they are inexpensive and, which is very important for microfludic devices, they can be easily bonded [36, 37] using thermal or plasma processes. PDMS is the most popular and used elastomer [20, 21, 32, 38-40] because it is very suitable for replica moulding due to its features like [20]:

- It cures at low temperatures, even at room temperature if the cured time is long enough.
- It allows reversible and irreversible bonding with itself and with a wide range of other materials.
- It is biologically compatible, it is possible to use in any biological application even in cell culture due to its permeability to oxygen.
- It is transparent down to 300nm, which allows optical inspection.

PDMS is able to reproduce structure with high fidelity at the micro-scale, so replica moulding using PDMS is a very useful technique to define microchannels for microfluidic devices, among other things. According to scopus more than 1200 works using the word "PDMS" have been published in 2009 alone.

3.2.2 Micromilling

One versatile technique to fabricate polymer microdevices rapidly is micromilling [37, 41-45]. It is based on the direct mechanical cut of the material with a specific cutting tool and machine. It can be use to define the whole device or to fabricate the masters used in replica molding [46]. Milling is a successful precision machining method, and the cutting mechanism as well as the cutting forces are well known [47].

The setup consists on a milling machine connected to a computer [36]. The computer controls the position of the cutting tool. That is why this technique is also known as computer numerical controlled or CNC milling. It is important to calibrate the relative position between the material holder and the tools, especially in the vertical direction. The precission of the defined microstructure depends on the calibration, which is manually done by the user in most cases.

Micromilling can be used with a wide range of solid materials from metals to polymers. They must be hard materials, so elastomer can not be milled.

The fabrication time highly depends on the complexity of the structure, and despite the fact that it can be relatively time consuming, it has the advantage that the design can be easily changed and three-dimensional structures can be fabricated directly. It is not, in general, a complicated process, so the user can become familiar with the system in a short time, making micromilling an important route to rapid prototyping.

The resolution depends on the size of the tool used to mill the polymer. It is possible to work with tools of down to 5-10 μm diameter, but they are extremely fragile and easily to break. Otherwise, a resolution of about 50/100 μm is enough for mainly of microfluidic applications or at least for applications where rapid prototyping is required. One important advantage is that the material is not chemically modified in the process, as it is just a mechanical process. Although, some stresses can appear around the defined structures [36], they can be reduced by a temperature treatment consisting of a cycle of heating and slow cooling.

Using micromilling

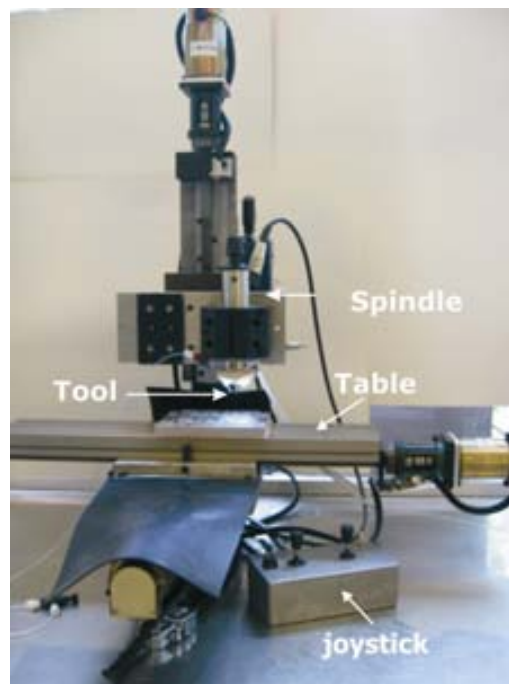Figure 3-4 shows a micromilling machine as the one used in this work, and its main parts,.

Figure 3-4: A micromilling machine and its main parts.

The substrate is fixed on a table that moves in the x-y plane. A high speed spindle is attached to the z-axis allowing direct 3-D structuring. Fixing thin substrates as the ones used in this work to the table is problematic because common clamping devices tend to bend the substrate, and this results in the production of faulty pieces. The problem was solved using double sided adhesive tape instead of clamps to fix the substrate to the table. Accurate tool alignment in z-direction was done manually using a microscope. This alignment is necessary after every tool change.

There are different kinds of tools used to achieve various profile geometries: end-mills produce rectangular grooves, ball-end mills produce round channels, and drills are used to drill holes. Although tool diameters as tiny as 5-10 μm are available, fabrication using these tools is challenging and success highly depends on the user's skills.

The three main parameters that have to be set for the milling process are: rotational velocity of the spindle and displacement velocities of the milling tool in the x-y plane and z-direction.

These parameters can be looked up in tables, depending on the material. However, these tables were calculated for "macro" milling and don't take effects of micro fabrication into account, *e.g.* heat dissipation. Hence, for optimum results, these values have to be adapted to the micromilling process individually.

Beside the machine itself, the controller part is also essential in micromilling fabrication. Basically, three software levels are required to achieve a product from a design on a computer. First, the geometry is defined using a CAD (Computer Aided Desing) software, which is then transferred to a CAM (Computer Aided Machinning) program. This allows to define the above described parameters as well as all the machining paths. The CAM software generates a standard code, also known as "g-code", which can be read by the software controlling the machine movements.

Micromilling allows obtaining prototypes in an economic and fast way. Moreover, as reproducibility is much better than other techniques such as CO_2-laser ablation, which is a quite popular rapid prototyping method, micromilling has become in a good choice to fabricate polymer devices.

3.3 Polymer Bonding

Microfluidic systems require additional processes to achieve tight sealing of different parts, and this is a critical point in large-scale production. During the polymer fabrication in this thesis, UV-assisted thermal bonding was used to bond two layers of PMMA. This is a two-step process in which after exposing to UV light the surfaces to bond, these are then pressed against each other in a hot press. The UV exposure reduces the glass transition temperature (T_g) of the polymer's surface and allows bonding the substrates at a temperature below the T_g of the bulk material. This enhances the bonding and prevents deformation. The parameters for UV-irradiation, pressure and temperature depend on the material and the layer thickness. In this work, to bond two layers of 3 mm thick PMMA, 90 seconds of exposure followed by 1 hour of pressure (1.5kN) at 88ºC was used.

3.4 Microfluidic interconnection

Microfluidic interconnections are vital to microfluidic devices. Their goal is to avoid leaks at the joints between parts while minimizing dead volume. Fluidic connections must be as simple as possible, and yet robust to withstand the high pressures prevalent in these small systems. There are many approaches to making microfluidic interconnections, and their sophistication depends on the user's ability and skills. This section describes the two approaches used during this thesis.

The first approach consists in using small pieces of silicone tubing to seal the interconnection between a needle and the channel defined in the PMMA holder. First, cylindrical channels of 0.8mm diameter were machined in the holder. For that purpose, it

was necessary to define grooves of 0.4mm depth and 0.8mm diameter in two layers of PMMA using a 0.8mm ball-end mill. These two layers were bonded (UV-assisted thermal bonding), thus creating cylindrical channels of the desired diameter. On the other hand, the tip of steel needles of 0.7mm diameter was filed flat and inserted in small bits of silicone tubing (0.5mm ID and 0.9mm OD). Once assembled, needle and silicone tube, were carefully inserted in the microdevice channels. When the needle is inserted, it pushes the silicone tubing against the PMMA walls and a tight seal is achieved. This is a quite simple way to obtain good seals between needles and cylindrical channels.

Another strategy for the microfluidic interconnection was used to simplify the fabrication of the holder. Fabrication of cylindrical channels in PMMA requires milling two different layers of PMMA, and bonding them together. Depending on the design, this can complicate the milling process. In our case it was necessary to mill both sides of the same PMMA slab. On one side hemispherical channels were defined and on the other side some other microfluidic features. Although this is not too difficult a process, two-side structuring requires special alignment and takes more time and effort.

In the new case, the microfluidic channels are just defined in one of the layers. Microchannels of 0.5mm wide and 0.5mm depth were fabricated using an end-mill tool. Steel needles of 0.5mm diameter are filed and inserted in the microchannel before the UV-assisted thermal bonding. Due to high temperatures the microchannel dimensions are slightly modified in the bonding process, so we take advantages of that deformation to seal the needles to the devices. After this, the needles are fixed to the microchannels, and to obtain an even better sealing, UV-curable glue (Norland products, USA) was applied to the joint. This second approach is perfect to make interconnections between rectangular section channels and needles.

3.5 Electrical connection

Miniaturised electroanalytical systems respond faster and are more sensitive than conventional electrodes, but they still need to function in a macroscopic world. This means that chip-based microelectrodes, as most electronic devices, need to be electrically connected to an interface that facilitates their manipulation in the laboratory, so that they can be plugged to a potentiostat and used to monitor the concentration of a target analyte. In this thesis we used two different approaches to connect our micro- and nanoelectrodes electrically: wire bonding and spring loaded pins. This section describes both techniques broadly.

Wire bonding:

Wire bonding is one of the most common techniques used in microtechnology to connect integrated circuits (IC) to printed circuit boards (PCB). It consists on connecting the pad defined on the chip with the external pad on the PCB using very thin bonding wires. The wire

used in wire bonding is usually made either of gold (Au), aluminium (Al) or cupper (Cu). In particular, the wire bonding used in IMB-CNM for this work was an Al wire of 25μm diameter and it was bonded by ultrasonic, where pressure is applied at room temperature.

Figure 3-5 shows one of our final devices. The chips are glued on a suitable PCB before the wire bonding can be applied. Besides, wire bonds need to be protected because they are very fragile, and this is typically done with encapsulating resins. In the case of our microelectrodes, protecting the connections is critical to avoid leak currents in electroanalytical measurements, which are done in solution.
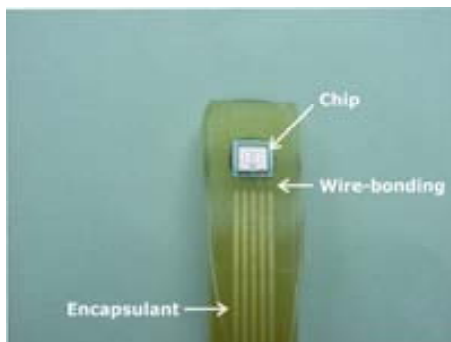

Figure 3-5: Picture of final chip bonded by wire bonding and encapsulated onto a PCB.

Although wire-bonding is a very reliable technique, its drawback is that it's a manual technique, which increases its cost and the time it takes for the chips to be used following their fabrication. Moreover, it is not the most suitable technique in microfluidic applications, as the ones described in the final chapters, so other alternatives were studied.

Spring-loaded pins:

Spring loaded pins are a very useful kind of connector because they can replace wire bonding in certain applications, like the microfluidic systems. Figure 3-6A shows a picture and the diagram of the kind of spring-loaded pins used in this thesis (Preci Clip, CH). The connection is established by direct contact of the pin with the pads on the chip, and the springs prevent the chip from breaking if the connector is pressed too strongly.
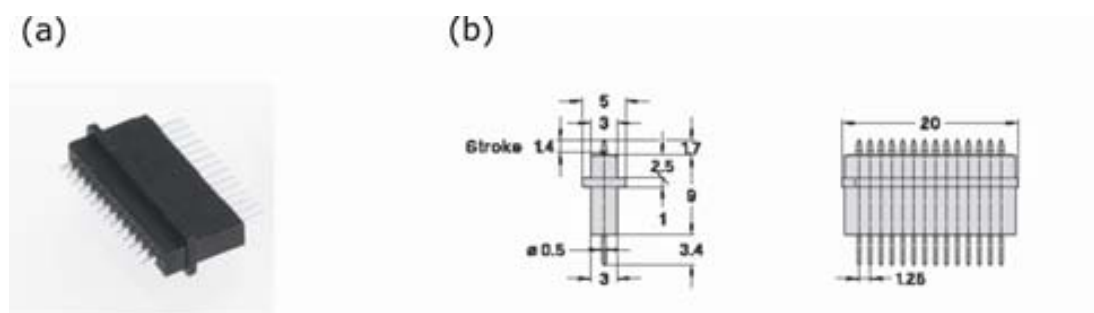

Figure 3-6: (a) Picture of the commercial spring loaded pins connector used in this thesis. (b) Schematic representation of the connector where the main dimensions are specified.

Because spring loaded pins have a standard pitch (either 0.1" or 0.05"), it is necessary to adjust the dimensions of the pads on the chip during the chip design stage.

In our case, the connector was fitted to the PMMA holder, as shown in Figure 3-7. Our miniaturised electroanalytical cell requires four connectors only, which sit in a customised pocket that is machined through the holder (Figure 3-6B). The electrical contact is made when the top and bottom parts of the holder are clamped together with the chip placed between them. However, correct alignment of the pins and the connection pads on the chip is critical.
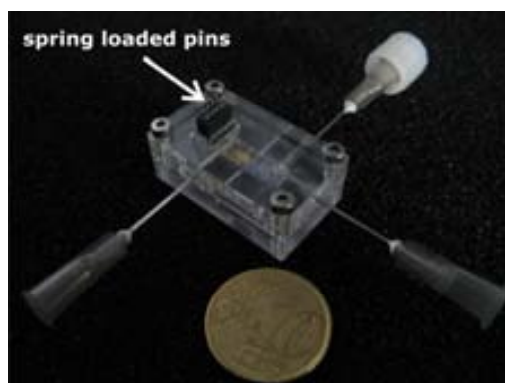

Figure 3-7: Picture of a final microdevice fabricated in this thesis. In this case, a spring loaded pin connector was used for electrical connection and fitted into the polymer holder.

There are cost and operational advantages to using spring loaded pins in a system like this. Time and cost savings mainly stem from their substitution for wire bonding, which is a manual operation, but the use of spring-loaded pins also eliminate the need for encapsulation. In our case, this is because the solution is confined in a separate PDMS compartment, and hence there is no danger of it reaching the contacts. Another advantage is that the chip can be replaced easily and quickly, as they are not a permanent electrical connection. It provides additional flexibility as chips with different layouts and functionalities can be used in the same holder.

In summary, spring-loaded pins are a simple and smart solution in very specific cases, but they are certainly not universal substitutes for wire-bonding, which is also a fundamental way to make electrical connections. The constraints of each particular application will dictate which is the most suitable approach.

3.6 Instrumentation

Table 3-1 summarises the instrumentation used during this thesis for the electrochemical measurements. Two different potentiostats were used. Although CHI700C is a bipotentiostat, this function was not used for the results showed in this thesis. The dissolved oxygen meter was used to control the level of the oxygen dissolved in the solution for the

microrespirometer device (Chapter 5). For the microfluidic experiments, the solution was always injected using a syringe pump.

The models were mainly solved using a personal computer (Pentium ® 4 CPU 3.00 GHz 2.0 GB RAM). A linux worstation (Sun Microsystems, USA) was used to solve the three-dimensional models reported in Chapter 6.

Table 3-1: List of intruments used to perform the measurements in this thesis.

Equipment	Model	Company
Potentiostast	μ-Autolab III	Metrohm-EcoChemie (NL)
	CHI700C	CH Instruments (USA)
Dissolved oxygen meter	HQ10	Hach (USA)
Syringe pump	NE1000	New Era Pump Systems (USA)

3.7 Reagents used

Table 3-2 summarises the chemical and biological reagents used in this thesis. All chemical were analytical grade and were used as received without any further purification. Aqueous solutions were prepared using de-ionised water (18M$\Omega\cdot$cm).

Table 3-2: List of chemical and biological reagents used in this thesis.

Reagent	Supplier
Nafion 117 solution in lower aliphatic alcohol	Sigma-Aldrich
Potassium hexacianoferrate (II) trihydratate ($K_4FeCN_6\cdot3H_2O$)	Sigma-Aldrich
Potassium hexacionaferrate (III) (K3FeCN6)	Panreac
Potassium chloride (KCl)	Sigma- Aldrich
Potassium nitrate (KNO_3)	Sigma- Aldrich
PBS tablets	Invitrogen
Magnesium sulphate ($MgSO_4$)	Sigma- Aldrich
Streptavidin-coated Dynabead ®	Invitrogen
β-galactosidase	Sigma- Aldrich
4-aminophenyl-β-D-galactopyranoside (PAPG)	Sigma- Aldrich
p-aminophenol	Sigma-Aldrich
N,N-dimethylformamide (DMF)	Sigma-Aldrich

3.8 References

[1] Feeney, R. and S.P. Kounaves, *Microfabricated ultramicroelectrode arrays: Developments, advances, and applications in environmental analysis.* Electroanalysis, 2000. 12(9): p. 677-684.

[2] Fiaccabrino, G.C. and M. Koudelka-Hep, *Thin-film microfabrication of electrochemical transducers.* Electroanalysis, 1998. 10(4): p. 217-222.

[3] Suzuki, H., *Advances in the microfabrication of electrochemical sensors and systems.* Electroanalysis, 2000. 12(9): p. 703-715.

[4] Nyholm, L., *Electrochemical techniques for lab-on-a-chip applications.* Analyst, 2005. 130(5): p. 599-605.

[5] Verpoorte, E., *Microfluidic chips for clinical and forensic analysis.* Electrophoresis, 2002. 23(5): p. 677-712.

[6] Wang, J., *Electrochemical detection for microscale analytical systems: a review.* Talanta, 2002. 56(2): p. 223-231.

[7] Crevillén, A.G., M. Hervás, M.A. López, M.C. González, and A. Escarpa, *Real sample analysis on microfluidic devices.* Talanta, 2007. 74(3): p. 342-357.

[8] Sassa, F., K. Morimoto, W. Satoh, and H. Suzuki, *Electrochemical techniques for microfluidic applications.* Electrophoresis, 2008. 29(9): p. 1787-1800.

[9] Beeby, S., G. Ensell, M. Kraft, and N. White, *MEMS Mechanical Sensors*. Microelectromechanical systems series. 2004: Artech House Inc.

[10] Plummer, J.D., M.D. Deal, and P.B. Griffin, *Silicon VLSI Technology: Fundamentals, Practice and Modeling*. 2000: Prentice Hall.

[11] Bushan, B., ed. *Handbook of nanotechnology*. 2004, Springer.

[12] Maluf, N. and K. Williams, *An introduction to microelectromechanical systems engineering*. Microelectromechanical systems series. 2004: Artech House Inc.

[13] Madou, M.J., *Fundamentals of microfabrication: the science of miniaturization*. 2nd ed. 2002: CRC Press.

[14] Vieu, C., F. Carcenac, A. Pépin, Y. Chen, M. Mejias, A. Lebib, L. Manin-Ferlazzo, L. Couraud, and H. Launois, *Electron beam lithography: Resolution limits and applications.* Applied Surface Science, 2000. 164(1-4): p. 111-117.

[15] Lang, W., *Silicon microstructuring technology.* Materials Science & Engineering R-Reports, 1996. 17(1): p. 1-55.

[16] Seidel, H., L. Csepregi, A. Heuberger, and H. Baumgartel, *Anisotropic Etching of Crystalline Silicon in Alkaline-Solutions .1. Orientation Dependence and Behavior of Passivation Layers.* Journal of the Electrochemical Society, 1990. 137(11): p. 3612-3626.

[17] Ohno, K.-i., K. Tachikawa, and A. Manz, *Microfluidics: Applications for analytical purposes in chemistry and biochemistry.* Electrophoresis, 2009. 29: p. 4443-4453.

[18] Kutter, J.P. and H. Klank, *Microfluidics-Theoretical Aspect*, in *Microsystem Engineering of Lab-on-a-Chip Devices*, O. Geschke, H. Klank, and P. Telleman, Editors. 2004, Wiley-VCH.

[19] Whitesides, G.M., *The origins and the future of microfluidics.* Nature, 2006. 442(7101): p. 368-373.

[20] McDonald, J.C., D.C. Duffy, J.R. Anderson, D.T. Chiu, H. Wu, O.J.A. Schueller, and G.M. Whitesides, *Fabrication of microfluidic systems in poly(dimethylsiloxane).* Electrophoresis, 2000. 21(1): p. 27-40.

[21] Ng, J.M.K., I. Gitlin, A.D. Stroock, and G.M. Whitesides, *Components for integrated poly(dimethylsiloxane) microfluidic systems.* Electrophoresis, 2002. 23(20): p. 3461-3473.

[22] Thorsen, T., S.J. Maerkl, and S.R. Quake, *Microfluidic large-scale integration.* Science, 2002. 298(5593): p. 580-584.

[23] Fiorini, G.S. and D.T. Chiu, *Disposable microfluidic devices: Fabrication, function, and application.* BioTechniques, 2005. 38(3): p. 429-446.

[24] Vilkner, T., D. Janasek, and A. Manz, *Micro total analysis systems. Recent developments.* Analytical Chemistry, 2004. 76(12): p. 3373-3386.

[25] Wheeler, A.R., W.R. Throndset, R.J. Whelan, A.M. Leach, R.N. Zare, Y.H. Liao, K. Farrell, I.D. Manger, and A. Daridon, *Microfluidic device for single-cell analysis.* Analytical Chemistry, 2003. 75(14): p. 3581-3586.

[26] Becker, H. and C. Gärtner, *Polymer microfabrication methods for microfluidic analytical applications.* Electrophoresis, 2000. 21(1): p. 12-26.

[27] Becker, H. and L.E. Locascio, *Polymer microfluidic devices.* Talanta, 2002. 56(2): p. 267-287.

[28] Bowden, M., O. Geschke, J.P. Kutter, and D. Diamond, *CO2 laser microfabrication of an integrated polymer microfluidic manifold for the determination of phosphorus.* Lab on a Chip - Miniaturisation for Chemistry and Biology, 2003. 3(4): p. 221-223.

[29] Klank, H., J.P. Kutter, and O. Geschke, *CO2-laser micromachining and back-end processing for rapid production of PMMA-based microfluidic systems.* Lab on a Chip - Miniaturisation for Chemistry and Biology, 2002. 2(4): p. 242-246.

[30] Snakenborg, D., H. Klank, and J.P. Kutter, *Microstructure fabrication with a Co2 laser system.* Journal of Micromechanics and Microengineering, 2004. 14(2): p. 182-189.

[31] *http://goldbook.iupac.org/.* [cited.

[32] Xia, Y. and G.M. Whitesides, *Soft lithography.* Annual Review of Materials Science, 1998. 28(1): p. 153-184.

[33] Zhao, X.M., Y. Xia, D. Qin, and G.M. Whitesides, *Fabrication of polymeric microstructures with high aspect ratios using shrinkable polystyrene films.* Advanced Materials, 1997. 9(3): p. 251-254.

[34] Whitesides, G.M., E. Ostuni, S. Takayama, X. Jiang, and D.E. Ingber, *Soft lithography in biology and biochemistry*, in *Annual Review of Biomedical Engineering*. 2001. p. 335-373.

[35] Weibel, D.B., W.R. DiLuzio, and G.M. Whitesides, *Microfabrication meets microbiology.* Nature Reviews Microbiology, 2007. 5(3): p. 209-218.

[36] Klank, H., *Polymer Micromachinning*, in *Microsystem Engineering of Lab-on-a-Chip Devices*, O. Geschke, H. Klank, and P. Telleman, Editors. 2004, Wiley-VCH.

[37] Becker, H. and C. Gärtner, *Polymer microfabrication technologies for microfluidic systems.* Analytical and Bioanalytical Chemistry, 2008. 390(1): p. 89-111.

[38] Anderson, J.R., D.T. Chiu, R.J. Jackman, O. Chemiavskaya, J.C. McDonald, H. Wu, S.H. Whitesides, and G.M. Whitesides, *Fabrication of topologically complex three-dimensional microfluidic systems in PDMS by rapid prototyping.* Analytical Chemistry, 2000. 72(14): p. 3158-3164.

[39] Duffy, D.C., J.C. McDonald, O.J.A. Schueller, and G.M. Whitesides, *Rapid prototyping of microfluidic systems in poly(dimethylsiloxane).* Analytical Chemistry, 1998. 70(23): p. 4974-4984.

[40] Jo, B.H., L.M. Van Lerberghe, K.M. Motsegood, and D.J. Beebe, *Three-dimensional micro-channel fabrication in polydimethylsiloxane (PDMS) elastomer.* Journal of Microelectromechanical Systems, 2000. 9(1): p. 76-81.

[41] Mecomber, J.S., D. Hurd, and P.A. Limbach, *Enhanced machining of micron-scale features in microchip molding masters by CNC milling.* International Journal of Machine Tools and Manufacture, 2005. 45(12-13): p. 1542-1550.

[42] Rainelli, A., R. Stratz, K. Schweizer, and P.C. Hauser, *Miniature flow-injection analysis manifold created by micromilling.* Talanta, 2003. 61(5): p. 659-665.

[43] Takács, M., B. Verö, and I. Mészáros, *Micromilling of metallic materials.* Journal of Materials Processing Technology, 2003. 138(1-3): p. 152-155.

[44] Yussuf, A.A., I. Sbarski, J.P. Hayes, M. Solomon, and N. Tran, *Microwave welding of polymeric-microfluidic devices.* Journal of Micromechanics and Microengineering, 2005. 15(9): p. 1692-1699.

[45] Zilch, L.W., G.A. Husseini, Y.Y. Lua, M.V. Lee, K.R. Gertsch, B.R. Cannon, R.M. Perry, E.T. Sevy, M.C. Asplund, A.T. Woolley, and M.R. Linford, *Rapid and convenient method for preparing masters for microcontact printing with 1-12 μm features.* Review of Scientific Instruments, 2004. 75(9): p. 3065-3067.

[46] Snakenborg, D., G. Perozziello, H. Klank, O. Geschke, and J.P. Kutter, *Direct milling and casting of polymer-based optical waveguides for improved transparency in the visible range.* Journal of Micromechanics and Microengineering, 2006. 16(2): p. 375-381.

[47] Rahman, M., A. Senthil Kumar, and J.R.S. Prakash, *Micro milling of pure copper.* Journal of Materials Processing Technology, 2001. 116(1): p. 39-43.

CHAPTER 4: Simulation

As the experimental chapters will show, simulation has been an essential prediction and validation tool in this thesis, so this is an introductory section where the basic models are described. Such models will be the foundation upon which more complex models will be developed later in this thesis.

Before getting down to the nitty-gritty of the various models, this section provides a description of the general features of working with COMSOL Multiphysics (COMSOLAB, Sweden) and a summary of three important aspects common to all the models. This is then followed by a more in-depth description of the different simulations, where each sub-section presents the relevant background theory, descriptions of how to set-up the models and discussions on their solutions. The electrochemical techniques covered in this section and, by extension, throughout the thesis, are based on potential step and potential sweep techniques both under diffusion-only and under hydrodynamic conditions. Special attention is paid to mass transport at two related electrode geometries: microelectrodes and microelectrode arrays.

4.1 Finite element methods (FEM) and COMSOL Mutiphysics

This section provides a brief overview of finite element methods (FEM). FEM are the numerical techniques used by COMSOL Multhipyshics [1] to solve partial differential equations. An in-depth discussion of these numerical techniques remains beyond the scope of this work, but there are some excellent books on this topic [2-5].

COMSOL Mutiphysics is the software used during this thesis to define and solve electrochemical models. It is a well-kown commercial software for the solution of partial differential equations (PDE). Thanks to its versatility, it is used in a broad range of research fields [1, 6-8].

4.1.1 Finite element methods (FEM)

The finite element method is a numerical technique for solving partial differential equations (PDE). The first step is to describe the domain geometry. Then this domain is discretizated in much smaller subdomains, named finite elements [5]. The set of these elements is called mesh [8]. The vertex of such elements are called nodes, although there can be nodes outside the vertex. Nodes are very important in FEM because it is where the solution is computed for the different variables.

The dimension of the elements is directly related to that of the domain. There are different kinds of elements depending on their geometry. The simplest geometry in one dimension is the linear segment, in two dimensions the triangle, and in three dimensions the tetrahedron [8]. Figure 4-1 schematises a simple domain where triangular elements are used to create a mesh.
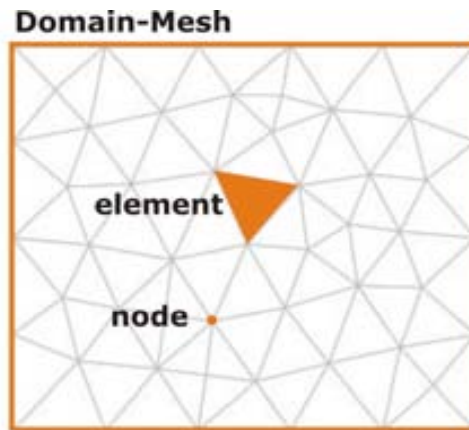

Figure 4-1: Schematic representation of the typical mesh used in this thesis for two dimensional domains. We used triangular second order elements, with a node on each corner.

But the elements are not just defined geometrically [5]. They are also characterised by the interpolation polynomials used to interpolate the solution in each node, called basis functions, φ_i. The idea is to approximate the solution, u, using the basis functions and a number of finite parameters, the so-called degrees of freedom (DOF). The solution is then described as:

$$u = \sum_i u_i \varphi_i \tag{4.1}$$

These degrees of freedom (u_i) are the solution values at each node point. The interpolation polynomial φ_i equals 1 at the ith node point, and 0 at the other node points.

The accuracy of the solutions depends on the order of the interpolation polynomial, but the number of calculations needed to evaluate the model also increases with this order. Note that the order of an element and the number of nodes are also connected. For instance, a quadratic interpolation function requires information from 3 nodes [8].

One of the most common finite elements is the lagrangian element, which uses Lagrange polynomials as interpolation polynomials [1]. Lagrangian elements are second order. We used these kind of elements in all of the two-dimensional models described in this work.

4.1.2 Using COMSOL Multiphysics

COMSOL Multiphysics is a commercial software package based on finite element methods (FEM). It has a user friendly graphical interface. The model geometry, called domain, is

simply drawn as in any other graphic design software. The partial differential equations needed to describe the physical phenomenon under study are defined in different modules. The user does not need to introduce the tedious mathematical equations and their boundary conditions. However, it is possible to do it if it is necessary to define an equation which is not readily available in COMSOL. It is worth noting that more than one partial differential equation can be solved in the same model [1]. This is an important features and where the concept of mutiphysics becomes meaningful.

Once the geometry and the equations are defined, it is necessary to discretizate the domain by defining a mesh. Generally, second order triangular elements were used to define most of the models in this work [1]. The procedure of meshing consists in dividing the whole domain in smaller elements until a good solution convergence is achieved (better than 1%). It is always important to refine the mesh; that is, to define smaller mesh elements in those domains regions or points where one expects to find steeper gradients. For example, in the regions near the electrode the elements are considerable smaller than in regions far from it. The concentration gradient near the electrode is higher so smaller elements are needed. Furthermore, on the microelectrode perimeter there is a discontinuity, so the mesh elements must be extremely small around them to ensure convergence.

COMSOL Mutiphysics allows different kinds of analysis, such as stationary, transient or parametric, depending on needs. There is an established solver for each kind of analysis, but this can be changed manually by the user. Absolute and relative tolerances for each variable can be defined which directly affect the accuracy of the solution.

Once the model is solved, there is a wide variety of solution postproceessing options. It is possible to create graphs in different dimensions, perform variable integration or, even, animations.

One important feature of COMSOL Mutiphysics is its compatibility with Matlab (Mathworks, USA). This allows converting the model into a Matlab file. The structure of this Matlab script is a complex object where the model is defined, so it is possible to change any of its characteristics, such as its geometry, its boundary conditions, its mesh or the solver used. Once it is modified, the model can be solved using the new conditions. The most important advantage is the possibility to introduce programming structures typical of the Matlab language, and hence automate parametric studies. Models were performed using COMSOL Mutiphysics 3.4 and Matlab 2007a, and earlier versions.

4.2 Modelling microelectrodes: generalities

Regardless of their complexity, all the models shared a few common aspects related to electrode kinetics and mass transport and how these affect their dimensionality, boundary conditions, and meshing.

Electrode kinetics: the electroanalytical models described in this section represent the transfer of electrons between a solution and a working electrode, where the latter always appears in one of the domain boundaries. The theoretical framework used to account for the kinetics of this heterogeneous electron transfer process is that of Butler and Volmer (equation 2.19). Reversible kinetics is assumed in nearly all the cases, which means fast electrode kinetics and a large exchange current density. Unless otherwise stated, the electron transfer constant in the simulations was k_s=0.1ms^{-1} and the charge transfer coefficient, α= 0.5 [9].

Mass transport: In the presence of fast electrode kinetics, mass transport governs the rate of electrochemical processes. Because the experiments were conducted in solutions of high conductivity, it has been possible to neglect the effects of migration in the simulations. Unless otherwise stated, diffusion [10] has been the main mode of mass transport throughout the models described in this thesis.

The importance of mass transport and particularly diffusion to the simulation of electrochemical problems cannot be emphasised too much, as understanding the prevalent diffusion regime has important implications in the definition of the model dimensionality.

In the absence of convection, the Einstein-Smoluchowski relation provides an estimation of the diffusion layer thickness, $\delta = \sqrt{2Dt}$. This parameter provides an estimation of the distance travelled by an electroactive species over a given period of –experimental- time. If convection is involved, then this expression is no longer valid and the diffusion layer thickness must be estimated by other means [11, 12]. There are mainly two diffusion regimes, namely planar diffusion and radial (or edge) diffusion (Figure 4-2). While planar diffusion (macroelectrodes) can be safely assumed to be one dimensional, the simulation of radial diffusion (microelectrodes) commonly requires two-dimensional models.

Faced with the question whether a small electrode behaves as a microelectrode or not, all that is needed is to compare the size of the diffusion layer with a relevant dimension of the electrode, e.g., electrode radius, r. Microelectrode behaviour is observed when radial diffusion predominates and δ>r. In all cases it is possible in principle to observe transitions between macro- and microelectrode behaviour depending on experimental conditions. Thus, at very short times, the size of the diffusion layer is always smaller than the electrode critical dimension, and planar diffusion dominates –macroelectrode behaviour (see Figure 4-2A)- [13-15]. At some point, the size of the diffusion layer grows enough so that the edges contribute significantly to the overall diffusional flux –microelectrode behaviour-. Of course, for large electrodes (macroelectrodes) the thickness of δ is normally much smaller than their critical dimension, and therefore the diffusional flux is mainly planar because natural convection prevents the development of large diffusion layers. Here the current depends solely on the electrode regardless of its shape. The current becomes "electrode shape dependent" when one of the electrode dimensions is smaller than δ, and we are effectively looking at a microelectrode [10] (Figure 4-2B). Once δ>r, something fascinating occurs, and

steady state currents appear [16]. In stark contrast to macroelectrodes, where the current decays as a function of $t^{-1/2}$ due to growth of the diffusion layer thickness, the current at microelectrodes remains constant in the absence of convention. For microelectrodes with spherical symmetry, as time evolves, the surface area of the hemisphere grows as a function of the square of the diffusion layer radius, R^2 and, although the distance from the electrode increases, more material is able to contribute to the flux and the current stabilises.
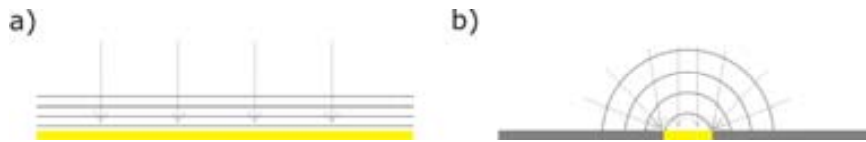
Figure 4-2: Representation of the concentration profiles: a) planar diffusion b) radial diffusion.

The effect of the radial diffusion contribution will be further explained when microelectrode array is modelled where interactions between neighbouring diffusion layers decreases the radial contribution and the total current is affected.

Dimensionality: As we have just seen, real experiments are inherently three-dimensional. However, it is usually possible to make some simplifying assumptions based on the symmetry of the real system and reduce the dimensions of the problem in the simulation. This makes the simulation process more efficient as less computational resources are required.

Figure 4-3A shows how the geometry of a macroelectrode can be simplified to a unidimensional model because the contribution of the edges to the total current is negligible compared to the contribution of the total surface. The electrode is homogenously accessible and the diffusion is mainly planar, so that only the component of diffusion normal to the electrode surface needs to be considered. The simulation of this kind of electrodes is the simplest because the three-dimensional model can be reduced to a one-dimensional model, as noted in Figure 4-3.
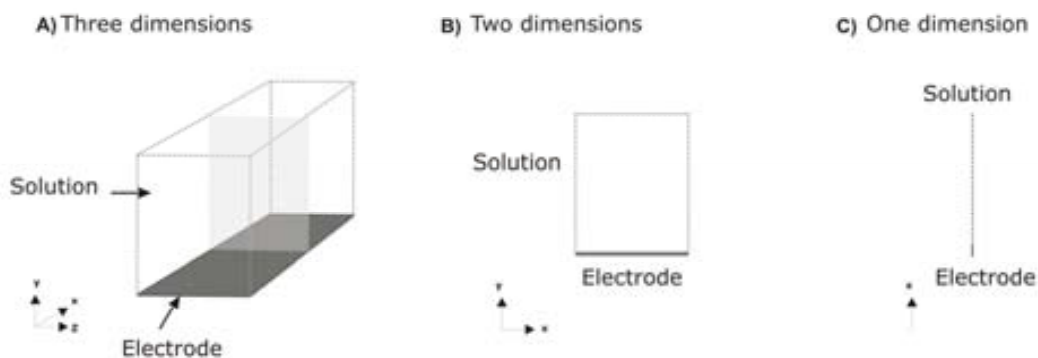

Figure 4-3: Schematic representation of the macroelectrode domain: A) three-dimensional B) two-dimensional C) unidimensional.

The case of microelectrodes is different, and the contribution of the edges to the total current cannot be neglected anymore. In the case of a microdisk, the most convenient three-dimensional domain is a cylinder concentric from the electrode. For a single microdisk, the radius and the height of such cylinder must be large enough to consider the concentration of the electroactive species at the walls of the cylinder to be the same as in the bulk. The dimensions of this domain can be reduced to two due to the symmetry around the θ axis, as shown in Figure 4-4.
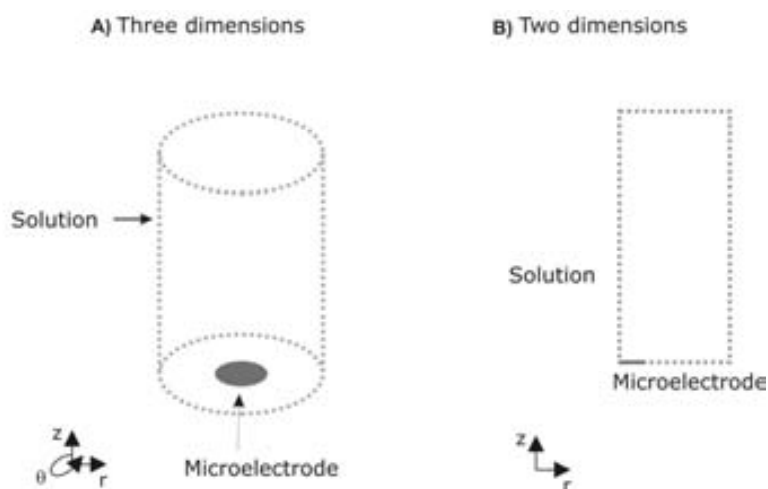
Figure 4-4: Schematic representation of the disk microelectrode domain: A) three dimensional B) two dimensional.

Boundary conditions: Figure 4-5 represents the boundary conditions and mass transfer diffusion equations used for the simulation of a macroelectrode (Figure 4-5A) and a microdisk electrode (Figure 4-5B). There is just mass flux through the boundary corresponding to the electrodes; the net mass flux through the other boundaries is zero. It is important to choose the coordinate system properly depending on the domain geometry to simplify the solution as much as possible. For the unidimensional model of a macroelectrode the most adequate system are Cartesian coordinates. However, for the two-dimensional model of a microdisk electrode the chosen coordinates are cylindrical.

Meshing: Meshing refers to the discretisation of the space domains into finite elements and it is a critical step in the solution of the simulations. The structure of the mesh and its density will have a direct impact on the efficiency and the accuracy of the solution. Therefore, the number and the size of the mesh elements usually depend on the geometry of the problem. In addition, the size of the elements also depends on where and how the variables under study change in the model. In the case of electrochemical simulations, smaller mesh elements are required in the vicinity of the electrode where the concentration gradients will be higher, and also on the edges, which are singular points because the boundary conditions drastically change from flux to no-flux (see Figure 4-2B).
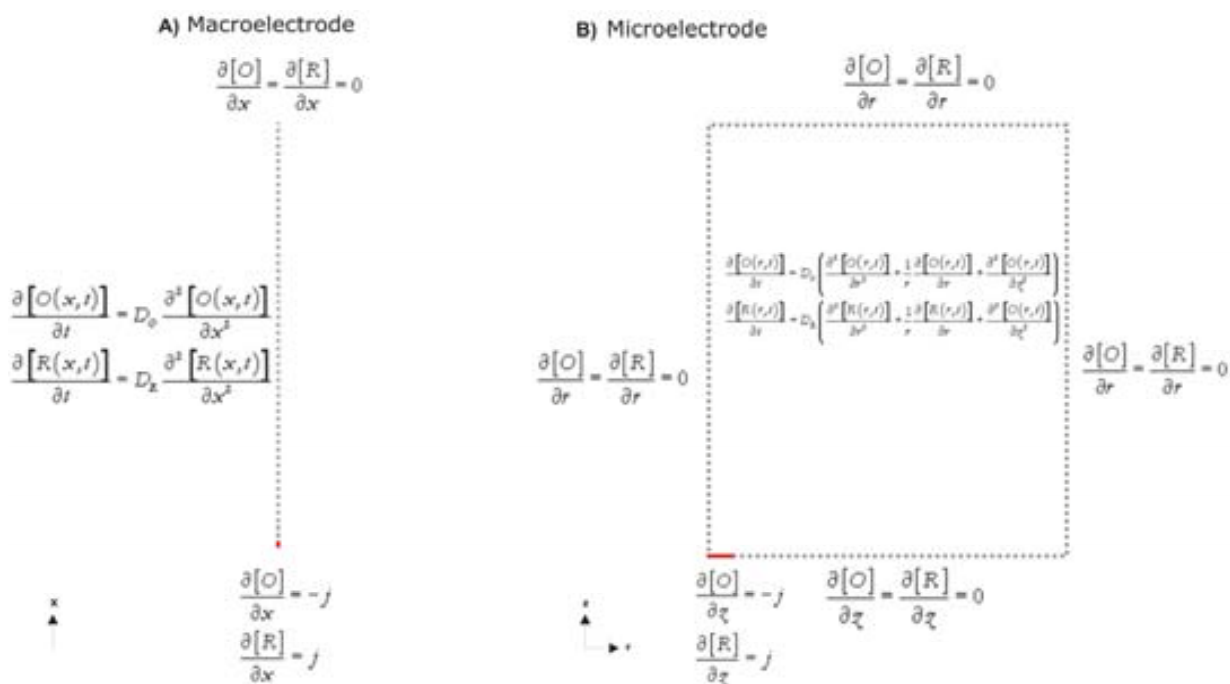
Figure 4-5: Representation of the domain definition used for the simulation of: A) macroelectrode B) disk microelectrode. In both cases, the mass transport equation and the boundary conditions are showed.

The nature of the mesh elements also depends on the dimensionality of the domain under simulation. Thus, the elements in a unidimensional model are segments while they can be polygons, typically triangles in two-dimensional models, and polyhedrons, typically tetrahedrons or cubes, in three-dimensional models.

In any case, convergence tests were performed which consisted in refining the mesh until two consecutive solutions differed from each other less than 1%. This way we ensured the consistency of the solution. Whenever possible, we verified the accuracy of the simulations further by comparing the results of the simulations to the corresponding analytical expressions when these were available.

Simulation parameters and solution: In all the models, the solution was considered diffusionally isotropic and the diffusion coefficients for both electroactive species, O and R, were assumed to be equal. Also, the simulations carried out in this thesis did not consider IR-drops between working and reference electrodes because excess supporting electrolyte and therefore high conductivity solutions were used in all the experiments.

On the other hand, when hydrodynamic conditions are considered it is also necessary to know the density and the viscosity of the solution. For water, these values are a density of 10^3 kg·m^{-3} and a viscosity of 10^{-3} Pa·s.

Once the model is solved and the mass flux through the electrode boundary is computed, the current can be calculated. For a planar macroelectrode, where the current density is constant, the current is calculated as:

$$I = -nFAD_R \frac{\partial[R]}{\partial x}\Big|_{x=0}$$ (4.2)

where x=0 corresponds with the electrode surface, n is the number of exchanged electrons, F is the Faraday constant and A is the electrode surface. As the current density for a microelectrode is not constant through the surface, it is necessary to integrate the concentration gradient. For a microdisk electrode:

$$I = -2\pi nF \int_{r=0}^{r=r_o} \frac{\partial[R]}{\partial z}\Big|_{z=0} r\,dr$$ (4.3)

where r_o is the microdisk radius and z=0 corresponds the microdisk surface.

4.3 Electrochemical techniques and models

The electrochemical techniques used in this thesis were amperometric, mainly based on potential steps (chroamperometry) and potential sweeps (linear and cyclic voltammetry). This section provides descriptions of these techniques and their simulation.

4.3.1 Potential step

Chronoamperometry consists on applying a potential step on the working electrode, typically from a value no net current flows between the electrode and the solution, to a potential where electron transfer proceeds [12].
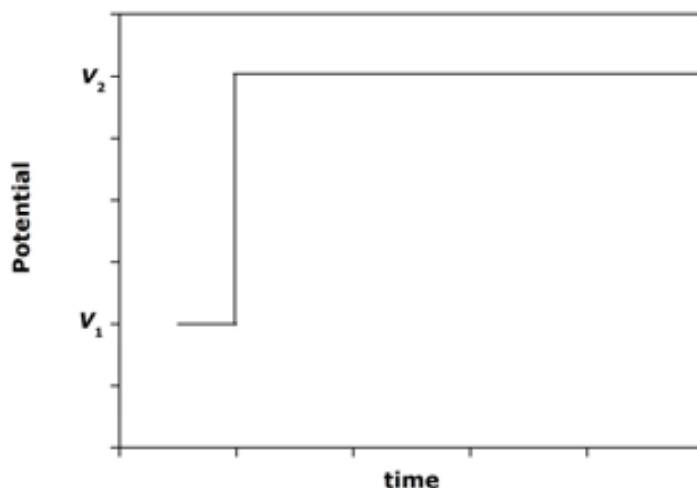

Figure 4-6: Representation of the potential function applied for the theoretical oxidation of reduced species R (V_1<$E^{o'}$<V_2).

Figure 4-6 shows the applied potential for the oxidation of species R. At V_1 species R is stable and no net current is observed. When the potential jumps to V_2 all of R present at the electrode surface is immediately oxidised, R $\rightarrow$ O + ne^- and a concentration gradient

develops that brings about diffusional transport according to Fick's laws. This transport is described below for a planar macroelectrode, a spherical macroelectrode and a microdisk electrode. In all cases, only diffusion is considered.

Diffusion is linear for a planar electrode, so Fick's second law is expressed as:

$$\frac{\partial \left[R(x,t) \right]}{\partial t} = D_R \frac{\partial^2 \left[R(x,t) \right]}{\partial x^2} \tag{4.4}$$

where is x is the coordinate perpendicular to the electrode surface. It is necessary to define the initial conditions and the boundary conditions to solve this differential partial equation. These conditions are:

- The initial concentration of R is the same for the whole solution: $\left[R(x,0) \right] = \left[R \right]_o$

- Immediately after the potential switched the concentration of R is zero at the electrode surface: $\left[R(0,t) \right] = 0 \quad t > 0$

- Regions distant from the electrode are not disturbed by the experiment $\lim_{x \to \infty} \left[R(x,t) \right] = \left[R \right]_o$

Equation(4.4) in combination with the previous boundary conditions yields an analytical solution [9]. The concentration profile is:

$$\left[R(x,t) \right] = \left[R \right]_o \left(1 - erfc \left(\frac{x}{2 \left(D_R t \right)^{1/2}} \right) \right) \tag{4.5}$$

where erfc(x) is the complementary error function. The current is related to concentration, equation (4.2), so it is described as:

$$I(t) = \frac{nFAD_R^{1/2} \left[R \right]_o}{\pi^{1/2} t^{1/2}} \tag{4.6}$$

This expression is the well known *Cottrell equation*. Current is proportional to $t^{-1/2}$ that means that current tends to zero as time increases for a chronoamperometric measurements using a planar macroelectrode.

If the geometry of the macroelectrode is spherical instead of planar, the most appropriate coordinate system is spherical (r,θ,φ) with the origin of coordinate r located at the electrode centre. Since diffusion is also spherical, there is symmetry around θ and φ, and the diffusion equation can be defined as [9]:

$$\frac{\partial \left[R(r,t) \right]}{\partial t} = D_R \left(\frac{\partial^2 \left[R(r,t) \right]}{\partial r^2} + \frac{2}{r} \frac{\partial \left[R(r,t) \right]}{\partial r} \right) \tag{4.7}$$

The boundary conditions in the new coordinate system are:
- The initial concentration of R is the same for the whole solution: $\left[R(r,0) \right] = \left[R \right]_o \quad r > r_o$

- Immediately after the potential switched the concentration of R is zero at the electrode surface: $[R(r_o,t)] = 0 \quad t > 0$

- Regions distant from the electrode are not disturbed by the experiment

$$\lim_{r\to\infty}\left[R\left(r,t\right)\right]=\left[R\right]_o$$

where r_o is the electrode radius. Equation (4.7) also has an analytical solution, and the corresponding current is described as:

$$I(t)=nFAD_R\left[R\right]_o\left(\frac{1}{\left(\pi D_R t\right)^{1/2}}+\frac{1}{r_o}\right) \tag{4.8}$$

It is important to point out that the current expression for a spherical electrode has two terms. If equations (4.6) and (4.8) are compared the latter can be expressed as:

$$I(t)_{spherical}=I(t)_{planar}+\frac{nFAD_R\left[R\right]_o}{r_o} \tag{4.9}$$

Therefore the current expressions for a planar electrode and for spherical electrodes are mainly different at long times, where the first tends to zero and the second to a constant value, as:

$$\lim_{t\to\infty}I_{planar}=0 \tag{4.10}$$

$$\lim_{t\to\infty}I_{spherical}=\frac{nFAD_R\left[R\right]_o}{r_o} \tag{4.11}$$

The convergence to a constant value for spherical diffusion is due to two opposite effects. First, there is an increase of the external surface of the diffusion layer, which means the diffusion layer is larger with time. But on the other hand, there is a relaxation of the concentration gradient between the bulk and the electrode [9]. Such convergence can be difficult to achieve for large spherical electrodes, as natural convection limits the diffusion layer thickness. However, this steady state situation due to hemispherical diffusion can be achieved when microelectrodes are used.

Microdisk electrodes are the third and last generic electrode geometry that we will address in this section, because it is one of the most popular configurations [9]. Due to the symmetry of the microdisk electrode the diffusion equation can be reduced to two dimensions (*r,z*), where *r* is centred at the microdisk and *z* is the coordinate perpendicular to its surface. The diffusion equation for a microelectrode is described by:

$$\frac{\partial\left[R(r,z,t)\right]}{\partial t}=D_R\left(\frac{\partial^2\left[R(r,z,t)\right]}{\partial r^2}+\frac{1}{r}\frac{\partial\left[R(r,z,t)\right]}{\partial r}+\frac{\partial^2\left[R(r,z,t)\right]}{\partial z^2}\right) \tag{4.12}$$

The boundary conditions in this case are:

- The initial concentration of R is the same for the whole solution: $[R(r,z,0)]=[R]_o$

- Bulk concentration of R is kept constant, so:

$$\lim_{r\to\infty}\left[R(r,z,t)\right]=[R]_o$$
$$\lim_{z\to\infty}\left[R(r,z,t)\right]=[R]_o$$

- There is not flux outside the microelectrode surface:

$$\frac{\partial\left[R(r,z,t)\right]}{\partial z}\bigg|_{z=0}=0 \qquad (r>r_o)$$

- The potential step is high enough to consider the concentration of R to be zero at the surface: $\left[R(r,0,t)\right]=0 \qquad (r\le r_o,t>0)$

The solution of this partial differential equation system is quite complex. Aoki and Osteryoung [17, 18] solved the equation dividing the approximate solution in two different series for small and large values of a temporal parameter named τ, $\tau=4D_R t/r_o^2$. Later, Shoup and Szabo [19] calculated a single expression valid for any range of τ with an accuracy of 0.6%. From a quantitative point of view, it is possible to differenciate between these two regions. At short times, the microdisk electrode behaves as a macroelectrode, where there is only a perpendicular component to the diffusion, so the diffusion layer is mainly planar and the current is described by Cottrell's equation, (4.6). At long times, the diffusion layer is comparable to the microdisk radius so radial diffusion is considerable and the measured current is higher than if just perpendicular diffusion was taken at play. This effect is known as "*edge effect*". In this case, the current achieves a steady state value that can be analytically calculated and described by [10]:

$$I_{\text{lim}}=\frac{4nFAD_R[R]_o}{\pi r_o}=4nFD_R[R]_o r_o \tag{4.13}$$

Simulation of potential step experiments

In this section we describe the simulation of potential step experiments at a planar macroelectrode and at a microdisk electrode. The results of these simulations will be compared to their corresponding analytical values.

The applied potential to the working electrode is:

$$\begin{aligned} E &< E^{o'} & t &= 0 \\ E &> E^{o'} & t &> 0 \end{aligned} \tag{4.14}$$

Fast electrode kinetics are considered. An initial R bulk concentration of 1 mol·m^{-3} was used and the diffusion coefficients of O and R were assumed to be equal.

The planar macroelectrode is modelled using a one-dimensional domain consisting of a segment of 500 μm long (as it is shown in Figure 4-3), an end of which is the electrode boundary. The mesh elements have a maximum size of 5 μm within the domain and 0.1 μm closed to the electrode boundary where the concentration gradient is expected to be steeper.

Figure 4-7 shows the transient current density obtained from the simulation together with that corresponding to the Cottrell equation (equation (4.6)) under the same experimental parameters. The agreement between the simulation and Cottell's expression is better than 99% over the entire range, which shows that the unidimensional model is adequate for the simulation of planar diffusion.
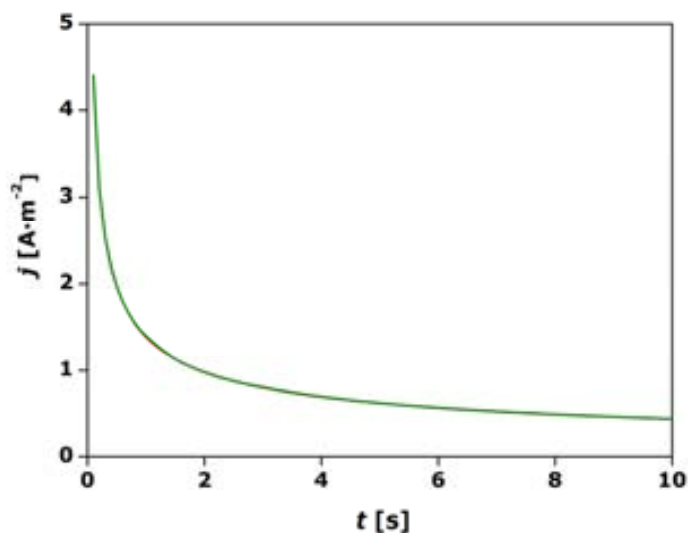

Figure 4-7: Comparison between the modelled current density (green line) and theoretical based on Cottrell expression (red line). Both results are so close that they are almost impossible to distinguish graphically. Conditions: $[R]_o$=1 mol·m^{-3}, k_s=0.1 m·s^{-1}, α=0.5, n=1 and D_R=6.5·10^{-10} m^2·s^{-1}.

Microdisk electrodes, on the other hand, are modelled using two dimensional domains. The present case consists in a square of 400 μm x 400 μm. The microdisk radius is defined as a boundary 10 μm long, as shown in Figure 4-4.

In this case, the mesh is composed of triangular elements of sizes ranging from 0.1 μm over the electrode boundary and 0.01 μm close to the singular point (r_o, z) = (10, 0) μm. The mesh needs to be particularly fine around this point because it represents a flux discontinuity; there is flux only through the electrode side of this point. Figure 4-8 shows the two-dimensional model of the microdisk electrode. Diffusion direction is schematised by arrows, so it is possible to see that diffusion is two-dimensional close to the microdisk perimeter (close to the point r_o=10 μm).
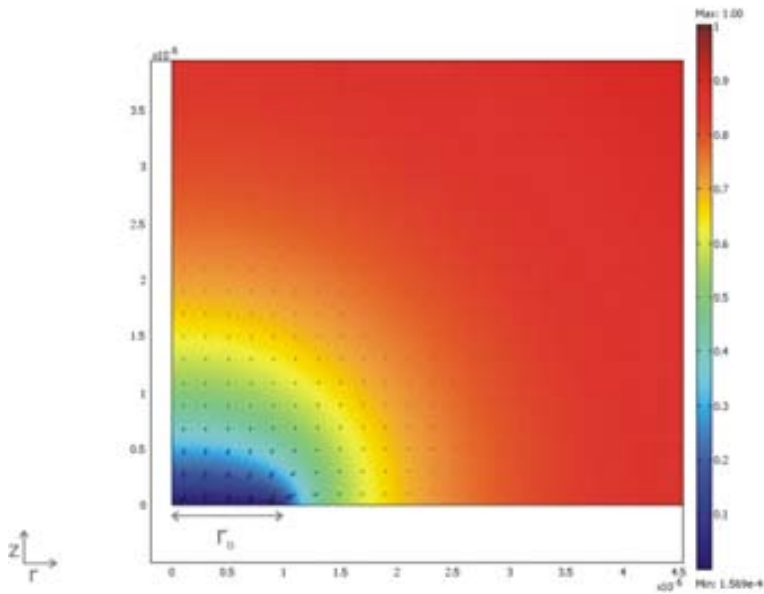
Figure 4-8: Two dimensional profile of the concentration of the specie R at 150s. The arrows indicate the diffusional flux of specie R.

The simulated transient current is showed in Figure 4-9. The theoretical limiting current, described by equation(4.13), is also drwan. The figure shows the good agreement between simulated and analytical steady-state values. Furthermore, Table 4-1 shows the modelled and theoretical limiting current for different microdisk radius as well as the relative error between them. In all cases, this error is well within 1%.
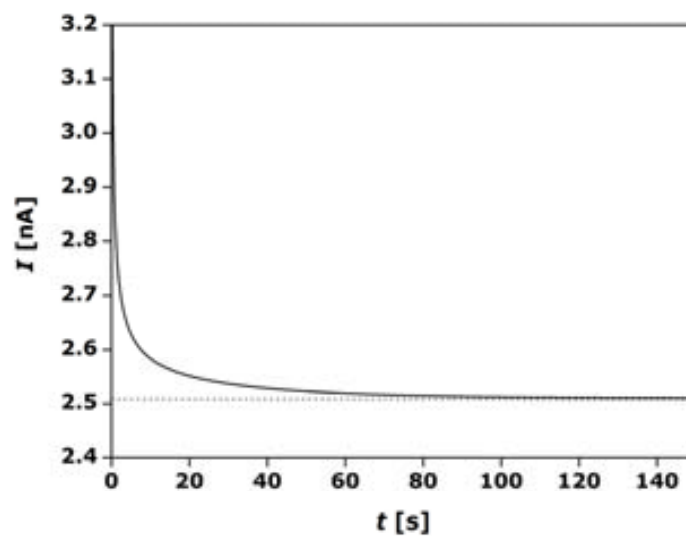

Figure 4-9: Comparison between the modelled current (solid line) for a 10μm radius disk microelectrode with the theoretical limiting current (dotted line). Conditions: $[R]_o=1$ mol·m^{-3}, $k_s=0.1$ m·s^{-1}, $\alpha=0.5$, n=1 and $D_R=6.5\cdot10^{-10}$ m^2·s^{-1}.

Table 4-1: Theoretical limiting current and modelled current for disk microelectrodes of different.

Radius (µm)	$I_{limiting}$ model (nA)	$I_{limiting}$ theory (nA)	Relative error (%)
5	1.26	1.25	<1
10	2.51	2.50	<1
12.5	3.15	3.14	<1
15	3.80	3.76	1

4.3.2 Potential sweep techniques

Potential sweep techniques are based on the application of a potential sweep on the electrode. There are two important techniques, namely linear sweep voltammetry and cyclic voltammetry depending on the number of applied cycles. Linear sweep voltammetry (LSV) consists in a single potential sweep:

$$E(t) = E_i \pm \upsilon t \tag{4.15}$$

where E_i is the initial potential and υ is the scan rate. Normally, the potential is scanned from a value where no electron transfer reactions occur towards potentials where a reaction of interest takes place. The measured current, I, is represented versus the potential, E, to define $I(E)$ representations called voltammograms, as it can be seen in Figure 4-10.
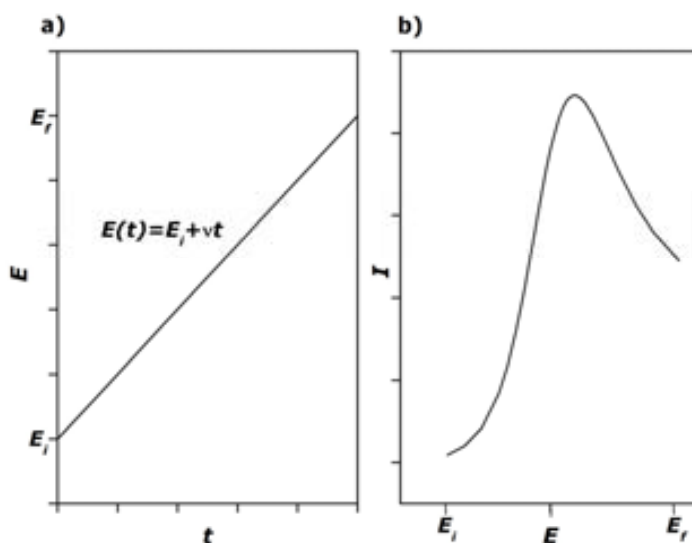

Figure 4-10: a) Potential function applied at the electrode to oxise the reduced specie R. b) Current profile vs potential.

Figure 4-10A shows the potential ramp applied to an electrode, and Figure 4-10B shows the resulting voltammogram for the case where the diffusion controlled oxidation of a species in solution is considered.

As in the previous section, linear sweep voltammetry will be studied at two different electrode geometries subject to different diffusion regimes: a macroelectrode subject to planar diffusion and disk microelectrode subject to hemispherical diffusion.

For a planar macroelectrode, Fick's second law is defined as [20]:

$$\frac{\partial[O]}{\partial t} = D_O \frac{\partial^2[O]}{\partial x^2} \tag{4.16}$$

$$\frac{\partial[R]}{\partial t} = D_R \frac{\partial^2[R]}{\partial x^2} \tag{4.17}$$

where x is the coordinate perpendicular to the electrode surface. Because we are assuming fast electron transfer kinetics at the electrode, the relation between the redox couple concentrations at the electrode surface follows Nernst equation [20], so it can be described as:

$$\frac{[O(0,t)]}{[R(0,t)]} = \exp\left(\frac{nF}{RT}(E_i - \upsilon t - E^o)\right) \tag{4.18}$$

Other boundary conditions are:

- Initially, only species R is present in the solution:

$$[R(x,0)] = [R]_o$$
$$[O(x,0)] \to 0 \tag{4.19}$$

- Regions distant from the electrode are not disturbed by the experiment:

$$\lim_{x \to \infty}[R(x,t)] = [R]_o$$
$$\lim_{x \to \infty}[O(x,t)] = [O]_o \tag{4.20}$$

To solve the partial differential equations (equation (4.16) and equation(4.17)), together with the boundary conditions (equation (4.18), equation (4.19) and equation (4.20)) requires complex mathematical treatments [9], which are out of the scope of this thesis. One of the most common and complete solution for these equation was developed by Nicholson and Shain [20]. In that work, the current is defined as:

$$I = nFAD_R\left(\frac{\partial[R(x,t)]}{\partial x}\right)_{x=0} = -nFAD_O\left(\frac{\partial[O(x,t)]}{\partial x}\right)_{x=0} \tag{4.21}$$

$$I = nFA[R]_o(\pi D_R \sigma)^{1/2} \chi(\sigma t) \tag{4.22}$$

Where $\sigma = nF\upsilon/RT$ and $\chi(\sigma t)$ is a function with a real value for each point of the voltammogram [20]. Figure 4-11 shows the function $\pi^{1/2}\chi(\sigma t)$ versus $n(E-E_{1/2})$. The shape is the same that was previous schematised in Figure 4-10B showing the typical peak current for a potential value close to the standard redox potential. $E_{1/2}$ is the half wave potential and it is defined as:

$$E_{1/2} = E^{o'} + \frac{RT}{nF}\ln\sqrt{\frac{D_R}{D_O}} \tag{4.23}$$

For fast electron transfer, the maximum value of the function is $\pi^{1/2}\chi(\sigma t) = 0.4463$. Therefore the current peak depends on the scan rate as:

$$I_p = 0.4463 \left(\frac{F^3}{RT} \right)^{1/2} n^{3/2} A D_R^{1/2} [R]_o \upsilon^{1/2} \tag{4.24}$$

and the potential where this current peak is located can be calculated as:

$$E_p = E_{1/2} + 1.109 \frac{RT}{nF} = E_{1/2} + 28.5/n \quad mV \; at \quad 25^o C \tag{4.25}$$

From equations (4.24) and (4.25) it is important to point out that for a electrochemically reversible system (nernstian), the peak potential is independent of the scan rate, υ, and the current peak is proportional to $\upsilon^{1/2}$.
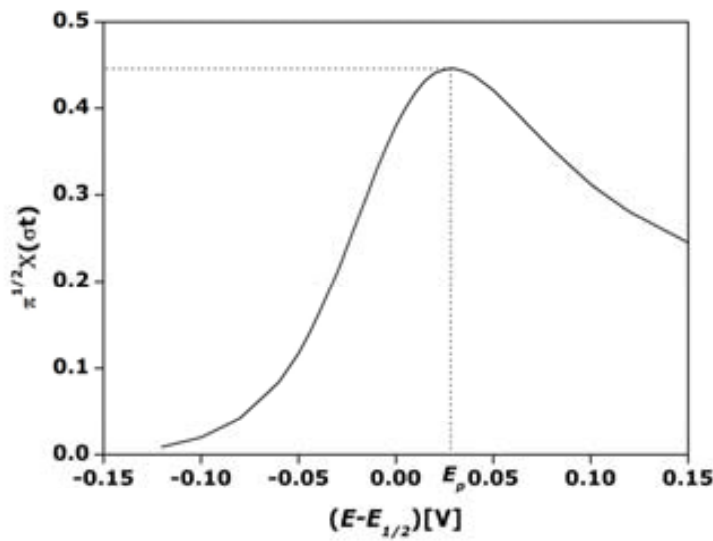

Figure 4-11: Adimensional current, $\pi^{1/2}\chi(\sigma t)$.

The previous theoretical description can be also used to define cyclic voltammetry (CV) where the potential is scanned in one direction for a certain time, λ, and then switched back in the opposite direction. Furthermore, cyclic voltammetry is one of the most popular electrochemical techniques, and is used to obtain more complete information about electrochemical processes [12]. This function is described as [9]:

$$\begin{aligned} E &= E_i \pm \upsilon t & 0 \leq t \leq \lambda \\ E &= E_i \pm 2\upsilon\lambda \mp \upsilon t & t > \lambda \end{aligned} \tag{4.26}$$

Figure 4-12A shows the typical triangular waveform potential applied on the working electrode and Figure 4-12B shows the measured current, *I(E)*.

For the backward scan, once the potential is switched, the opposite electrochemical reaction will take place, as shown in Figure 4-12B, which shows a typical voltammogram for a fully reversible redox couple. Peak current value and separation between peaks are related to

electrode kinetics as well as coupled homogeneous chemical reactions, e.g.: the separation between the oxidation peak ($E_{p,a}$) and the reduction peak ($E_{p,c}$) is an indicator of the electron transfer rate. For a totally reversible system, the separation between the two peaks is described by [9]:

$$\Delta E_p = 2.218 \frac{RT}{nF} \qquad (4.27)$$

As the electronic transfer rate decreases, peak-to-peak separation increases [21]. This effect is showed in ANNEX 1 where cyclic voltammetry models for a planar macroelectrode and for a microdisk electrode to study irreversibility are described.
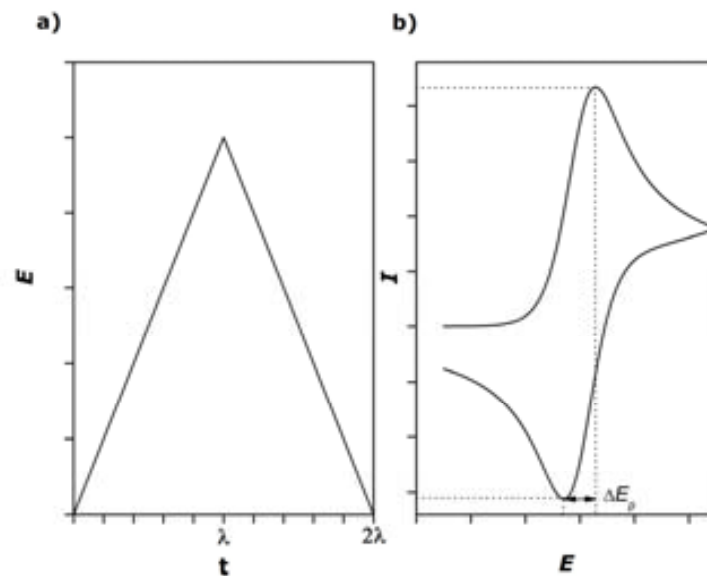

Figure 4-12: a) Potential function applied in cyclic voltammetry to oxidised the reduced specie R. b) Current profile vs potential.

The analytical description of potential sweep technique at a microelectrode is much more complex because there are two dimensions involved [16, 22, 23]. However, in a first approximation, the voltammetric response for any microelectrode can be divided in two components [12]:

$$I = I_{planar} + I_{radial} \qquad (4.28)$$

Particularly for a microdisk electrode of radius r_o, the relation between the planar and the radial contribution to the total current depends on the ratio between such radius and the diffusion layer. This ratio is described by the parameter Dt/r_o^2. At long values, $Dt/r_o^2 > 1$, the diffusion layer is larger than the critical dimension (r_o) and the current tends to a steady state value. However, for a small value, $Dt/r_o^2 < 1$, planar diffusion governs over radial diffusion and not steady state value is achieved, in that case the microelectrode response is similar to the macroelectrode behaviour [12].

This time dependency can be translated to scan rate values, so depending on the scan rate it is possible to achieve steady state currents or, if the scan rate is sufficiently fast, microelectrodes may display current peaks in a similar way to macroelectrodes. The steady state values were shown in Table 2.1, for different microelectrode configurations and for the microdisk electrode case is:

$$I_{stationary} = 4nFDcr_o \qquad (4.29)$$

Given the difficulty to solve the mass transport equations to a microelectrode during a potential sweep, most authors prefer to use numerical simulations to validate their experimental results [24-27].

Simulation of potential sweep experiments

The only difference between the simulation of potential step and potential sweep experiments is the potential function applied, which in the case of a linear sweep is:

$$E = E_i + \upsilon t \qquad t > 0 \qquad (4.30)$$

As was described in the theory section, the scan rate is an important parameter in voltammetric measurements. We will study the behaviour of macroelectrodes and disk microelectrodes as a function of scan rate.

Figure 4-13 shows the dependency between peak currents and the square root of the scan rate for a macroelectrode, as expected from equation (4.24), and it shows the excellent agreement between the theoretical and modelled data.
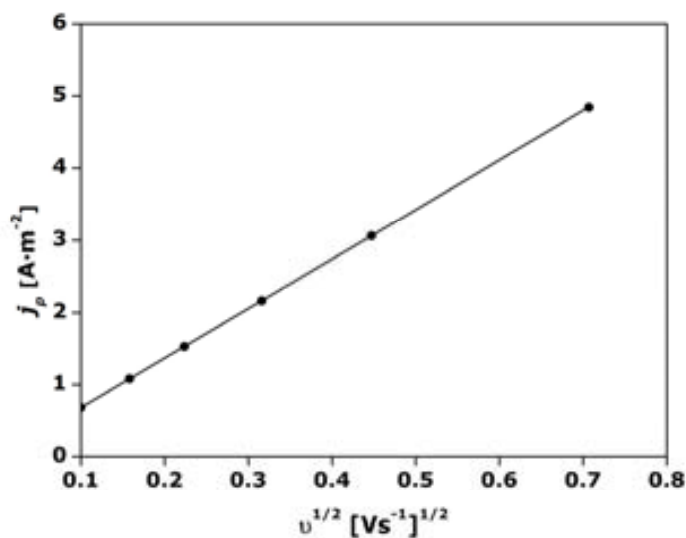

Figure 4-13: Relation between the peak current and the square root of the scan rate for: theoretical current (solid line) and modelled current (dots). Conditions: $[R]_o$=1 mol·m^{-3}, k_s=0.1 m·s^{-1}, α=0.5, n=1 and D_O=D_R=6.5·10^{-10} m^2·s^{-1}.

For the microdisk electrode model, two different radii were simulated (10 μm and 1μm) to demonstrate the different behaviours that may be observed depending on the ratio between

scan rate and microelectrode size. Figure 4-14 shows the current density for a 10 μm radius model. It is possible to differentiate the two mentioned behaviours, for scan rate smaller than 100 mV·s^{-1} the current tends to the steady state value (equation (4.29)) as the scan rate is slow enough to allow the development of a hemispherical diffusion layer. A current peak appears at faster scan rates, which means that the diffusion layer is comparable or smaller than the microdisk radius, and that the importance of planar diffusion is comparable to that of radial diffusion.
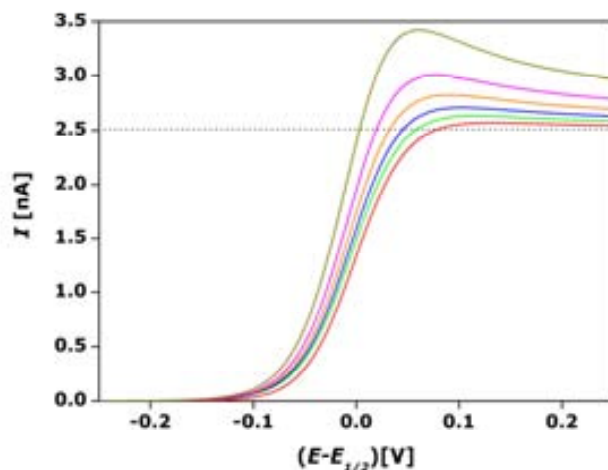

Figure 4-14: Current vs potential for a 10 μm radius microelectrode for different scan rates: 10 mVs^{-1} (red line), 25 mVs^{-1} (green line), 50 mVs^{-1} (blue line), 100 mVs^{-1} (orange line), 200 mVs^{-1} (pink line) and 500 mVs^{-1} (yellow line). Conditions: [R]$_o$=1 mol·m^{-3}, k_s=0.1 m·s^{-1}, α=0.5, n=1 and D_O=D_R=6.5·10^{-10} m^{2}s^{-1}.

Figure 4-15 shows the current vs. potential for the 1 μm radius model. In that case, there is not scan rate dependency of the current, and the current reaches the steady state value described by equation (4.29) over the entire scan rate range studied. The relative error between the modelled current and the theoretical value is less than 2%.
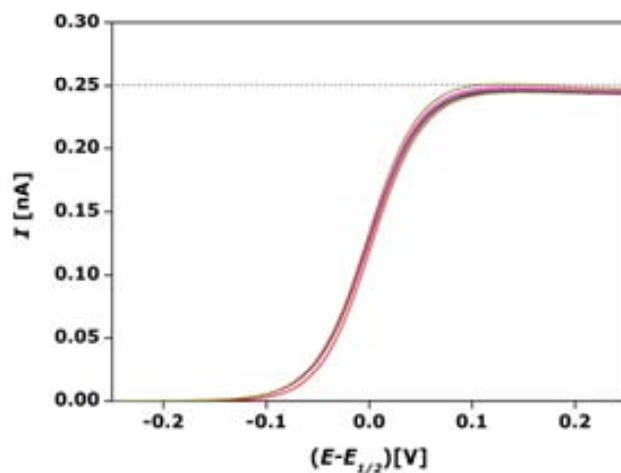

Figure 4-15: Current vs potential for a 1 μm radius microelectrode for different scan rates: 10 mVs^{-1} (red line), 25 mVs^{-1} (green line), 50 mVs^{-1} (blue line), 100

mVs^{-1} (orange line), 200 mVs^{-1} (pink line) and 500 mVs^{-1} (yellow line). Conditions: $[R]_o$=1 mol·m^{-3}, k_s=0.1 m·s^{-1}, α=0.5, n=1 and D_O=D_R=6.5·10^{-10} m^{2}s^{-1}.

4.3.3 Mass transport under hydrodynamic conditions

The voltammetric techniques described in the previous section can also be used in the presence of forced convection. The electrochemical techniques applied under convection are named hydrodynamic techniques. One common hydrodynamic technique is the rotating disk electrode [11], where the electrode rotation inside the solution creates a continuous stream of material towards it. However, we focus on channel microelectrodes, where the microelectrode has a fixed postion on one of the walls of a fluidic channel and fluid flows over it.

Hydrodynamic techniques have significant advantages compared to the same techniques used in stagnant solutions because they afford control over the diffusion layer thickness, which leads to steep concentration gradients that are constant over time.

In this thesis we focus on pressure driven systems with one or several microelectrodes placed on its microchannel walls. Figure 4-16 shows an example of this configuration, consisting in a band microelectrode. From the electroanalytical point of view, channel electrodes offer some advantages [28]:

- The movement of the fluid towards the channel allows the continuous monitoring in electroanalysis.
- One product generated on an upstream electrode can be easily detected downstream by another electrode.
- Linear velocity is controlled over a wide range, so it is possible to use flows with orders of magnitude of difference. The mass transport is related to the channel features and the size of the electrode.
- The measured current is steady state and proportional to flow cube root which allows the study of broad range of reactions and differentiate between different mechanisms.
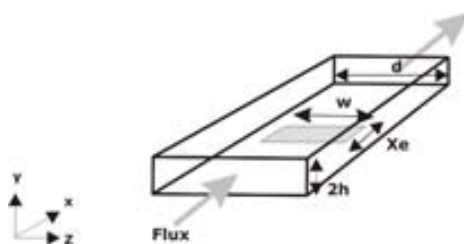

Figure 4-16: Representation of a microband channel electrode. The channels dimensions are: height (*2h*) and width (*d*). The microband dimensions are: width (*w*) and length (*x$_e$*). The arrows shows the fluid direction.

The most common electrode configuration in microfluidic channels is the microband electrode [29-32]. In this thesis, we focus on the study of microband channel electrodes. In

hydrodynamic cases, simulation is an essential tool, as it is necessary to solve fluid dynamics which are not linear partial differential equations which, except for very specific conditions [28, 33], can not be solved analytically. There are many good works on the simulation of amperometric detection under hydrodynamic conditions [29-31, 34-37].

One of the most popular analytical solutions for the Navier-Stokes equation is the well-known Poiseuille flow [33]. In this case, the fluid is flowing through a straight and rigid channel due to pressure gradient between the input and the output of the channel, and laminar flow is considered, so inertial terms of the Navier- Stokes equations can be omitted as it means small Reynolds numbers [38]:

$$\bar{v} = \left(v_x, 0, 0 \right)$$
$$\eta \left(\frac{\partial^2 v_x}{\partial y^2} + \frac{\partial^2 v_x}{\partial z^2} \right) - \frac{\partial p}{\partial x} = 0 \qquad (4.31)$$

where η is viscosity and p pressure. Therefore, the analytical solution, considering a duct of circular cross section and that the fluid velocity at the channel walls is zero, has the well-know parabolic profile [38]:

$$v_x(r) = \frac{\Delta p}{4\eta L} \left(R^2 - r^2 \right) \qquad (4.32)$$

where r is the radial coordinate from the centre of the circular cross section, Δp is the pressure gradient between the input and the output of the channel, L is the length of the channel and R is the radius of the circular cross section. From equation (4.32) it is possible to deduce that the volume flow rate, Q, is:

$$Q = \frac{\pi R^4}{8\eta L} \Delta p \qquad (4.33)$$

The coefficient $8\eta L/\pi R^4$ is known as the fluidic resistance. Note that the fluidic resistance in a circular cross section channels is proportional to $1/R^4$, and that it increases dramatically as the radius decreases. Consequently, the pressure gradient to move a liquid becomes higher as the channel dimensions shrink.

For a rectangular cross-section channel which width is significantly larger than its height, the velocity profile is described by:

$$v_x(y) = \frac{\Delta p}{2\eta L} \left(2h - y \right) y \qquad (4.34)$$

where $2h$ is the height of the channel. In that case the fluidic resistance is $3\eta L/2wh^3$, where w is the width of the channel.

Mass transfer equations close to a circular section channel under laminar flow was solved by Levich [33]. Levich estimated the necessary input length of a tub of radius R to be able to consider laminar flow for fluid with a Reynold number Re<2500 as:

$$h_{inlet} \sim 0.1 R \cdot \mathrm{Re} \qquad (4.35)$$

As is schematised in Figure 4-17, after h_{inlet} the fluid flows in the axial direction with parabolic profile described by Poiseuille's expression:

$$v = v_{max}\left(1 - \frac{r^2}{R^2}\right)$$

(4.36)

where v_{max} is the maximum linear velocity achieved at the centre of the tube and r is the radial coordinate.
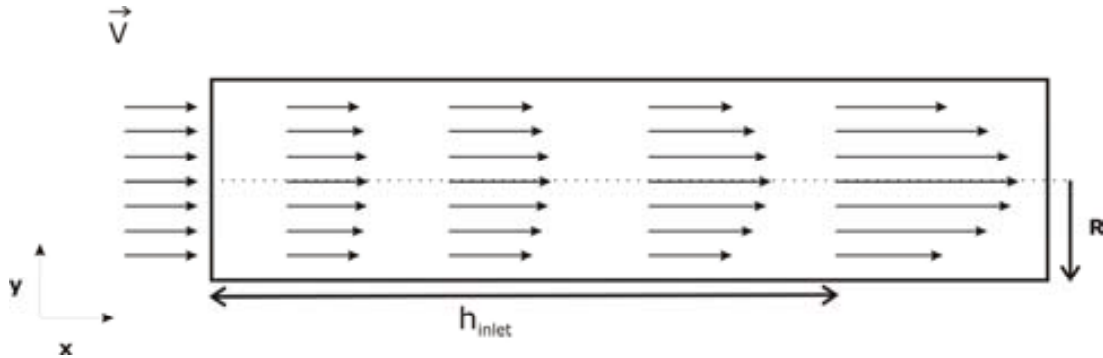

Figure 4-17: Velocity profile evolution from at initial point where the profile is planar until the final parabolic profile is achieved.

To solve the mass transfer equation close to the walls ($r \approx R$) it is necessary to make the following assumptions:

- Linear velocity profile:

$$v = v_{max}\left(1 - \frac{r^2}{R^2}\right) \rightarrow v \approx v_{max}\frac{2y}{R} \quad where \quad y = R - r$$

(4.37)

- Diffusional transport perpendicular to the wall.

The mass transport equation including diffusion and convection in Cartesian coordinates is:

$$\frac{\partial c_j}{\partial t} = D_j\left(\frac{\partial^2 c_j}{\partial x^2} + \frac{\partial^2 c_j}{\partial y^2}\right) - \left(v_x\frac{\partial c_j}{\partial x} + v_y\frac{\partial c_j}{\partial y}\right)$$

(4.38)

Assuming that flow is stationary and the previous considerations, the mass transfer equation can be described by:

$$\frac{2v_{max}}{R}y\frac{\partial c}{\partial x} = D\frac{\partial^2 c}{\partial y^2}$$

(4.39)

To solve equation (4.39), it is necessary to define some boundary conditions as:

- The concentration is zero at the walls:

$$c = 0 \quad at \quad y = 0$$

(4.40)

- The concentration at the centre of the tube is constant:

$$c \rightarrow c^o \quad when \quad y \rightarrow \infty$$

(4.41)

Equation (4.39) together with the boundary conditions (equation (4.40) and equation (4.41)) has an analytical solution that can be found in [33]. We are interested in the flux density in

the vicinity of the electrode where there is a stagnant layer known as Nernst diffusion layer with just diffusional mass transfer [39]. Such flux is described as:

$$j = D\left(\frac{\partial c}{\partial y}\right)_{y=0} = 0.67c^{o}D\left(\frac{v_{max}}{DRx}\right)^{1/3}$$

(4.42)

The diffusion flow for a section segment from $x=x_a$ to $x=x_b$ is calculated as:

$$J = 2\pi R\int_{x_a}^{x_b} jdx$$

(4.43)

If the channel section is rectangular instead of circular, with a width, d, much larger than its height, $2h$, as it can be considered as two parallel walls, the parabolic velocity profile is defined as [38]:

$$v_x(y) = v_{max}\left[\frac{2y}{h} - \frac{y^2}{h^2}\right]$$

(4.44)

where $v_{max}=\Delta ph^2/2\eta L$. For small values of y-coordinate that means close to the wall, equation (4.44) can be approximated to:

$$v \approx v_{max}\frac{2y}{h}$$

(4.45)

Equations (4.37) and (4.45) are pretty much the same, just changing radius (R) for height (h), so mass transfer equation (equation (4.39) can be solved using the same approximations and boundary conditions and lead to the same solution, equation (4.42) Therefore, the theoretical current, for one exchanged electron and totally reversible electrode kinetics, can be calculated as:

$$I = FJ = Fd\int_{0}^{x_e} jdx = Fd\int_{0}^{x_e} 0.67c^{o}D\left(\frac{v_{max}}{Dhx}\right)^{1/3} dx$$

(4.46)

Where x_e and d are the length and the width of the band electrode. Solving this integral leads to the current expression for band electrodes within a rectangular section channel [30]:

$$I = 0.925Fcw(x_eD)^{2/3}\left(\frac{4}{3}\frac{v_{max}}{h}\right)^{1/3}$$

(4.47)

This current expression, equation (4.47), does not take radial diffusion into consideration. Since only plannar diffusion was considered to reach this expression, it will not hold when radial diffusion is important . A microband electrode inside a microchannel is modelled in the next section, and we show the cases in which equation (4.47) applies or not due to the presence of radial diffusion.

Simulation of transient currents at a channel microband electrode

Here we describe a model to study voltammetric processes at microband electrodes in a microchannel of rectangular section. Mass transfer is governed by diffusion and convection, as migration is neglected considering a high concentration of supporting electrolyte [9]. Figure 4-18A represents a microband inside a microchannel and Figure 4-18B depicts the

two-dimensional domain used to model the microband. It is possible to use a two-dimensional domain, corresponding to a plane in the axial direction, because channel width (*d*) is higher than the channel height (*2h*). Figure 4-18B also shows the initial conditions for the concentration as well as for the velocity field and the boundary conditions. Mass flux, j, is controlled by the applied potential *E* and electron transfer follows Butler-Voltmer kinetics (equation 2.19). Microelectrodes must be placed outside the inner region, in a zone where the parabolic velocity profile is already achieved [33, 40].
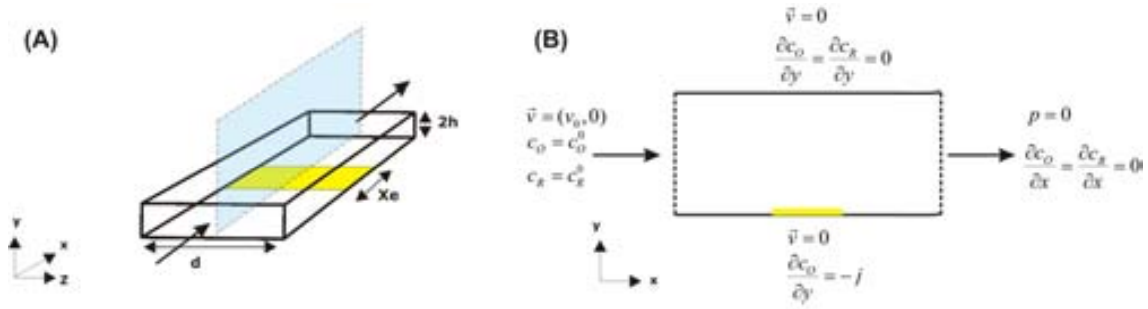

Figure 4-18: Representation of the modelled microband. (A) The microchannel is *2h* high and *d* wide, and the microband is x_e long and its width is the same as the microchannel. (B) Representation of the modelled domain which is a two dimensional cut of the three dimensional structure, as it is showed in (A).

According to equation (4.35) the inner region for a 10 $\mu L \cdot min^{-1}$ is around 3 μm. in the two-dimensional model, considering diffusion and convection, the mass transfer equation is described as:

$$D_i\left(\frac{\partial^2 c_i}{\partial^2 x} + \frac{\partial^2 c_i}{\partial^2 y}\right) - \left(v_x \frac{\partial c_i}{\partial x} + v_y \frac{\partial c_i}{\partial y}\right) = 0 \tag{4.48}$$

where c_i is the concentration of the specie, in that there are two different species (O and R) so two different equation, (v_x, v_y) are the components of the linear velocity field. The fluid movement is defined by Navier- Stokes equation [31, 32] considering a incompressible and Newtonian fluid, as:

$$\rho\left(v_x \frac{\partial v_x}{\partial x} + v_y \frac{\partial v_x}{\partial y}\right) - \eta\left(\frac{\partial^2 v_x}{\partial x^2} + \frac{\partial^2 v_x}{\partial y^2}\right) + \frac{\partial p}{\partial x} = 0 \tag{4.49}$$

$$\rho\left(v_x \frac{\partial v_y}{\partial x} + v_y \frac{\partial v_y}{\partial y}\right) - \eta\left(\frac{\partial^2 v_y}{\partial x^2} + \frac{\partial^2 v_y}{\partial y^2}\right) + \frac{\partial p}{\partial y} = 0 \tag{4.50}$$

$$\frac{\partial v_x}{\partial x} + \frac{\partial v_y}{\partial y} = 0 \tag{4.51}$$

where ρ and η are the density and the viscosity of the fluid, and *p* is pressure. The two-dimensional model was solved considering a microband of 20 μm length and 5 $mol \cdot m^{-3}$ of concentration of electroactive specie (ferro/ferricyanide) in a channel 95 μm wide and 77 μm high. Figure 4-19 shows the ratio of the modelled steady state current compared to that

predicted by Levich for a flow rate range 0-5 μL·min^{-1}. For low flow rate values the "edge effect" is more important and causes a significant difference between both currents [30, 32]. Levich's approximation does not considerer radial diffusion, but only diffusion normal to the channel walls. At high flow rates, diffusion layer thickness and shape are controlled by forced convection, but at low flow rates edge diffusion contributes more to the total current. In that case, it is essential to consider that for a microelectrode there are two contributions to the current. This radial diffusion at the perimeter of the microelectrodes, also known as "edge effect" causes the difference between the modelled current and theoretical values.
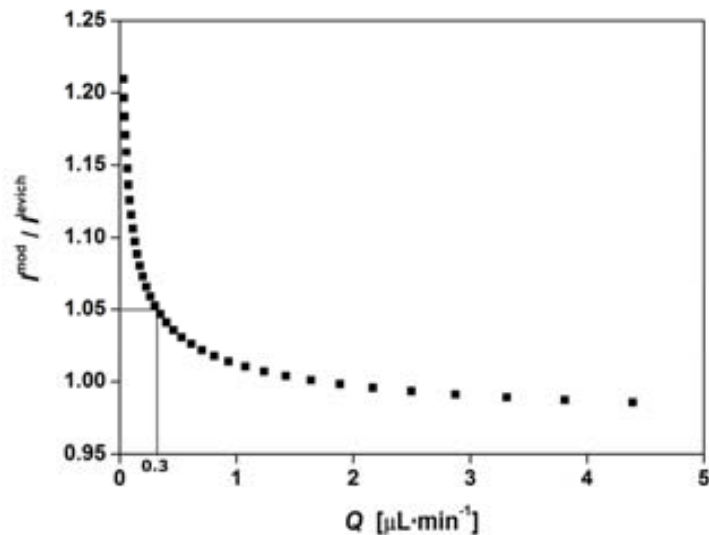

Figure 4-19: Ratio between the modelled current and theoretical channel microband defined by Levich, I^{mod}/I^{levich} vs the flow rate.

Figure 4-20 shows the diffusion layer at the same electrode under two different flow rates. For 10 μL·min^{-1} the diffusion layer is flatter than for 1 μL·min^{-1}, that means less radial diffusion or in other words, planar contribution to the diffusion is more important and diffusion can be described as just perpendicular to the electrode.
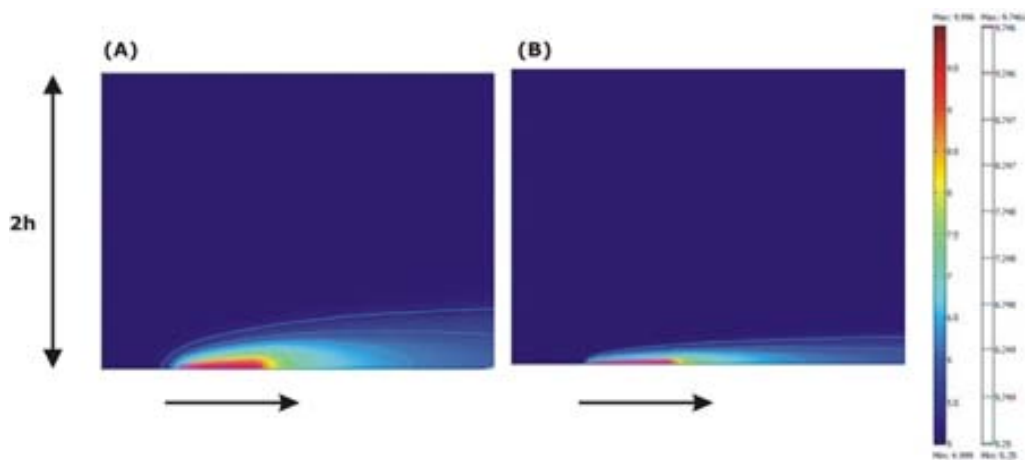

Figure 4-20: Diffusion layer at the same electrode (20 μm long) for: (A) 1 μL·min^{-1} and (B) 10 μL·min^{-1} flow rates.

This effect is also described by Amatore and co-workers in [41]. They distinguished between convective zone, where Levich's approximation is valid, and a "thin layer" zone, where currents are higher respect to Levich's prediction due to hemispherical diffusion. These two zones depend on microband dimensions, microchannel geometry and flow rates. Hence, simulation of electroanalytical techniques under hydrodynamic conditions is an essential tool to validate experimental results as such measurements highly depend on the channel configuration and experimental features.

4.4 Disk microelectrode arrays

An important drawback of microelectrodes is their small output currents, which are often engulfed by the presence of electrical noise in the signal. One way to overcome this limitation is the parallel arrangement of a large number of microelectrodes, giving rise to microelectrode arrays. Microelectrode arrays are attractive compared to macroelectrodes because they provide currents of similar magnitude with considerably less background/capacitive current [10]. The most popular arrangements are hexagonal, cubic and random [42]. In this thesis, we focus on modelling arrays of square lattice. For any microelectrode array configuration, maximum current density is achieved when all the microelectrodes work independently and act as single, isolated microelectrodes where radial diffusion dominates mass transport. To reach this situation, it is important to control the separation between microelectrodes to avoid overlapping of neighbouring diffusion layers. Therefore some guidelines are required for the design of such microelectrode arrays. Girault *et. al.* [42] suggested that some of the accepted guidelines are not absolutely correct and a better theoretical treatment is required. In that work, they used a three-dimensional model of a microelectrode array to study the effect of the distance between microelectrode for potential sweep techniques. However, these simulations were too cumbersome and other approaches based on the reduction from three to two dimensions are more practical. Davies *et. al.* [43] describe a two dimensional method based on the diffusion domain approach first proposed by Amatore and co-workers [44] to model microelectrode arrays and study the most effective guidelines to achieve the best centre-to-centre separation.

Moreover, most of the microelectrode arrays fabricated using lithographic methods lead to slightly recessed microelectrodes, which display a slightly different response than inlaid microelectrodes.

Therefore, after explaining how a microelectrode array is modelled a brief section about recessed microelectrode is included. The technique used to show the effect of the recess to the steady state current is a potential step although the effect is independent of the electrochemical technique applied.

4.4.1 Simulation of mass transport to disk microelectrode arrays

Depending on the prevalent experimental conditions, microelectrode arrays may go through the diffusion regimes shown in Figure 4-21, as described in [43, 45]. Figure 4-21A shows the

first category when the diffusion layer thickness is small compared to the size of the microelectrode. In this case, diffusion can be considered mainly planar, so the resulting current is like the macroelectrode response. Experimentally, this regime corresponds to very short times or very fast scan rates. In Figure 4-21B the diffusion layer thickness is comparable to the microelectrode dimension and diffusion is hemispherical although there is still no interaction or overlap between neighbouring microelectrodes. The response of the microelectrode array under this regime is that of a single microelectrode multiplied by the number of microelectrode in the array. Mainly, microelectrode arrays are designed and fabricated to work in this category. In the case showed in Figure 4-21C adjacent diffusion layers begin to overlap, which causes a reduction in the current compared with the previous case where the microelectrodes were independent. A current peak appears as no steady state current value can be achieved. The last case (Figure 4-21D) corresponds to the complete overlap of neighbouring diffusion layers. Diffusion is basically planar and the microelectrode array behaves as a macroelectrode of same total area as that occupied by the microelectrode array (microelectrodes and insulating area between them).
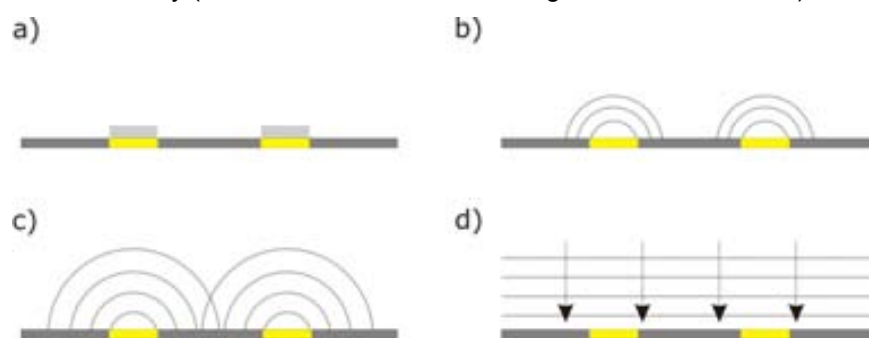

Figure 4-21: Representation of the microelectrode array behaviour. For a) and b) the diffusion layers of neighbouring electrodes are independent and for c) and d) the diffusion layers are overlapped.

These four categories showed in Figure 4-21 are related to the microelectrode radius (r), the centre-to-centre distance (d), the experimental time (for potential sweep technique the experimental time depends on the scan rate) and the diffusion coefficient of the electroactive species (D). For higher diffusion coefficient values, the diffusion layers will overlap earlier. Therefore, numerical studies as those presented by Davies *et. al.* [43] are required to determine the optimum working conditions for a given microelectrode array. They base their simulation of regular arrays on the diffusion domain approach in order to reduce the simulation to a two-dimensional model and avoid the complexity of working with three-dimensional ones without losing accuracy

Figure 4-22 shows a schematic diagram of the definition of the diffusion domain approach for a cubic arrangement microdisk array. It consists in assigning a diffusionally independent unit cell to each microelectrode in the array. The walls of this unit area are equidistant from all the neighbouring microdisks, so the net mass flux is zero. However, these unit cells do not have a convenient shape to be simulated as it would be necessary to use a three

dimensional model to simulate a diffusion domain like this. So, the diffusion domain approach is based on the approximation of the square base to a round cylinder of the same area and centred at the microdisk ($\pi R^2 = d^2$). This new unit cell has cylindrical symmetry and allow to reduce the system to a two dimensional plane, as shown in Figure 4-22.
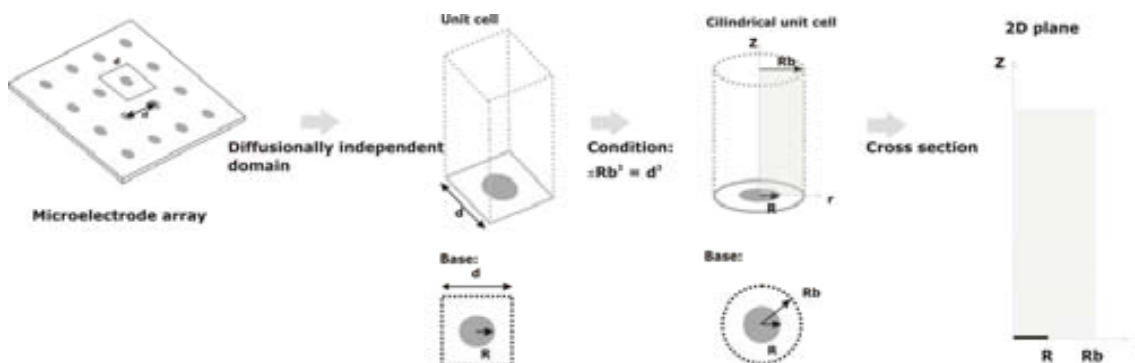

Figure 4-22: Representation of the diffusion domain approach. The two dimensional plane represents one microdisk electrode within an array.

It is important to point out that the diffusion domain approach does not account well for microelectrodes on the perimeter of the array. However, the error is insignificant when the number of inner microelectrodes widely exceeds the number of microelectrodes on the perimeter, which is a quite usual situation.

We use the diffusion domain approach to model a cubic arrangement microelectrode array of 256 microdisks of 10 μm radius and 100 μm of centre-to-centre distance. To demonstrate the different categories schematised in Figure 4-21 linear sweep voltammetry is perfomed for 5, 10, 25, 50, 75, 100, 200, 500 and 1000 mVs^{-1}.
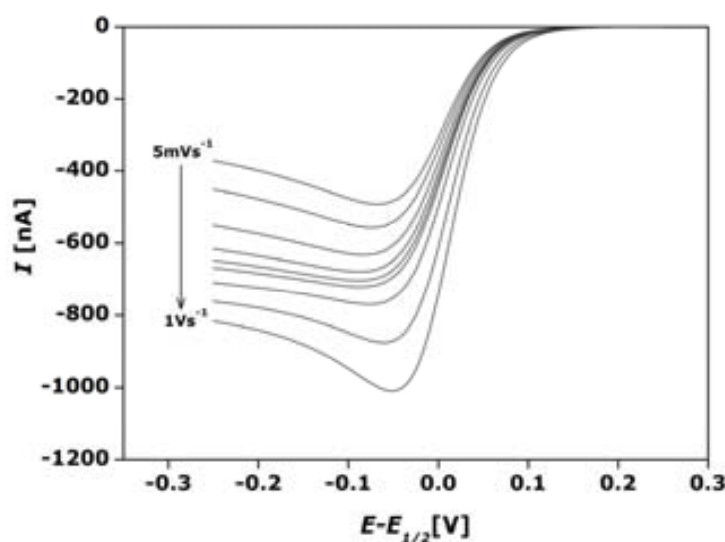

Figure 4-23: Current vs potential for an array of 256 microdisks of 10 μm radius at different scan rates. Scan rates: 5, 10, 25, 50, 75, 100, 200, 500 and 1000

mVs⁻¹. Conditions: $[O]_o$=1 mol·m⁻³, k_s=0.1 m·s⁻¹, α=0.5, n=1 and $D_O=D_R$=6.5·10⁻¹⁰ m²·s⁻¹.

As it is showed in Figure 4-23 macroelectrode behaviour is observed for low and high scan rates, where planar diffusion is more important than radial diffusion. At low scan rates such behaviour is due to the diffusion layer of neighbouring microdisks are overlapped and the microelectrode array behaves as a macroelectrode of the same area as the area occupied by the whole array. However at high scan rate, the microdisks are independent but the time is too short to be able to achieve the steady state due to radial diffusion.

These modelled results are in concordance with the results presented by Davies *et. al.* in [45], where they affirm that a scan rate higher than 75 mVs⁻¹ is needed to avoid overlapping between microdisks in an array of 10 µm radius and 100 µm of centre-to-centre distance, if the electroactive species has a diffusion coefficient of 8·10⁻¹⁰ m²s⁻¹.

4.4.2 A note on recessed microelectrodes

Some authors have addressed the electrochemical response of protruding and recessed microelectrodes [34, 36, 46-51], as well as the recessed microelectrode arrays [35, 43, 51, 52]. For an inlaid microdisk electrode, the steady state current is described by [10]:

$$I = 4nFDcr_o \tag{4.52}$$

where n is the number of exchanged electrons, F is the Faraday constant, D is the diffusion coefficient, c is the concentrations and r_o is the microdisk radius. Bond *et al*. [49] reached an analytical solution based on two assumptions. First, that the microelectrode is deeply recessed and second that the concentration gradient across the mouth of the recess is constant. The steady state current value presented by Bond [49] for these cases, is:

$$I = \frac{4nFcDr_o}{\left(\dfrac{4L}{\pi r_o} + 1\right)} \tag{4.53}$$

where L is the recess height. Later, Bartlett and Taylor [47], presented a more accurate semi empirical approximation for photolithographic microlectrodes, which are not so deeply recessed. In that work, they solved a chronoamperometric model using FEM to obtain the following expression:

$$I(t) = 4nFDr_o c \left[B'\left(\frac{Dt}{r_o^2}\right)^{-1/2} + C' e^{-D'\left(\frac{Dt}{r_o^2}\right)^{-1/2}} \right] \tag{4.54}$$

This approximated solution for recessed microelectrodes is based on the seminal work by Shoup and Szabo [19]. In their work, these authors showed the importance of the ratio between electrode radius and recess height. The first term in equation (4.54), which is proportional to $t^{-1/2}$, can be easily identified as the cottrellian contribution that corresponds with plannar diffusion at short times. The second term is an exponential function with time

that smoothes the transition between the transient and the steady state regions. Parameters *B'*, *C'* and *D'* depend on the quotient L/r_o and they are tabulated in [47].

It is absolutely necessary to consider the recess of the microelectrodes and include it in the voltammetric models described in the previous sections. As showed in Table 4-2, the difference between inlaid microdisk currents and recessed microdisk currents depends on the relation between the recess height and the microdisk radius and this difference is higher as the ratio between height and radius increases. For instance, we chose a recess height of 1 μm which is approximately the thickness of the isolating layer deposited to fabricate some of the microdisk used in this thesis [45]. The effect is higher for a 5 μm radius microdisk than for a 10 μm radius disk, so the same recess has higher effect as the radius of the microdisk decreases.

Table 4-2: Effect of 1 μm recessed on the current for 10 μm and 5 μm microdisk radius

Electrode radius, r_o / μm	10	5
Recess height, L / μm	1	1
$I_{inlaid} = 4nFDcr_o$ / nA	2.51	1.25
$I_{recessed} = 4\pi nFDcr_o^2/(4L+\pi r_o)$ / nA	2.23	1.00
$(I_{recessed}-I_{inlaid})/(I_{inlaid})$ x 100	**-12**	**-20**

Figure 4-24 shows the results for a chronoamperometric model of a single microelectrode of 5 μm of radius and 1 μm of recess. The single microdisk model is a two-dimensional model as depicted in Figure 4-5B but considering a recessed geometry, which is a step of height *L* at $r=r_o$.. Figure 4-24 compares our simulations with the theoretical values resulting from Bond's equation (4.53), and Bartlett and Taylor's expression (4.54).
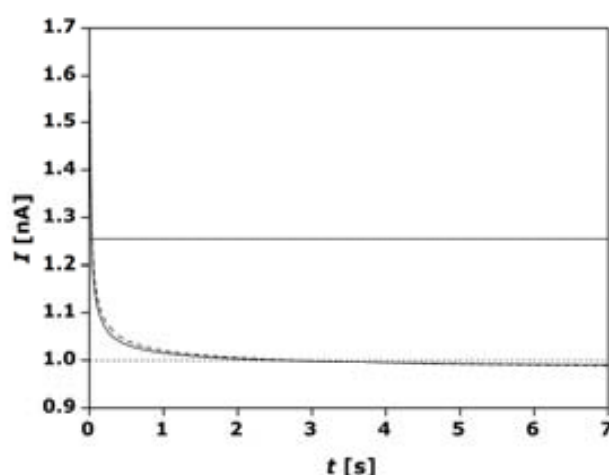

Figure 4-24: Comparison between the modelled current (solid line) and the Bartlett and Taylor expression (dotted line). The limiting value corresponds with the microdisk theoretical current without considering the recess (1.25 nA) and Bond's expression (1nA).

The figure shows good agreement between modelled current and the theoretical Barlett and Taylor's expression, and both convergence towards Bond's expression for the steady state current. The deviation between our simulation and Barlett and Taylor's expression is always below 2%. This error fits with the expected error of the simulation and the expected error described by the authors in [47].

Bartlet and Taylor's expression cannot be used to predict chronoamperometric measurements at microelectrode arrays because it does not consider the overlap between diffusion layers of neighbour microelectrodes. In chronoamperometric measurements using microelectrode arrays there is always overlapping of diffusion layers at long times. To demonstrate such effect some experimental chronoamperometric measurements were carried out in 1mM of ferrocyanide in 0.5 M KNO_3 using a microdisk array of 256 microelectrodes of 5 μm radius, recessed by one micron and displaying 100 μm intercentre distance. The experimental currents were normalised to the number of electrodes to obtain the current for a single electrode and facilitate comparison with the simulated and the theoretically expected values. Figure 4-25 shows the experimental normalised current, as well as the modelled and Bartlett and Taylor's values.
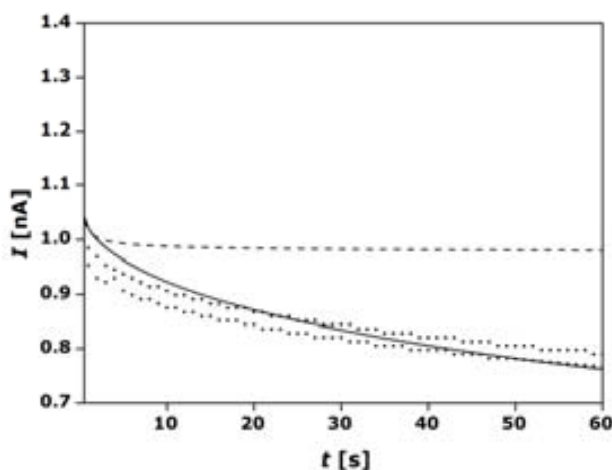
Figure 4-25: Comparison between the experimental data for the oxidation of 1mM of ferrocyanide in 0.5 M KNO_3 (dots) with the Bartlett and Taylor's expression (dotted lined) and our modelled current (solid line) for a 5 μm microdisk radius within an array.

Microdisk electrode arrays do not achieve a steady state current, which gradually decreases instead. This effect is due to the overlapping of neighbouring diffusion layers. At long times, the microdisk array behaves as a macroelectrode that occupies the same area than the array [10, 43]. Such overlapping is not predicted by the theoretical equations previously described so simulations are essential in the interpretation of results at microelectrode arrays.

4.5 Summary

In this chapter, we are able to simulate mass transport to macro- and microelectrodes for a range of amperometric techniques and under different conditions, stagnant and hydrodynamic. Each model has been successfully compared with theoretical expressions or bibliographic works. The use of microelectrode arranged in arrays is very popular in electrochemistry, as it increases the signal level with considerable less background/capacitive current compared to conventional macroelectrode. Microelectrode arrays are modelled in this thesis using the diffusion domain approach, which has been extensively described by Compton and co-workers. Moreover, one feauture of microfabricated electrode is that they are slighted recessed, such effect is successfully simulated in this chapter. In summary, we have demonstrated the feasibility of our models to simulate the fundamental electrochemical techniques as well as important features when using microelectrodes. Such models will be further used in the simulation of real devices in the following chapters.

4.6 References

[1] COMSOL, *COMSOL Mutuphysics: User's Guide*. 2005: COMSOL AB.

[2] Hughes, T., *The Finite Element Method: Linear Static and Dynamic Finite Element Analysis*. 2000: Courier Dover Publicationts.

[3] Zienkiewicz, O.C., *Finite element method*. 1974: Springer.

[4] Zienkiewicz, O.C. and R.L. Taylor, *The Finite Element Method for Solid and Structural Mechanics*. 2005: Elsevier.

[5] Zienkiewicz, O.C., R.L. Taylor, and J.Z. Zhu, *The Finite Element Method: Its Basis and Fundamentals*. 2005: Elsevier.

[6] Berthier, J. and P. Silberzan, *Microfluidics for biotechnology*. 2006: Artech House.

[7] http://www.comsol.com/.   .

[8] Zimmerman, W.B.J., *Process Modelling and Simulation With Finite Element Methods*. 2004: World Scientific.

[9] Allen J. Bard, L.R.F., *ELECTROCHEMICAL METHODS. Fundamentals and Applications*. 2nd ed. 2001, New York: John Wiley & sons.

[10] Amatore, C., *Electrochemistry at ultramicroelectrodes*, in *Phyical Electrochemistry. Principles, methods and applications*, I. Rubinstein, Editor, Marcel Dekker, Inc.

[11] Albery, W.J. and M.L. Hitchman, *Rong-disc electrodes*. 1971: Clarendon Press Oxford.

[12] Wang, J., *Analytical Electrochemistry*. Second Edition ed. 2000: Wiley-VCH.

[13] Amatore, C., Y. Bouret, E. Maisonhaute, H.D. Abruña, and J.I. Goldsmith, *Electrochemistry within molecules using ultrafast cyclic voltammetry.* Comptes Rendus Chimie, 2003. 6(1): p. 99-115.

[14] Amatore, C. and E. Maisonhaute, *When voltammetry reaches nanoseconds.* Analytical Chemistry, 2005. 77(15).

[15] Amatore, C., E. Maisonhaute, and G. Simonneau, *Ultrafast cyclic voltammetry: Performing in the few megavolts per second range without ohmic drop.* Electrochemistry Communications, 2000. 2(2): p. 81-84.

[16] Oldham, K.B., *All Steady-State Microelectrodes Have the Same Ir Drop.* Journal of Electroanalytical Chemistry, 1987. 237(2): p. 303-307.

[17] Aoki, K. and J. Osteryoung, *Diffusion-controlled current at the stationary finite disk electrode: Theory.* Journal of Electroanalytical Chemistry, 1981. 122: p. 19-35.

[18] Aoki, K. and J. Osteryoung, *Formulation of the diffusion-controlled current at very small stationary disk electrodes.* Journal of Electroanalytical Chemistry, 1984. 160(1-2): p. 335-339.

[19] Szabo, A., D.K. Cope, D.E. Tallman, P.M. Kovach, and R.M. Wightman, *Chronoamperometric current at hemicylinder and band microelectrodes: Theory and experiment.* Journal of Electroanalytical Chemistry, 1987. 217(2): p. 417-423.

[20] Nicholson, R.S. and I. Shain, *Theory of Stationary Electrode Polarography - Single Scan + Cyclic Methods Applied to Reversible Irreversible + Kinetic Systems.* Analytical Chemistry, 1964. 36(4): p. 706-&.

[21] Saveant, J.M. and D. Tessier, *Convolution potential sweep voltammetry: V. Determination of charge transfer kinetics deviating from the butler-volmer behaviour.* Journal of Electroanalytical Chemistry, 1975. 65(1, Part 1): p. 57-66.

[22] Bond, A.M., K.B. Oldham, and C.G. Zoski, *Theory of Electrochemical Processes at an Inlaid Disk Microelectrode under Steady-State Conditions.* Journal of Electroanalytical Chemistry, 1988. 245(1-2): p. 71-104.

[23] Myland, J.C. and K.B. Oldham, *General theory of steady-state voltammetry.* Journal of Electroanalytical Chemistry, 1993. 347(1-2): p. 49-91.

[24] Galceran, J., D.J. Gavaghan, and J.S. Rollett, *2-Dimensional Implementation of the Finite-Element Method with Singularity Correction for Diffusion-Limited Current at an Unshielded Disc Electrode.* Journal of Electroanalytical Chemistry, 1995. 394(1-2): p. 17-28.

[25] Gavaghan, D.J., *An exponentially expanding mesh ideally suited to the fast and efficient simulation of diffusion processes at microdisc electrodes. 1. Derivation of the mesh.* Journal of Electroanalytical Chemistry, 1998. 456(1-2): p. 1-12.

[26] Gavaghan, D.J. and J.S. Rollett, *Correction of Boundary Singularities in Numerical-Simulation of Time-Dependent Diffusion-Processes at Unshielded Disk Electrodes.* Journal of Electroanalytical Chemistry, 1990. 295(1-2): p. 1-14.

[27] Michael, A.C., R.M. Wightman, and C.A. Amatore, *Microdisk Electrodes .1. Digital-Simulation with a Conformal-Map.* Journal of Electroanalytical Chemistry, 1989. 267(1-2): p. 33-45.

[28] Cooper, J.A. and R.G. Compton, *Channel electrodes - A review.* Electroanalysis, 1998. 10(3): p. 141-155.

[29] Amatore, C., A. Oleinick, and I. Svir, *Simulation of diffusion-convection processes in microfluidic channels equipped with double band microelectrode assemblies: approach through quasi-conformal mapping.* Electrochemistry Communications, 2004. 6(11): p. 1123-1130.

[30] Compton, R.G., A.C. Fisher, R.G. Wellington, P.J. Dobson, and P.A. Leigh, *Hydrodynamic Voltammetry with Microelectrodes - Channel Microband Electrodes - Theory and Experiment.* Journal of Physical Chemistry, 1993. 97(40): p. 10410-10415.

[31] Henley, I.E., K. Yunus, and A.C. Fisher, *Voltammetry under microfluidic control: Computer-aided design development and application of novel microelectrochemical reactors.* Journal of Physical Chemistry B, 2003. 107(16): p. 3878-3884.

[32] Stevens, N.P.C. and A.C. Fisher, *Finite element simulations in electrochemistry .2. Hydrodynamic voltammetry.* Journal of Physical Chemistry B, 1997. 101(41): p. 8259-8263.

[33] Levich, V.G., *Physicochemical Hydrodynamics.* 1962, Englewood Cliffs, N. J.: Prentice-Hall, Inc.

[34] Amatore, C., O.V. Klymenko, and I. Svir, *In situ and online monitoring of hydrodynamic flow profiles in microfluidic channels based upon microelectrochemistry: Optimization of electrode locations.* Chemphyschem, 2006. 7(2): p. 482-487.

[35] Amatore, C., A.I. Oleinick, and I. Svir, *Construction of optimal quasi-conformal mappings for the 2D numerical simulation of diffusion at microelectrodes.: Part 2. Application to recessed or protruding electrodes and their arrays.* Journal of Electroanalytical Chemistry, 2006. 597(1): p. 77-85.

[36] Ferrigno, R., P.F. Brevet, and H.H. Girault, *Finite element simulation of the amperometric response of recessed and protruding microband electrodes in flow channels.* Journal of Electroanalytical Chemistry, 1997. 430(1-2): p. 235-242.

[37] Matthews, S.M., G.Q. Du, and A.C. Fisher, *Microfluidic voltammetry: simulation of the chronoamperometric response of microband electrodes sited within microreactors.* Journal of Solid State Electrochemistry, 2006. 10(10): p. 817-825.

[38] Bruus, H., *Theoretical microfluidics*, in *MIC-Department of Micro and Nanotechnology*. 2004, Technical University of Denmark.

[39] Skoog, D.A., F.J. Holler, and T.A. Nieman, *Análisis instrumental.* 1992: McGRAW-HILL.

[40] Thompson, M. and R.G. Compton, *Voltammetric monitoring of transient hydrodynamic flow profiles in microfluidic flow cells.* Analytical Chemistry, 2007. 79(2): p. 626-631.

[41] Amatore, C., N. Da Mota, C. Sella, and L. Thouin, *Theory and experiments of transport at channel microband electrodes under laminar flows. 1. Steady-state regimes at a single electrode.* Analytical Chemistry, 2007. 79(22): p. 8502-8510.

[42] Lee, H.J., C. Beriet, R. Ferrigno, and H.H. Girault, *Cyclic voltammetry at a regular microdisc electrode array.* Journal of Electroanalytical Chemistry, 2001. 502(1-2): p. 138-145.

[43] Davies, T.J. and R.G. Compton, *The cyclic and linear sweep voltammetry of regular and random arrays of microdisc electrodes: Theory.* Journal of Electroanalytical Chemistry, 2005. 585(1): p. 63-82.

[44] Amatore, C., J.M. Saveant, and D. Tessier, *Charge transfer at partially blocked surfaces: A model for the case of microscopic active and inactive sites.* Journal of Electroanalytical Chemistry, 1983. 147(1-2): p. 39-51.

[45] Davies, T.J., S. Ward-Jones, C.E. Banks, J. del Campo, R. Mas, F.X. Munoz, and R.G. Compton, *The cyclic and linear sweep voltammetry of regular arrays of microdisc electrodes: Fitting of experimental data.* Journal of Electroanalytical Chemistry, 2005. 585(1): p. 51-62.

[46] Alden, J.A., J. Booth, R.G. Compton, R.A.W. Dryfe, and G.H.W. Sanders, *Diffusional Mass-Transport to Microband Electrodes of Practical Geometries - a Simulation Study Using the Strongly Implicit Procedure.* Journal of Electroanalytical Chemistry, 1995. 389(1-2): p. 45-54.

[47] Bartlett, P.N. and S.L. Taylor, *An accurate microdisc simulation model for recessed microdisc electrodes.* Journal of Electroanalytical Chemistry, 1998. 453(1-2): p. 49-60.

[48] Beriet, C., R. Ferrigno, and H.H. Girault, *Simulation of the chronoamperometric response of a regular array of micro-disc electrodes.* Journal of Electroanalytical Chemistry, 2000. 486(1): p. 56-64.

[49] Bond, A.M., D. Luscombe, K.B. Oldham, and C.G. Zoski, *A comparison of the chronoamperometric response at inlaid and recessed disc microelectrodes.* Journal of Electroanalytical Chemistry, 1988. 249(1-2): p. 1-14.

[50] Ferrigno, R., P.F. Brevet, and H.H. Girault, *Finite element simulation of the chronoamperometric response of recessed and protruding microdisc electrodes.* Electrochimica Acta, 1997. 42(12): p. 1895-1903.

[51] Sandison, M.E., N. Anicet, A. Glidle, and J.M. Cooper, *Optimization of the geometry and porosity of microelectrode arrays for sensor design.* Analytical Chemistry, 2002. 74(22): p. 5717-5725.

[52] Amatore, C., A.I. Oleinick, and I. Svir, *Numerical simulation of diffusion processes at recessed disk microelectrode arrays using the quasi-conformal mapping approach.* Analytical Chemistry, 2009. 81(11): p. 4397-4405.

CHAPTER 5:

Simulation of a microrespirometer

This chapter presents the construction of a numerical model that describes the behaviour of a biofilm-based microrespirometer. The model uses finite element methods to solve the mass transport equations for oxygen as it travels from the bulk of the solution towards the microelectrode array through the biofilm and a protective Nafion® layer, whose main purpose is to avoid electrode fouling. The model highlights some of the issues related to the mass transport at arrays of slightly recessed microelectrodes. It provides further evidence of the validity of the diffusion domain approach as a basic tool to model microelectrode arrays. The model is used to interpret amperometric data and provide metabolic rate constants that agree reasonably well with measurements performed in bacterial suspensions under similar experimental conditions.

5.1 Introduction

Respirometry consists in monitoring the metabolic activity of living organisms. In the present case, we use respirometry to determine the toxicity of a certain environment. This chapter is related to a previous work [1] where a new solid state microrespirometer, based on the amperometric reduction of oxygen going through a biofilm grown over a Nafion modified array of gold microelectrodes, was presented. Briefly, as the metabolic activity of the biofilm increases in the presence of nutrients and oxygen consumption occurs, the oxygen reduction current drops, and changes in the measured current can be interpreted in terms of bacterial metabolic activity.

This chapter presents a theoretical framework describing the basic operation of such a microelectrode array-based microrespirometer. The model is built using data obtained electrochemically and optically from a series of controlled experiments. It provides a better understanding of some of the physico-chemical processes involved in the detection. This will in turn lead to the optimisation of the device at the design stage. Optical experiments, as well as biofilm grown, were perfomed by the Environmental Microbiology group of Universitat Autònoma de Barcelona (UAB).

Ultra-microelectrode arrays are used to enhance sensitivity, and a Nafion coating avoids electrode passivation arising from the deposition of macroscopic debris as well as unwanted organic material over the electrode surface. Other materials different from Nafion could also be used for these purposes. However, due to the overall negative charge of its polymer backbone, Nafion offers the additional advantage of preventing certain electroactive species (such as the hypochlorite commonly used as disinfectant in drinking waters) from reaching

the electrode and causing erroneous respiration readings. This is particularly important because the final application is the monitoring of acute toxicity in drinking water supply lines. The detection method consists in exposing the microrespirometer to a test sample containing nutrients. If toxic substances are present in the sample, the bacteria forming the biofilm are inactivated, respiration ceases and a higher concentration of oxygen reaches the electrode surface, thus resulting in a higher current reading. Although the method is unselective and the analyst can never know the nature of the substances present, it can be used to predict whether a sample is toxic or not, and to what extent.

Finite element models have been developed based on the diffusion domain approach [4-6] to predict their performance. The combined use of simulations and semi-empirical expressions enabled us to determine the values of important oxygen transport parameters such as the diffusion coefficient in water and Nafion, and its distribution coefficient. Respiration rate constants were determined using optical oxygen sensors in a bacterial culture broth under conditions similar to those met by the biofilm. Such measured respiration rates were later compared to estimates made using our numerical models from measured currents. The correlation between the rates obtained from optical and electrochemical data showed the reliability of our model and, in addition, these estimated kinetic parameters were found to be in good agreement with published data for similar systems.

5.2 Experimental

5.2.1 Computation.

The limiting current of voltammograms was simulated using COMSOL Multiphysics 3.3 (COMSOL AB, Sweden) and Matlab 7.0.4 (MathWorks, USA). The values of the parameters used throughout our simulations were: diffusion coefficient of ferrocyanide, and ferricyanide, $D=6.5 \cdot 10^{-10}$ $m^2 \cdot s^{-1}$; [2] symmetry coefficient α was 0.5. The temperature, T, was 298 K. All physical magnitudes used in the simulation files were expressed in S.I. units.

5.2.2 Chemicals and instrumentation

KCl (99%), $K_4Fe(CN)_6 \cdot 3H_2O$ (99%), Nafion 117 solution (5% in lower aliphatic alcohols), were purchased from Sigma-Aldrich. D-glucose (>98 %) was supplied by Fluka. All chemicals were ACS analytical grade and were used without any further purification. Aqueous solutions were prepared using pure de-ionised water (18M$\Omega \cdot$cm). Solutions containing dissolved oxygen were achieved by means of an in-house-built system consisting of air and nitrogen lines which flow could be controlled by means of individual rotameters [1].

A bioreactor for biofilm formation was assembled in the Environmental Microbiology laboratory at UAB. A pure culture of *Pseudomonas putida* was grown in a continuous culture with controlled oxygen supply at 37ºC. The bacteria grew in a minimum medium AB (MMAB), which only contained salts and glucose as the nutrient, to control their growth [3],[4]. Biofilms developed readily on the solid-state microrespirometer surface.

All electrochemical measurements were performed using a three electrode cell configuration and a µ-Autolab III (Eco-Chemie, The Netherlands) potentiostat connected to a PC computer using version 4 of the GPES software for Windows®. A gold microelectrode array as a working electrode, a platinum wire as a counter electrode and a Ag/AgCl (3M KCl) from Crison was used as a reference electrode. pH was monitored using a Hanna Instruments HI-300 pH meter. Oxygen concentrations were measured using an optical Hach HQ10 oxygen handheld probe with temperature control.

Bacterial growth conditions

Pseudomonas putida (KT2442) was grown for 20 h in AB mineral medium at 37ºC and inoculated in a thermostatic water-jacked glass reactor containing 700 mL of the same medium. Glucose at a concentration of 20% was aseptically added to the medium after autoclaving. The reactor was kept at room temperature and oxygenated by bubbling with air at a constant rate of 400 L/h using an air pump. In order to keep a homogeneous medium, the culture was mixed at 500 rpm with a magnetic stir bar. During experiments, samples for absorbance measurements and bacterial plaque counts were taken. These measurements were kindly perfomed by the Enveriomental Microbiology group at UAB.

Oxygen measurements

A FOXY fiber optic oxygen sensor system from Ocean Optics was used for oxygen measurements. The FOXY sensor consists of a probe containing a ruthenium complex in a sol-gel substrate and coated in RTV silicone. The sensor is connected to an excitation source and a spectrometer, which interfaces with a PC via an A/D converter.

In order to measure the oxygen consumption, the culture was allowed to reach an optical density of 0.3 at 550nm. Then the sensor was immersed in the culture. After 20 minutes the signal stabilised at an oxygen concentration of 7.18 mg/L and the air pump was turned off. Figure 5-1 shows the consumption of oxygen in the bacterial suspension after the oxygen supply is cut off. After a few minutes, the concentration stabilises at a minimum value of 0.57 mg L^{-1}. 10 minutes later the aeration was turned on again and the oxygen level returned to its initial value. This procedure was repeated three times in the same culture allowing the signal to stabilise at each maximum and minimum value for around 10 minutes. At the end of the experiment, the sensor was submerged in a saline solution containing glucose in order to prove that no bacteria, which could affect the measurements, were attached to the sensor. These measurement were taken by the Environmental Microbiology group at UAB.
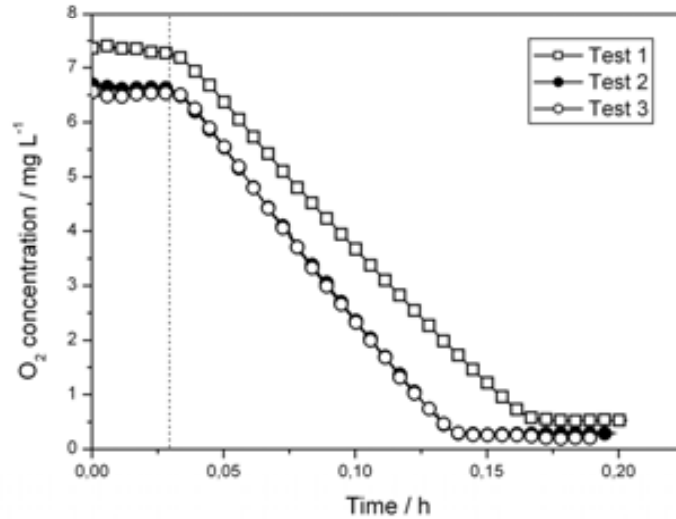
Figure 5-1: Oxygen consumption kinetics in a *Pseudomonas putida* culture. The figure shows data from three independent experiments. The vertical dotted line indicates the point at which oxygen supply to the culture was interrupted.

5.2.3 Fabrication and modification of electrodes

The micro-respirometer used in this work is conformed by a gold disc microelectrode array modified with a Nafion thin layer. Over this structure, a *Pseudomonas putida* biofilm was grown spontaneously in a microbial culture. The microrespirometer system is schematically depicted in Figure 5-2.
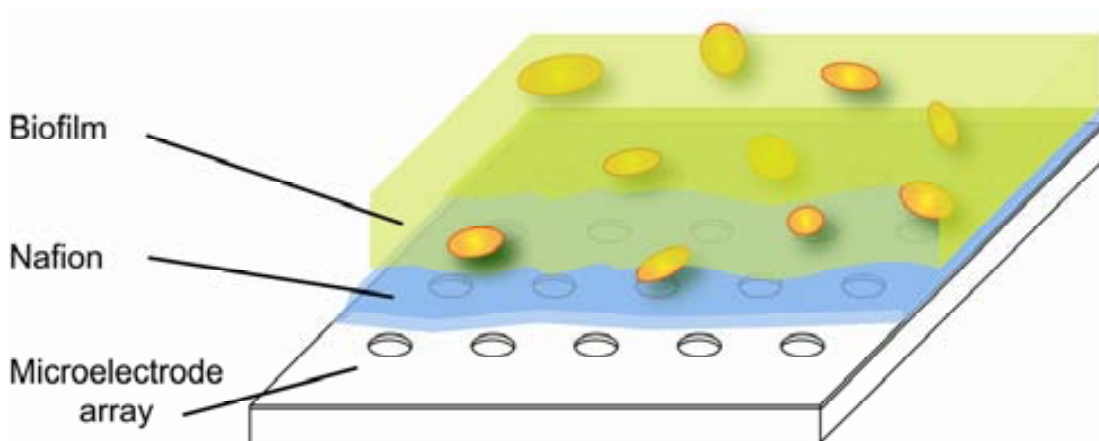
Figure 5-2: Schematic representation (not to scale) of the microrespirometer. The biofilm rests over a thin Nafion layer which protects the microelectrodes from fouling

Electrode fabrication and modification with Nafion®

The arrays consist of 256 gold discs, 10 μm in diameter and arranged under a cubic distribution with 100 μm of separation between the centre of one individual microelectrode and its nearest neighbour. The microfabrication steps are schematised in Figure 5-3.

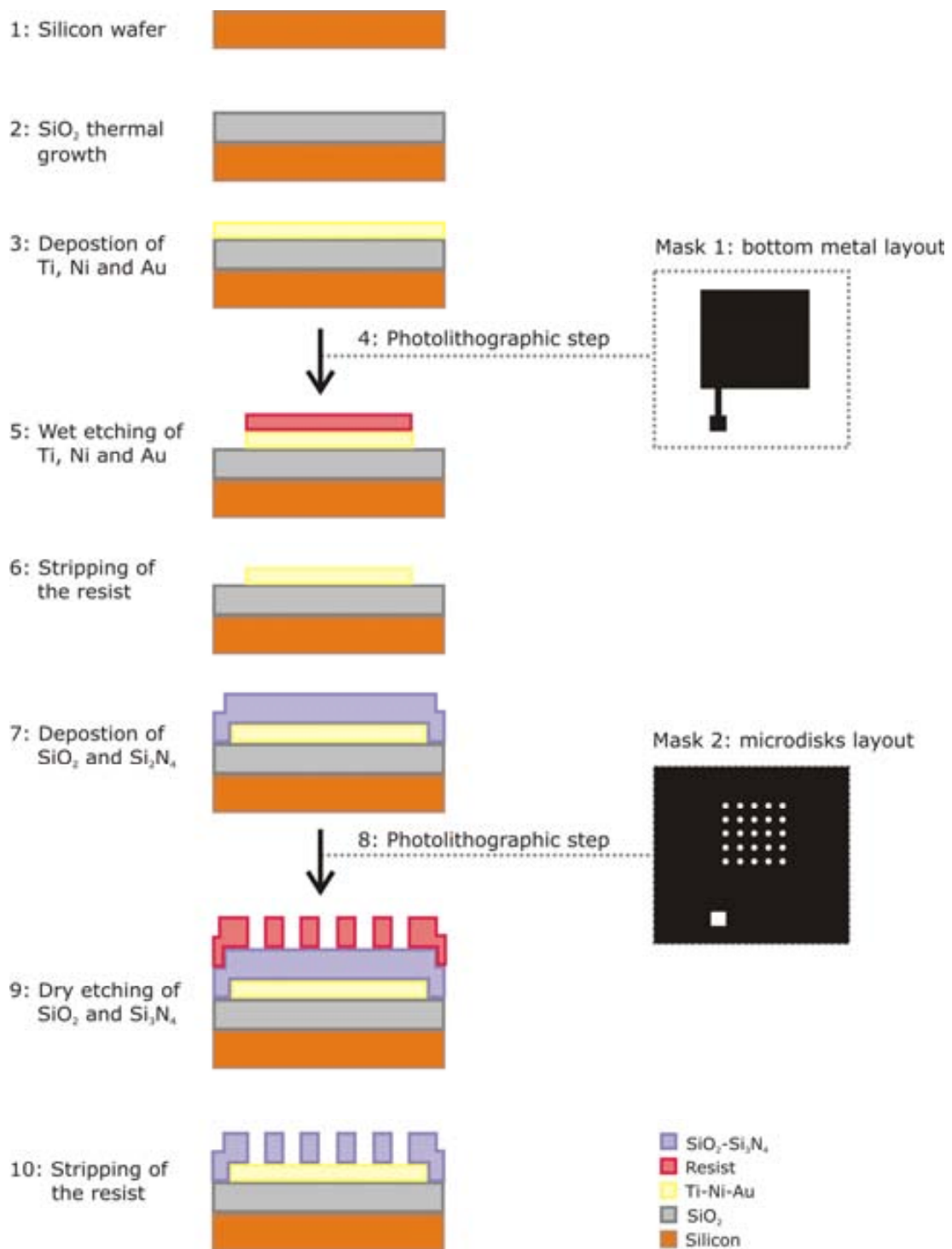|		
1: Silicon wafer		
2: SiO$_2$ thermal growth		
3: Depostion of Ti, Ni and Au		Mask 1: bottom metal layout
4: Photolithographic step		
5: Wet etching of Ti, Ni and Au		
6: Stripping of the resist		
7: Depostion of SiO$_2$ and Si$_3$N$_4$		Mask 2: microdisks layout
8: Photolithographic step		
9: Dry etching of SiO$_2$ and Si$_3$N$_4$		
10: Stripping of the resist		SiO$_2$-Si$_3$N$_4$ / Resist / Ti-Ni-Au / SiO$_2$ / Silicon

Figure 5-3: Microfabrication steps of a microdisk electrode array.

The substrate is a silicon wafer 4" diameter n-type (phosphorus doped) (Figure 5-3(1)). The silicon wafer is oxidised (800nm of silicon oxide, SiO$_2$) at 1100ºC. This silicon oxide layer insulates the following metal layers from the silicon (Figure 5-3(2)). Titanium, nickel and gold are sputtered to yield the metal parts (Figure 5-3(3)). First, 50 nm of Titanium is deposited to enhance the adhesion of the gold over SiO$_2$. Then 50 nm of Nickel is deposited to act as a diffusion barrier and avoid the diffusion of the gold into the Titanium and last, 100 nm of Gold

is sputtered over the Nickel. Later there is a photolithographic step (Figure 5-3(4)). This step consists in spinning a suitable photoresist, insolating it through a chromium mask (Deltamask, NL), and developing it. In most cases, 1.2 μm of HiPR6512 (Fujifilm electronic materials, JP) photoresist is spun and patterned. This photoresist is positive, so a clear field mask is used to define the desired metal patterns during the following etching step. The photolithograpy step is followed by wet etching of the metals (Figure 5-3(5)). Three different etching mixtures are used to etch the different layers: iodine/iodide for gold, nitric acid/water (1:4) for nickel and glycol/hydrofluoric acid/ water for titanium. Once the metal patterns are defined, the wafer is immersed in a stripping bath where the excess photoresist is removed (Figure 5-3(6)). Afterwards, a passivation layer is deposited (Figure 5-3(7)).The usual passivation layer consists of a mixed layer of silicon oxide and silicon nitride, deposited by PECVD. This layer helps to define the microelectrodes and the contacts on the metal parts. The passivation layer must be waterproof and impermeable to the species in the solution. First, 400 nm of SiO_2 are deposited on the wafer. Next, 700 nm of Si_3N_4 are deposited over the silicon oxide. Si_3N_4 layer is more hydrophobic than SiO_2 and hence it is a better material to avoid solution penetration. The reason to combine it with a sub-layer of silicon oxide is because the latter presents less stress compared to Si_3N_4 layer when deposited over gold, and this makes for more durable devices. Figure 5-3(8) represents a new photolithography. As previously a positive photoresist is spun and patterned. However, since in this case a dark field mask is used as the parts to be etched are only the microelectrodes and the contact pads. SiO_2 and Si_3N_4 layers are etched by RIE to define (Figure 5-3(9)). Finally, after stripping the resist in acetone, the microfabrication process is complete (Figure 5-3(10)).

Generally, the wafer is covered with a resin to protect the microestrucutres during the wafer-cutting process. This resin is easily removed by immersing the individual chips in acetone.
It is important to highlight that due to the fabrication process, the electrodes are recessed *ca.* 1 micron (passivation layer).
Next, the microelectrode array was protected by a spin coated thin layer of Nafion as described in [1]. The coating was carried out in a POLOS MCM-TFM spinner in a class 100000 clean room. Individually mounted chips were placed on top of the chip. The arrays were spinned for 1 min at 800 rpm and with an initial acceleration of 1000 rpm^2. This operation was repeated three times with waiting intervals of 3 min to allow evaporation of the solvent. The surface topology of the Nafion layer was characterised in three stages by perfilometry using KLA-Tencor P15 perfilometer controlled by Profiler v7 software run on Windows XP. First, a profile of the clean and bare microelectrode array was obtained and used as the baseline. Next, the Nafion was deposited as described above and left to cure for not less than 60 min. The deposited layers is so thin that 60 minutes is time enough for the solvent to evaporate. Finally, the Nafion membranes were hydrated by immersion in water for another 60 minutes, after which a new profile mesurament was performed. The Nafion layer (unhydrated) was *ca.* 300 nm thick and it homogenously followed the

ultamicroelectrode array profile. Once hydrated, the Nafion layer reached a thickness of *ca.* 450 nm, which represents a 50% volume increase.

Biofilm modified electrodes

A thermostatic water-jacketed glass reactor with a total volume of 700mL was inoculated with *Pseudomonas putida* (KT2442). The microorganism was grown in mineral medium AB [4], using glucose as a carbon source. The system was continuously supplied with oxygen and the temperature was kept constant at 37ºC. The dilution rate was set to 0.01 h^{-1}.

Nafion modified arrays were immersed in a culture as described above for several days (over a month in some instances). Although it was possible to observe the formation of biofilm on top of the electrodes by sight after the second day, maturity was reached after 4-5 days [1].

To know the thickness of a mature biofilm, different microscope slides were covered in Nafion 117. Slides were kept in the *Pseudomonas* culture reactor for 12 days. Then the biofilm structure was observed using specific fluorescent probes in conjunction with confocal laser scanning microscopy (Leica TCS SP2 AOBS) with 0.2μm resolution. Biofilm thickness was found to be 103$\pm$5 μm (N=5).

Then bacterial mass concentration must be calculated in order to model the metabolic activity of biofilm. The microorganisms were stained with DAPI (4',6-diamidino-2-phenylindole) but the glycoconjugates of biofilms were stained with Concanavalin A and WGA using the following procedure. Fresh samples were incubated at room temperature for 30 minutes with 0.01M of concanavalin A, a lectin from *Canavalia ensiformis*, which has affinity for N-acetyl-D-galactosamine. The samples were then carefully rinsed three times with PBS in order to remove unbound marked probe. Then, the samples were incubated with WGA (wheat germ agglutinin), a lectin from *Wisteria floribunda* that has affinity for terminal α-D-mannosyl and α-D-glucosyl residues, for 30 minutes. The samples were rinsed three times and finally, the biofilms were incubated for 30 minutes with DAPI, rinsed again and examined by confocal scanning laser microscopy (CSLM). The surface concentration of bacteria was 10^{11} cfu·m^{-2} (cfu is a popular microbiological unit which means colony-forming). All of these biofilm parameters were measured by the Environmental Microbiology group at UAB.

5.3 Theory

The microrespirometer consists of three parts: biofilm, Nafion layer and microelectrode surface, as shown in Figure 5-2. Strict modelling of such device would require defining the mass transport equations of oxygen and nutrients for every part and the net material flux that is able to go through each interface.

Biofilms are defined as *matrix-exclosed bacterial populations adherent to each other and/or to surfaces or interfaces* [5] (*sic.*). Biofilms can be regarded as a specific type of bacterial protection structure developed to improve bacterial survival in a hostile environment [6].

Microscopic observations show that biofilms can have complex structures such as voids, cavities and channels, where nutrients can flow [6]. In spite of these complex structures, a wide number of studies in the literature consider diffusion as the main mass transport through the biofilm [13-18].

Metabolic activity and biofilm growth is usually described by a saturation kinetics equation [13, 14, 17, 19]:

$$\frac{dC}{dt} = D_C \nabla^2 C - \frac{\upsilon_{max} C M_t}{K_m + C} \tag{5.1}$$

where C is the substrate concentration, M_t is the biomass concentration, υ_{max} is the maximum substrate utilisation rate and K_m is the half saturation coefficient. D_c is the diffusion coefficient of the species within the biofilm. For the sake of simplicity, we have assumed the diffusivity of oxygen and nutrients across the biofilm to be constant. This is overlooking the true nature of biofilms, which are actually random and heterogeneous in structure. Thus, the diffusion coefficients used in our model refer to *apparent* diffusion coefficients. Modelling of biofilms a few millimetres thick involves the division of the biofilm in a discrete number of independent layers in order to account for the significant nutrient and oxygen differences between distant regions. Under these circumstances, mass transport of the nutrients is also important as it may become rate limiting in regions far from the biofilm surface. Our system, however, is very different. Indeed, since our biofilm is under a millimetre thick, it has been modelled as one layer with constant diffusion coefficients.

The metabolic activity studied in this chapter is the aerobic respiration of the biofilm, expressed as:

$$C_6H_{12}O_6 + 6O_{2(g)} \rightarrow 6CO_{2(g)} + 6H_2O \tag{5.2}$$
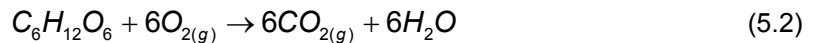
As equation (5.2) shows, there are two main species involved in the metabolic activity: glucose and oxygen. In this case, we will focus our work on transport and consumption of oxygen because (i) it is the species detected by the microrespirometer and (ii) under our experimental conditions it is rate limiting. This second hypothesis is based on the comparison between the half saturation coefficients K_m and our initial concentrations of oxygen and glucose. In [7], the half saturation coefficient K_m for oxygen and glucose for *E.coli* are 0.19 μM and 13 μM, respectively. Oxygen concentration will be limiting when the concentration in the biofilm is similar to K_m. Translated to our experimental conditions, having the oxygen concentration drop to 0.19 μM would represent a depletion of 99.9%, and the corresponding consumption of glucose would account for less than 2% its initial concentration. This is because the initial concentration of glucose is almost ten times higher than that of oxygen and because the consumption rate, according to equation (5.2), is six times faster for oxygen than for glucose. This simplified the formulation of our model by eliminating the need for the diffusional term of glucose in equation (5.1), since glucose can be safely assumed to be constant in the whole biofilm.

Glucose is always kept at sufficiently large concentrations so that it does not become rate limiting. Oxygen consumption due to the metabolic activity within the biofilm can be expressed by:

$$K_{O_2} = \frac{d[O_2]}{dt} = -\upsilon_{max}[X_{bact}]\frac{[O_2]}{K_m + [O_2]} \tag{5.3}$$

where $[X_{bact}]$ is the bacterial concentration of the biofilm, υ_{max} is the respiration rate constant and $[O_2]$ is the concentration of oxygen. The mass transfer equation of oxygen in the biofilm layer is defined as:

$$\frac{\partial[O_2]}{\partial t} = D_{O_2/Biofilm}\left(\frac{\partial^2[O_2]}{\partial r^2} + \frac{1}{r}\frac{\partial[O_2]}{\partial r} + \frac{\partial^2[O_2]}{\partial z^2}\right) + K_{O_2} \tag{5.4}$$

where r and z are the radial and normal coordinates to the microelectrode surface and $D_{O2/Biofilm}$ is the diffusion coefficient of oxygen in the biofilm layer which, according to the literature, is lower than in water [8].

The amount of oxygen not consumed by the bacterial metabolic activity goes through the biofilm and into the Nafion. The mass transfer parameters of oxygen in Nafion are different from the values in water or in the biofilm [9, 10].Their experimental determination is described below. The diffusion equation of oxygen in Nafion can be expressed as:

$$\frac{\partial[O_2]}{\partial t} = D_{O_2/Nafion}\left(\frac{\partial^2[O_2]}{\partial r^2} + \frac{1}{r}\frac{\partial[O_2]}{\partial r} + \frac{\partial^2[O_2]}{\partial z^2}\right) \tag{5.5}$$

where $D_{O2/Nafion}$ is the diffusion coefficient of oxygen in Nafion.

Finally, oxygen arrives at the microelectrode surface where it is reduced. The overall reaction in a neutral to basic environment is [11]:

$$O_2 + 4e^- + 2H_2O \rightarrow 4OH^- \tag{5.6}$$

We assume Butler-Volmer kinetics [12] at the electrode and the current through disk microelectrode is calculated as:

$$I = -2\pi nFD_{O_2/Nafion}\int_0^{r_0} \left.\frac{\partial[O_2]}{\partial z}\right|_{z=0} rdr \tag{5.7}$$

where n is the number of electrons transferred. For the reduction of oxygen $n=4$. Note that we use the diffusion coefficient of oxygen in Nafion ($D_{O2/Nafion}$) because the microelectrode surface is directly in contact with the polymer layer.

The net fluxes of oxygen passing through the different interfaces of the microrespirometer system are treated according to the model for film-coated electrodes described by Saveant *et al.* [13]. The interface between the solution and the layer covering the electrode is described by:

$$D_s\left.\frac{d[O_2]}{dx}\right|_{x=\phi^-} = \chi_f\left[O_2\left(\phi^+\right)\right] - \chi_b\left[O_2\left(\phi^-\right)\right] = D\left.\frac{d[O_2]}{dx}\right|_{x=\phi^+} \tag{5.8}$$

where D_s and D are the diffusion coefficient inside the layer and in the solution, respectively. The notation ϕ^- and ϕ^+ means that the process takes place at the side of the interface corresponding to the covering layer or to the solution. χ_f and χ_b are the heterogeneous mass transfer constants from the solution to the layer and vice versa. Moreover, if χ_f and χ_b are high enough, at the equilibrium the relation between both constant at the interface is described as:

$$\left[O\left(\phi^-\right) \right] = \kappa \left[O\left(\phi^+\right) \right] \tag{5.9}$$

where $\kappa = \chi_f/\chi_b$. The heterogenous mass transfer constants are calculated as the ratio between the oxygen solubility between the two different media multiplied by a high factor. Furthermore, $\kappa = 1$ for the biofilm-solution interface which means oxygen solubility inside the biofilm is considered as the same of the oxygen solubility in water. The heterogenous mass transfer constant for the Nafion layer will be calculated experimentally in the following section, as the oxygen solubility is higher in Nafion than in water [9, 10]. So, $\chi_f > \chi_b$ at biofilm-Nafion interface.
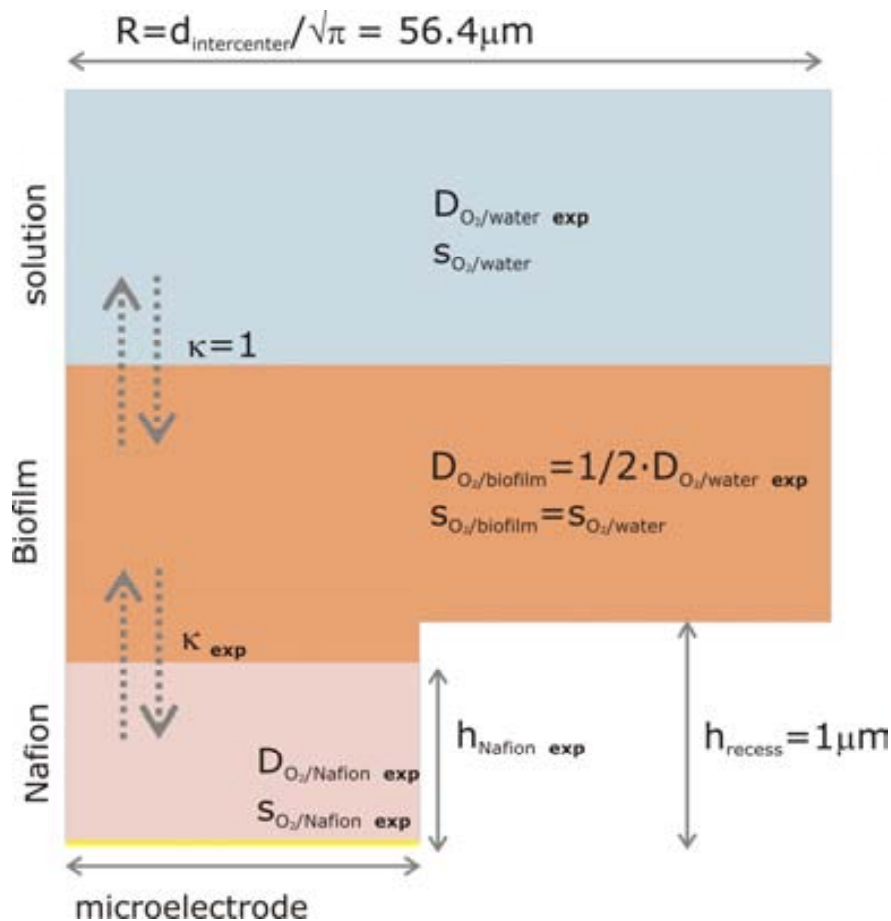

Figure 5-4: Diagram scheme (not to scale) of the microrespirometer model domain. The electrode recess (h_{recess}) and the diffusion domain (R) are considered in the definition of the domain. The main domain is divided in three subdomains: solution, biofilm and Nafion. It is necessary to know the mass transfer parameters for oxygen in each subdomain. Some of them are

calculated experimentally in the following sections, so they are labelled with **exp** abbreviation.

Figure 5-4 shows the microrespirometer model domain. The different mass transport and concentration parameters are highlighted; some of them are taken from literature and the rest will be experimentally calculated in the following sections.

The disk microelectrodes are arranged in a regular cubic array. The diffusional independence of each microelectrode in the array needs to be kept in order to optimise the array response. Ideally, the observed current corresponds to that of a single microdisk multiplied by the number of elements in the array [14]. The width (R) of the two dimensional model showed in Figure 5-1 is defined using the diffusion domain approach, as it was described in Chapter 4. It mainly consists on dividing the whole domain in diffusionally independent subdomains corresponding with each microelectrode. Moreover, it was showed in the microelectrode array fabrication that the electrodes are slighted recessed due to the passivation layer. Their theoretical threatment was also explained in Chapter 4.

5.4 Results and Discussion

The main objective of our model is to describe the metabolic activity of the biofilm and compare the results with experimental data obtained by an optical probe. We first discuss the effect of the different solubilities of oxygen in water and Nafion, [9, 10] which acts as an oxygen sink that enables the detection under the adequate conditions. We then use these oxygen parameters to estimate the thickness of the thin layer of Nafion 117 from current data. We compare experimental linear sweep voltammograms obtained at Nafion modified microdisk arrays with the results of simulating a hypothetical Nafion coated model.

Finally, we will present the description of the whole microrespirometer model and the simulated metabolic kinetic results are compared with experimental data obtained from optical measurements.

5.4.1 Determination of oxygen parameters and Nafion layer thickness

A range of values for the diffusion coefficient of oxygen in water has been found in the literature which spans between 2.69 and 3.40 x 10^{-5} cm^2s^{-1} [15]. Therefore, we performed our own chronoamperometric measurements in water. For the sake of simplicity, single recessed microdisk currents have been fitted by least squares to the approximate analytical current expression of Bartlett and Taylor [16]:

$$I(t) = 4nFDrc \left[B'\left(\frac{Dt}{r^2}\right)^{-1/2} + C'e^{-D'\left(\frac{Dt}{r^2}\right)^{-1/2}} \right] \qquad (5.10)$$

where r and L, are the microdisk radius and the recess height. Parameters B', C' and D' depend on the quotient L/r and they are tabulated in [16]. Single Au recessed microelectrodes of r=10μm and L=1μm were used. Following their characterisation with ferrocyanide, they were immersed in an oxygen saturated solution and a series of potential step measurements were performed for each microelectrode to extract the diffusion coefficient value of oxygen from current transients, assuming a four electron reduction, as per equation (5.6). The oxygen concentration in water was measured for every set of cronoamperograms. The experimental current values were fitted to equation (5.10) by least squares using Matlab. To obtain better fittings between theory and experimental data, two parameters were estimated, the diffusion coefficient of oxygen ($D_{O2/water}$) and the microdisk radius (r). The radius value was forced to be within a 5% of its nominal value. In all fittings, the linear correlation coefficient was better than 0.98 which means a correlation better than 99% for the number of used points (N=100) [17]. The average values and their associated errors are:

$$D_{O_2/water} = (2.2 \pm 0.1) \times 10^{-9} m^2 s^{-1}$$
$$r = (10.3 \pm 0.3) \ \mu m$$

The value of diffusion coefficient of oxygen in water is perhaps on the low side, but in agreement with other literature values [15]. The errors correspond to a 95% confidence interval for the number of measurements perfomed (N=27).

The availability of oxygen transport parameters in Nafion is much more limited [9, 10] than in aqueous media. In order to calculate the diffusion coefficient and solubility of oxygen in Nafion 117 we coated the chip surface with a thick layer of Nafion 117. This ensures that the diffusion layer of oxygen is contained within the Nafion layer and hence we can make the assumption that only mass transport parameters within the Nafion are involved significantly.

The methodology was the same as in the case of the oxygen in water and the same single microelectrode configuration was used. After recording chronamperograms, three parameters $D_{O2/Nafion}$, $s_{O2/Nafion}$ and r were fitted for each used microelectrode. The mesuarements were taken after a certain time to ensure that the Nafion layer was satured with oxygen, so the concentration of oxygen at that point is the same as the solubility of the layer. Again, the microelectrode radius was forced to be within a 5% of its nominal value. Then the linear correlation coefficient was higher than 0.9, implying a correlation better than 99% for the number of datapoints (N=80) [17] in each dataset (N_{sets}=5) and confidence levels (95%). The values obtained are:

$$D_{O_2/Nafion} = (1.5 \pm 0.1) \times 10^{-11} m^2 s^{-1}$$
$$s_{O_2/Nafion} = (8.0 \pm 0.2) \ mol \cdot m^{-3}$$
$$r = (9.7 \pm 0.3) \ \mu m$$

The values of diffusion coefficient and solubility of oxygen in Nafion 117 are in agreement with the bibliography [9, 10].

5.4.2 Estimation of the Nafion layer thickness

Once the actual number of active electrodes in the array is known [18], the chips, containing microdisk arrays of 5 μm radius, 100 μm of intercenter distance and 1 μm recess, are modified with a thin Nafion layer, as described in a previous section. Comparing experimental and simulated current results we will estimate the thickness of this layer using the calculated oxygen parameters in Nafion. The experimental oxygen reduction current is recorded at -1V vs Ag/AgCl (3M KCl) for each modified chip. First, the active number of electrodes in an array was determined according to [18] before modifying the array. Therefore, after the modification, it was possible to calculate the current for a single microdisk dividing the experimental current by the previously measured number of active microdisks. The average measured current is 2.5±0.2 nA.

We used the described 2D geometry and the oxygen mass transfer parameters for water and Nafion. The key was to adjust the thickness of the Nafion subdomain, τ_{nafion}, until convergence between simulated and experimental steady state current value was found (Figure 5-5).
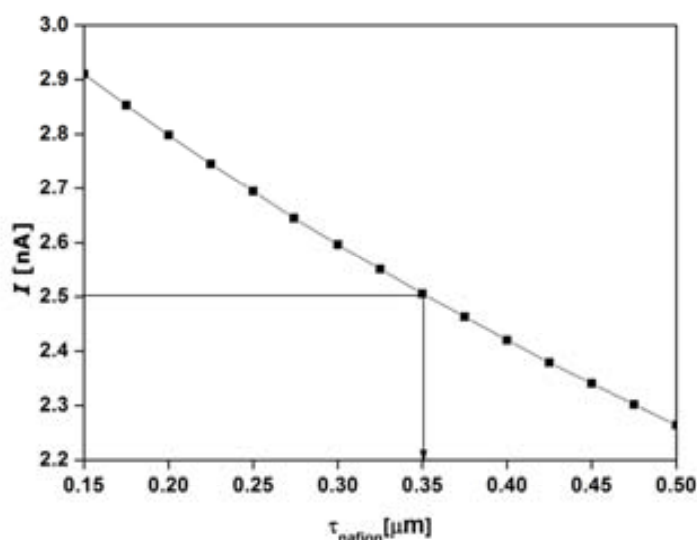

Figure 5-5: Effect of the Nafion layer thickness on the oxygen reduction current. The oxygen parameters considered in the simulations used to construct this chart, were: D_{aq}=2.2x10^{-9} m^{2}s^{-1}, c_{O2}=8.1 ppm, D_{naf}=1.5x10^{-11} m^{2}s^{-1}, s_{naf}=8mM. From the experimental current it was possible to estimate an average thickness for the Nafion layer.

The surface topology of the Nafion layer was characterised previously by perfilometry resulting in thicknesses of *ca.* 300 nm unhydrated and *ca.* 450 nm hydrated. These contact measurements of thickness were used as a reference to check the analysis of our electrochemical measurements. The Nafion thickness calculated from electrochemical data is *ca.* 350 nm, which is within reasonable agreement compared to previous perfilometry data for a hydrated Nafion layer. The difference can be due to different factors, such as

inhomogeneity of the Nafion layer, or due to errors in the adjustment of the mass transport parameters for oxygen in Nafion (diffusion coefficient and solubility). However, both results are clearly consistent. In the following section, where the study and modelling of the biofilm is addressed, this estimated thickness will be used as the Nafion layer thickness.

5.4.3 Metabolic activity of biofilm

The metabolic activity of the biofilm was optically calculated by the Environmental Microbiology group at UAB. This experimental value will be used to corroborate the accuracy of our model.

Optical measurements

As mentioned before, absorbance measurements and culture samples were taken during the experiment in order to know the bacterial concentration and the growth rate. Initial and final absorbance values showed the approximate bacterial growth rate every time the oxygen supply was interrupted. This was confirmed with later bacterial plaque counts. The total length of the experiment was 5 h. Table 5-1 shows the data obtained and used to calculate the oxygen consumption rate in a *Pseudomonas putida* culture, where:

$$\upsilon_{max} = \frac{\left([O_2]_o - [O_2]_f\right)}{\Delta t \left(\dfrac{[C_{bact}]_o + [C_{bact}]_f}{2}\right)} \tag{5.11}$$

Table 5-1: Conditions given in the determination of the respiration rates in a bacterial suspension by means of an optical oxygen probe, and resulting kinetic data

Initial O_2 / mg·L^{-1}	7.11	6.56	6.50
Final O_2 / mg·L^{-1}	0.57	0.29	0.27
Initial t / h	1.15	2.06	2.74
Final t / h	1.37	2.24	2.92
Δt / h	0.22	0.18	0.18
Initial bacterial concentration / cell·L^{-1}	2.54 x 10^{11}	3.02 x 10^{11}	3.62 x 10^{11}
Final bacterial concentration / cell·L^{-1}	2.59 x 10^{11}	3.38 x 10^{11}	4.11 x 10^{11}
υ_{max} / mg$_{O2}$ cell^{-1}·h^{-1}	1.17 x 10^{-10}	1.15 x 10^{-10}	9.76 x 10^{-11}

The average oxygen consumption rate, considering the three measurements was found to be:

$$\upsilon_{max} = \left(5.75 \pm 0.64\right) \times 10^5 \quad mol_{O_2} \cdot mol_{bact}^{-1} \cdot s^{-1}$$

Microrespirometer model

Here we use the microrespirometer model to interpret real microrespirometry data. Using the data obtained so far for the oxygen transport and consumption parameters across the various parts making up the biofilm, we estimated a rate constant for the metabolic activity of the biofilm and compared it with optical data recorded in a broth under similar conditions. As presented in [1], the current reduction when glucose was added was about 15-20% for a mature biofilm. We then used this current measurements to estimate the metabolic activity of the biofilm when glucose was added.

Table 5-2 provides a summary of the parameters used in the model and which have been estimated from experimental data up to now.

Table 5-2: Parameters estimated experimentally for use in the simulation of the microrespirometer

Oxygen coefficient of oxygen in water, $D_{O2/water}$	$2.2 \cdot 10^{-9}$ m^2·s^{-1}
Oxygen coefficient of oxygen in Nafion, $D_{O2/Nafion}$	$1.5 \cdot 10^{-11}$ m^2·s^{-1}
Solubility of oxygen in Nafion, $s_{O2/Nafion}$	8.0 mM
Average Nafion thickness	350nm
Average biofilm thickness	100μm
Average biofilm surface concentration	10^{11}cfu·m^{-2}

Note that our model rests on the following assumptions:

- The solubility of oxygen in the biofilm is the same as in water [19, 20] The diffusion coefficient of oxygen in the biofilm is approximately half of the value of diffusion coefficient of oxygen in water, as it is described in [8].

- The biofilm is considered a homogeneous medium of constant bacterial concentration. Although we know the latter assumption to be inaccurate, it has been used previously and it is required to simplify the model definition [19, 21] because it means a constant consumption in the biofilm subdomain. To calculate the bacterial concentration of the biofilm, the latter is considered as a volumetric structure composed by several layers of bacteria. *Pseudomas putida* are rods of approximately 1μm wide and 3 μm long [22, 23]. We considered each layer to be about 5 μm high. Given this assumption, the volumetric concentration of bacteria is calculated using experimental data from surface concentration (10^{11} cfu·m^{-2}) and biofilm thickness (100 μm), so the value is $3 \cdot 10^{-8}$ mol$_{bact}$·m^{-3}.

- We have used a K_m value of 0.19 μM for *Pseudomas putida* (see equation (5.3)). This value was extracted from literature [24] for *E.coli*, which is known to behave very similarly.

- We have assumed that the glucose added for the biofilm respiration is always in excess. That means it can be considered a constant concentration (2.2mM).

At this point we are able to solve the microrespirometer model. As it was showed in Figure 5-4, this consists on three different subdomains (solution, biofilm and Nafion) where just the mass transport equations for oxygen are defined. The only unknown remaining from our experimental data is the kinetic constant of the biofilm respiration. To find it out, we solve for a range of υ_{max}, the maximum substrate utilisation rate in equation. (5.3)

First, the model is solved considering that there is no metabolic activity in the absence of glucose. In this case, the biofilm is only an oxygen diffusion barrier. As in the experimental part, this provides the baseline current data. Then, the consumption of oxygen is incorporated in the model, and υ_{max} is varied from $2.5\cdot10^5$ to $7.5\cdot10^5$ $molO_2$ $mol_{bact}^{-1}\cdot s^{-1}$. The current reduction percentage due to respiration is calculated as:

$$\frac{\left(I_o - I_{\upsilon_{max}}\right)}{I_o} \times 100 \tag{5.12}$$

where I_o is the current where there is no metabolic activitity and $I_{\upsilon max}$ is the current for each value of υ_{max}. Figure 5-6 shows the results for the studied range of maximum substrate utilisation rate.
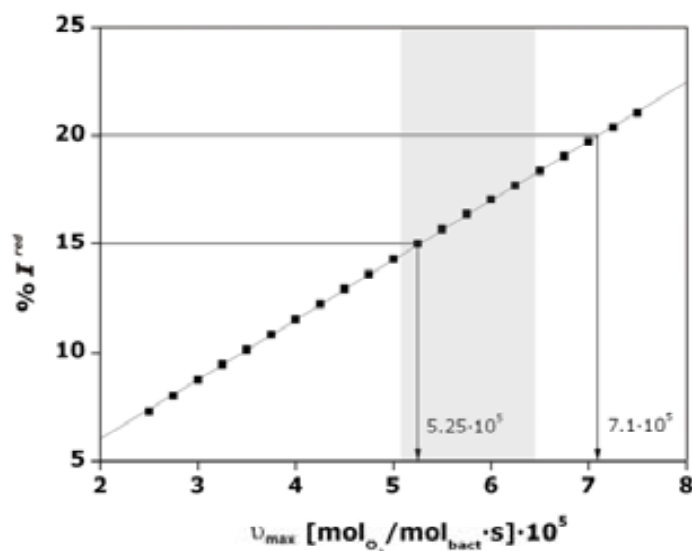

Figure 5-6: Determination of the respiration rate constant of the biofilm using experimental data from [1]. Curve corresponds to simulated current changes as a function of the respiration rate. According to this and previous respirometric data, the respiration rate of the biofilm is in agreement with optical data (greyed area).

Figure 5-6 also shows the experimental consumption rate measured optically, $(5.75\pm0.64)\cdot10^5$ $molO_2$ $mol_{bact}^{-1}s^{-1}$. Electrochemically, the current reduction measured was between 15-20% when glucose was added. If we relate this current reduction to the metabolic activity, it means a range between from $5.25\cdot10^5$ $molO_2$ $mol_{bact}^{-1}s^{-1}$ to $7.10\cdot10^5$ $molO_2$ $mol_{bact}^{-1}s^{-1}$, which is in a really good agreement with the optical results. So, our model can be used as a tool to estimate certain biofilm parameters.

If biofilm thickness were in the millimetre range, the model would have to be reformulated to account for transport of the nutrients. However, under our experimental conditions this is not necessary, and the calculations can be greatly simplified. The present model can, in conjunction with empirical data, be used to estimate toxicity parameters in water samples from effluents or natural sources. Since the measurement of toxicity is indirect, as it is based on monitoring the respiration of the biofilm, it provides no information about the nature of the toxic substance. However, microrespirometry still represents a valuable diagnostic tool that can be used in the determination of important water quality parameters such as biological oxygen demand (BOD).

5.5 Summary

We have described the step by step construction of a theoretical model capable to faithfully describe the behaviour of an electrochemical microrespirometer. The original microrespirometer [1] was based on a biofilm-modified array of microdisk electrodes wired in parallel. There, oxygen is reduced and the resulting current can be related to bacterial metabolism and, ultimately, to environmental toxicity.

In this chapter we have described a technique to successfully model mass transport to an array of slightly recessed electrodes using finite element methods. This technique has been shown to be reliable for the simulation of single recessed microdisks compared to previously published methods [16, 25] which, on the other hand, could not cope with arrays of microelectrodes. By using the diffusion domain approach we have been able to supersede this and model the response of the entire array.

However, the microrespirometer is a complex system comprised of three parts: the microelectrode array, a protective Nafion layer and a mature biofilm. Modelling the whole system requires knowledge of all the parameters related to the fate of oxygen across the different parts making up the microrespirometer. Such data has been collected from the literature whenever possible. Otherwise we conducted the necessary electrochemical and optical measurements, and used that information in our model to resolve biofilm metabolic rate constants from current data. Spectrophotometric measurements were carried out in parallel to determine the consumption rate of oxygen by a culture of *Pseudomonas putida*, the same bacteria found in the biofilm. The spectrophotometric data were used as a reference in the verification of the electrochemical results. It was found that the kinetic rates found by our numerical model from amperometric measurements were in excellent agreement with the spectrophotometric measurements, which provided further support for our electrochemical model.

We are confident that the present model can be used to extract bacterial metabolic information from a relatively simple electrochemical set-up and that it can be a very valuable tool in the determination of parameters related to the toxicity of a sample. Thus, it is not only possible to use transient current data to determine the degree of toxicity of a certain

environment but, in conjunction with numerical simulations, such data can also be used to determine kinetic parameters related to specific substances and bacteria.

5.6 References

[1] Del Campo, F.J., O. Ordeig, N. Vigues, N. Godino, J. Mas, and F.X. Munoz, *Continuous measurement of acute toxicity in water using a solid state microrespirometer.* Sensors and Actuators B: Chemical, 2007. 126: p. 515-521.

[2] Bard, A.J. and L.R. Faulkner, *Electrochemical Methods: fundamentals and applications.* 2001, Chichester: Wiley.

[3] Madigan, M.T., J.M. Martinko, P.V. Dunlap, and D.P. Clark, *Brock Biology of Microorganisms.* 2006: Prentice Hall. 1088.

[4] Balestrino, D., J.A.J. Haagensen, C. Rich, and C. Forestier, *Characterization of type 2 quorum sensing in Klebsiella pneumoniae and relationship with biofilm formation.* Journal of Bacteriology, 2005. 187(8): p. 2870-2880.

[5] Costerton, J.W., Z. Lewandowski, D.E. Caldwell, D.R. Korber, and H.M. Lappinscott, *Microbial Biofilms.* Annual Review of Microbiology, 1995. 49: p. 711-745.

[6] Costerton, J.W., P.S. Stewart, and E.P. Greenberg, *Bacterial biofilms: A common cause of persistent infections.* Science, 1999. 284(5418): p. 1318-1322.

[7] Button, D.K., *Kinetics of Nutrient-Limited Transport and Microbial-Growth.* Microbiological Reviews, 1985. 49(3): p. 270-297.

[8] Stewart, P.S., *A review of experimental measurements of effective diffusive permeabilities and effective diffusion coefficients in biofilms.* Biotechnology and Bioengineering, 1998. 59(3): p. 261-272.

[9] Lehtinen, T., G. Sundholm, S. Holmberg, F. Sundholm, P. Bjornbom, and M. Bursell, *Electrochemical characterization of PVDF-based proton conducting membranes for fuel cells.* Electrochimica Acta, 1998. 43(12-13): p. 1881-1890.

[10] Parthasarathy, A., C.R. Martin, and S. Srinivasan, *Investigations of the O-2 Reduction Reaction at the Platinum Nafion Interface Using a Solid-State Electrochemical-Cell.* Journal of the Electrochemical Society, 1991. 138(4): p. 916-921.

[11] Paliteiro, C., *(100)-Type Behavior of Polycrystalline Gold Towards O-2 Reduction.* Electrochimica Acta, 1994. 39(11-12): p. 1633-1639.

[12] Allen J. Bard, L.R.F., *ELECTROCHEMICAL METHODS. Fundamentals and Applications.* 2nd ed. 2001, New York: John Wiley & sons.

[13] Leddy, J.A., A.J. Bard, J.T. Maloy, and J.M. Saveant, *Kinetics of Film-Coated Electrodes - Effect of a Finite Mass-Transfer Rate of Substrate across the Film Solution Interface at Steady-State.* Journal of Electroanalytical Chemistry, 1985. 187(2): p. 205-227.

[14] Davies, T.J. and R.G. Compton, *The cyclic and linear sweep voltammetry of regular and random arrays of microdisc electrodes: Theory.* Journal of Electroanalytical Chemistry, 2005. 585(1): p. 63-82.

[15] George W. Hung, R.H.D., *Diffusivity of oxygen in electrolyte solutions.* J. Chem. Eng. Data, 1972. 17: p. 449-451.

[16] Bartlett, P.N. and S.L. Taylor, *An accurate microdisc simulation model for recessed microdisc electrodes.* Journal of Electroanalytical Chemistry, 1998. 453(1-2): p. 49-60.

[17] Caulcutt, R., *Data Analysis in the Chemical Industry. Volume 1: Basic Techniques.* 1989: Ellis Horwood.

[18] Ordeig, O., C.E. Banks, T.J. Davies, J.d. Campo, F.X. Munoz, and R.G. Compton, *The linear sweep voltammetry of random arrays of microdisc electrodes: Fitting of experimental data.* Journal of Electroanalytical Chemistry, 2006. 592(2): p. 126-130.

[19] Abrahamson, M., Z. Lewandowski, G. Geesey, G. SkjakBraek, W. Strand, and B.E. Christensen, *Development of an artificial biofilm to study the effects of a single microcolony on mass transport.* Journal of Microbiological Methods, 1996. 26(1-2): p. 161-169.

[20] Beyenal, H. and Z. Lewandowski, *Modeling mass transport and microbial activity in stratified biofilms.* Chemical Engineering Science, 2005. 60(15): p. 4337-4348.

[21] Rittmann, B.E. and P.L. McCarty, *Model of Steady-State-Biofilm Kinetics.* Biotechnology and Bioengineering, 1980. 22(11): p. 2343-2357.

[22] Li, Z.S., A.J. Clarke, and T.J. Beveridge, *A major autolysin of Pseudomonas aeruginosa: Subcellular distribution, potential role in cell growth and division, and secretion in surface membrane vesicles.* Journal of Bacteriology, 1996. 178(9): p. 2479-2488.

[23] Whitehead, K.A., J. Colligon, and J. Verran, *Retention of microbial cells in substratum surface features of micrometer and sub-micrometer dimensions.* Colloids and Surfaces B-Biointerfaces, 2005. 41(2-3): p. 129-138.

[24] Rice, C.W. and W.P. Hempfling, *Oxygen-Limited Continuous Culture and Respiratory Energy-Conservation in Escherichia-Coli.* Journal of Bacteriology, 1978. 134(1): p. 115-124.

[25] Bond, A.M., D. Luscombe, K.B. Oldham, and C.G. Zoski, *A comparison of the chronoamperometric response at inlaid and recessed disc microelectrodes.* Journal of Electroanalytical Chemistry, 1988. 249(1-2): p. 1-14.

CHAPTER 6:

Mass transfer to disk nanoelectrode array

Nanotechnology has become one of the most interesting areas for many researchers due to its challenging nature and wide applicability to many fields. In our case, nanotechnology allowed us to fabricate electrodes in the nanoscale which means more than just a simple downsizing. Electrochemically, nanoelectrodes are faster than conventional microelectrodes, however, the reduction to such small dimensions leads to different mass transport behaviours from expectations based on the "micro" experience. This chapter provides an overview of the principles and assumptions underpinning the diffusion domain approach, which then applies to the study of nanoelectrode arrays. The apparent disagreement between theory and experimental data, due to the importance of radial diffusion to nanoelectrode arrays compared to microelectrode arrays, is explained using simulations and experiments.

6.1 Introduction

Nanoelectrodes and nanoelectrode arrays are the natural next step in electrode miniaturisation after microelectrodes and their arrays. However, only recent advances in nanofabrication techniques and metrology have enabled the controlled fabrication of such devices. This, together with the fact that such techniques are very costly and not so widely available, has limited the number of publications to date in this field. Early reports date back to the late 1990's, but the field did not seem to boom until fifteen years later with the works of Arrigan et al.[1-3], White [4, 5] and Murray [6] who reported on the mass transport properties of nanoelectrodes of various geometries and their arrays.

One common and intriguing feature of the results presented in these works is the sigmoidal shape of the voltammograms recorded at nanoelectrode arrays even at moderate and low scan rates. This may seem striking if we draw an analogy between the mass transport behaviour of nanoelectrode arrays and microelectrode arrays. Compton *et al.* [7, 8] have pointed to four main regimes of behaviour affecting diffusional transport to microelectrode arrays. According to the relationship between size of the individual diffusion layer thicknesses, δ, microelectrode size described by their radius, r, and the inter-centre distance between microelectrodes, d, and with increasing diffusion layer thickness, these four regimes are: (i) planar diffusion to each microelectrode as $\delta << r$, (ii) radial diffusion to each microelectrode as $\delta = r < d$, (iii) a transition zone when $r < \delta = < d$ and (iv) planar diffusion to the microelectrode array when $\delta >>> d$. Regime-ii is the optimum one and it corresponds to the case when the response of the whole array is equivalent to that of a single microdisk, times the number of microelectrodes integrating the array. Regime-iv, on the other hand, consists

in a complete overlap of individual diffusion layers that results in the array behaving as an electrode of the size of the entire micro- or nano-electrode array. Hence for most microelectrode arrays steady-state currents are observed in regime-ii, and then as the diffusion layer grows the current tails off in regime-iv. However, nanoelectrode arrays are a special case because their size is typically a few microns, so they show steady-state currents corresponding to microelectrode behaviour, regardless of the extent of overlap between adjacent diffusion layers.

This motivated us to study diffusion at nanoelectrode arrays in more detail, combining simulations and experiments with nanoelectrode arrays fabricated using electron-beam lithography [9]. We first attempted to simulate the behaviour of nanoelectrode arrays using the diffusion domain approach that has been so helpful in the study of microelectrode arrays. However, the results cast by this approach conflicted with the empirical observations reported in the past and, as we will show here, also with our own experimental data.

Models of nanoelectrode arrays were built based on three-dimensional domains and the results compared with those from two-dimensional models and the available experimental data. The three-dimensional simulations were in agreement with the experimental results, and showed that nanoelectrode arrays working under regime-iv behave as single microelectrodes under most conditions.

The main reason why a two-dimensional approach fails to correctly model the behaviour of such nanoelectrode arrays is because it considers the particular case of a micro –or nano-electrode completely surrounded by other electrodes like itself, and ideally far from the edges of the array. In other words, the diffusion domain approach is best suited for large micro- and nanoelectrode arrays with significantly more microelectrodes in *inner* than in *perimetric* positions. This is partly why the diffusion domain approach fails to simulate the response of small nanoelectrode arrays in regime iv accurately. Perhaps another constraint should be added when dealing with small nanoelectrode arrays, regarding the size of the array vis-à-vis the size of the diffusion layer at the array. Since diffusion at microelectrodes is radial, supply of material to each nanoelectrode in an array of micrometric dimensions depends heavily on its position. Inner positions are characterised by being completely surrounded by neighbouring microelectrodes, and hence less material is able to reach them by diffusion compared to perimetric electrodes. Edge effects are magnified at small nanoelectrode arrays, where the hemispherical nature of the diffusion layer corresponding to the whole array is not accurately accounted for by this two-dimensional domain approach.

Therefore, in this chapter we alert of the risks entailed by the indiscriminate application of the diffusion domain approach to nanoelectrode arrays regardless of their size. We show that while the behaviour of nanoelectrode arrays is to some extent analogous to that of microelectrode arrays, different approaches ought to be used to model them depending on their overall size. Our conclusion is that while the diffusion domain approach is a powerful technique, it can only be applied to nanoelectrode arrays occupying a large area, such as large ensembles of interdigitated nanoband electrodes or nanopatterned electrodes as the ones described by Compton and co-workers in [10].

6.2 Experimental

6.2.1 Chemicals and instrumentation

KCl (99%) and $K_4Fe(CN)_6.3H_2O$ (99%) were purchased from Sigma-Aldrich. They were ACS analytical grade and were used as received without any further purification. Solutions were prepared using pure de-ionised water (18MΩ·cm). All electrochemical measurements were performed using a three-electrode configuration and a CHI700C bipotentiostat (CH Instruments, Texas, USA) connected to a PC. All electrodes were made from gold, A Pt ring was used as auxiliary electrode and a Metrohm Ag/AgCl (3M KCl) was used as reference electrode. Nanoelectrode geometry was characterised by atomic force microscopy (AFM) [9, 11] using a Veeco Dimension 3100 (Veeco Instruments) in Tapping Mode.

6.2.2 Fabrication of disk nanoelectrode arrays

Disk nanoelectrode arrays were made by e-beam lithography to corroborate our theoretical results. Such arrays were fabricated over gold microband electrodes that had previously been made using standard photolithographic techniques (Figure 6-1(1)) and it was detailed in Chapter 3. Arrays displaying a different number of nanodisks (6x6, 31x31 and 61x61) and inter-centre distance between nanoelectrodes (250nm and 1.5μm) were fabricated. First, the individual chips containing gold microbands were spin-coated with a 100nm layer of PMMA 950K, a popular resist in e-beam lithography (Figure 6-1(2)). Nanostructures are transferred by e-beam lithography (Figure 6-1(3)). The conditions of exposure to achieve nanodisks of around 100nm of diameter for two different centre-to-centre distances (250nm and 1.5μm) are: dose=0.016pC for the 250nm pitch dots and 0.02pC for the 1.5um pitch dots; accelerating voltage=10kV and at WD=10mm. Development is carried out in a standard solution of methyl isobutyl ketone (MIBK) and isopropanol (IPA) with a ratio 1:3 during 30sec and stopped with IPA for 30sec.
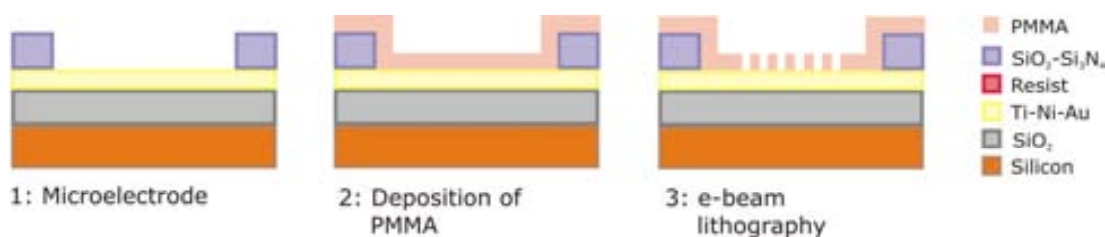

Figure 6-1: Nanofabrication step of a disk nanoelectrode array.

6.3 Theory

The current response of micro- and nano-electrode arrays was simulated in two- and three-dimensional domains using COMSOL Multiphysics 3.3 (COMSOL, SE) in combination with Matlab (The Mathworks, Inc.).

We simulated the one-electron reduction process of a species in solution, corresponding to:

$$O + e^{-} \underset{k_b}{\overset{k_f}{\rightleftharpoons}} R \tag{6.1}$$

where k_f and k_b are heterogeneous rate constants defined by Butler-Volmer kinetics. [12]

$$k_f = k_s e^{-\alpha F\left(E-E^{o'}\right)/RT} \tag{6.2}$$

$$k_b = k_s e^{(1-\alpha)F\left(E-E^{o'}\right)/RT} \tag{6.3}$$

k_s is the standard kinetic rate constant and indicates the degree of a system lability. In the present case a value of 10^{-2} ms^{-1}, representing a fast system, was used in the simulations. For the sake of comparison, experimental values are usually between 10^{-2} and 10^{-7} ms^{-1} [12, 13]; α is the charge transfer coefficient –assumed to be 0.5 in our simulations- [14], $E^{o'}$ is the formal potential of the redox couple, which we fixed at 0.25V to facilitate later comparison with experimental data. Finally, F is the Faraday constant, R is the gas constant and T is absolute temperature, set at 298 K in our simulations.

We wanted to emphasise the importance of electrode geometry on diffusional transport alone, and therefore convection and migration were disregarded in our simulations. Only Fickian diffusion towards the electrodes was considered according to:

$$\frac{\partial c_i}{\partial t} = D_i \left(\frac{\partial^2 c_i}{\partial x^2} + \frac{\partial^2 c_i}{\partial y^2} + \frac{\partial^2 c_i}{\partial z^2} \right) \tag{6.4}$$

where c is the concentration and D the diffusion coefficient of the species in solution. The diffusion coefficient used in the models was $6.5 \cdot 10^{-10}$ m^{2}s^{-1}, which corresponds to ferrocyanide in 0.1M KCl [12].

The convergence of our solutions was heavily influenced by the quality of the mesh. Therefore, for each set of boundary conditions, we progressively refined the mesh until a convergence better than 1% between two consecutive solutions was obtained. While this did not represent a particular problem in the case of two-dimensional domains, it turned the solution of three-dimensional cases extremely time consuming. Accuracy, on the other hand, was affected by the size of the domains, which we set large enough to ensure bulk-like conditions at the boundaries. Given the recessed nature of our nanoelectrode arrays [2, 3, 15, 16], made by electron beam lithography over a thin polymethyl-methylacrilate (PMMA) layer, the current was not compared with the expression for the steady-state current at an inlaid microdisk, namely *I=4nFcDr*. Instead, we used the expression for recessed microelectrodes[17]:

$$I = \frac{4nFcDr_o}{\left(\dfrac{4L}{\pi r_o} + 1 \right)} \tag{6.5}$$

where n is the number of transferred electrons, r_o is the radius of the electrode, and L is the value of the recess height.

6.4 Results and Discussion

6.4.1 Nanoelectrode arrays and the diffusion domain approach

It is known that the size and shape of the diffusion layer at an electrode array depends on several factors such as: (a) experimental timescale, (b) microelectrode geometry, (c) inter-electrode distance and (d) diffusion coefficient of the electroactive species involved [7]. The diffusion domain approach is a widely used technique to simulate disk microelectrode arrays [7, 8, 18], as it was widely described in Chapter 4. Briefly, it consists in assigning its own space to each microelectrode in an array, so that it is diffusionally independent from its neighbours. The main advantage is that it enables the accurate simulation of diffusional transport to a three-dimensional array of microelectrodes solving the mass transport problem in a two-dimensional domain which solution is then integrated around the z axis to obtain the current at a single microdisk. Last, this current is multiplied by the number of electrodes in the array to obtain the total current.

This approach works well both for regular [7, 8], and random arrays [19] of microelectrodes as well as for partially blocked electrodes [20, 21]. However, our results suggest that it is not suitable for the general simulation of nanometric-scale systems. In fact, this approach may be inaccurate in the case of disk nanoelectrode arrays where the footprint of the whole array is only a few microns square.

To show this, we used the diffusion domain approach [18] and solved two-dimensional models for the reduction of species O, over square-lattice arrays of micro- and nano- disk electrodes.
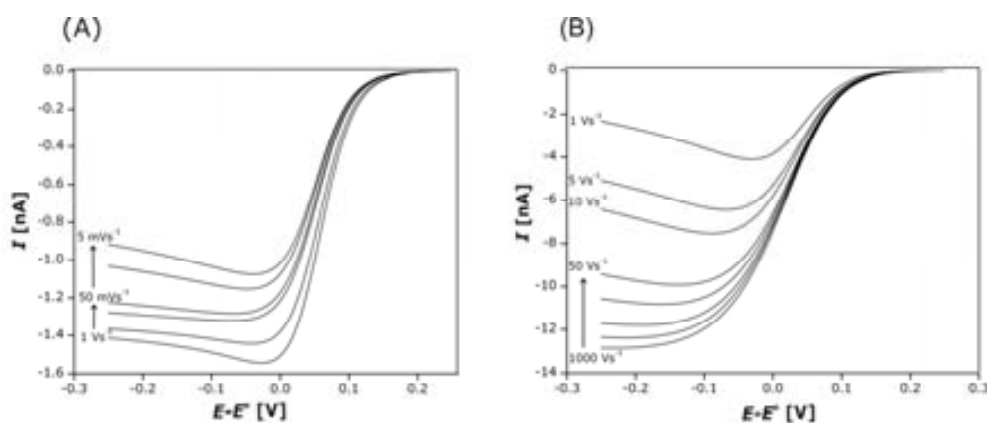

Figure 6-2: Simulated linear sweep voltammograms at different disk electrodes within an array, using the diffusion domain approach. (A) Microdisk radius of 5 μm and an inter-center distance of 100 μm for 0.005, 0.01, 0.05, 0.1, 0.5 and 1 Vs^{-1}. (B) Nanodisk radius of 50 nm and an inter-center distance of 1 μm for 1, 5, 10, 50, 100, 250, 500 and 1000 Vs^{-1}. In both cases $E^{o'}$=0.25V, D=6.5·10^{-10}m^{2}s^{-1} and [O] =1mM.

Figure 6-2A shows linear sweep voltammograms obtained for the case of a 5 μm radius inlaid microelectrode separated by 100 μm from its closest neighbors. The scan rates range

from 5mVs^{-1} up to 1Vs^{-1}. Figure 6-2B, on the other hand, shows the results for the case of a 50 nm radius nanodisk separated by 1 μm from its immediate neighbors at scan rates going from 1Vs^{-1} up to 1000Vs^{-1}. For fixed solution composition and centre-to-centre distance in the array, the degree of overlapping of the diffusion layers mainly depends on the scan rate used [7, 8].

Our simulation results for the microelectrode array (Figure 6-2A) agreed with previous results presented in [8]. The transition across the different regimes can be seen in the figure, and further confirmation may be obtained using Einstein's relation $\delta = \sqrt{2Dt} = \sqrt{2D\Delta E / v}$, where a value of 0.150 V may be used for ΔE, and v is the scan rate in Vs^{-1}. Thus, at scan rates faster than 1 Vs^{-1} the voltammograms show a peak associated to planar diffusion governing mass transport to the microelectrodes (Figure 6-2A). As the scan rate decreases, diffusion becomes hemispherical. Around 50 mVs^{-1} the microelectrodes still behave independently from each other and the current recorded by the array corresponds to the limiting current of a single microelectrode times the number of elements in the array. As the scan rate continues to decrease, the degree of overlapping between diffusion layers increases and eventually the array behaves as a macroelectrode of the same area as that occupied by the array.

In the case of nanoelectrode arrays the diffusion domain approach casts a similar landscape, and it would seem that the only difference is that, for the nanoelectrodes in the array to be diffusionally independent, faster scan rates would be required (50 Vs^{-1} or higher in our example). This seems perfectly normal, but it does not fit with the available experimental results reported by several authors [1-3, 22-24]. These works show clearly sigmoidal voltammograms obtained at moderate-to-low scan rates using nanoelectrode arrays.

We believe that when the electrode geometry shifts from the micro- into the nano-scale, all other parameters –diffusion coefficients, concentrations and experiment duration- being the same, special attention needs to be paid to the concentration profiles across the diffusion layer of the whole array. This means that voltammetric peaks might be observed for species with sufficiently low diffusion coefficients, such as ionic liquids, but also for nanoelectrode arrays occupying an area of millimetricr dimensions.

The four different behaviour cases of microelectrode arrays, which depend on the overlapping of the individual diffusion layers, were explained in Chapter 4. Usually, the different regimes may be reached by changing either the inter-electrode distance or the duration of the experiment for a given analyte. In the case of microelectrode arrays, which occupy areas in the order of a few square millimetres, the diffusion domain approach works because the consumption of material is large enough to change the concentration profiles very significantly in the vicinity of the array. Nanoelectrodes on the other hand, present a much smaller area and hence the amount of material that they are able to electrolyse is also very small to affect the solution composition to a great extent, even if they operate long enough to result in the complete overlap of their diffusion layers –at least so long as the

footprint of the array is of micrometric dimensions!-. In fact, the sigmoidal voltammograms reported in the literature [1-3, 22-24] seem almost independent of scan rate.

To test these ideas we performed another kind of two-dimensional simulations. We modelled a sectional plane containing the central row of electrodes in a 10x10 array. Again, the domain was drawn large enough to avoid misleading results due to the proximity of the boundaries and the mesh was duly refined. Figure 6-3 shows close-up images of the concentration maps in the vicinity of the micro- (Figure 6-3A) and the nano-electrode array (Figure 6-3B). They are clearly different. Figure 6-3A corresponds to a microelectrode array sweeping the potential at 5 mVs^{-1}; the diffusion layers of the individual electrodes clearly overlap, and diffusion to the array is nearly planar. This is within reasonable agreement with the diffusion domain approach, which predicts a planar diffusion layer under these conditions.

On the other hand, the concentration map for the nanoelectrode array sweeping at 1 Vs^{-1}, shown in Figure 6-3B, suggests that the diffusion domain approach, which according to Figure 6-2B pointed to mildly planar diffusion, was inaccurate. Figure 6-3B shows that the diffusion layer for the array, where the diffusion layers of the individual nanoelectrodes are completely overlapped, is actually hemispherical [6]. We believe that this is why the data shown in Figure 6-2B and the experimental results presented in bibliography [1-3, 22-24] differ. The implication is that while the domains of each nanoelectrode may be diffusionally independent, it would be wrong to assume that these nanoelectrodes are equivalent. This is particularly so for arrays occupying an area of micrometric dimensions, where the consumption on the part of the nanoelectrodes is so little that the solution bulk can readily supply fresh material to the diffusion layer so that the concentration in the vicinity of the array remains very close to the bulk value. Therefore, the contribution of radial diffusion to nanoelectrode arrays is more important than it is for microelectrode arrays [6].

We believe that very large nanoelectrode arrays would be required for the diffusion domain approach to predict the behaviour of the system as accurately as in the case of microelectrode arrays. However, a system like that may be treated as a partially blocked electrode rather than as an array of nanoelectrodes.
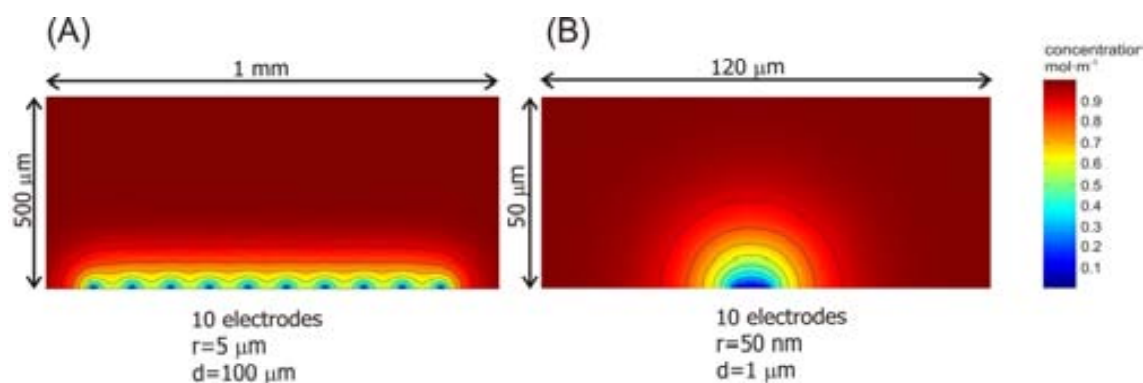

Figure 6-3: Details from 2D simulations of a plane perpendicular to a row of disk electrodes within an array of 10x10 electrodes. (A) 10x10 microdisks of 5 μm of

radius at 100 s (*r*) and 100 μm of intercenter distance at 0.5 s (*d*) (B) 10x10 nanodisks of 50 nm of radius and 1 μm of intercenter distance. In both cases [O] =1mM and *D*=6.5·10^{-10}m^{2}s^{-1}.

6.4.2 3D Modelling of recessed-disk nanoelectrode arrays

It seems that the consumption of electroactive species by the nanoelectrodes is so small that diffusion from the bulk quickly replenishes the consumed material. The result is that the nanoelectrodes in the array are no longer equivalent and reducing the system dimensions from 3D to 2D for the sake of modeling becomes inadequate. Radial contribution is so high in these systems that it is necessary to introduce 3D-domain models because the diffusion domain approach cannot simulate these devices accurately. Therefore we built three-dimensional models of nanoelectrode arrays (3x3, 6x6 and 9x9) and used them to study the effect, on the system response, of scan rate, nanoelectrode separation and nanoelectrode population. In all cases, the nanoelectrodes were disks of 50 nm radius that were recessed 100 nm in an insulating material. We chose these values because they are easy to achieve using standard nanofabrication techniques such as electron beam lithography (EBL) or focused ion beam (FIB) [9].

Figure 6-4 shows the geometry for a 6x6 nanoelectrodes with 250 nm intercenter distance, the nanoelectrode array is magnified for clarity. The bulk solution is represented by a cube 100 μm wide, 100 μm long and 50 μm high. The nanoelectrode array is defined at the bottom side of this cube, as shown in Figure 6-4. As the nanodisks are recessed 100 nm, the corresponding domain for each nanodisk is a cylinder 100 nm high and a radius of 50 nm. The bottom side of the cylinder corresponds to the electrode surface, so iwhere the mass flux is defined according to Butler and Volmer's expression, equation 2.19.

Creating the mesh is always an important step. For geometries as those showed in Figure 6-4 is even more difficult due to two main reasons. First, it is a 3D model and it requires using a number of elements as less as possible to reduce computation time, and second, there are huge size differences between some parts of the domain as the bulk is hundred of microns and the nanoelectrodes are in the nanoscale range. These reasons make impossible to mesh the whole domain with the same kind of mesh. The solution is to divide the domain in different subdomains with different mesh requirements. Moreover, for our particular case it was also necessary to define an internal subdomain with smaller elements than the required for the rest of the bulk domain. The requirement for the elements inside such subdomain was 1 μm as maximum element size. On the other hand, for the nanoelectrode subdomains, a convergence study was performed and a maximum element size of 25 nm was necessary to achieve a convergence better than 1%. So, the mesh is created sequentially, first nanoelectrode domains are meshed, then the internal subdomain, and finally the rest of the bulk domain. Those previous conditions were used in the definition of each disk nanoelectrode array presented in this chapter.

To obtain voltammogram which clearly shows the steady state achieved by the nanoelectrode array is necessary to solve the model using a transient solver and a tolerance of $1 \cdot 10^{-6}$ was always demanded.

In all cases, the diffusion coefficient used was $6.5 \cdot 10^{-10}$ m^{2}s^{-1}, corresponding to ferrocyanide in 0.1M KCl [12]. The simulated concentration of species O was 20mM in all cases to facilitate direct comparison with experimental data.
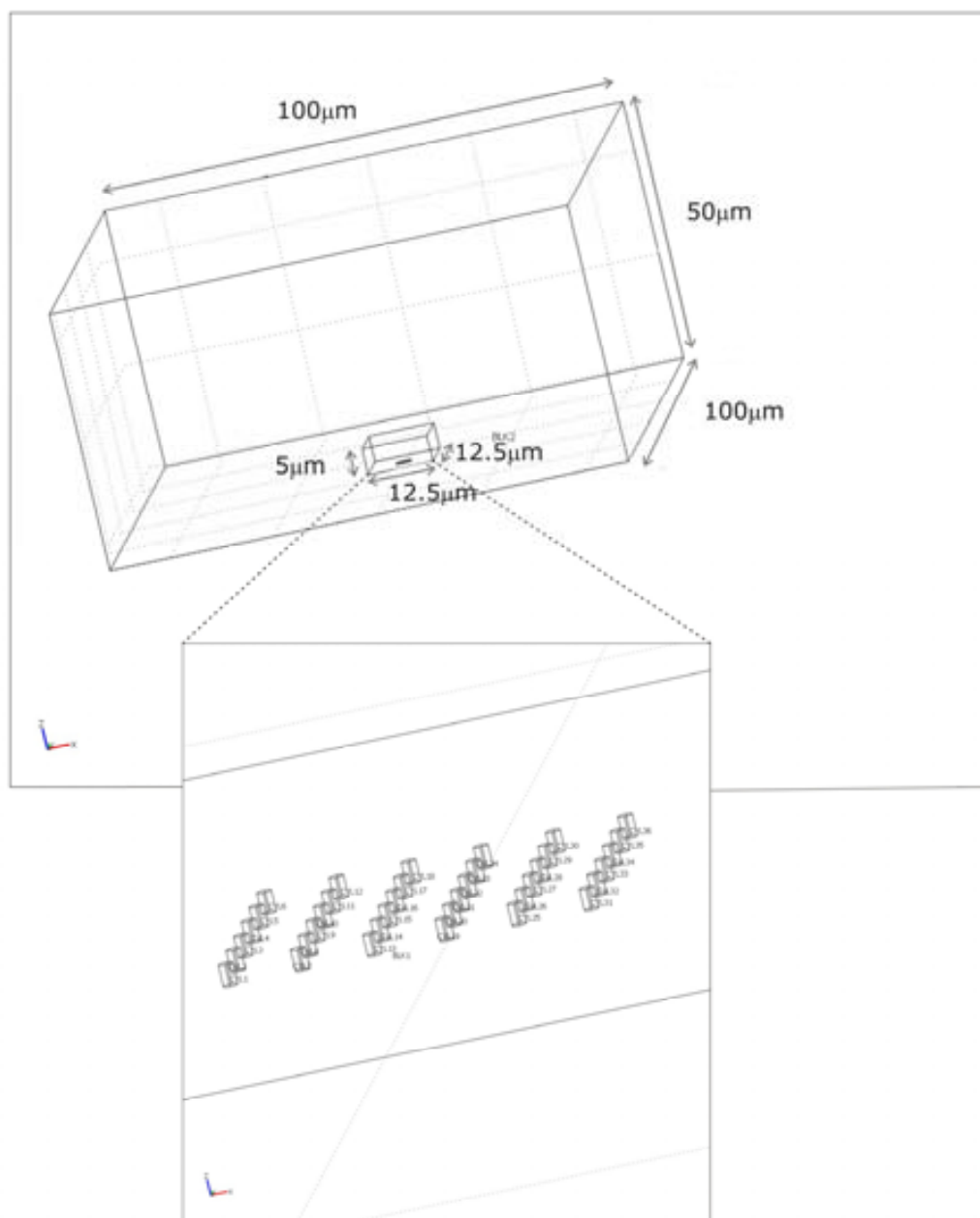

Figure 6-4: Diagrammatic scheme of the 3D disk nanoelectrode array domain.

Effect of scan rate

Figure 6-5 shows the results of two 6x6 nanoelectrode arrays with different intercenter distances, 250nm and 1.5µm, for scan rates ranging from 0.1 up to 5000 Vs^{-1}. As the scan

rate increased, the resulting currents for both distances seemed to converge. In other words, the nanoelectrodes in the array were gradually becoming diffusionally independent and hence closer to being equivalent to each other. The effect was more manifest with decreasing inter-nanoelectrode distance because overlapping of neighboring diffusion layers at low scan rates was more significant.

It is important to point out that for scan rates below $1Vs^{-1}$, where overlap of adjacent diffusion layers was complete, the current still presented stationary values and the voltammograms were sigmoidal, as shown in Figure 6-6. This result is in agreement with the experimental observations from other authors [1-3, 22-24], and differs from the typical behaviour that a microelectrode array would show. That is, when the diffusion layers of neighboring microelectrodes in an array overlap completely, the behaviour of the array becomes that of a macroelectrode and the voltammograms tail off due to planar diffusion. The low scan rate behaviour of nanoelectrode arrays, on the other hand, resembles that of a microelectrode.
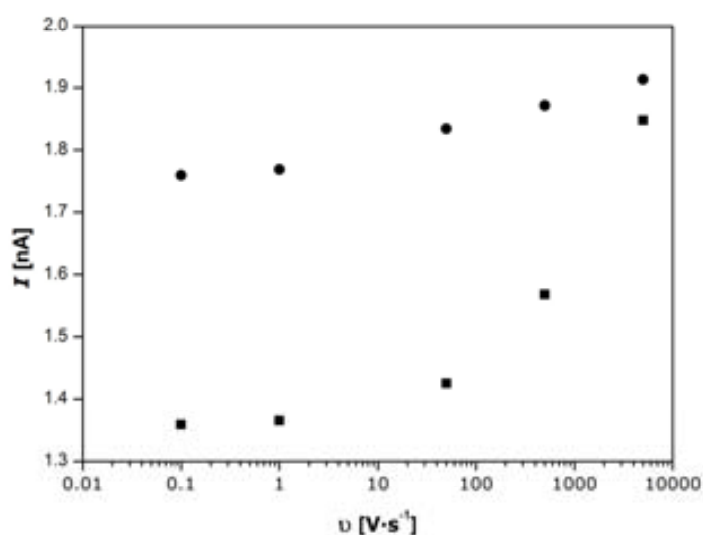
Figure 6-5: Simulation results for steady state current at (E-E^o)=-0.25V vs scan rate for a 6x6 nanodisks array of 50 nm of radius, 100 nm of recess and an intercenter distance of 1.5 μm (●) and 0.250 μm (■). In both cases [O] =20mM and D=6.5·10^{-10} m^2s^{-1}. A logarithmic axis is used in order to represent a wide range of scan rates.

Effect of nanoelectrode separation

The second parameter studied was the centre-to-centre distance between nanoelectrodes. The simulated results for a 6x6 nanoelectrode array at $1Vs^{-1}$ are showed in Figure 6-7. As the intercenter distance increases the steady state current is close to the theoretical current, equation (6.5) multiplied by the number of electrodes in the array (36 electrodes). This raises questions regarding the practical aspects of nanoelectrode array design: is it really necessary to ensure diffusional independence between nanoelectrodes? And, if so, are those nanoelectrode arrays still true nanometric devices? Taking our 6x6 nanoelectrode array, if diffusional independence was to be achieved at a scan rate of approximately $1Vs^{-1}$,

then the nanoelectrodes would have to be separated at least 3μm from each other -about 30 times their size!-. This would lead us to a device 18 x 18 μm, equivalent to an approximately 10 micron radius microelectrode, except for the fact that the current at the 10 micron radius electrode would be higher. Under these circumstances, nanoelectrode arrays should contribute with other advantages such as decreased capacitive currents and the possibility to work in even more resistive media than a conventional microelectrode, which might be of interest in fast voltammetry or *in-vivo* studies.
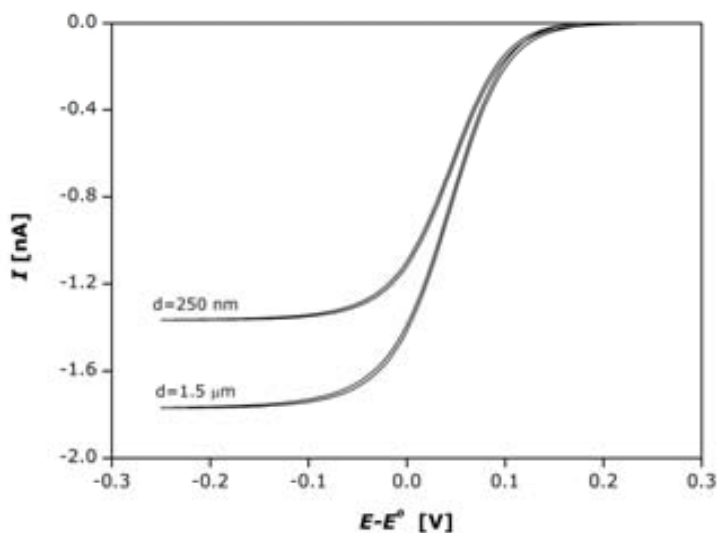
Figure 6-6: Simulated voltamograms at 1Vs^{-1} for a 6x6 nanodisks array of 50 nm of radius, 100 nm of recess and two intercenter distances (d): 1.5 μm and 0.250 μm. In both cases [O] =20mM and D=6.5·10^{-10}m^{2}s^{-1}.
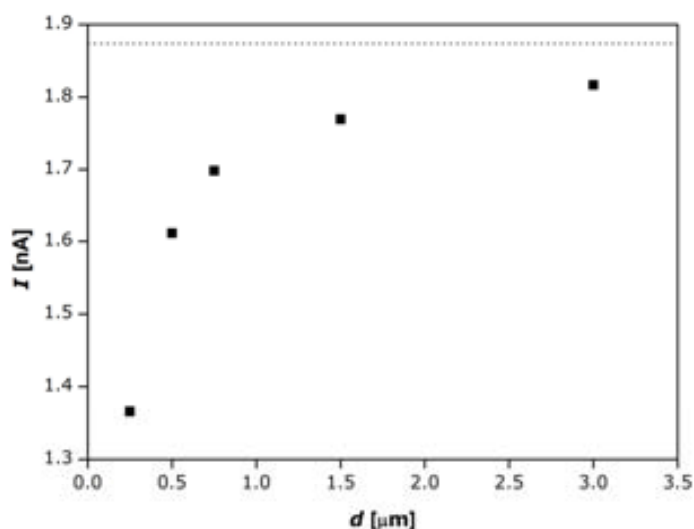
Figure 6-7: Simulation results for steady state current at (E-E_o)=-0.25V and 1 Vs^{-1} vs intercenter distance (d) for a 6x6 nanodisks array of 50 nm of radius and 100 nm of recess. In both cases [O] =20mM and D=6.5·10^{-10}m^{2}s^{-1}. The dotted line represents the theoretically expected current at an array of diffusionally independent nanoelectrodes as per equation (6.5)

Effect of nanoelectrode population

Finally, we considered nanoelectrode population as the last parameter affecting the behaviour of nanoelectrode arrays. Figure 6-8 shows the results for three different nanoelectrode arrays (3x3, 6x6 and 9x9) for scan rates ranging between 0.1 and 5000 Vs^{-1}.
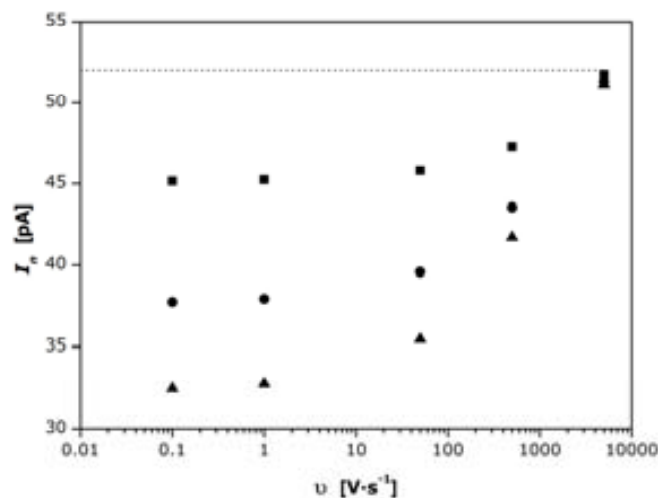

Figure 6-8: Simulation results for normalised steady state current at (E-E^o)=-0.25V vs scan rate for a 3x3 nanodisks array (■), 6x6 nanodisks array (●) and 9x9 nanodisks array (▲). It is normalised to the total number of electrodes per array. In all cases r= 50 nm, L=100 nm, d=250 nm, [O] =20mM and D=6.5·10^{-10}m^{2}s^{-1}.

For the sake of comparison, the simulated steady-state currents were normalised with respect to the number of electrodes in each array. These normalised currents were regarded as the average current observed by each nanoelectrode in the array. This is only an approximation because, as we showed earlier, the nanoelectrodes in an array are far from equivalent. Figure 6-8 also depicts, as a dotted line, the theoretical current for an infinitely isolated nanoelectrode of identical geometry, based on equation (6.5). It was found that the normalised current approached the theoretical value for the isolated electrode as the scan rate increased, independently from the number of electrodes integrating the array. These were obvious results that reminded of the behaviour of microelectrode arrays. As the scan rate increases, the degree of overlap between adjacent diffusion layers decreases and the current recorded by each nanoelectrode in the array approaches the theoretical response of a single nanoelectrode, regardless of the population size of the nanoelectrode array. At slow scan rates, on the other hand, the average current was found to depend heavily on the number of the nanoelectrodes in the array. The simulations showed that as the nanoelectrode population in an array increased, the average current per nanoelectrode decreased. This is also in line with the behaviour observed at microelectrode arrays; as the number of electrodes in an array increases, there are more electrodes at inner positions competing for the diffusing material. These inner positions are actually diffusionally

equivalent and the ones that we believe are successfully modelled by the diffusion domain approximation. The situation is different in the case of those electrodes located around the edges of the array. Not being completely surrounded by other electrodes, they face less competition for the diffusing species and hence they experience higher current densities than *inner* electrodes. The trend to observe less and less current (per nanoelectrode) as nanoelectrode population in the array increases also has a limit. Hypothetically, this limit is reached when the nanoelectrodes inside the array far outnumber perimetric ones.

6.4.3 Experimental results

The three kinds of nanoelectrode arrays described earlier in section 6.2.2 were used in cyclic voltammetry experiments to study their mass transport properties compared to microelectrode arrays. Also, the experimental results were of great help to validate our three-dimensional models. Nanoelectrode arrays presenting different inter-nanoelectrode separations and nanoelectrode populations were produced, and Table 6-1 provides a summary of their main geometric features, measured using by AFM. Figure 6-9 shows AFM pictures from two arrays presenting inter-nanoelectrode separations of 1.5 μm and 0.250 μm, respectively.
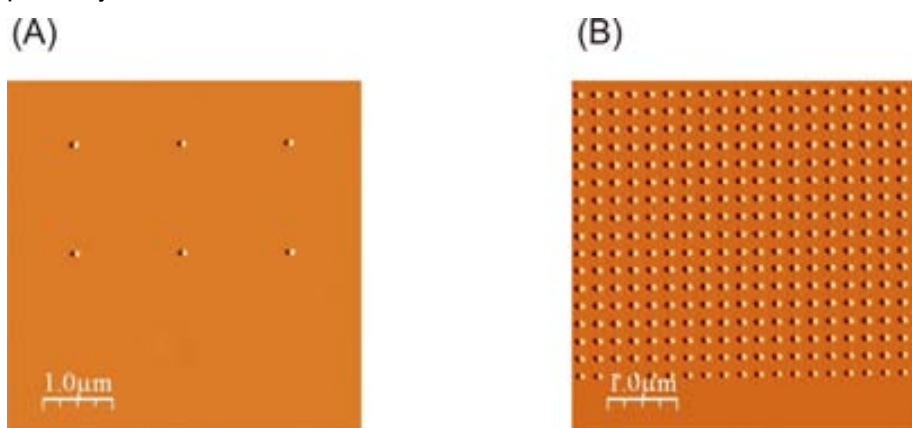

Figure 6-9: AFM image of an array of (A)1.5 μm and (B) 250 nm of intercenter distance.

Table 6-1: Geometric features for each array configuration. Errors are calculated based on 10 measurements.

Number of electrodes	6x6 array	31x31 array	61x61 array
Diameter / nm	114±8	133±8	180±14
Recess height/ nm	152±5	156±10	73±6
Intercenter distance	1.5 μm	250 nm	250 nm

Although the nanoelectrodes described in Table 6-1 present important differences in their size and recess height, they were of the same magnitude and could be qualitatively compared with the simulated currents reported in the previous section.

Figure 6-10 shows the voltamograms at 100mVs^{-1} for each array in a 20 mM ferrocyanide solution. It is remarkable that all voltamograms are sigmoidal and reach a steady-state current. This is so even for the densely populated arrays B and C, where the diffusion layers of the individual nanoelectrodes are certainly overlapping, and the number of inner nanoelectrodes (3721) is far greater than that of perimetric (240) nanoelectrodes for the 61x61 array. This clearly points to the importance of radial diffusion to these devices, likely explained by the overall size of the array, which occupies a 15x15 micron square area. This is roughly the area of a microelectrode of 8.5-micron radius.
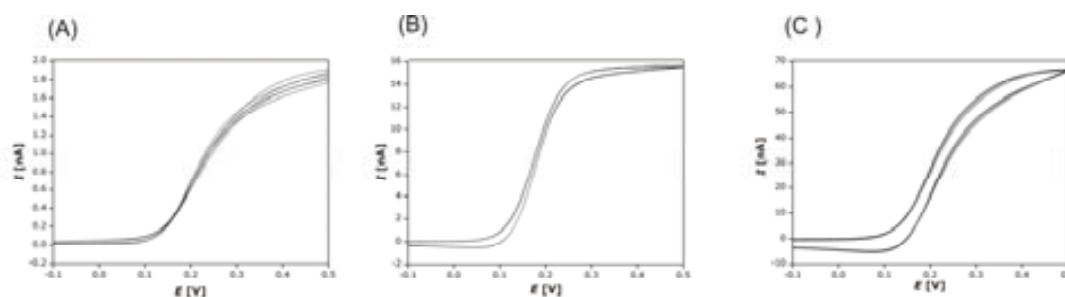

Figure 6-10: Experimental voltamograms for each array configuration at 100 mVs^{-1} in 20 mM ferrocyanide / 0.1 M KCl solutions   (A) 6x6 nanoarray, (B) 31x31 nanoarray and (C) 61x61 nanoarray. Three measurements are shown to demonstrate reproducibility.

We then took the data obtained from the 6x6 nanoelectrode array and compared them to our simulations. The other two arrays were too large and their simulation was abandoned because we were unable to solve models of that size.

Figure 6-5 shows the average steady-state currents per electrode, measured at different scan rates for a 3D-modelled 6x6 nanoelectrode array with an intercenter distance of 1.5 μm. At 100 mVs^{-1} the simulated current was 1.76 nA, which compared very favorably with an experimental value of 1.7±0.1 nA at the same scan rate.   This experimental value was obtained from triplicate measurements conducted at five different nanoelectrode arrays of this kind.

Figure 6-11 shows the experimental steady-state currents for the other two nanoarray configurations. Again, the data have been normalised with respect to the number of electrodes in each array. The figure shows that at higher scan rates the two sets of data deviate from each other, as each is affected to a different extent by capacitive currents. The more nanoelectrodes in the array, the higher its capacitive current will be. This was sistematically found when comparing the 61x61 array to the 31x31, even at the lowest scan rates. This can also be seen in Figure 6-10 C and B. Nevertheless, when we compared Figure 6-11 and Figure 6-8 we reached the following conclusions. First, the normalised current values at low scan rates are very similar in both arrays, around 15 nA and, as

expected, they are also considerably lower than the values obtained for the simulated arrays of 3x3, 6x6 and 9x9 (Figure 6-8). The coincidence in average current per nanoelectrode found for arrays 61x61 and 31x31 can be explained by the fact that in both cases there are many more inner nanoelectrodes than perimetric ones.

At higher scan rates, the shape of the experimental results followed the same trend as predicted by the simulations. This means that, as the scan rate increases, the individual diffusion layers overlap less and less until they eventually become independent from each other (Figure 6-8), and this upper limit may be estimated using equation (6.5)
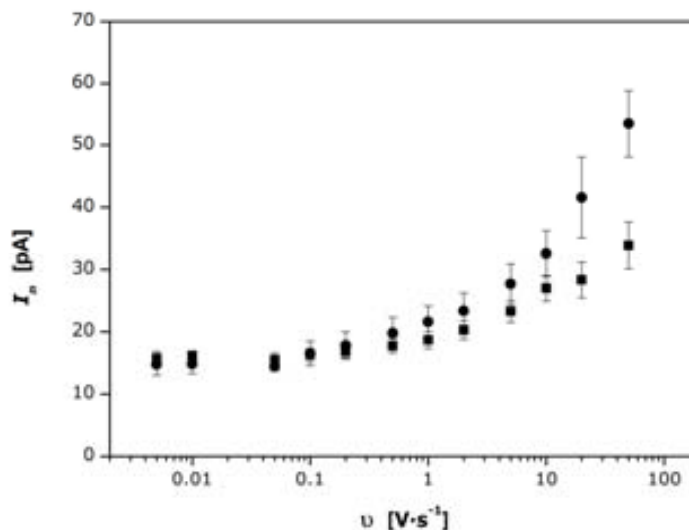

Figure 6-11: Experimental results for normalised steady state current at E=0V *vs* scan rate for a 31x31 nanodisks array (■) and 61x61 nanodisks array (●). It is normalised to the total number of electrodes per array. Concentration of ferrocyanide used is 20 mM. Error bars are calculated using 4 different nanoarrays for each configuration and measurements were done in triplicate for each scan rate.

Our experimental results are in high concordance with previous results published by several authors [1-3, 22-24]. In all these works the behaviour for the their nanoelectrode arrays was sigmoidal, even working at quite low scan rates. Furthermore, our experimental results also corroborated the modelled results described in the previous section.

6.5 Summary

We have shown that diffusion to nanoelectrode arrays depends very much on the size of the array. Thus, nanoelectrode arrays occupying areas of a few micron square observe steady state even if the diffusion layers of adjacent nanoelectrodes overlap completely. In this case, the magnitude of the observed current is expected to be slightly lower than that experienced by a microelectrode of comparable dimensions, which experiences radial diffusion when $Dt>r^2$.

This has important implications related to the design and characterisation of this kind of nanoelectrode-based devices. For example, theoretical paradigms that are valid to explain the behaviour of microelectrode arrays and nanopatterned macroelectrodes are very likely unsuitable for the study of nanoelectrode arrays. We have shown this using several two- and three-dimensional models together with recessed-nanoelectrode arrays fabricated by electron beam lithography.

We have shown the effect of inter-nanoelectrode spacing and also nanoelectrode population in different regular arrays arranged in a square lattice. The currents observed at nanoelectrode arrays seem to have an upper and a lower limit. Drawing an analogy to microelectrode arrays, the upper limit is reached at short operation times and corresponds to regimes i and ii. The lower current limit is reached for regime-iv, when the diffusion layers of adjacent nanoelectrodes are completely overlapped and the array effectively behaves as a microelectrode. This means that radial diffusion to nanoelectrode arrays is more important than in microelectrode arrays, and hence theoretical approaches that were valid for the latter may be no longer applicable to nanoelectrode arrays of micrometric size. If this is the case then new theoretical approaches are needed to model these devices and improve our understanding of them.

6.6 References

[1] Arrigan, D.W.M., *Nanoelectrodes, nanoelectrode arrays and their applications.* Analyst, 2004. 129(12): p. 1157-1165.

[2] Lanyon, Y.H. and D.W.M. Arrigan, *Recessed nanoband electrodes fabricated by focused ion beam milling.* Sensors and Actuators, B: Chemical, 2007. 121(1): p. 341-347.

[3] Lanyon, Y.H., G. De Marzi, Y.E. Watson, A.J. Quinn, J.P. Gleeson, G. Redmond, and D.W.M. Arrigan, *Fabrication of nanopore array electrodes by focused ion beam milling.* Analytical Chemistry, 2007. 79(8): p. 3048-3055.

[4] Zhang, B., Y. Zhang, and H.S. White, *The nanopore electrode.* Analytical Chemistry, 2004. 76: p. 6229-6238.

[5] Zhang, B., Y. Zhang, and H.S. White, *Steady-State Voltammetric Response of the nanopore Electrode.* Analytical Chemistry, 2006. 78(477-483).

[6] Murray, R.W., *Nanoelectrochemistry: Metal nanoparticles, nanoelectrodes, and nanopores.* Chemical Reviews, 2008. 108(7): p. 2688-2720.

[7] Davies, T.J. and R.G. Compton, *The cyclic and linear sweep voltammetry of regular and random arrays of microdisc electrodes: Theory.* Journal of Electroanalytical Chemistry, 2005. 585(1): p. 63-82.

[8] Davies, T.J., S. Ward-Jones, C.E. Banks, J. Del Campo, R. Mas, F.X. Muñoz, and R.G. Compton, *The cyclic and linear sweep voltammetry of regular arrays of microdisc electrodes: Fitting of experimental data.* Journal of Electroanalytical Chemistry, 2005. 585(1): p. 51-62.

[9] Bushan, B., ed. *Handbook of Nanotechnology.* 2nd ed. 2007.

[10] Compton, R.G., G.G. Wildgoose, N.V. Rees, I. Streeter, and R. Baron, *Design, fabrication, characterisation and application of nanoelectrode arrays.* Chemical Physics Letters, 2008. 459: p. 1-17.

[11] Horcas, I., R. Fernández, J.M. Gómez-Rodríguez, J. Colchero, J. Gómez-Herrero, and A.M. Baro, *WSXM: A software for scanning probe microscopy and a tool for nanotechnology.* Review of Scientific Instruments, 2007. 78(1).

[12] Allen J. Bard, L.R.F., *ELECTROCHEMICAL METHODS. Fundamentals and Applications.* 2nd ed. 2001, New York: John Wiley & sons.

[13] Scholz, F., ed. *Electroanalytical Methods: Guide to Experiments and Applications.* 2002, Springer.

[14] Wang, J., *Analytical Electrochemistry.* Second Edition ed. 2000: Wiley-VCH.

[15] Bartlett, P.N. and S.L. Taylor, *An accurate microdisc simulation model for recessed microdisc electrodes.* Journal of Electroanalytical Chemistry, 1998. 453(1-2): p. 49-60.

[16] Galceran, J., S.L. Taylor, and P.N. Bartlett, *Steady-state currents at inlaid and recessed microdisc electrodes for first-order EC' reactions.* Journal of Electroanalytical Chemistry 1999. 476(2): p. 132-147.

[17] Bond, A.M., D. Luscombe, K.B. Oldham, and C.G. Zoski, *A comparison of the chronoamperometric response at inlaid and recessed disc microelectrodes.* Journal of Electroanalytical Chemistry, 1988. 249(1-2): p. 1-14.

[18] Amatore, C., J.M. Saveant, and D. Tessier, *Charge transfer at partially blocked surfaces: A model for the case of microscopic active and inactive sites.* Journal of Electroanalytical Chemistry, 1983. 147(1-2): p. 39-51.

[19] Ordeig, O., C.E. Banks, T.J. Davies, J.d. Campo, F.X. Muñoz, and R.G. Compton, *The linear sweep voltammetry of random arrays of microdisc electrodes: Fitting of experimental data.* Journal of Electroanalytical Chemistry, 2006. 592(2): p. 126-130.

[20] Davies, T.J., C.E. Banks, and R.G. Compton, *Voltammetry at spatially heterogeneous electrodes.* Journal of Solid State Electrochemistry, 2005. 9(12): p. 797-808.

[21] Davies, T.J., R.R. Moore, C.E. Banks, and R.G. Compton, *The cyclic voltammetric response of electrochemically heterogeneous surfaces.* Journal of Electroanalytical Chemistry, 2004. 574(1): p. 123-152.

[22] Baker, W.S. and R.M. Crooks, *Independent geometrical and electrochemical characterization of arrays of nanometer-scale electrodes.* Journal of Physical Chemistry B, 1998. 102(49): p. 10041-10046.

[23] Ito, T., A.A. Audi, and G.P. Dible, *Electrochemical characterization of recessed nanodisk-array electrodes prepared from track-etched membranes.* Analytical Chemistry, 2006. 78(19): p. 7048-7053.

[24] Sandison, M.E. and J.M. Cooper, *Nanofabrication of electrode arrays by electron-beam and nanoimprint lithographies.* Lab on a Chip - Miniaturisation for Chemistry and Biology, 2006. 6(8): p. 1020-1025.

CHAPTER 7:

Modular microfluidic system

Integration of electrochemical detection in a microfluidic device is one of the objectives of this thesis. The interest of microfluidic devices lies in their high degree of integration, portability, minimal reagent consumption, high performance, and speed compared to conventional methods.

In this chapter we present the fabrication and characterisation of a versatile lab on a chip system that combines magnetic capture and electrochemical detection. Particles are captured upstream from the detector and we demonstrate how to take further advantage of the system fluidics to determine enzyme activities or concentrations, as flow velocity can be adjusted to the rate of the reactions under study. Moreover, simulations of the system were also performed helping us to understand how the different mechanisms involved affect the detection, and to increase sensitivity.

The design and fabrication of the system was carried out during a stay at the Department of Micro and Nanotechnology (DTU-Nanotech) of the Technical University of Denmark.

7.1 Introduction

Magnetic particles and amperometry have been combined in the past for (bio)electroanalytical purposes [1-6] and several literature reports describe systems where particles are directly immobilised on a channel wall opposite the electrodes [1, 2]. Choi and co-workers used interdigitated microelectrode structures operated under generator-collector mode in an example close to our approach [1]. More recently, a system was reported where the magnetic particles are elegantly immobilised by means of an array of NiFe permalloy blocks [2]. However, we believe that the overall performance of those systems may improve if the magnetic particles are captured upstream from the electrodes and not opposite them. This modification would take full advantage of the system microfluidics, which provides controlled and well-defined mass transport conditions leading to higher steady state currents. Amperometry is a relatively simple but very important detection technique in lab-on-a-chip devices because currents recorded in channel electrodes [7, 8] under laminar flow are directly proportional to analyte concentration [9-13]. The main advantages of this system are its re-usability and that its configuration can be changed easily so the user can try several electrode configurations with the same holder. Moreover, because the functionalised beads are magnetically captured upstream from the electrodes, the user can adjust the fluid flow rate to the kinetic parameters of the chemical reactions under study to optimise detection. Later, the magnetic particles are released blocking the magnetic field. This is easy to

achieve sliding a thin soft-iron piece between the magnets and the chip, and flushing a buffer solution through the system.

We are presenting a versatile lab-on-a-chip that can be used in a broad range of (bio)electroanalytical assays. It is also important to point out that this system does not require wire bonding nor resin based encapsulation as it was mentioned in Chapter 3, thus eliminating two of the most important sources of cost in traditional microsystems. The system avoids these burdens thanks to its modular construction consisting of the following three main parts, which will be further described below: (i) a demountable rigid plastic body, (ii) a soft PDMS gasket that simultaneously provides the microfluidic channel and sealing and (iii) a silicon chip featuring a set of microelectrodes that are connected using spring-loaded pins.

The present system has been designed to develop electrochemical immunoassays, [12, 14] and can perform two different operations: the capture of magnetic beads, including the mixing of different solutions, and the electrochemical detection of species present in solution. Note, that there are variations to the way the system may be operated, particularly during the sample extraction and labelling stages, but broadly the system works as follows: after extracting an enzyme-labelled analyte from a sample using suitably functionalised magnetic particles, these are injected by a syringe pump into the capture chamber moulded in the PDMS gasket. There, the strong magnetic field exerted by two permanent magnets captures and spreads them over the side of the chip upstream from the microelectrodes. Next, a solution containing a non-electroactive enzyme substrate is pushed through the system, at a flow rate chosen to take advantage of the prevailing reaction kinetics. The electroactive enzymatic product is then detected downstream at the electrodes before the solution leaves the system. On the other hand, thanks to the complete absence of wire bonds or encapsulating resin in the system, the chip can easily be replaced if the electrodes become irreversibly damaged.

We demonstrate the operation of our cell using streptavidin coated magnetic beads and a biotinylated β-galactosidase as model system. To enable electrochemical detection, we use 4-aminophenyl-β-D-galactopiranoside, PAPGP, as the enzyme substrate because it yields p-aminophenol, PAP, a well known reversible electroactive species that is readily oxidised at a mild potential of 0.25 V vs. Ag/AgCl [2, 14-19]. We also use finite element methods to aid in the characterisation of the system and to interpret the enzyme kinetics from measured transient currents [20].

7.2 Experimental

7.2.1 System Fabrication and Characterisation

Holder fabrication

The system holder consists of three parts: The top part was made in polymethylmethacrylate (PMMA) and the bottom in polycarbonate (PC). The middle part was a polydimethylsiloxane (PDMS) inlay as shown in Figure 7-1. This PDMS part provided watertight sealing and contained all the microfluidic features of the system. Direct micromilling [21] and casting were used to define the various geometric features of the three parts.
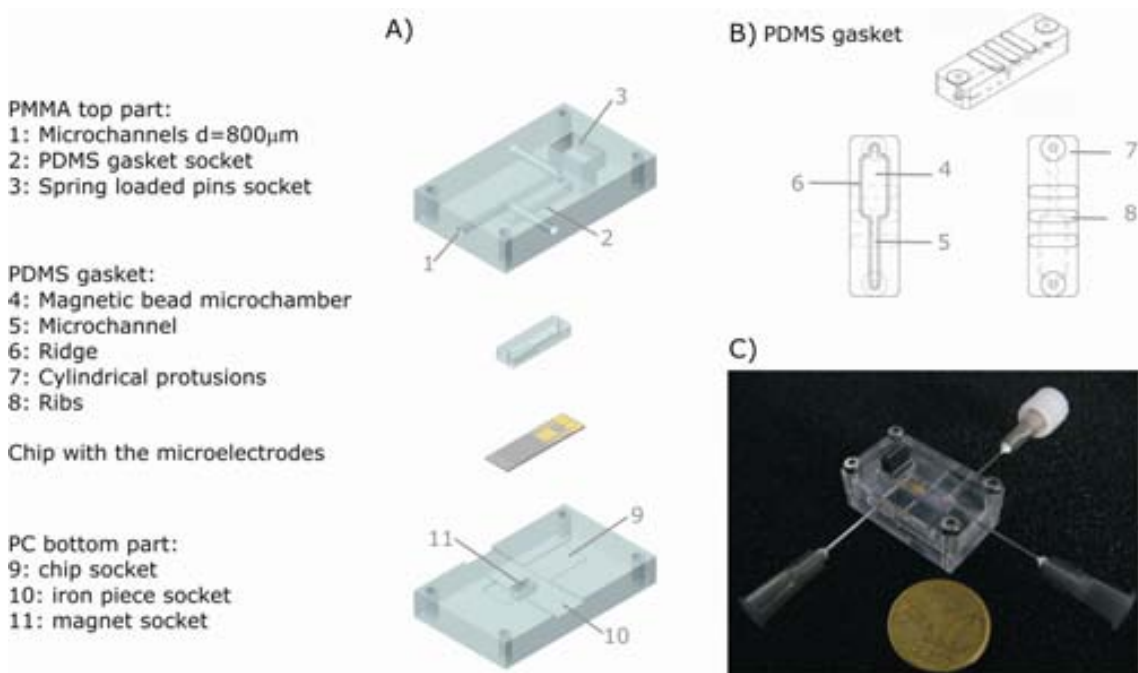
Figure 7-1: A) 3D Schematic representation of the system assembly (to scale). The top part is made in PMMA; a PDMS gasket contains the microfluidics and provides sealing against a chip featuring a set of microband electrodes; the chip base is made in PC. B) Three different perspectives of PDMS gasket: general, bottom and top C) Photograph of the system.

The top part features the fluidic interconnections and a pocket for the PDMS inlay. Short pieces of silicone tubing (about 5mm long, 0.8mm OD) were inserted in the channels to seal the fluidic connections water-tight. The solutions are fed in and out of the system through blunt syringe needles with an outer diameter slightly larger than the inner diameter of the silicone tubing. Thus, when the needles are inserted, they push the silicone tubing against the PMMA holder and a tight seal is achieved. The round cross-section of the channels in the PMMA substrate was achieved by structuring two PMMA sheets (3mm thick) using a 0.8mm ball-end milling tool and subsequent UV-assisted thermal bonding [22, 23]. Finally,

spring-loaded pins (Preci-dip, Switzerland) were locked into holes, drilled through both PMMA layers, to provide electrical connections to the chip.

The gasket was fabricated by micromiling a PMMA mould and subsequent casting of PDMS [24, 25]. It contained all microfluidic features, consisting of a cavity 2 mm wide, 150 μm high and 5 mm long joined to a channel 500 μm wide and of the same height that leads the solution out of the system after passing over the detector. The cell was designed so that the wide part of the channel sat on the chip directly above the permanent magnets where magnetic beads would be captured. Downstream, the length of the electrodes was controlled by the width of the 500 μm exit channel. A series of special features moulded on the top and bottom faces of the PDMS piece improved the sealing. Three centred ribs 4 mm wide, 1 mm long and 150 μm high were built on the top face to distribute the pressure evenly over the gasket, and a ridge 200 μm wide and 80 μm high, protruding out the bottom side of the PDMS around the chamber and the microchannel, improved the sealing against the chip; these features reduced the required clamping force and thereby the risk of channel deformation.

The bottom part contains two pockets for housing the chip and two magnets as well as a notch that allows sliding a metal piece between the magnets and the chip. Two Nd-Fe-B permanent magnets (Lika, Denmark, 2x2x2 mm^3) were inserted into the pocket, with opposite vertical polarisation, to maximise the magnetic force on the beads in the channel [26]. The purpose of the iron piece (500 μm thick) was to shield the chip from the magnetic field and hence release the beads held inside the microchannel. This allowed performing consecutive experiments without altering the geometric features of the system, and improved the reproducibility of the measurements.

The purpose behind using a PDMS inlay in combination with a rigid holder was to have a permanent piece of hardware that could perform different operations depending on the geometry of this PDMS gasket; in this particular case this meant magnetic bead capture followed by electrochemical detection. Other possibilities include filtration, ion exchange or solid phase extraction operations, to name but three.

Chip design and fabrication

The electrode chip design consists of 4 microbands, 3 bands of 500 μm widths and 1 band of 1 mm width, separated by 100 μm gaps. The wider band is intended for use as counter electrode while the remaining three bands may be used as working or pseudo-reference electrode in any combination. However, to avoid potential shifts during measurements, the first band upstream was used as the reference electrode. The main fabrication steps are showed in Figure 7-2. A 4" diameter n-type (phosphorus doped) silicon wafer is used as a susbstrate (Figure 7-2(1)). The silicon wafer is oxide (1 μm thermal oxide layer) to provide electrical insulation between the silicon and the metal layers (Figure 7-2(2)). In that case the microelectrodes are defined by lift-off, so a photolithography step is previous to the metal deposition (Figure 7-2(3)). Here we used an image reversal resist (AZ5214E) to obtain

negative resist sidewalls using a positive resist which is cheaper, less susceptible to ageing, and prone to yield steep sidewalls. The resist is spun (1.5 μm) and it is first irradiated by UV-light through a clear field mask. Before development, a flood exposure is performed. After development the resist presents a profile as showed in Figure 7-2(4), such profile reduces the coverage of coated film onto the resist sidewalls and enhance to remove the resist in the stripping process. The metal deposition consists in a 50nm adhesion layer of Ti and a 200nm layer of Au (Figure 7-2(4)) and they are sequentially deposited by evaporation. later, the remaining resist under the metal is removed, finishing the lift-off process (Figure 7-2(5)) and finally, a thin layer of resist is spin coated over the wafer to protect the chips during wafer dicing.
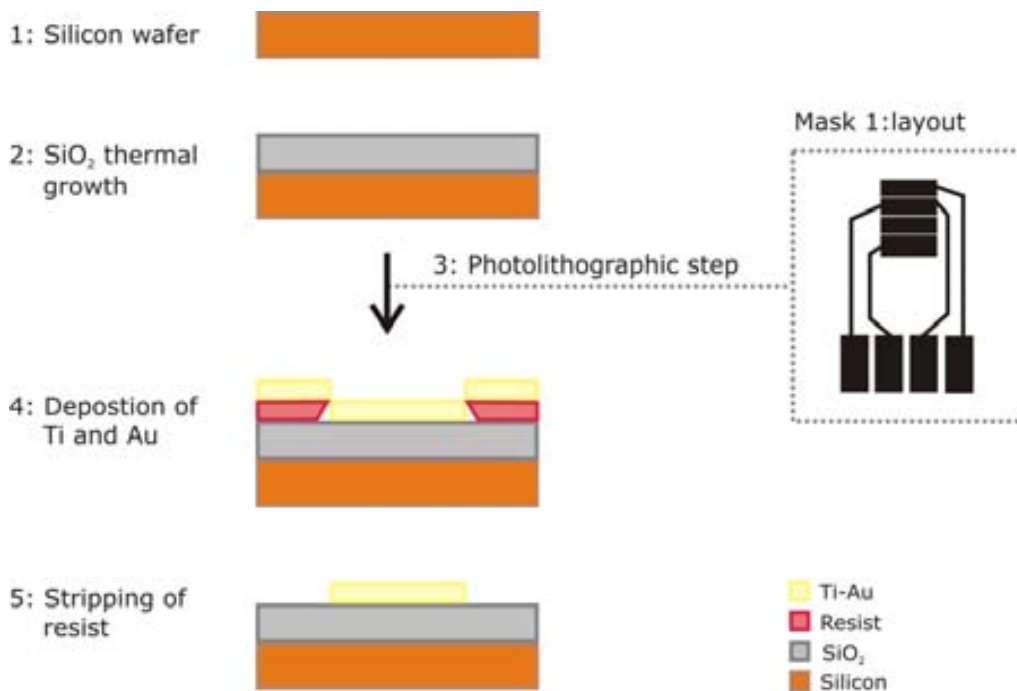
Figure 7-2: Microfabrication steps of band microelectrodes.

7.2.2 Chemicals and instrumentation

KCl (99%), KNO_3 (99%), $K_4Fe(CN)_6 \cdot 3H_2O$ (99%), p-aminophenol, N,N-Dimethylformamide, DMF (99.8%, spectrophotometric grade) were purchased from Sigma-Aldrich. All chemicals were ACS analytical grade and were used as received without any further purification. Aqueous solutions were prepared using pure de-ionised water (18MΩ·cm). Buffer Z was prepared using commercial PBS tablets (Invitrogen) reaching a 0.1 M concentration and adding 1 mM $MgSO_4$ and 20 mM KCl.

The magnetic beads were streptavidin coated Dynabead ® MyOne (Invitrogen), 1μm diameter (3.14 μm^2). Their nominal binding capacity is 20μg protein per mg of beads. The interbead volume once inserted and immobilised on the system, assuming a monolayer of particles packed evenly over the surface of the reaction chamber, is approximately 0.48 nL (note that the total volume in the capture chamber is 150 nL). All electrochemical

measurements were performed using a three-electrode configuration and a CHI700C bipotentiostat (CH Instruments, Texas, USA) connected to a PC. All electrodes were made in gold, including the pseudo-reference electrode, and were integrated on the same silicon chip. The flow was controlled using a syringe pump, NE1000 (New Era Pump Systems, NY). The electrodes were occasionally passivated from prolonged operation in p-aminophenol solutions. In those cases the electrodes were removed and cleaned by rinsing the chip in DMF [27], or directly replaced by new ones.

7.2.3 Bead functionalisation

Magnetic beads were functionalised outside the device following a protocol described elsewhere [28]. Briefly, a 40 μL volume of streptavidin-coated beads (10 mg·mL^{-1}), 1 μm in diameter, was first rinsed several times using buffer Z. Next, 150 μL of buffer and 10 μL of 1mg·mL^{-1} biotinylated β-galactosidase were added, and the solution was stirred for 30 minutes at room temperature. The excess enzyme physisorbed on the beads was removed in a new wash. The functionalised magnetic beads solution was diluted to a concentration of 3.33 mg·mL^{-1}.

7.2.4 Operation of the system

The working principle of our system is as follows: first, a given volume of functionalised beads containing the labelled target is captured inside the microfluidic holder by permanent magnets. Then, a solution containing the substrate is introduced in the channel and the product of the enzyme reaction is electrochemically detected downstream using a microband electrode under controlled-flow conditions. The capture of the target and the necessary incubations are physically separated from the electrochemical detector. The magnetics beads are easily released by blocking the magnetic field with a thin iron slab between the magnets and the chip. This allows carrying out several measurements sequentially without changing any geometrical features and increasing reproducibility.

7.2.5 Set-up

Working with microfluidic devices requires a dedicated set up. Air bubbles inside the device, for instance, may affect the fluid flow, due to compliance effects, as well as the measurement itself. Hence, it is important to avoid trapping air during the filling procedure and ensure a gas tight set-up. Before the experiments, the entire system was flushed with liquid through all inlets Figure 7-3 shows the set up used in our experiments. Needles were inserted, as previously mentioned, allowing direct connection to syringes. In our case, three different inputs were needed corresponding with the three reagent solutions used: magnetic beads, substrate and buffer Z. As the holder provides only two inlets, a 3-port valve was used to connect two syringes to one of the inlets. This way, it is possible to switch between two reagents without the need to change a syringe, and thereby reducing the probability injecting air into the system. The disadvantage of this method is an increase of dead volume. The

volume added to the system by the 3-port valve was experimentally measured and to be approximately 120 μL. Duringthe experiments, only one syringe pump was available. Therefore, the different syringes were sequentially placed on the pump corresponding to the reagent needed for the measurement.
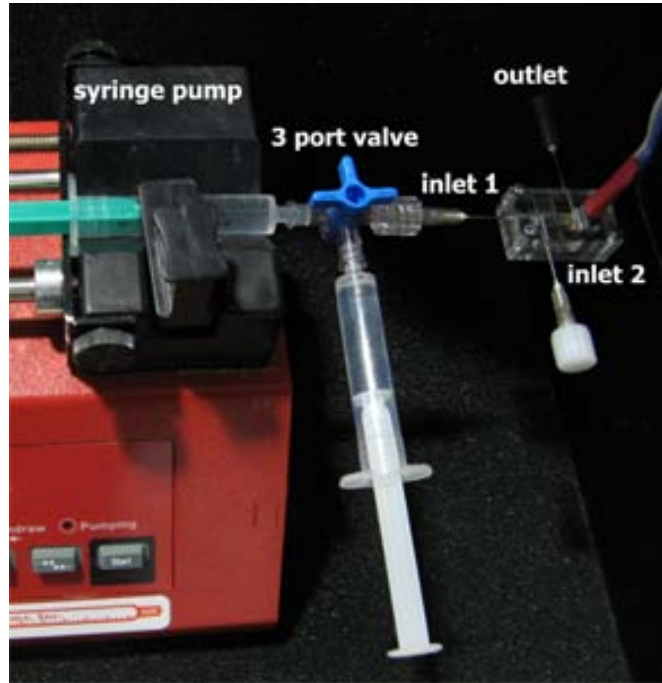

Figure 7-3: Picture of the set-up used. Inlet 1 is connecto to 3 port valve. Microbeads solution is always injected by inlet 2, although this syringe is not showed in the picture.

7.3 Theory

The sequence of operation in the system can be divided in three steps: (i) magnetic bead capture, (ii) enzymatic reaction and (iii) amperometric detection. This section describes the simulation of the detection, as the principles underpinning movement and capture of magnetic beads are out of the scope of this work and it was widely described by Hansen and co-workers in [26, 29, 30].

The model is summarised in Figure 7-4 and it is based on the model presented in Chapter 4 for a microband placed on a microfluidic channel. Fluid flow is described by the steady-state Navier-Stokes equations for an incompressible Newtonian fluid:

$$\rho\left(\vec{v}\cdot\nabla\right)\vec{v} - \eta\nabla^2\vec{v} + \nabla p = 0 \tag{7.1}$$

$$\nabla\cdot\vec{v} = 0 \tag{7.2}$$

where ρ and η are the density and the viscosity of the fluid, $\vec{v}$ is the velocity vector and p is the pressure, and the mass transport of species within the channel is defined by convection and diffusion

$$\frac{\partial c_i}{\partial t} = D_i \nabla^2 c_i - \vec{v} \cdot \nabla c_i \qquad (7.3)$$

where c_i is the concentration and D_i is the diffusion coefficient of each species involved. The special feature of this model, compared with the one presented in Chapter 4, is the enzyme reaction that takes place in the reaction/capture chamber upstream from the detection. For the sake of simplicity, the captured magnetic beads are represented in our model by a boundary where the mass flux is controlled by the enzyme reaction, as shown in Figure 7-4. The reaction between 4-aminophenyl-β-D-galactopyranoside (PAPGP) and β-galactosidase (βGAL) produces p-aminophenol (PAP) as summarised in the following scheme:

PAPGP   galactose   p-aminophenol
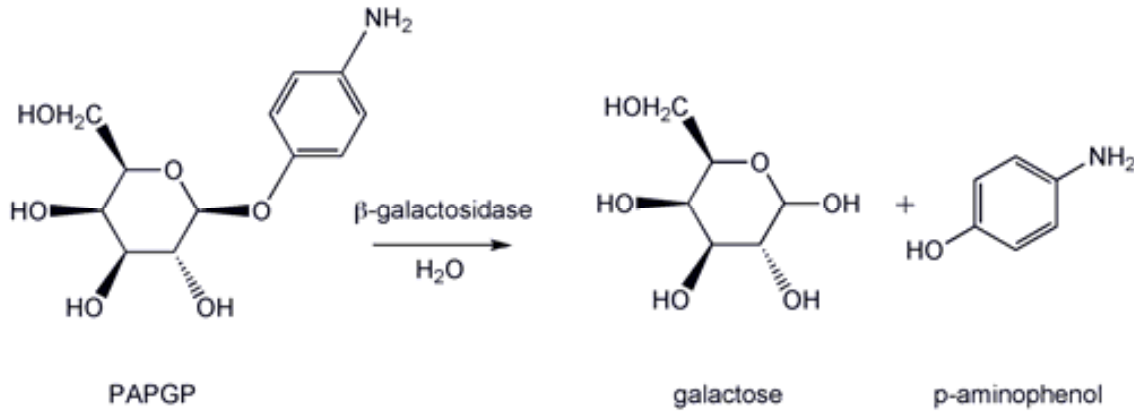
Reaction scheme 1

A Michaelis-Menten type mechanism [31] is assumed to govern the kinetics of this reaction:

$$E + S \underset{k_{-1}}{\overset{k_1}{\rightleftharpoons}} ES \xrightarrow{k_{cat}} P + E \qquad (7.4)$$
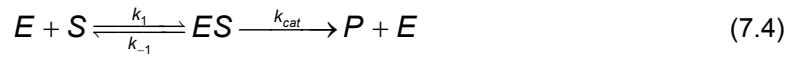
Therefore, the activity of the β-galactosidase immobilised on the beads is described by:

$$\frac{\partial [S]}{\partial t} = -k_{cat} \left[E_{\beta GAL} \right] \frac{[S]}{K_m + [S]} \qquad (7.5)$$

where [S] is the concentration of PAPGP, [E$_{\beta GAL}$] is the enzyme concentration linked to the beads, and k_{cat} is the turn over number in s^{-1} and K_m is the Michaelis Menten constant in mol L^{-1}.

At the electrode, we consider the two-electron oxidation of PAP to p-iminoquinone (PIQ) as:
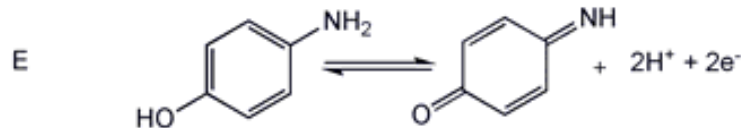
Reaction scheme 2.

We assume infinitely fast electrode kinetics such that the current is limited by diffusion [32] and described by the following integral:

$$I = nFD_{PAP}w \int_0^{x_e} \left. \frac{\partial [PAP]}{\partial y} \right|_{y=0} dx \qquad (7.6)$$

where D_{PAP} is the diffusion coefficient of PAP, [PAP] is the concentration of p-aminophenol, n is the number of exchanged electrons, F is the Faraday constant, w is the width, and x_e is the length of the microband electrode.
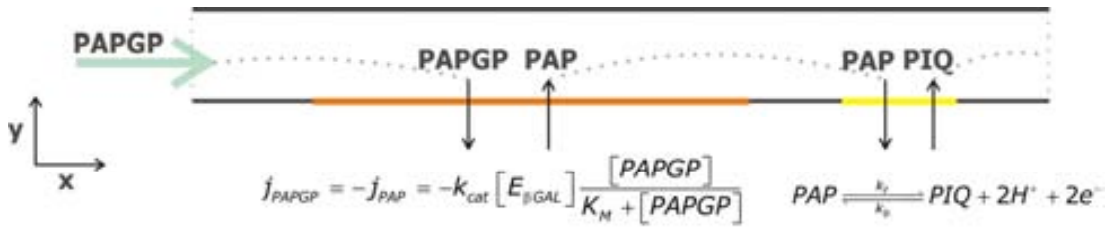

Figure 7-4: Schematic representation of the model. 2-dimensional section of the microchannel (not to scale). The enzyme activity over the surface of immobilised beads is considered as a flux boundary condition.

7.3.1 Electrochemical detection

The mass transport rates inside the cell were investigated by cyclic voltammetry using equimolar solutions of ferro/ferricyanide. Figure 7-5A shows typical cyclic voltammograms (CVs) obtained at 50 mVs^{-1} for flow rates of 2 and 10 μL min^{-1}, respectively. The fact that the voltammetric waves are centred around 0V is due to the potential of the gold pseudo-reference employed.

The electrodes were always electrochemically activated prior to any measurements. This activation step consisted in the application of a series of 10s potential pulses, alternating between -1V and 0V in a 0.5 M KNO$_3$ electrolyte solution.

The current measured by a microband band inside a microfluidic channel is described by [33]:

$$I = 0.925 nFcw \left(x_e D \right)^{2/3} \left(\frac{Q}{h^2 d} \right)^{1/3} \tag{7.7}$$

where h is half of the height of the microchannel and Q is the (volumetric) flow rate. c is the concentration of the electroactive species and, for ferro/ferricyanide, D is $6.5 \cdot 10^{-10}$ m^{2}s^{-1} [32].

One of the most important features of the system is its simplicity and reproducibility, so that the microfluidic cell is easily opened and closed to clean or replace the chip inside it. According to equation (7.7), channel geometry has a direct effect on the faradaic current, so the PDMS gasket was specially designed to minimise variability in channel height due to compression of the PDMS when the system is closed. This particular design facilitated an even distribution of the pressure over the entire channel and kept the height variation over the channel within a narrow tolerance.

We thoroughly tested our system by repeatedly opening and closing the cell; we used different gaskets, and recorded CVs at a range of fluid flow rates. Figure 7-5B shows that the system behaved in agreement with equation (7.7) within the chosen range of flow rates. The current residual standard deviation (RSD) in ferrocyanide value was systematically better than (below) 3%. Steady state currents, measured in ferro/ferricyanide solutions, were used

in combination with equation (7.7) to calibrate the actual geometry of the channel prior to further studies. Figure 7-5B also shows the theoretical steady state currents according to equation (7.7) for a microchannel of height $105\pm5\mu m$. This 5 μm interval corresponds to a 3% change in the measured current only, and we relied on this approach to calibrate our system.
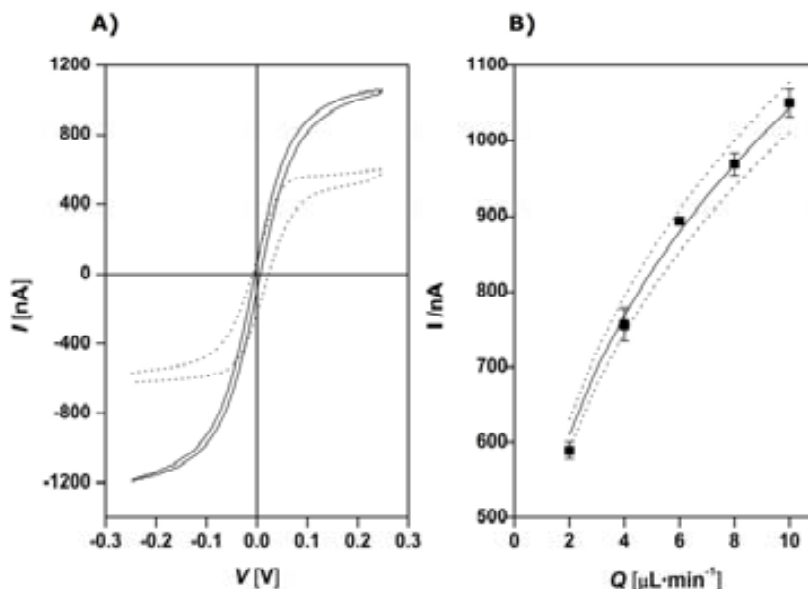

Figure 7-5: A) Cyclic voltammograms for 1mM equimolar solutions of ferro/ferricyanide at 50 mVs^{-1} at 2 (···) and 10 μL min^{-1}(—); the potential was measured vs. a Au pseudo-reference electrode. B) Steady state currents for 1mM equimolar solutions of ferro/ferricyanide at 50 mVs^{-1} for different flow rates: experimental (■), theoretical response for a 105 μm channel height (—) and for deviations of ±5 μm (···) error bars based on 6 measurements. RSD is below 3%.

In addition, cyclic voltammetry of known ferro/ferricyanide concentrations was also used to check the working condition of the system between experiments.

7.3.2 Concentration of β-galactosidase linked to the beads

We have chosen the enzyme β-galactosidase as model system to demonstrate the capabilities of our microfluidic cell because of the availability of a substrate (4-aminophenyl-β-D-galactopiranoside) yielding p-aminophenol, a small electroactive molecule which electrochemistry has been extensively described in the literature [15, 32]. Since we are conjugating this enzyme to the surface of magnetic beads, it is important to know the final enzyme concentration present. The oxidation potentials of the substrate (>0.3 V vs. Au pseudo-reference) and p-aminophenol (>0.1 V vs. Au pseudo-reference) were checked to ensure that the current measured in subsequent experiments at 0.25V vs. Au pseudo-reference was due to the oxidation of p-aminophenol only.

We first determined the activity of known concentrations of the enzyme in solution (500 ng·mL^{-1}, 1mg·mL^{-1}, 4.5mg·mL^{-1} and 8.35mg·mL^{-1}) at different flow rates (1μL·min^{-1}, 5μL·min^{-1}

and 10μL·min^{-1}). Each enzyme concentration was incubated with 1mM substrate solutions for 30 min in order to have a measurable amount of p-aminophenol. The results are shown in Figure 7-6. Fitting a logarithmic function between the measured current and the enzyme concentration for each flow rate, it is possible to find a relation as follows:

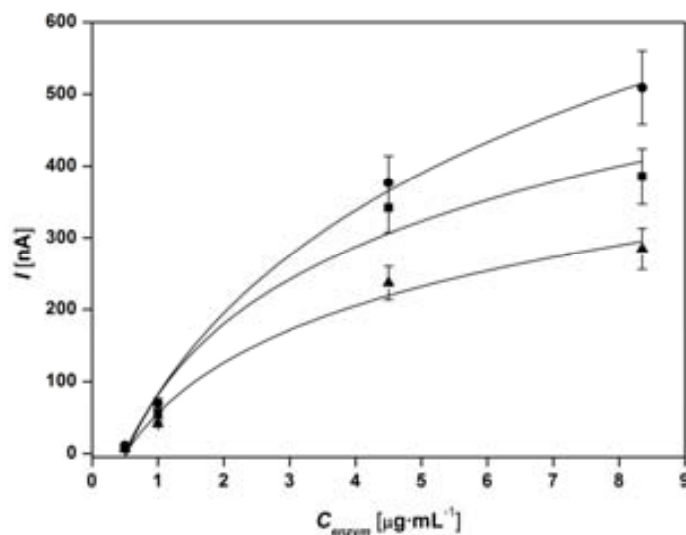$$I_{measured} = A + B\ln(c_{enzyme} + C) \qquad (7.8)$$

Figure 7-6: Steady state currents at different enzyme concentrations at 1μL·min^{-1}(▲), 5μL·min^{-1}(■) and 10μL·min^{-1}(●). Each enzyme concentration was incubated with 1mM substrate for 30 min prior to measuring at 0.25V vs. Au (pseudo-reference). Error bars are calculated as 10% of the current value

Once the relation between the measured current and the enzyme concentration in solution is known, the equivalent enzyme concentration on the beads is estimated measuring the current and calculating the enzyme concentration using the logarithmic fitting. Therefore, we performed an analogous experiment only substituting the enzyme solutions for suspensions of enzyme modified beads at different dilution levels. These dilution levels, relative to the original bead suspension, were 1:120, 1:240 and 1:480. Aggregation and deposition of the beads was avoided by vigorous stirring of the suspensions prior to their injection into the system. The current was measured under the same potential and flow conditions as in the previous experiment.

The resulting estimation of the enzyme concentration on the beads can be found in Table 7-1. This table also shows the maximum concentration of enzyme possible according to the beads manufacturer's specifications and the molecular weight of β-galactosidase (MW=465412 Dalton). In principle, the initial concentration of beads is 10 mg·mL^{-1} and the maximum concentration of protein that could be linked to them is *ca.* 20 μg$_{protein}$·mg$^{-1}_{bead}$. Therefore, a rough approximation for the maximum concentration of β-galactosidase linked to the beads is around 620μg·mL^{-1} and the estimation of the maximum concentration for

each dilution is obvious. The experimental concentration is calculated averaging the value for 1 μL·min^{-1}, 5 μL·min^{-1} and 10 μL·min^{-1}. For each dilution, the experimentally obtained enzyme concentration seems highly plausible.

Table 7-1: Experimental enzyme concentrations vs. maximum possible concentration in a bead suspension according to the beads manufacturer's specifications. The percentage corresponds to actual enzyme load with respect to the maximum.

Dilutions	Experimental concentration (μg·mL^{-1})	Maximum concentration (μg·mL^{-1})	%
1:480	0.78$\pm$0.02	1.29	60
1:240	1.61$\pm$0.13	2.58	62
1:120	3.25$\pm$0.13	5.17	63

7.3.3 Study of enzyme activity: simulations explain system behaviour

An important objective of this work was to demonstrate the suitability of this detection system for electrochemical immunoassays. To demonstrate the operation of the system, we present an enzyme activity study under different flow rate conditions. We analysed the relation between enzyme activity, flow rate and measured current. In addition to the experimental work, we used numerical modelling to improve our understanding of the system behaviour.

In the experiments, 50μL of a bead suspension was injected at 50 μL·min^{-1} and trapped by the magnets. The substrate PAPGP was then introduced through the channel with immobilised beads at a lower flow rate (0.1-10 μL·min^{-1}) to minimise bead loss during the operation. The rate of enzyme product generation was controlled by the flow rate of the substrate solution. Thus, although a high flow rate might be beneficial from the viewpoint of the electrochemical detection, it would not leave enough time to generate a measurable amount of enzyme product, and therefore a smaller current would be detected. Conversely, at lower flow rates, the enzyme will be able to turn more substrate into product, leading to an increased current. Figure 7-7 shows this for a 1:480 bead dilution measured at 0.25V vs. Au at different flow rates. The flow rate was held constant at a certain value for some time and then it was swiftly changed to a (much) higher or lower value, which resulted the appearance of current spikes. The injected substrate concentration was 1mM to ensure its excess compared to the enzyme concentration.

Simulations were used to interpret and predict the behaviour of the system. In our case, several physico-chemical phenomena were occurring simultaneously and, despite the approximations, simulations helped to understand how these phenomena related to each

other. Note that there are two different channel widths in the PDMS gasket; 2 mm in the magnetic bead capture chamber and 500 μm along the detection channel. This means that the symmetry of the real geometry cannot be accounted for by our 2D model, and a 3-dimensional model would be needed to model the geometry more accurately. Our approximation was to assume the same width both for the capture chamber and the detector channel (500 μm) and then multiplying the enzyme kinetic constant by a geometrical factor, K_g=16. We used kinetic values obtained from an independent experiment using gold commercial macroelectrode of 1 mm diameter for the enzyme kinetics of β-galactosidase according to a Michaelis-Menten mechanism. The resulting values were a K_m of $3.15 \cdot 10^{-4}$ mol·L^{-1} and a k_{cat} of 0.18 s^{-1} (equation (7.5)). The channel height was estimated electrochemically as described in section 7.3.1 (105 μm). The diffusion coefficient values for PAPGP and PAP were estimated by the Wilke-Chang method [34], which yields values accurate to within 10% or better for small molecules. These values were $3.6 \cdot 10^{-10}$ m^2·s^{-1} for PAPGP and $8.6 \cdot 10^{-10}$ m^2·s^{-1} for p-aminophenol. As the simulation is two dimensional, it is necessary to calculate the enzyme surface concentration to introduce that parameter in the model. First, knowing the enzyme concentration on the beads for a 1:480 dilution, 0.8 mg·mL^{-1}, which was calculated in the previous section, and the volume injected (50 μL), it is possible to estimate the quantity of enzyme, $8.6 \cdot 10^{-14}$ mol. Second, it is necessary to calculate the surface occupied by the beads. Our approximation was as follows: according to the manufacturer, the initial bead concentration is 10^{10} beads·mL^{-1}. Therefore, there should be about 10^6 beads in 50 μL of a 1:480 dilution. Asuming that the beads are spread in a monolayer and that each occupies 1 μm^2, then the surface taken by this monolayer is approximately 10^{-6}m^2, and the enzyme surface concentration around is $8.6 \cdot 10^{-8}$ mol·m^{-2}.

The experimental sequence was simulated and Figure 7-7 shows the agreement between the experimental and the simulated transient currents. As expected, the current increased inversely with the flow rate due to the longer residence time of the substrate in the bead capture zone containing the enzyme. Note the positive and negative current peaks appearing when the flow rate is switched from a higher to a lower speed and vice versa. These peaks were explained considering that a product concentration corresponding to the previous flow rate was displaced at a different flow rate over the electrode, and hence influenced the current as predicted by equation (7.7). If we for instance consider the switch from 0.1μl·min^{-1} to 1μL·min^{-1} ((d) to (c) in Figure 7-7), there was a higher product concentration in the system at 0.1μL·min^{-1} because the substrate and the immobilised enzyme had more time to react. Then, the flow rate was increased and the solution containing this concentration of product was suddenly pushed at 1μL·min^{-1} and, as expected from equation (7.7), the recorded current increased. Once all the solution containing the higher product concentration was flushed over the electrode, a new steady state current of lower magnitude was achieved. Figure 7-7 shows that although there was very good agreement between the experimental and simulated steady state currents, the peaks were somewhat different. The simulated peaks were in general higher and sharper than the

experimental ones. This is explained if we take into account the fact that the experimental system was driven by a syringe pump, where the switch from one flow rate to another was not immediate, and that stabilisation of the new conditions was delayed. The simulation, on the other hand, did not consider these non-idealities and abruptly changed from one flow rate to the next. However, what matters is the remarkable agreement between the experimental and the simulated steady-state currents, as shown in Figure 7-7. Experimental measurements were repeated several times to demonstrate the reproducibility of the system. In each measurement, a new aliquot of magnetic beads was introduced, measured and released. Moreover, control of the flow rate in this system allows the study of chemical kinetics in general, but also of enzyme kinetics. Kinetic parameters can be estimated with our system because the measured currents reflect the competition between transport of the reagents and the rate of the chemical reaction under study. Our system can work under a very wide range of flow rates, which allows both access to kinetic parameters of different magnitudes and the detection of very small amounts of electroactive material, as will be shown below.

Table 7-2: Experimental and simulated steady state currents at different flow rates as depicted in Figure 7-7. The experimental error is reported as the standard deviation of three independent measurements.

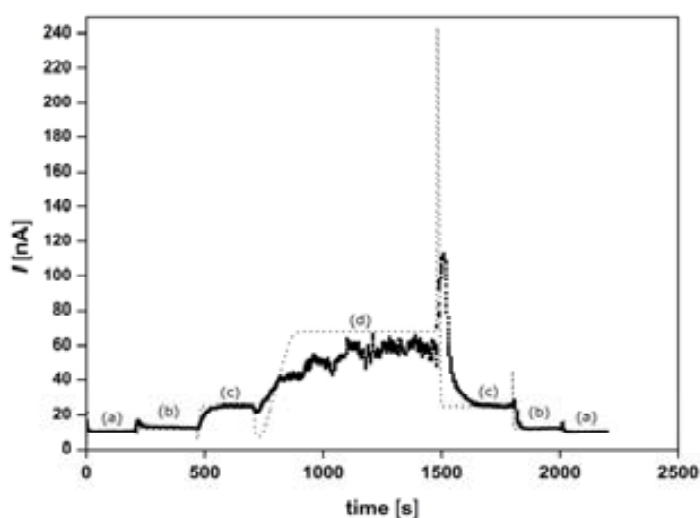|	I $_{experimental}$ (nA)	I $_{modeling}$ (nA)	RSD / %
0.1 μL·min^{-1}	60.1±3	68.1	5.0
1 μL·min^{-1}	26.0±1.6	25.1	6.2
5 μL·min^{-1}	12.1±0.9	12.0	7.5
10 μL·min^{-1}	9.3±1.0	11.0	10.8

Figure 7-7: (■) Experimental current at 0.25V vs. Au pseudo-reference and different flow rates for 50μL of a 1:480 beads dilution captured in the system

and a substrate concentration of 1mM. (a) 10 μL·min^{-1}, (b) 5 μL· min^{-1}. (c) 1 μL·min^{-1} and (d) 0.1 μL· min^{-1}. The dotted line corresponds to the simulated current under the same conditions.

7.3.4 Detection of β-galactosidase by pulsed or stopped flow

The appearance of peaks during the transition between flow rates (Figure 7-7) served as the basis for an operation mode that increases the sensitivity of the system. This is similar to the technique described by Karlberg in [35], or Merkoçi et al. in [6], and it is of paramount importance in biosensors, and more specifically in immunoassays, aiming at the detection of very small concentrations down to ng·L^{-1} or even pg·L^{-1}. Figure 7-7 shows the current peaks for the different flow rate transitions. The height of the positive peaks was several times larger than the preceding steady state current, which represents a substantial signal enhancement.

To exploit this feature, rather than measure under a continuous flow of substrate, we operated under stopped-flow conditions for a short period of time. During this time the reaction proceeded under stagnant conditions and its rate was controlled by diffusion of the substrate to the bead surface. Next, the pump was switched on and this volume, containing the electroactive PAP, was pushed over the working microband electrode and a current peak was observed. Simulations were able to model these events and Figure 7-8 shows a series of simulated peaks obtained after different incubation times.
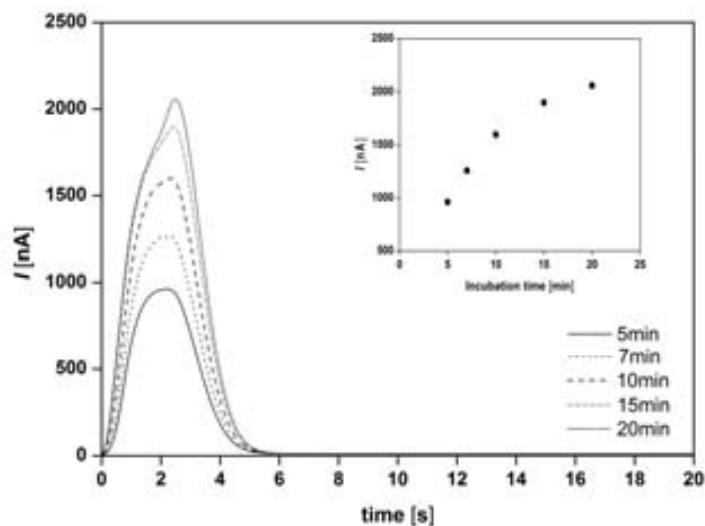

Figure 7-8: Simulated peaks after different incubation times: 5, 7, 10, 15 and 20 minutes. Following incubation the solution was pushed at 5 μL·min-1 for a 1:480 beads dilution capture.

The model was solved using the same conditions as those from Figure 7-7. However, to model the pulsed flow behaviour, the solution was left to react for a certain time and then pushed at 5μl·min^{-1}. Figure 7-8 shows how these peaks increase with incubation time, and it

is interesting to note that the peak currents seem to reach a plateau at longer incubation times. This is because after long incubation periods, the immobilised enzyme consumes most of the substrate present in the solution. This may be a problem because diffusion of the product into the detector channel may be detrimental to sensitivity. To avoid problems like this, incubation times must be carefully watched.

Another interesting feature is the duration of the simulated flow pulses, which was always less than 5s. This may explain the different shape and height of the experimental peaks because our syringe pump took longer than this to reach the desired flow rates.

Figure 7-9 shows the experimental results for 1:480 and 1:960 dilutions at different incubation times. The experimental peaks were considerably lower than the simulated ones. This difference increased with incubation times as the concentration of product also increased. However, the current ratio between both dilutions was constant for every incubation time, which was an excellent indication of a consistent and reproducible bead capture. The fact that the current peak for the 1:480 dilution was twice as high as the peak at 1:960 dilution implied that the enzyme concentration also doubled due to the amount of captured beads. Every measurement was repeated at least three times and the results were highly reproducible. This also suggested that the captured beads were very stable and that very few beads were lost during the measurements.
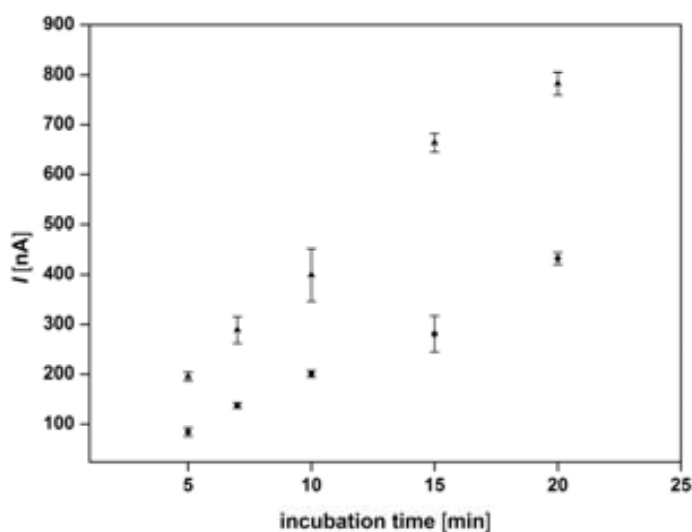

Figure 7-9: Comparison of experimental current peaks for particles captured from two different magnetic bead dilutions: 1:480(▲) and 1:960 (●) (The initial concentration of magnetic beads is 10 mg·mL^{-1}. The measurements were done at 0.25V vs. Au pseudo-reference at different incubation times. Solution was pushed at 5 μL·min^{-1} after the incubation.

We can conclude that this operational mode leads to outstanding sensitivity enhancements. For example, in the case of a 1:480 dilution at 0.1 μL·min^{-1} the steady-state current was around 60nA (see Figure 7-7). However, after only 10 minutes of incubation the signal increased six times, up to around 400nA for the same flow rate. Therefore, using stopped-

flow operation may be very beneficial for cases where the biological target is present in the sample at extremely low concentrations. During testing, it was possible to detect presence of enzyme products in a $1:10^4$ dilution of magnetic beads, equivalent to approximately 50 ng·mL^{-1}.

7.4 Summary

Lab-on-a-chip devices are understood as an engineering challenge involving integration of new processes, new materials and geometry scaling. From this point of view, we aimed to produce an easy-to-use and reusable device. We focused this work to improve the control over the chemical or biological reactions taking place during bioassays by adjusting flow rate. This is what we have presented here: a very versatile lab on a chip system that integrates magnetic capture and electrochemical detection in a microfluidic environment and where flow can be adjusted depending on the chemical kinetics of the system to optimise the detection. The system versatility stems from its highly modular nature, where both the PDMS embedded microfluidics and the chip-based microelectrode set can be readily replaced without need for wire bonding or encapsulation. The PDMS gasket incorporates a 150 µm high channel containing two distinct regions: a chamber 2mm wide where the magnetic beads can be trapped by a permanent magnetic field, and a 500µm microchannel, leading directly to the set of microband electrodes where enzyme reaction products are detected. Such microfluidic features can be easily changed replacing this PDMS gasket for a new one of different channel configuration. This allows the final user to adapt the whole system to new experimental needs. Moreover, once the detection has been carried out and the particles are no longer needed, they can be easily released by blocking the magnetic field by sliding a thin iron slab between the magnets and the chip.

Although the system presented here was designed to immobilise magnetic particles upstream from the working electrode in electrochemical immunoassays, it could also be used more generically in other electroanalytical applications. We have used the well-known β-galactosidase and PAPGP enzyme and substrate system, and we have been able to determine the enzyme surface concentration over our magnetic beads. Thus, we have demonstrated its operation and possible applicability to the field of bioassays and we conclude that the system could be used in any enzyme-based bioassay (e.g., displacement or sandwich immunoassays based on conventional ELISA). Time of analysis and/or sensitivity could be further improved with the use of interdigitated microband structures operated in generator-collector mode, or by extending the incubation time of the substrate in the presence of immobilised enzyme-modified magnetic particles when the system is operated in stopped-flow mode.

Finite element simulations were of great help in understanding the system behaviour. Our simulations suggested that the system flow suffers some delay before it reaches the desired velocity. In spite of this, the system affords high levels of reproducibility and sensitivity, which

makes it an attractive tool for the development of novel electrochemical bioassays. In addition to immunoassays, the system can also be used in comparative studies of enzyme activities towards different substrates, or in different media, or to compare the activity of different enzymes on a given substrate.

7.5 References

[1] Choi, J.W., K.W. Oh, J.H. Thomas, W.R. Heineman, H.B. Halsall, J.H. Nevin, A.J. Helmicki, H.T. Henderson, and C.H. Ahn, *An integrated microfluidic biochemical detection system for protein analysis with magnetic bead-based sampling capabilities.* Lab on a Chip - Miniaturisation for Chemistry and Biology, 2002. 2(1): p. 27-30.

[2] Do, J. and C.H. Ahn, *A polymer lab-on-a-chip for magnetic immunoassay with on-chip sampling and detection capabilities.* Lab on a Chip - Miniaturisation for Chemistry and Biology, 2008. 8(4): p. 542-549.

[3] Farrell, S., N.J. Ronkainen-Matsuno, H.B. Halsall, and W.R. Heineman, *Bead-based immunoassays with microelectrode detection.* Analytical and Bioanalytical Chemistry, 2004. 379(3): p. 358-367.

[4] Gabig-Ciminska, M., A. Holmgren, H. Andresen, K. Bundvig Barken, M. Wümpelmann, J. Albers, R. Hintsche, A. Breitenstein, P. Neubauer, M. Los, A. Czyz, G. Wegrzyn, G. Silfversparre, B. Jürgen, T. Schweder, and S.O. Enfors, *Electric chips for rapid detection and quantification of nucleic acids.* Biosensors and Bioelectronics, 2004. 19(6): p. 537-546.

[5] Goral, V.N., N.V. Zaytseva, and A.J. Baeumner, *Electrochemical microfluidic biosensor for the detection of nucleic acid sequences.* Lab on a Chip - Miniaturisation for Chemistry and Biology, 2006. 6(3): p. 414-421.

[6] Llopis, X., M. Pumera, S. Alegret, and A. Merkoçi, *Lab-on-a-chip for ultrasensitive detection of carbofuran by enzymatic inhibition with replacement of enzyme using magnetic beads.* Lab on a Chip - Miniaturisation for Chemistry and Biology, 2009. 9(9): p. 213-218.

[7] Alden, J.A., M.A. Feldman, E. Hill, F. Prieto, M. Oyama, B.A. Coles, R.G. Compton, P.J. Dobson, and P.A. Leigh, *Channel Microband Electrode Arrays for Mechanistic Electrochemistry. Two-Dimensional Voltammetry: Transport-Limited Currents.* Analytical Chemistry, 1998. 70(9): p. 1707-1720.

[8] Morland, P.D. and R.G. Compton, *Heterogeneous and Homogeneous EC and ECE Processes at Channel Electrodes: Analytical Wave Shape Theory.* Journal of Physical Chemistry B, 1999. 103(42): p. 8951-8959.

[9] Amatore, C., N. Da Mota, C. Sella, and L. Thouin, *General concept of high-performance amperometric detector for microfluidic (bio)analytical chips.* Analytical Chemistry, 2008. 80(13): p. 4976-4985.

[10] Cooper, J.A. and R.G. Compton, *Channel Electrodes - A Review.* Electroanalysis, 1998. 10(3): p. 141-155.

[11] Rees, N.V. and R.G. Compton, *Hydrodynamic microelectrode voltammetry.* Russian Journal of Electrochemistry, 2008. 44(4): p. 368-389.

[12] Rossier, J.S. and H.H. Girault, *Enzyme linked immunosorbent assay on a microchip with electrochemical detection.* Lab on a Chip - Miniaturisation for Chemistry and Biology, 2001. 1(2): p. 153-157.

[13] Tokuda, K. and H. Matsuda, *Theory of stationary current-voltage curves of redox-electrode reactions in hydrodynamic voltammetry. IX. Double electrodes in channel flow.* Journal of Electroanalytical Chemistry, 1974. 52(3): p. 421-431.

[14] Másson, M., Z. Liu, T. Haruyama, E. Kobatake, Y. Ikariyama, and M. Aizawa, *Immunosensing with amperometric detection, using galactosidase as label and p-aminophenyl-B-D-galactopyranoside as substrate.* Analytica Chimica Acta, 1995. 304: p. 353-359.

[15] Compton, R.G. and C.E. Banks, *Understanding Voltammetry.* 2007, Singapore: World Scientific Publishing. 371.

[16] Conant, J.B. and M.F. Pratt, *The irreversible oxidation of organic compounds I. The oxidation of aminophenols by reagents of definite potential.* Journal of the American Chemical Society, 1926. 48(12): p. 3178-3192.

[17] Niwa, O., Y. Xu, H. Brian Halsall, and W.R. Heineman, *Small-volume voltammetric detection of 4-aminophenol with interdigitated array electrodes and its application to electrochemical enzyme immunoassay.* Analytical Chemistry, 1993. 65(11): p. 1559-1563.

[18] Plichon, V. and G. Faure, *Thin-Layer Electrochemistry - Applications to Chemical-Kinetics - Example of Para-Aminophenol.* Journal of Electroanalytical Chemistry, 1973. 44(2): p. 275-290.

[19] Yamaguchi, S. and S. Mitsugi, *Sensitive amperometry of 4-aminophenol (4AP) based on the catalytic current produced by the 4AP-diphorase-NADH system at a glassy carbon*

electrode and its application to enzyme assay. Effect of the inhibition of diaphorase by NADH. Analytical Sciences, 1997. 13: p. 307-309.

[20] Nicholson, R.S. and I. Shain, *Theory of stationary electrode polarography single scan and cyclic methods applied to reversible, irreversible, and kinetic systems.* Analytical Chemistry, 1964. 36(4): p. 706-723.

[21] Snakenborg, D., G. Perozziello, H. Klank, O. Geschke, and J.P. Kutter, *Direct milling and casting of polymer-based optical waveguides for improved transparency in the visible range.* Journal of Micromechanics and Microengineering, 2006. 16(2): p. 375-381.

[22] Shinohara, H., J. Mizuno, and S. Shoji, *Low-temperature direct bonding of poly(methyl methacrylate) for polymer microchips.* IEEJ Transactions on Electrical and Electronic Engineering, 2007. 2(3): p. 301-306.

[23] Tsao, C.W., L. Hromada, J. Liu, P. Kumar, and D.L. DeVoe, *Low temperature bonding of PMMA and COC microfluidic substrates using UV/ozone surface treatment.* Lab on a Chip - Miniaturisation for Chemistry and Biology, 2007. 7(4): p. 499-505.

[24] Duffy, D.C., J.C. McDonald, O.J.A. Schueller, and G.M. Whitesides, *Rapid prototyping of microfluidic systems in poly(dimethylsiloxane).* Analytical Chemistry, 1998. 70(23): p. 4974-4984.

[25] McDonald, J.C. and G.M. Whitesides, *Poly(dimethylsiloxane) as a material for fabricating microfluidic devices.* Accounts of Chemical Research, 2002. 35(7): p. 491-499.

[26] Smistrup, K., M. Bu, A. Wolff, H. Bruus, and M.F. Hansen, *Theoretical analysis of a new, efficient microfluidic magnetic bead separator based on magnetic structures on multiple length scales.* Microfluidics and Nanofluidics, 2008. 4(6): p. 565-573.

[27] Goncalves, D., R.C. Faria, M. Yonashiro, and L.O.S. Bulhoes, *Electrochemical oxidation of o-aminophenol in aqueous acidic medium: Formation of film and soluble products.* Journal of Electroanalytical Chemistry, 2000. 487(2): p. 90-99.

[28] Baldrich, E. and F.X. Muñoz, *Enzyme shadowing: Using antibody-enzyme dually-labeled magnetic particles for fast bacterial detection.* Analyst, 2008. 133(8): p. 1009-1012.

[29] Lund-Olesen, T., H. Bruus, and M.F. Hansen, *Quantitative characterization of magnetic separators: Comparison of systems with and without integrated microfluidic mixers.* Biomedical Microdevices, 2007. 9(2): p. 195-205.

[30] Mikkelsen, C., M. Fougt Hansen, and H. Bruus, *Theoretical comparison of magnetic and hydrodynamic interactions between magnetically tagged particles in microfluidic systems.* Journal of Magnetism and Magnetic Materials, 2005. 293(1): p. 578-583.

[31] Voet, D. and J. G.Voet, *Biochemistry*. Second ed. 1995: John Wiley & Sons.

[32] Bard, A.J. and L.R. Faulkner, *Electrochemical methods: Fundamentals and Applications*. 2001, Chichester: Wiley.

[33] Compton, R.G., A.C. Fisher, R.G. Wellington, P.J. Dobson, and P.A. Leigh, *Hydrodynamic Voltammetry with Microelectrodes. Channel Microband Electrodes: Theory and Experiment.* Journal of Physical Chemistry, 1993. 97: p. 10410-10415.

[34] Wilke, C.R. and P. Chang, A. I. Ch. E. Journal, 1955. 1: p. 264.

[35] Francis, P.S., S.W. Lewis, K.F. Lim, K. Carlsson, and B. Karlberg, *Flow analysis based on a pulsed flow of the solution: theory, instrumentation and applications.* Talanta, 2002. 58: p. 1029-1042.

CHAPTER 8: Rotary microvalve

Integrating active microfluidic components is a challenging but necessary process to enable the performance of several chemical operations using the same device. This chapter presents the design, fabrication and characterisation of a miniaturised electroanalytical lab on a chip that allows the performance of a complete bioassay, from the capture of magnetic particles through their functionalisation and sample incubation to the detection of electroactive reaction products. The system is built using mainly polymeric materials such as PMMA and PDMS and fast prototyping techniques such as milling and moulding. The novelty lies in the design of the rotary microvalve, which contains a microreactor so that various reaction and incubation steps can be carried out in isolation from the detection event with zero dead volume. This avoids contamination and fouling of the electrodes by proteins or other organic matter, and extends the useful lifetime of the detector. Although the system is intended for the development of enzyme-based electrochemical bioassays, the concept of its rotary microreactor can be applied more broadly.

The design and fabrication of the system was carried out during a second stay at the Department of Micro and Nanotechnology (DTU-Nanotech) of the Technical University of Denmark

8.1 Introduction

This chapter focuses on the development of a versatile miniaturised analytical system device for the performance of electrochemical bioassays. This system builds on the architecture of a previous system, described in Chapter 7, adding a rotary valve to it. The fact that the rotary valve also integrates a reaction chamber where magnetic particles can be captured represents a fabrication challenge particularly from the point of view of sealing moving parts.

In the previous chapter, we presented a versatile electroanalytical microsystem, easy to fabricate, use and re-configure. That system allowed the performance of a broad range of enzyme-based bioassays. The microsystem permitted the capture of enzyme labelled magnetic beads, and their incubation with a relevant substrate, upstream from an electrochemical detector. After the reaction took place, the flow was restored and a current peak corresponding to the products was easily detected as in any other plug-flow system.

However, the simplicity in its design was both the main strength and the main pitfall of the system. The fact that there was a single channel meant that all the solutions used in the different operations – bead capture, sample and substrate injection, product detection and

washing - had to flow over the electrodes. The consequence was that part of the biological materials passing through the system adsorbed on the electrodes and caused gradual losses of sensitivity and reproducibility.

To preserve active electrodes longer, we want to minimise the contact of solutions containing biological material with them. Our approach consists in the integration of a microvalve in the flow path between the biochemical reaction chamber and the detector. This way we ensure that only the reaction products flow over the electrodes, while any other potentially fouling solutions are diverted through an alternative waste channel.

We have been able to integrate a microvalve in our original system due to its flexible architecture based on flexible building blocks. Despite its small dimensions, the different parts are sufficiently tolerant to accommodate new functionalities.

We developed an externally-actuated rotary valve, made in the same materials as the rest of the device. An important advantage of this new feature is that it minimises the dead volume between the reaction chamber and the detector, so the configuration also reduces peak broadening due to smearing/diffusion of detectable products inside the detector channel. A similar approach was presented in 2005 by H. Yin *et al.* [1], who integrated a packed column within a small valve in a fully automated chromatographic system for peptide analysis. However, the microsystem we present here is much simpler and, more importantly, the valve is based on sealing achieved by contact with 2 surfaces. This allows the definition of microchannels in the rotary part for direct use on silicon or glass chips. This is in contrast to most systems, based on single sealing surfaces, which require the channels to be defined both in the rotary part and in the chip, complicating the chip layout and its fabrication. In addition, while our rotary system can be connected through simple holes punched in the PDMS, conventional rotary valves need to consider precise channel alignment.

Our system behaves like a revolving microreactor because it is actuated by an external moving part [2]. Its working principle is similar to the pulsed/stopped flow also known as lab-on-valve (LOV) described by Kalberg [3], which consists in stopping the flow while a reaction proceeds, and eventually start a pump to push the reaction products towards the electrodes. As it was demonstrated in Chapter 7, simply stopping the flow for a few minutes increases the detection current several times. The system presented in this chapter builds on that approach and improves its performance because (i) the capture and the detection chambers are independent, and (ii) the beads are captured upstream from the detector and this makes it possible to vary the flow rate to amplify the generated current.

The use of magnetic beads is becoming increasingly popular in lab-on-a-chip devices for the practice of bioassays [4-11]. They can be easily captured and moved around with the aid of a magnet, and virtually any biomolecule can be immobilised on their surface following conventional chemical approaches. Suitably modified magnetic particles can be used to pre-concentrate a sample, they can then be driven towards the detector, where the assay may be finished after performing any necessary intermediate steps. Once the assay is complete,

they are released in a very simple way: blocking the magnetic field sliding a thin soft-iron piece between the magnets and the chip, and flushing a buffer solution through the system.

This almost continuous mode of operation is not possible with immunosensors where the transducer is directly functionalised, because the sensing surface must be regenerated after each assay [12]. The problem is, particularly in electrochemical systems, that this necessary regeneration of the transducer shortens the electrode lifetime, and increases important parameters such as cost, time and user effort.

In this chapter we first describe the design and fabrication of a novel miniaturised analytical system. We then show that the microvalve can cope with flow rates well above the usual ones applied in this type of analytical systems, and finally we demonstrate the operation of the system loading magnetic particles with an enzyme which product is subsequently detected.

8.2 Experimental methods

This section describes the fabrication of our microsystem, how the system works and the set-up used.

8.2.1 Microdevice

Our microsystem comprises three main parts: the rotary valve assembly, a silicon microchip featuring a series of microelectrodes where the detection will take place, and a holder where the other parts fit and which facilitates handling and usage.

The rotary valve assembly

The rotary valve consists of two main functional elements (see Figure 8-1): a cylindrical part that acts as a rotor, and a stator part that contains a cylindrical opening to house the rotor. While the stator facilitates connection to inlet and outlet channels, the rotor also includes a reaction chamber (see Figure 8-1). Turning the rotor allows the operator to connect the outlet of the reaction chamber either to the waste or the detection channel. The valve assembly is positioned so that the the detection channel are positioned on top of the electrodes on the microchip (see Figure 8-1b).

Both rotor and stator are fabricated in PDMS using casting methods [13, 14]. This configuration allows establishing a proper seal (i) between rotor and stator as well as (ii) between the rotor-stator-assembly and a planar surface, e.g. a silicon or glass chip (as depicted in Figure 8-1b). In the latter case, sealing is achieved by contact, simply clamping chip and assembly. In the case of sealing rotor and stator to each other, the vertical clamping force acting on the PDMS structures results in a lateral deformation that, in turn, generates a lateral stress that provides sufficient sealing between both elements.

Four brass pins connect the rotor to a shaft (see Figure 8-1b). This allows the operator to apply the necessary clamping force for sealing and to rotate the valve.

The rotor has a diameter of 4 mm and a height of 2 mm. The four bottom flat holes that were cast into the rotor have a diameter of 0.8 mm and a depth of 1.5 mm. The reaction chamber has an ID of 3.2 mm and a height of 200 μm, the inlet and outlet are 400 μm wide. The stator (13 mm long, 5 mm wide, 2 mm high) contains the opening for the rotor (ID 4 mm) and the inlet and outlet channels (200 um x 400 um).

Although the elasticity of the PDMS is essential for the function of the microvalve, it increases the risk of collapsing the reaction chamber under excessive clamping force. Therefore, the softness of the silicone is an important parameter for the design of a working rotary microvalve. In this work we used R21-2615 (Nusil Silicone Technology) with a hardness value of 75 (shore A) for the rotor and Sylgard ® 184 (Dow Conning) with a hardness of 50 (shore A) for the stator.

While the shaft is fabricated in polycarbonate, PC, to strengthen the system, the moulds to cast the PDMS components were made in PMMA because this material yields smoother surfaces. In both cases, micromilling was the fabrication method.
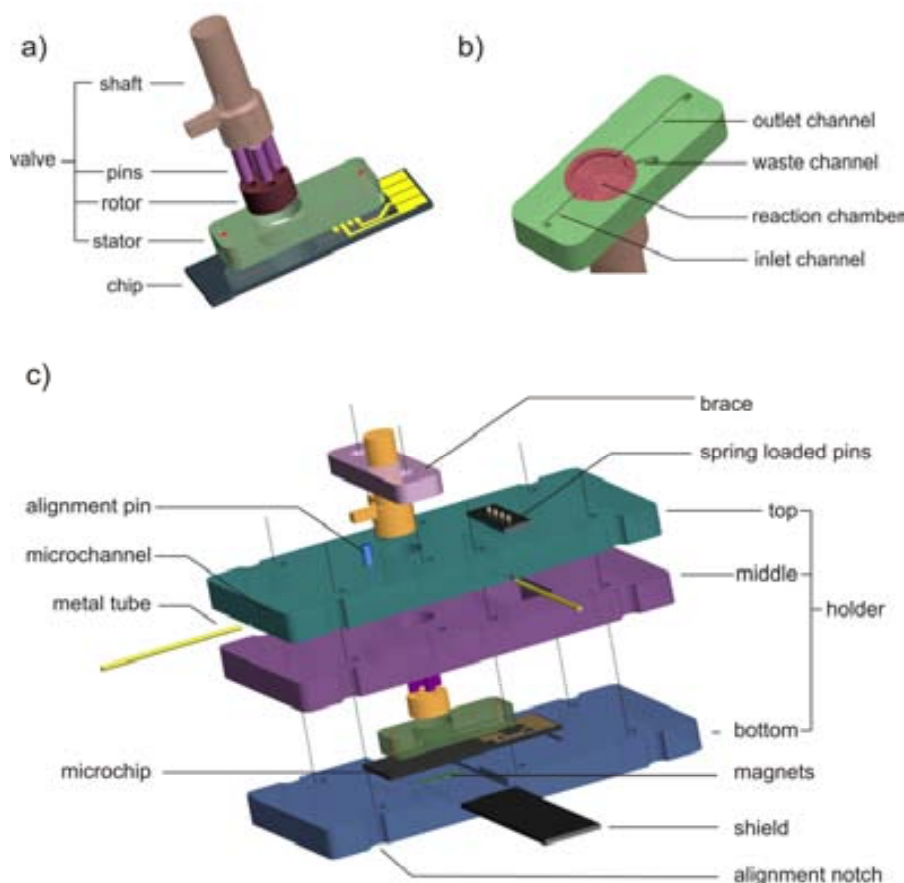

Figure 8-1: a) Bottom view of the rotary valve: switching between two positions allows flushing liquid from the reaction chamber either to waste or to the detection channel. b) The valve assembly is aligned so that the electrodes are positioned below the detection channel. Pressing the PDMS rotor and stator against a microchip provides sufficient sealing to prevent leaks. c) Three elements (top, middle and bottom part) were connected to provide a packaging housing the valve components as well as the microchip. Microchannels in

combination with glued-in metal tubes and spring loaded pins allowed easy fluidic and electrical interconnection. Permanent magnets provided a magnetic field that could be shielded from the chip sliding in a metal plate.

The silicon microchip

The silicon-based electrode chip (5mm x 17 mm) featured four microbands (three bands of 500 μm width and 1 band of 1 mm width, respectively) each separated by 100 μm gaps and fabricated as described in the previous chapter.

The holder

The holder was designed to house and align the valve components as well as the chip and magnets. The top and middle parts (20 x 40 x 3 mm PMMA) were bonded together using UV assisted bonding (2 min UV exposure and subsequent clamping at 80 °C). Integrated microchannels (500μm x 500μm cross-section) with glued-in metal tubing (OD 500 um) acted as fluidic inlet and outlet and allowed for easy interconnection. Different pockets housed the rotary valve components while spring-loaded pins connected the microchip pads. Through-holes allowed attaching the bottom part to the top-middle assembly with an adjustable clamping force using screws. While this clamping force ensured the sealing of the stator to the chip as well as to the interconnection channels of the holder, an aluminium brace was fixed to the top part allowing the application of an adjustable pressure onto the shaft of the rotary valve assembly. Fixing the brace to the top part ensured that the same pressure was applied after disassembling and subsequent assembly of the bottom part (e.g.: to replace the chip).

The sealing pressure was adjusted by assembling the holder on a transparent dummy chip. In contrast to silicon chips, this transparency permitted visual inspection and helped to avoid collapsing the reaction chamber under excessive pressure. Alignment pins (see Figure 8-1c) inserted in the holder's top part allowed turning the shaft only a certain angle, which ensured reproducible alignment of rotor and stator channels when switching between the two positions.

In addition, the bottom part also hosted two permanent magnets (Nd-Fe-B, Lika, Denmark, 2 x 2 x 2 mm^3), a pocket for the silicon chip and a second pocket for insertion of an iron slab (20 x 5 x 0.5 mm) to shield the chip from the magnetic field of the magnets (see Figure 8-1c). The two magnets are placed with opposite vertical polarisation to maximise the magnetic force on the beads in the channel [15]. On the other hand, this configuration of the magnets allows blocking the magnetic field and flushing the beads out of the microchamber by just inserting the iron slab between the chip and the magnets.

Micromilling and -drilling were used to fabricate the holder components.

8.2.2 System operation

Figure 8-2a schematises the system operation steps. There are two positions, corresponding to the two different outlets: waste and detection. When the waste channel is open there is no contact between the solution and the electrodes as will be demonstrated in the following section. In this position, it is possible to inject biological solutions without the risk of fouling the electrodes and decreasing sensitivity. Moreover, once the magnetic beads are captured in the capture/reaction chamber, further biochemical reactions can be carried out without contaminating the detector. This allows for the performance of a wide range of electroanalytical experiments, making our system very flexible and attractive.
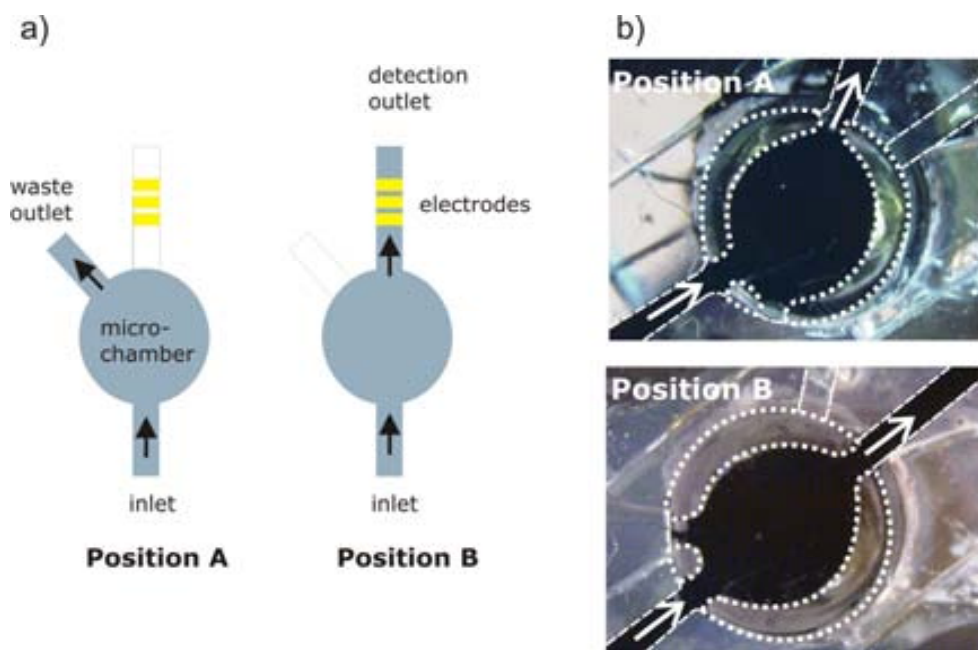
Figure 8-2: a) Schematic diagram of the working system. Position A opens the waste outlet. This is the position for the injection and capture of the magnetic beads and all the biological reactions -processes not directly related with the detection. The microvalve is turned to position B only for the purposes of detection, to avoiding contact of the electrodes with other solutions. b) Photographs of the valve in its two positions: the reaction chamber is connected to the waste (Position A, top) or to the detection channel (Position B, bottom). The contours of the PDMS parts are highlighted to show clearly the different pieces and positions.

To demonstrate such versatility and flexibility, we used a model system based on the enzymatic loading of magnetic particles performing some enzymatic assays. Enzyme-based detection is very frequent in electrochemical immunoassay [16-18]. In these indirect measurements, the target is directly related to the enzyme activity. Electrochemical detection requires that the enzyme reaction products are electroactive in the working potential window allowed by the experimental configuration.

Three common steps in enzymatic bioassay were tested. They consisted in: (i) linking biotinylated enzyme over streptavidin-coated magnetic beads, (ii) enzymatic reaction between the capture enzyme and its substrate and, last, (iii) detection of the enzymatic

product at the electrodes. These steps are all carried out on the chip, the first two in the capture/reaction microchamber and the last one in the detection channel. As the capture/reaction chamber is integrated in the PDMS rotor, when the reaction finishes the valve is turned so that the products can be detected at the electrodes. The enzymatic system, chosen for demonstration purposes, was the well-known β-galactosidase using 4-aminophenyl-β-D-galactopyranoside (PAPGP) as its substrate. The same enzymatic system was used in a previous chapter, where it was described in more detail. The enzymatic reaction produces p-aminophenol (PAP), which is electroactive and can be detected amperometrically at a mild oxidation potential. The oxidation potential of PAP using the same electrode configuration was also previously studied. The oxidation potential of the substrate is around 0.3V and for PAP is around 0.1V.

The main difference between both works is the integration of the rotary microvalve, which allows performing more complex biological processes on the chip without negatively affecting the detection. The working principle of this new system is very straightforward: in a first step, the system is flushed with buffer to remove air bubbles, both in the detector and waste channels. Then the valve is opened to the waste channel, and we can inject the bead suspension. After the magnets have captured a set of particles inside the reaction microchamber, an enzyme solution is introduced until it effectively displaces the buffer filling the microchamber. Then the flow is stopped for a few minutes during which the particles become loaded with enzyme through streptavidin-biotin interactions. The non-specifically bound enzyme is removed by passing a buffer. Next, the enzyme substrate is pumped into the chamber and the flow is stopped to allow the enzymatic reaction to generate a detectable amount of product.

All these steps are conducted with the microvalve in waste position, switching to the detection position immediately before the detection is going to take place. This ensures that only the enzymatic product (PAP) is allowed to flow over the electrodes, and only for a few seconds per measurement. We showed previously that this procedure can easily amplify the signal by at least one order of magnitude.

Note, that it is possible to perform sequential measurements as the captured beads are released using an iron slab to turn off the magnetic field resulting in an increase of the reproducibility and reusability of the system.

8.2.3 Set- up

As it was mentioned above, the set-up is a critical element when working with microfluidic devices. Based on the experience we gained from the previously described set-up (Chapter 7), we designed a second generation one, which overcomes two disadvantages of the former version: the limited number of inlets and the large dead volume. In the first set-up, the number of inlets was duplicated using external 3-port valves connected to the two inlets of

the device providing four independent ports. However, this set-up is not versatile enough if more than four inlets are necessary for a certain experiment. Moreover, each 3-port valve increases the dead volume by more than 100 μL, which is a significant volume compared to the volumes used for the measurements. For that purpose, a set-up, as shown in Figure 8-3 was fabricated. It is composed of four main parts, all fabricated in PMMA or PC using micromilling or –drilling and connected by silicone/PVC tubing (0.3 ID). To facilitate the handling of the different parts as well as the microdevice during the experiments, all parts were fitted on a baseplate. The baseplate contained an array of 2 mm holes, in which 2 mm pins could be inserted to align and fix the different components

To simplify the injection with multiple syringes, a support was fabricated fixing the syringes as shown in Figure 8-3. Self-made, miniaturised hose clips acted as valves allowing to individually close the different inlets by tightening screws and thereby clamping the tubing. To avoid cutting the screw into the tube material, small ball bearings (2mm diameter) were inserted into the screw holes between tube and screw. An inverted multiplexer component joined the six inlet channels to be connected to a single inlet of the device.

The working procedure was as follows: the entire system was first flushed with liquid through all inlets to remove air bubbles inside the system. Subsequently, the different inlets were closed ensuring a gas tight set-up and only being opened when needed. It is important to note that the configuration using silicone/PVC tubes in combination with the valves reduces the total inner volume to around 10 μL. Furthermore, although in our experiments we only used six channels, the system is easily scalable to a higher number of inlets and can be easily adapted to various experimental conditions.
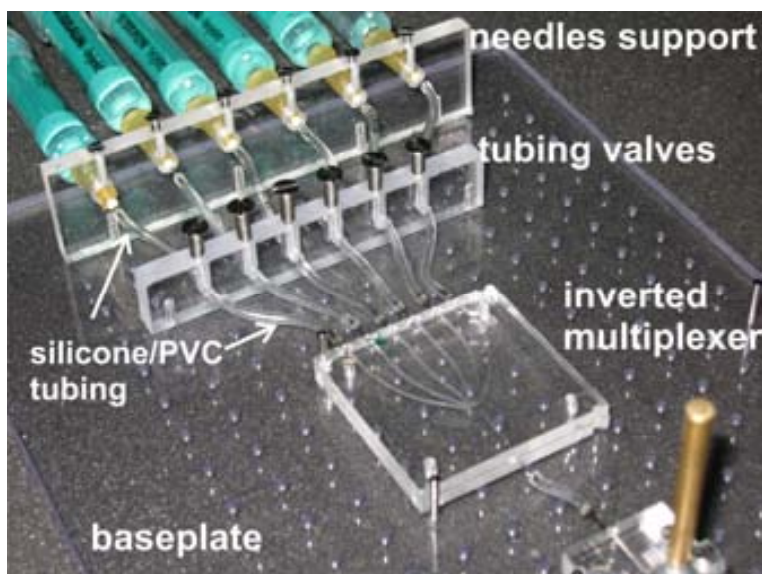

Figure 8-3: Experimental set-up. It consists on four main parts: needles support, tubing valves, inverted multiplexer and detector.

8.3 Results and discussion

8.3.1 Validation of the rotary microvalve

Figure 8-2b shows pictures of the two different positions of the microvalve. Position (a), connecting reaction chamber to the waste channel, is used for most processes in this work including capturing magnetic beads in the microchamber, cleaning or functionalisation. In position (b), the liquid can flow from the reaction chamber into the detection channel instead being exposed to the electrodes. Switching between the two positions avoids direct contact between chemical or biological reagents and the electrodes, and only the target species required for detection gains access to the micro-electrochemical detection cell. Switching the configuration is done manually by turning the shaft. Reproducibility is achieved by the above mentioned alignment features of shaft and holder.

To evaluate the sealing of the rotary valve, the holder was assembled using a transparent chip. Subsequently, black ink was injected to provide better contrast and the assembly was visually inspected from the bottom using a microscope (see Figure 8-2b).

Once the system was properly closed and adjusted by an adequate clamping force, no leakage could be observed. The valve could be switched repeatedly without degrading its performance. Although tests of the mean lifetime of the PDMS rotor were not performed, we did not observe degradation of its performance after repeated switching over a period of several weeks of continuous measurements.

One of the most important drawbacks of using PDMS to fabricate the rotor is that while turning the valve, a "twisting effect" can be observed describing different turning angles between top and bottom of the PDMS rotor. As a result, perfect alignment of rotor and stator inlets and outlets is hampered. This problem was minimised using a harder PDMS and inserting four pins symmetrically distributed to strengthen the rotor structure and distribute the stress more evenly. As the rotor is more rigid, the turning angles between top and bottom part of the rotor are smaller and alignment of rotor and stator become possible.

One of the most important features of the system is its simplicity. It is easy to open and close, to clean or replace its parts, e.g. the chip or the PDMS rotor. However, the dimensions of the detection channel must be the same after opening and closing in order to not modify the measured current. For a microband inside a microfluidic channel, the relation between the stationary current and the dimensions of the channel was described by Compton *et al.* [19] as:

$$I = 0.925 nFcw \left(x_e D \right)^{2/3} \left(\frac{Q}{h^2 d} \right)^{1/3} \tag{8.1}$$

where n is the number of exchanged electrons, F is the Faraday constant, c and D are the concentration and the diffusion coefficient of the electroactive species, w and x_e are the width and the length of the microband electrode, h and d are the half of the microchannel height and width, and Q is the (volumetric) flow rate. As in the previous chapter, the

electrochemical characterisation consists in cyclic voltammetry (CV's) at 50mVs[-1] for different flow rates using an equimolar solution of ferro/ferrycianide (1mM) in 0.5 KNO_3.

Figure 8-4 shows mean values of the stationary current after opening and closing the holder several times. As the sealing of the system is based on the compression of the PDMS gasket and rotor, the height of the channel in the PDMS stator is the most affected parameter. The thick line corresponds to the theoretical value of the stationary current for a height of 80µm and dotted lines for 85 and 75 µm, respectively. This 5µm interval represents around a 6% change in the measured current. Another way to calculate the height of the channel consists in adjusting a linear fit between the mean current values and $Q^{1/3}$. Channel height can then be calculated from the slope of this graph as: $2h = 84 \pm 4$ µm. This implies a height compression higher than 50% as the channel height nominal value was 200µm.
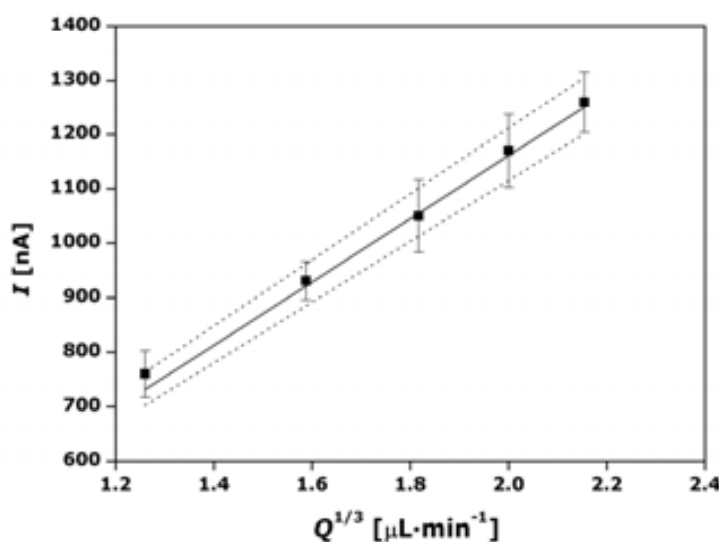

Figure 8-4: Stationary current for 1mM equimolar solution of ferro/ferricyanide in 0.5 KNO3 at different flow rates: experimental (filled square), theoretical response for 80 µm channel height (thick line) and for deviations of ±5 µm (dotted line). Error bars are based on 3 independent tests, opening and closing the holder every time. Every test consists of 3 measurements. As a gold pseudo-reference is used, the redox potential of the couple is centred at 0V, so measurements were performed at 0.2V. A diffusion coefficient value of 6.5·10[-10] m^2s^{-1} was used for ferrocyanide [20].

Finally, it is important to ensure that there is no leak at any time. To test the sealing we applied a range of high pressures at the inlet, injecting solution at high flow rates. This range extends two orders of magnitude beyond the flow rate used to make the final measurements, proving sufficient sealing. The quality of the sealing is measured by electrochemical characterisation. In this case, the electrodes are used as leakage detector. Any current observed while the detection channel is closed indicates the presence of leaks between the capture/reaction chamber and the detection output. These measurements consisted in opening the waste output, keeping this position while injecting an electroactive substance at different flow rates while current was measured in the detection channel. This measured

current remains zero unless the valve is incorrectly turned or leaks appear. After ten minutes, the microvalve was turned, the detection outlet was opened and, as the electrodes were still polarised, the current increased sharply. Figure 8-5 shows the results for a solution of 1mM of ferro/ferricaynice in 0.5 KNO_3 at a flow rate of 100μL·min^{-1}. As expected, no current was recorded over the first ten minutes, which means that the sealing was working properly. The same kind of measurement was repeated for 150, 200, 250, 300, 500 and 1000 μL·min^{-1} and there was no current detectable in any case. This demonstrates that the valve is leak tight. It has to be noted that this range exceeds typical values used in microfluidics, but they were chosen to study the system's operation under high pressure conditions without any leakage
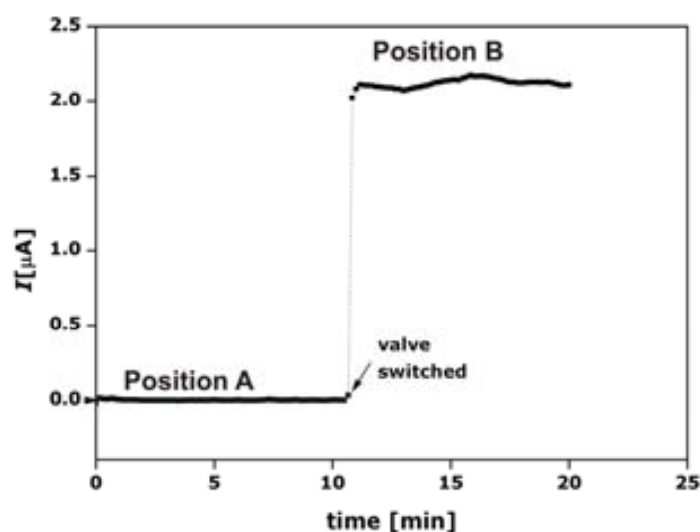

Figure 8-5: Chronoamperometric results at 0.2V versus a Au pseudo-reference for a solution of 1 mM of ferro/ferricyanide in 0.5 KNO3 at a flow rate of 100 μL·min^{-1}. After ten minutes, the valve was switched to position B and the oxidation of ferrocyanide was detected.

Figure 8-6 shows a picture of the assembled system. For visualisation, fluorescent ink was injected to facilitate the observation of both positions. The valve was switched manually turning the brass rod attached to the shaft.
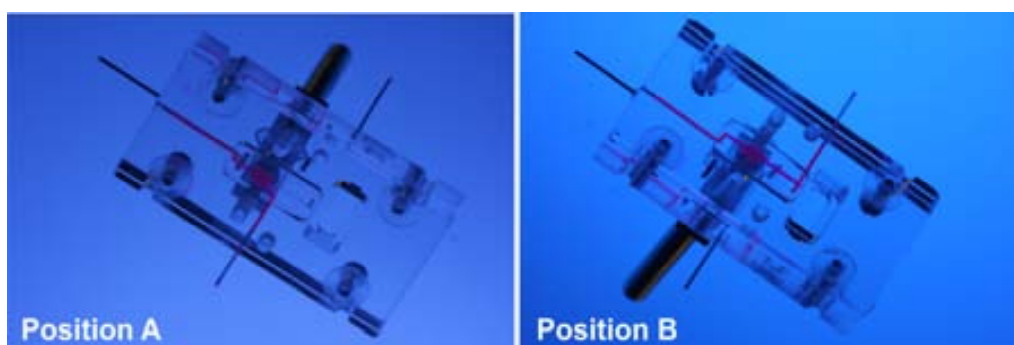

Figure 8-6: Picture of the assembled system without the electrodes using a transparent dummy chip. In position A the reaction chamber is connected to the

waste channel, while position B allows to flush the products from the reaction chamber to the electrodes (not shown). For visualisation, fluorescence ink was injected.

8.3.2 Enzymatic assay

The main motivation to integrate the microvalve is to separate as many operations as possible from the detection, to avoid direct contact between the electrodes and the chemical and biological reagents and extend electrode lifetime. To demonstrate the correct function of our system, an enzymatic assay was performed. The first experiments demonstrate that in a single channel system contamination of the electrodes occurs naturally as biomolecules adsorb on them over time of operation. To show the necessity of the microvalve integration contamination experiments were carried out allowing direct contact between the enzyme and the electrodes. Finally, an enzymatic assay is performed, in which a certain amount of magnetic beads are injected, captured and functionalised inside the capture/reaction chamber.

Reduction of contamination

Functionalisation is often achieved by physisorption[21], which means direct incubation of antibodies or enzymes with a given surface for a controlled period of time. To demonstrate that non-specific adsorption of the enzyme over the electrodes may affect flow measurements, a solution of $10\mu g \cdot mL^{-1}$ concentration of β-gal was incubated for 10 minutes in the detection chamber, and then flushed with a buffer..
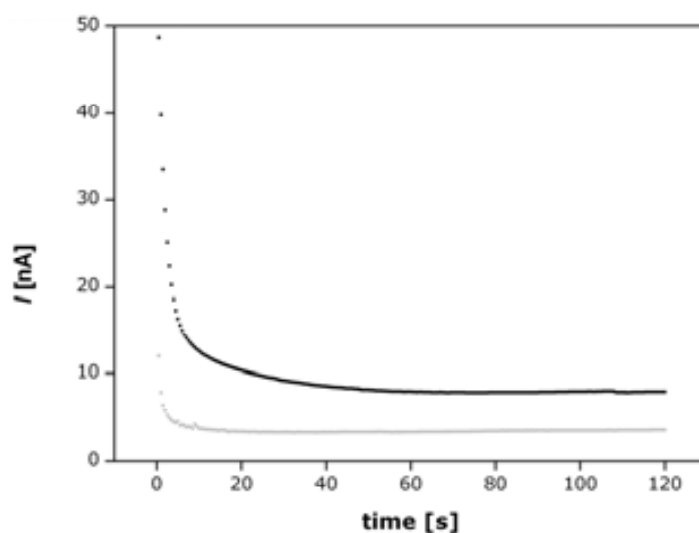
Figure 8-7: Results for the non-specific adsorption of the enzyme on the electrode surface. When the electrode is clean (grey filled square) the stationary current measured at 0.25 V versus an Au pseudo-reference is 3.5 nA for a solution of 1 mM of substrate (PAPG) injected at 10 $\mu L \cdot min^{-1}$. 10 minutes after exposing the electrodes to the enzyme, the current increases to 8 nA (black filled square).

Figure 8-7 reveals the presence of trace enzyme left in the system, adsorbed on the electrodes. The figure shows the current measured when a solution of 1mM of substrate (PAPGP) was injected at $10\mu L\cdot min^{-1}$ before and after the enzyme had been in the detector chamber. There are two limiting cases: (i) when the electrodes are clean and (ii) when they are contaminated by adsorbed enzyme. Before injecting the enzyme, the stationary current was around 3.5 nA, which corresponds to the typical blank signal level. However, after exposing the electrodes to an enzyme solution for 10 minutes, the current increased to 8 nA. This shows that a short contact time is enough to contaminate the electrodes and affect the measurements; p-aminophenol is produced as soon as the enzyme substrate is introduced in the system and the background signal increases, which may lead to erroneous data interpretation. Therefore, using a microvalve, the introduction of positive errors during sequential measurements is drastically reduced.

Bead functionalisation

The reaction chamber of the microvalve is connected to the waste outlet during the process of functionalisation of the beads (Figure 8-2). This prevents the reagents from adsorbing and fouling the electrodes while the magnetic beads are functionalised inside the capture/reaction chamber. This represents a number of advantages such as volume reduction of sample and reagents, better reproducibility and possibility of automation.

In this case the magnetic beads are coated with streptavidin, which easily links to the biotynilated β-gal. The experiment consists in first introducing 50 μL of $53\mu g\cdot mL^{-1}$ magnetic beads at 50 $\mu L\cdot min^{-1}$ which are captured by the magnets under the microchamber. Next, $25\mu L$ of $10\mu g\cdot mL^{-1}$ concentration of β−gal is introduced at $50\mu L\cdot min^{-1}$ and the flow it is stopped for a short period of time. After the incubation, buffer solution (Buffer Z) is introduced at the same rate to clean and push the excess enzyme. When the microchamber is cleaned, a small volume of substrate (1mM) is injected and the flow is stopped for 10 minutes. This last step allows the enzyme to react with the substrate and build up a detectable concentration of the product. It also amplifies the detection, as described in Chapter 7. After this, the detection channel is opened and the product of the enzymatic reaction is pushed towards the electrodes at $10\mu L\cdot min^{-1}$ and detected by chronoamperometry. Figure 8-8 shows the results for different incubation times. As expected, there is a sigmoidal increase of the current with incubation time before a saturation value is achieved. This saturation means that no more biotynilated enzyme is available to link the streptavidin over the beads.
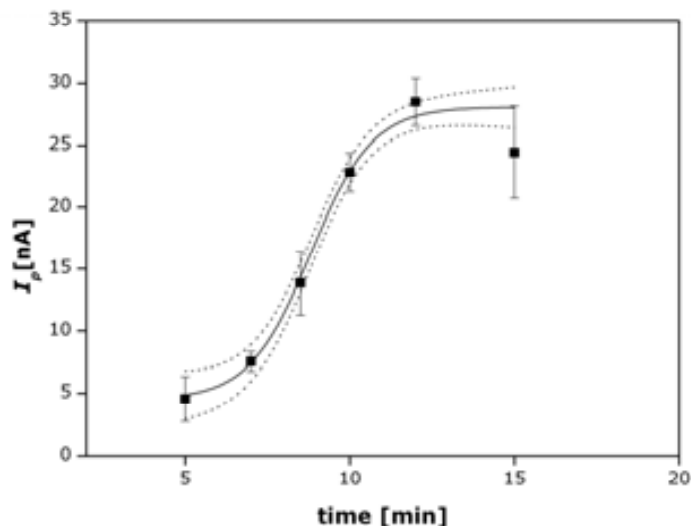
Figure 8-8: Stationary current at 0.25 V versus an Au pseudo-reference for a solution of 1 mM of substrate (PAPG) injected at 10 μL·min^{-1} for different incubation times between a known concentration of magnetic beads and enzyme.

8.4 Summary

We have described the fabrication of a rotary microvalve in PDMS and its integration in an electrochemical miniaturised analytical system. This integration has been possible thanks to the flexible architecture of the original system, which allowed the capture of magnetic beads and the electrochemical detection of electroactive products. The new system represents an improvement over the original system because it allows the physical separation of the various reaction and incubation steps, *e.g.*: functionalisation, necessary in bioassays from the detection event. This avoids contamination and fouling of the electrodes by proteins or other organic matter, and extends the useful lifetime of the detector.

We have described the design and fabrication of all the parts comprising our electroanalytical microsystem. The system is built from readily accessible materials, mainly PMMA and PDMS, using standard fabrication techniques such as milling, moulding and photolithography.

The main innovation is the open structure of the rotary microvalve, which is sealed on the one hand by the walls of the PDMS stator surrounding it, and on the other by the chip on which it sits. This suppresses the need to define the channels on the chip, which facilitates chip design, simplifies fabrication and ultimately reduces overall cost. But despite the fact that this rotary valve is used in this work to preserve a set of working electrodes, the concept can find application in other fields beyond electroanalysis; we have shown that, despite its sophistication, the system is easy to operate, very reliable, and allows the performance of operations such as capture of magnetic particles, their functionalisation with a model

enzyme, β-galactosidase, and reaction with a substrate, and the detection of the resulting electroactive products down to the low nanogram range.

We believe that this concept system can be used to develop a broad range of bioassays, which is the subject of ongoing work.

8.5 References

[1] Yin, H., K. Killeen, R. Brennen, D. Sobek, M. Werlich, and T. Van De Goor, *Microfluidic chip for peptide analysis with an integrated HPLC column, sample enrichment column, and nanoelectrospray tip.* Analytical Chemistry, 2005. 77(2): p. 527-533.

[2] Zhang, C., D. Xing, and Y. Li, *Micropumps, microvalves, and micromixers within PCR microfluidic chips: Advances and trends.* Biotechnology Advances, 2007. 25(5): p. 483-514.

[3] Francis, P.S., S.W. Lewis, K.F. Lim, K. Carlsson, and B. Karlberg, *Flow analysis based on a pulsed flow of the solution: theory, instrumentation and applications.* Talanta, 2002. 58: p. 1029-1042.

[4] Choi, J.W., K.W. Oh, J.H. Thomas, W.R. Heineman, H.B. Halsall, J.H. Nevin, A.J. Helmicki, H.T. Henderson, and C.H. Ahn, *An integrated microfluidic biochemical detection system for protein analysis with magnetic bead-based sampling capabilities.* Lab on a Chip - Miniaturisation for Chemistry and Biology, 2002. 2(1): p. 27-30.

[5] Do, J. and C.H. Ahn, *A polymer lab-on-a-chip for magnetic immunoassay with on-chip sampling and detection capabilities.* Lab on a Chip - Miniaturisation for Chemistry and Biology, 2008. 8(4): p. 542-549.

[6] Farrell, S., N.J. Ronkainen-Matsuno, H.B. Halsall, and W.R. Heineman, *Bead-based immunoassays with microelectrode detection.* Analytical and Bioanalytical Chemistry, 2004. 379(3): p. 358-367.

[7] Gabig-Ciminska, M., A. Holmgren, H. Andresen, K. Bundvig Barken, M. Wümpelmann, J. Albers, R. Hintsche, A. Breitenstein, P. Neubauer, M. Los, A. Czyz, G. Wegrzyn, G. Silfversparre, B. Jürgen, T. Schweder, and S.O. Enfors, *Electric chips for rapid detection and quantification of nucleic acids.* Biosensors and Bioelectronics, 2004. 19(6): p. 537-546.

[8] Gijs, M.A.M., *Magnetic bead handling on-chip: New opportunities for analytical applications.* Microfluidics and Nanofluidics, 2004. 1(1): p. 22-40.

[9] Goral, V.N., N.V. Zaytseva, and A.J. Baeumner, *Electrochemical microfluidic biosensor for the detection of nucleic acid sequences.* Lab on a Chip - Miniaturisation for Chemistry and Biology, 2006. 6(3): p. 414-421.

[10] Llopis, X., M. Pumera, S. Alegret, and A. Merkoçi, *Lab-on-a-chip for ultrasensitive detection of carbofuran by enzymatic inhibition with replacement of enzyme using magnetic beads.* Lab on a Chip - Miniaturisation for Chemistry and Biology, 2009. 9(9): p. 213-218.

[11] Verpoorte, E., *Beads and chips: new recipes for analysis.* Lab. Chip., 2003. 3: p. 60N.

[12] Muñoz-Berbel, X., N. Godino, O. Laczka, E. Baldrich, F.X. Muñoz, and F.J. del Campo, *Principles of Bacterial Detection: Biosensors, Recognition Receptors and Microsystems*, in *Impedance-Based Biosensors for Pathogen Detection* S.N. York, Editor. 2008.

[13] Duffy, D.C., J.C. McDonald, O.J.A. Schueller, and G.M. Whitesides, *Rapid prototyping of microfluidic systems in poly(dimethylsiloxane).* Analytical Chemistry, 1998. 70(23): p. 4974-4984.

[14] McDonald, J.C., D.C. Duffy, J.R. Anderson, D.T. Chiu, H. Wu, O.J.A. Schueller, and G.M. Whitesides, *Fabrication of microfluidic systems in poly(dimethylsiloxane).* Electrophoresis, 2000. 21(1): p. 27-40.

[15] Smistrup, K., M. Bu, A. Wolff, H. Bruus, and M.F. Hansen, *Theoretical analysis of a new, efficient microfluidic magnetic bead separator based on magnetic structures on multiple length scales.* Microfluidics and Nanofluidics, 2008. 4(6): p. 565-573.

[16] Rossier, J., F. Reymond, and P.E. Michel, *Polymer microfluidic chips for electrochemical and biochemical analyses.* Electrophoresis, 2002. 23(6): p. 858-867.

[17] Rossier, J.S. and H.H. Girault, *Enzyme linked immunosorbent assay on a microchip with electrochemical detection.* Lab on a Chip - Miniaturisation for Chemistry and Biology, 2001. 1(2): p. 153-157.

[18] Warsinke, A., A. Benkert, and F.W. Scheller, *Electrochemical immunoassays.* Fresenius' Journal of Analytical Chemistry, 2000. 366(6-7): p. 622-634.

[19] Compton, R.G., A.C. Fisher, R.G. Wellington, P.J. Dobson, and P.A. Leigh, *Hydrodynamic Voltammetry with Microelectrodes. Channel Microband Electrodes: Theory and Experiment.* Journal of Physical Chemistry, 1993. 97: p. 10410-10415.

[20] Bard, A.J. and L.R. Faulkner, *ELECTROCHEMICAL METHODS. Fundamentals and Applications*. 2nd ed. 2001, New York: John Wiley & sons.

[21] Laczka, O., E. Baldrich, F.J. Del Campo, and F.X. Muñoz, *Immunofunctionalisation of gold transducers for bacterial detection by physisorption.* Analytical and Bioanalytical Chemistry, 2008. 391(8): p. 2825-2835.

CHAPTER 9: Conclusions

The main results presented in this thesis are:

Simulations can be used to describe and explain mass transport to microelectrodes and their arrays. This was the first step in the evolution of simulations as optimisation, validation and prediction tool. Before using simulations to study real and complex devices, it was necessary to perform basic models which could be validated with well-know theoretical results. That is why we first modelled amperometric detection using microelectrodes under different conditions (stagnant and hydrodynamic). Then we moved on to the simulation of microelectrode arrays composed by recessed microelectrodes. In all cases, the models agreed well with experimental data.

Simulations uncovered metabolic parameters of a biofilm in a microrespirometry application. We have used simulations to successfully model an existing device, namely a microrespirometer used to determine the toxicity of certain water samples. We were able to use simulation as validation and inspection tool. Using simulations we were first able to model an array of recessed electrodes, based on the results of the basic models defined on Chapter 4. For that model, it was necessary to use diffusion domain approach, to model a disk microelectrode array, and the effect of the recess in the total current. Other parts of the microrespirometer were also included in the study. First, the protective Nafion layer thickness was estimated using simulation, fitting experimental data. The result was in clear agreement with the data obtained by perfilometry. Finally, the complete device was simulated and metabolic biofilm information, biofilm respiration rate constant, was extracted from the modelled results, which was in good agreement with the optical measurements made previously. So, we believe that similar models can be built and used to extract bacterial metabolic information from a relatively simple electrochemical set-up and that it can be a very valuable tool in the determination of parameters related to the toxicity of a sample.

Simulation of mass transport to nanoelectrode arrays requires 3D models. Simulations were used for prediction and validation. Based on the knowledge of simulating disk microelectrode arrays, we built a two- dimensional disk nanoelectrode array model and such model was compared with the experimental results found in the literature. The lack of agreement between our simulations and

previously published data encouraged us to fabricate disk nanoelectrode arrays using e-beam, and thus obtain our own experimental data. Those results were in agreement with the bibliographic data and in disagreement with the two dimensional model based on diffusion domain approach. However, three dimensional models did in fact agree with experiment. We concluded that that theoretical paradigms that were valid for microelectrode arrays and nanopatterned macroelectrodes were unsuitable for the study of nanoelectrode arrays. Simulations showed that radial diffusion to nanoelectrode arrays is even more important than in microelectrode arrays, and hence theoretical approaches that were valid for the latter may be no longer applicable to nanoelectrode arrays of micrometric size.

Band microelectrodes were integrated in a versatile lab on a chip combining electrochemical detection and magnetic beads. An easy-to-use and reusable microdevice was fabricated using fast prototyping techniques and materials like PDMS, PMMA and polycarbonate. We have demonstrated its operation and possible applicability to the field of bioassays and that it could be used in any enzyme-based bioassay. Sequential measurements could be performed as the magnetic field could be blocked sliding an iron slab between the chip and the permanent magnets fitted in the holder. The part in the system most likely to get damaged by use is the detector, as microelectrodes may be easily fouled after several measurements. This microdevice was designed to allow for easy microchip replacement without any further modification. The replacement could be done just opening the polymer holder and changing the chip for a new one.

Simulations enabled the optimisation of detection in our miniaturised system. The microdevice presented in this thesis has two chambers: one where magnetic beads are captured and a second one downstream where detection takes place. The capture chamber was placed upstream from the detectors, as this was the optimum position according to simulation. Such configuration allowed us to enhance the detection sensitivity controlling the flow rate. We operated under stopped-flow conditions for a short period of time. During this time the reaction proceeded under stagnant conditions and its rate was controlled by diffusion of the substrate to the bead surface. Next, the pump was switched on and this volume was pushed over the working microband obtaining considerable current increases. Moreover, the experimental results were supported by simulations to better justify why this way of working improve sensitivity so much.

A rotary microvalve reactor was integrated in a microfluidic electroanalytical system. Integrating a microvalve was a necessary step to

perform certain operations on the same microfluidic device. Such microvalve was fabricated using the same materials (PDMS and polycarbonate) as the microdevice where it was integrated, so using the same fast prototyping techniques. The novelty lied in the smart design which contains a microreactor within the microvalve so that various reaction and incubation steps could be carried out in isolation from the detection and any dead volume is introduced. Moreover, using a microvalve contamination and fouling of the electrodes by organic matter is highly reduced, so the useful lifetime of the detector is successfully extended.

In summary, the broad objectives set at the beginning of the thesis, consisting in the combined use of numerical simulations and microfabrication techniques have been successfully achieved. Simulations were a fundamental part in the process of optimisation, validation and prediction throughout the different works performed, and microelectrodes were successfully integrated in microfluidic devices, since versatile, easy-to use and re-usable microdevices were fabricated. Considering these two new lines, the future work may focus on exploring new electrode materials and configurations, and how these changes may further enhance detection. Further, more complex and realistic models may be developed to simulate other electrochemical techniques, and which account for nonidealities stemming from ohmic resistance in microchannels, or cross talk between the different microelectrodes integrated in a coplanar system.

The long term goal of this line of miniaturised electroanalytical systems is to create new opportunities for Electroanalysis, and turn it into a valuable asset beyond academic research.

ANNEX 1: Study of electrode kinetics

We study the effect of the electrode kinetics on the current using cyclic voltammetric models. First, there is a theoretical introduction to the effect and later, macro- and microelectrode models are presented.

During the thesis we have always considered fast electron transfer at the electrode, which means electron transfer rates of 0.1 m·s^{-1}. Under these conditions, the electrons exchanged are limited by the diffusion rate of the electroactive material from the bulk to the electrode, which is electrochemically reversible. However, real electrodes can present electron transfer rate values between 1 and 10^{-5} cm·s^{-1} [1, 2], which represent slower electron transfers. In this section, we use cyclic voltammetry to demonstrate that electron transfer limited system can also be simulated are also possible to simulate using COMSOL Mutiphysics.

The case of totally reversible system was described in Chapter 4. In that case, the current peak for oxidation and reduction processes is defined by:

$$I_p = 0.4463nFAc\sqrt{\frac{nFDv}{RT}} \tag{1}$$

where F is the Faraday constant, R the gas constant, T de temperature, n the number of exchanged electrons, A the electrode area, D the diffusion coefficient, $[R]_o$ the initial concentration and v the scan rate.

If the system is irreversible from the perspective of electron transfer, which means that the electrode kinetics is not fast enough to keep Nernst equilibrium at the electrode surface [3], then the nernstian boundary condition equation is replaced by:

$$\frac{I}{nFA} = D_R \left.\frac{\partial\left[R(x,t)\right]}{\partial x}\right|_{x=0} = k_b(t)\left[R(0,t)\right] \tag{2}$$

Where $k_b(t)$ is the electron transfer rate constant for the oxidation reaction, defined in Chapter 1. This rate constant depends on potential so given that in this case the potential is a function of time, the rate constant is presented as time-dependent. Diffusion equations together with this new boundary condition were also solved by Nicholson and Shain in [4]. If only one electron is involved in the process, then the peak current is described by:

$$I_p = 0.4958\left(\frac{\alpha F^3}{RT}\right)^{1/2} AD_R^{1/2}\left[R\right]_o v^{1/2} \tag{3}$$

Therefore, any experimental peak current must be found between both peak current values (equations (1) and (3)). These equations represent the limiting cases of a totally reversible system (equation (1)) and totally irreversible system (equation (3)), and most real systems are halfway between these two cases.

Peak current value and separation between peaks are related to electrode kinetics as well as coupled homogeneous chemical reactions, e.g.: the separation between the oxidation peak ($E_{p,a}$) and the reduction peak ($E_{p,c}$) is an indicator of the electron transfer rate. For a totally reversible system, the separation between the two peaks is described by [1]:

$$\Delta E_p = 2.218 \frac{RT}{nF} \tag{4}$$

Next we will show the effect electrode kinetics on the simulated voltammetric response. Cyclic voltammograms were simulated considering different values of electro transfer rate constants from totally reversible to an irreverble electrode kinetics.

The potential function used in the cyclic voltammetry simulations is:

$$E = E_i + \upsilon t \qquad 0 \le t \le \lambda$$
$$E = E_i + 2\upsilon\lambda - \upsilon t \qquad t > \lambda \tag{5}$$

The initial potential, E_i, is a value where specie R is stable and the potential is swept in the positive direction allowing the oxidation of specie R so creating specie O. At certain point, λ, the swept direction is switched. To study the effect of the electron transfer irreversibility in the measured current, the scan rate, υ, is kept constant (100 mV·s^{-1}) and the electronic transfer constant, k_s, is parametrized for certain values: 10^{-1} m·s^{-1}, $5 \cdot 10^{-2}$ m·s^{-1}, 10^{-2} m·s^{-1}, $5 \cdot 10^{-3}$ m·s^{-1}, 10^{-3} m·s^{-1}, $5 \cdot 10^{-4}$ m·s^{-1}, 10^{-4} m·s^{-1}, $5 \cdot 10^{-5}$ m·s^{-1}, 10^{-5} m·s^{-1}, $5 \cdot 10^{-6}$ m·s^{-1} and 10^{-6} m·s^{-1}.

Figure 1 shows the modelled adimensional current Ψ for a planar macroelectrode, which is calculated as:

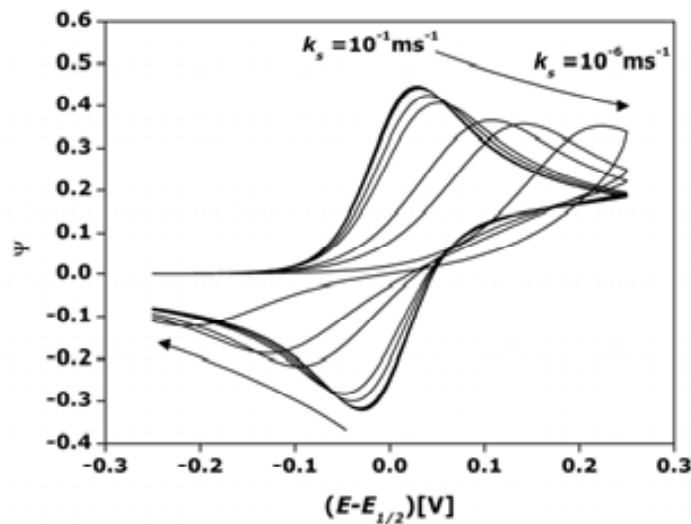$$\Psi = \frac{I}{\left(\dfrac{F^3}{RT}\right)^{1/2} A D_R^{1/2} [R_o] \upsilon^{1/2}} \tag{6}$$

Figure 1: Adimensional current for a macroelectrode vs applied potential. The arrow shows the electron transfer decrease. Such effect means a peak current displacement as well as peak current decrease. The electron transfer values used are: 10^{-1}, $5 \cdot 10^{-2}$, 10^{-2}, $5 \cdot 10^{-3}$, 10^{-3}, $5 \cdot 10^{-4}$, 10^{-4}, $5 \cdot 10^{-5}$, 10^{-5}, $5 \cdot 10^{-6}$ and 10^{-6} m·s^{-1}. Conditions: $[R]_o=1$ mol·m^{-3}, $k_s=0.1$ m·s^{-1}, $\alpha=0.5$, n=1 and $D_O=D_R=6.5 \cdot 10^{-10}$ m^{2}s^{-1}.

Table 1 shows the adimensional peak current for the oxidation process ($\Psi_{p,a}$) and the peak-to-peak separation (ΔE_p). A totally reversible system has an adimensional current value of 0.446 and for a totally irreversible this value is 0.351. The potential difference between the oxidation ($\Psi_{p,a}$) and the reduction peak ($\Psi_{p,c}$) is also an indicator of the reversibility of the system. For a totally reversible system with one exchanged electron the potential difference between both peaks is 57 mV. As shown in Table 1, there is good agreement between the simulated results and the theoretical values for totally reversible (high electron transfer rate constant) and totally irreversible (low electron transfer rate constant) electrode kinetics. For electron transfer rate constant values lower than $5 \cdot 10^{-4}$ m·s^{-1}, the difference between $\Psi_{p,a}$ and ΔE_p from the totally reversible system to the modelled values are higher than 10%, so it means that the system can not be considered reversible anymore and it is in quasi-reversible conditions. This difference is also possible to appreciate graphically in Figure 1, values below $5 \cdot 10^{-4}$ m·s^{-1} have significant changes in the voltammogram shape. For electron transfer rate of 10^{-6} m·s^{-1}, the current peak value is 0.351 as the value expected for a totally irreversible system.

Table 1: Adimensional current peak and separation between oxidation and reduction peak for a macroelectrode at different electron transfer values as shown in Figure 1.

k_s[ms^{-1}]	$\Psi_{p,a}$ [Am^{-2}]	ΔE_p[V]
10^{-1}	0.446	0.058
$5 \cdot 10^{-2}$	0.446	0.058
10^{-2}	0.446	0.058
$5 \cdot 10^{-3}$	0.446	0.059
10^{-3}	0.443	0.060
$5 \cdot 10^{-4}$	0.441	0.062
10^{-4}	0.423	0.080
$5 \cdot 10^{-5}$	0.407	0.099
10^{-5}	0.364	0.203
$5 \cdot 10^{-6}$	0.356	0.269
10^{-6}	0.351	0.434

In the microelectrode case, irreversibility is reflected as the displacement of the steady state current value towards higher potentials [1]. Figure 2 shows the simulated values for a microdisk of 1 μm radius, a scan rate of 100 mV·s^{-1} and electronic transfer constants: 10^{-1} ms^{-1}, $5 \cdot 10^{-2}$ ms^{-1}, 10^{-2} ms^{-1}, $5 \cdot 10^{-3}$ ms^{-1}, 10^{-3} ms^{-1}, $5 \cdot 10^{-4}$ ms^{-1}, 10^{-4} ms^{-1}, $5 \cdot 10^{-5}$ ms^{-1}, 10^{-5} ms^{-1}, $5 \cdot 10^{-6}$ ms^{-1} and 10^{-6} ms^{-1}.
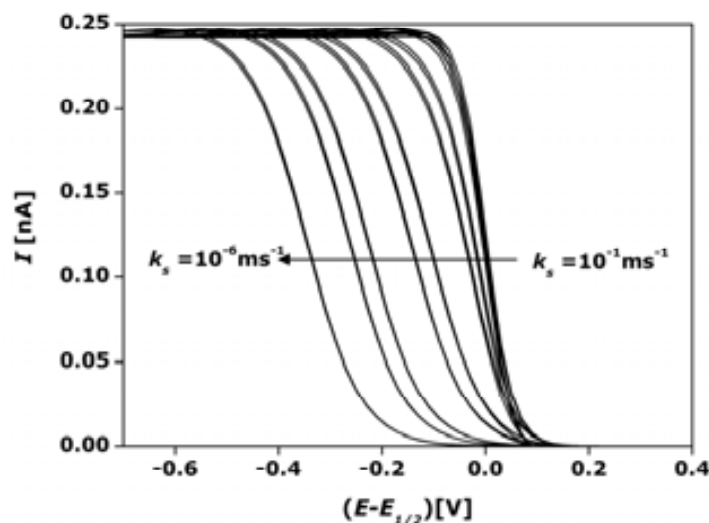
Figure 2: Current values for a microdisk of 1 μm radius. The arrow shows the electron transfer decrease. Such effect means a steady state current displacement towards higher $|E-E_{1/2}|$. The electron transfer values used are: 10^{-1}, $5 \cdot 10^{-2}$, 10^{-2}, $5 \cdot 10^{-3}$, 10^{-3}, $5 \cdot 10^{-4}$, 10^{-4}, $5 \cdot 10^{-5}$, 10^{-5}, $5 \cdot 10^{-6}$ and 10^{-6} m·s^{-1}. Conditions: $[R]_o$=1 mol·m^{-3}, k_s=0.1 m·s^{-1}, α=0.5, n=1 and $D_O=D_R$=6.5·10^{-10} m^{2}s^{-1}.

In that case, the graphical difference can be appreciated for higher electronic transfer constants compared to the planar macroelectrode case. For electronic transfer constants around 10^{-3} m·s^{-1} it is possible to see a certain difference between the voltammogram shape comparing to the total reversible case. So, as it was expected microdisk electrodes are faster compared to planar macroelectrode and changes in the electronic transfer are detected at higher transfer constant values.

To sum up, irreversibility effect can be perfectly modelled with our cyclic voltammetry models. Although electrode kinetics can also be successfully simulated using COMSOL, the models presented in this thesis assume fast electron transfer.

References:

[1] Allen J. Bard, L.R.F., *ELECTROCHEMICAL METHODS. Fundamentals and Applications*. 2nd ed. 2001, New York: John Wiley & sons.
[2] Scholz, F., ed. *Electroanalytical Methods: Guide to Experiments and Applications*. 2002, Springer.
[3] Cooper, J.A. and R.G. Compton, *Channel electrodes - A review*. Electroanalysis, 1998. 10(3): p. 141-155.
[4] Nicholson, R.S. and I. Shain, *Theory of Stationary Electrode Polarography - Single Scan + Cyclic Methods Applied to Reversible Irreversible + Kinetic Systems*. Analytical Chemistry, 1964. 36(4): p. 706-&.

ANNEX 2: Wall effect in channel microelectrodes

This short article is a contribution to the 2007 COMSOL held in Grenoble (France). It focuses on the study of the wall effect in the measured current within microfluidic channels. For that purpose, two and three dimensional models of a channel microband electrode were built. The study is based on the suitability of using two dimensional models when the microband electrodes are not centered inside the microchannel but they span over the full channel width.

Microband Electrodes in Microchannels: Edge diffusion and Wall effects.

Neus Godino[1], F. Javier del Campo[*,2] and F. Xavier Muñoz[1]

[1]Instituto de Microelectrónica de Barcelona, IMB-CNM-CSIC, Esfera UAB, 08193 – Bellaterra, Barcelona, Spain [2]Institut de Biotecnologia i Biomedicina "Vicent Pallar Palasí", Universitat Autónoma de Barcelona, 08193-Bellaterra, Barcelona, Spain.

*Corresponding author: [2]Institut de Biotecnologia i Biomedicina "Vicent Pallar Palasí", Universitat Autónoma de Barcelona, 08193-Bellaterra, Barcelona, Spain, fjcampo@cnm.es

Abstract: Microfluidics enables the miniaturisation and integration of sensors in advanced analytical devices. Electrochemical detection is currently one of the preferential techniques of use in microfluidic devices due to its sensitivity, low cost and compatibility with new microfabrication techniques. [1]

In this work, we first model the electrochemical response of a set of microband electrodes placed inside a microfluidic duct of square or rectangular section. Our aim is to determine how accurately can a 2D model predict the behaviour of a microband embedded in a microchannel, and compare it with Levich's current predictions for a range of flow rates. Our 2D model successfully accounts for "Edge" diffusion effects at the microelectrodes, which are responsible for significant deviations from classical Levich-type behaviour. This is particularly so at low flow rates. However, 2D models still fail to account for other flow effects that may occur in the vicinity of the channel walls. Can 2D models still be used to model microchannels?

Keywords: Microfluidics, Electrochemistry, Microband Electrodes.

1. Introduction

Electrochemical detection is currently one of the preferential techniques of use in microfluidic devices due its sensitivity, low cost and compatibility with new microfabrication techniques. Modelling the response of this kind of devices is a challenging but important task. At the design stage, it can be a key cost saving tool, helping to choose between different arrangements of the system components. After fabrication, numerical modelling may help in the assessment of the system performance, but it can also provide insight into mechanistic information which may lead to novel applications and technological breakthroughs.

Hydrodynamic electrochemistry encompasses a range of techniques in which a solution containing electroactive species is made to move under laminar flow conditions over an electrode surface, so as to allow diffusion to control the final approach of material to the electrode through a steady *diffusion layer*. One example of such hydrodynamic methods are channel flow cells. These devices consist of a square section duct hosting smoothly embedded electrodes (typically rectangular) in one of their faces. The electrodes are positioned in a region where the flow profile is fully developed so that the current data can be interpreted according to Levich's equation for a band electrode [2]:

$$I = 0.925 n F c w \left(x_e D \right)^{2/3} \left(\frac{U}{h^2 d} \right)^{1/3} \qquad [1]$$

Where I is the steady state current, F the Faraday constant, 96485 C mol^{-1}, x_e is the electrode length, c the bulk concentration of the electroactive species, w is the electrode width, U is the flow rate, d is the channel width and 2h the channel height. Levich [3] reached this expression based on the assumptions that (i) the flow is laminar, (ii) that The parabolic profile of the velocity can be approximated to a linear function in the vicinity of the walls and (iii) that axial diffusion can be neglected so that the only contributions to mass transport to the electrode arise from axial convection and normal diffusion (diffusion is perpendicular to the walls). This set of conditions are usually met by most macroscopic systems. In order to validate the electrochemical results obtained by channel electrodes it is necessary to know the hydrodynamic conditions accurately. Some authors show more caution and postulate that the electrodes should not reach the channel walls, so that the effect of the walls on the lateral flow profile does not affect the observed current [2, 4]. This ensures fulfilment of Eq. 1 for most cells of macrometric dimensions. However, deviations from ideality are more likely as the scale of the

channels and the electrodes is reduced. In spite of this, it may be interesting to use microbands that extend over the full channel width in order to obtain larger currents as well as simplifying the fabrication of the device. In this work, we discuss the effect of the walls in the electrochemical current, and the optimal geometrical features of the channel in order to obtain 2D model which describe correctly such current.

Microelectrodes are known to experience very high mass transport rates due to the relative importance of *edge diffusion* compared to electrodes of millimetric size [5]. In this work we study the behaviour of a microband electrode in a microchannels of different dimensions. In a first approach we developed 2D models and assessed their validity versus previously published data [2, 4, 6] as well as Levich's prediction. Our results were in good agreement with both, which proved the validity of our work. However, these models only account for the average flow velocity but neglect the effect of the side walls on mass transport. To overcome this, we defined 3D models and compared the results to their 2D counterparts. According to our results, there are cases in which the differences between the currents obtained from the 2D approximation and the full blown 3D model are virtually inexistent. This means that, in many practical cases, the balance between accuracy and computational effort will shift towards the simpler 2D approach. Here we attempt to present a set of conditions where a 2D model already describes the behaviour of a microchannel electrode correctly.

2. Theory and Governing Equations
The models described here were developed using the Chemical Engineering module of COMSOL 3.3a. The fluidics and Electrochemical sides of the problem were defined separately and eventually coupled to reach the final solutions. In this section we will outline the basic equations and boundary conditions used in the model.

1.1 Defining the Electrochemistry
In this work, we consider a reversible one-electron reduction of a specie O:

$$O + e^- \rightleftharpoons R \qquad\qquad [2]$$

Mass transport is governed by convection and diffusion. Migration effects may be neglected due the presence of an excess of supporting electrolyte [7]. Therefore, for the stationary state, the three dimensional mass transfer equation is described by:

$$D_o\left(\frac{\partial^2 c_o}{\partial^2 x} + \frac{\partial^2 c_o}{\partial^2 y} + \frac{\partial^2 c_o}{\partial^2 z}\right) - \left(v_x\frac{\partial c_o}{\partial x} + v_y\frac{\partial c_o}{\partial y} + v_z\frac{\partial c_o}{\partial z}\right) = 0 \; [3]$$

where D_O is the diffusion coefficient of the electroactive species, considered here as $6.5 \cdot 10^{-10} m^2 s^{-1}$, c_o is the inlet concentration of the species considered, and (v_x, v_y, v_z) are the three components of the velocity of the fluid.

The boundary conditions at the electrode is that electron transfer at the electrode follows Butler-Volmer type kinetics [7]:

$$j = j_0 \frac{c_o}{c_o^0}\exp\left[\frac{-\alpha F}{RT}(E - E^{o'})\right] \qquad\qquad [4]$$

where j_0 is the exchange current density, α is the charge transfer coefficient, which was set to 0.5 in our models, $E^{o'}$ is the formal potential, F is the Faraday constant, R is the universal gas constant, T is the temperature and c_o^0 is the concentration value of species O in the bulk solution or at the channel inlet.

The electrochemical current measured by a microband electrode is calculated as:

$$I = -dFD_o \int_0^{x_e}\left(\frac{\partial c_o}{\partial y}\right)_{y=0} dx \qquad microband \begin{cases} 0 \le x \le x_e \\ y = 0 \end{cases} [5]$$

The Convection and Diffusion mode of the Chemical Engineering module of COMSOL Multiphysics 3.3a was used to implement the model.

1.2 Defining the Fluidics
Regarding the fluid motion inside the microchannel, we consider a Newtonian and incompressible fluid. Thus, the three dimensional steady-state incompressible Navier-Stokes and the continuity equation are described by:

$$\rho\left(v_x\frac{\partial v_x}{\partial x} + v_y\frac{\partial v_x}{\partial y} + v_z\frac{\partial v_x}{\partial z}\right) - \eta\left(\frac{\partial^2 v_x}{\partial x^2} + \frac{\partial^2 v_x}{\partial y^2} + \frac{\partial^2 v_x}{\partial z^2}\right) + \frac{\partial p}{\partial x} = 0$$

$$\rho\left(v_x\frac{\partial v_y}{\partial x} + v_y\frac{\partial v_y}{\partial y} + v_z\frac{\partial v_y}{\partial z}\right) - \eta\left(\frac{\partial^2 v_y}{\partial x^2} + \frac{\partial^2 v_y}{\partial y^2} + \frac{\partial^2 v_y}{\partial z^2}\right) + \frac{\partial p}{\partial y} = 0 \; [6]$$

$$\rho\left(v_x\frac{\partial v_z}{\partial x} + v_y\frac{\partial v_z}{\partial y} + v_z\frac{\partial v_z}{\partial z}\right) - \eta\left(\frac{\partial^2 v_z}{\partial x^2} + \frac{\partial^2 v_z}{\partial y^2} + \frac{\partial^2 v_z}{\partial z^2}\right) + \frac{\partial p}{\partial z} = 0$$

$$\frac{\partial v_x}{\partial x} + \frac{\partial v_y}{\partial y} + \frac{\partial v_z}{\partial z} = 0 \qquad\qquad [7]$$

where ρ is the density of water, considered 10^3kgm^{-3}, η is the viscosity of water, considered 10-3 Pa·s, and p is the hydrodynamic pressure.
The fluid movement is computed using the Incompressible Navier-Stokes mode from the Chemical Engineering module.

Figure 1 shows the three-dimensional channel with the microband electrode inside it. It also depicts the two dimensional section used in the simplifying 2D models.
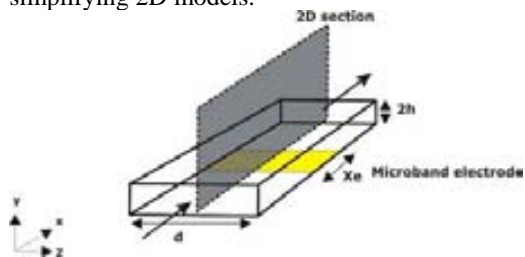

Figure 1 3D view of a microband electrode inside a microchannel, x_e is the microband length, d the microband and channel width and $2h$ the channel height. The shaded plane corresponde to the the 2D model domain.

3. Results and Discussion

Thus, when a microband electrode operates in a flow cell, there is a lower limit for the flow rate under which the current deviates from equation [1] because the contribution of axial diffusion becomes significant [2, 8]. This is shown in Figure 2, where a series of concentration profiles are depicted for the same microband working under decreasing flow rates.
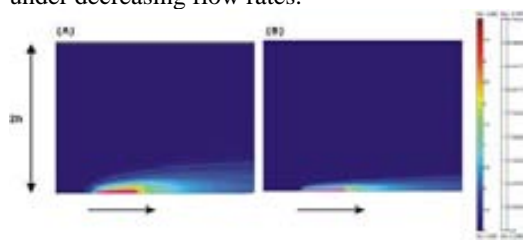

Figure 2 Concentration profiles around a microband electrode embedded in a microchannel. The effect of flow-rate on diffusion layer thickness is clear. (A) 1.7 m^{3}s^{-1} (B) 17m^{3}s^{-1}. The arrows show the direction of the flow.

Axial diffusion increases mass transport to the electrode, thus increasing the measured current and bringing about deviations from Eq. 1.
In order to quantify the contribution of axial diffusion we have computed the steady state electrochemical current measured by a microband electrode inside a channel, of $2h$=73μm and d=100μm. Figure 3 show the ratio between the current computed by the 2D model and the Levich equation (equation [1]) The model was solved for a flow rate range from $2.2 \cdot 10^{-13}$ m^{3}s^{-1} to $7.3 \cdot 10^{-11}$ m^{3}s^{-1}. As the figure shows, the modelled current and the theoretical expression are practically identical at high flow rates, when the flow rate is sufficiently high to keep the diffusion layer at the upstream electrode edge under control. However, at low flow rates, positive deviations appear as a result of axial diffusion kicking in. In our particular example, at $7.5 \cdot 10^{-12}$m^{3}s^{-1} the difference between modelled current and Levich's expression is 5%. For flow rates under this value the axial diffusion must be taken into account to predict the system behaviour more faithfully.
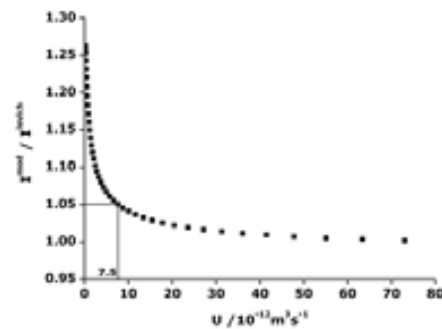

Figure 3 Ratio between modeled current (I^{mod}) and theoretical Levich current (I^{levich}) for a typical volumetric flow rate (U) range.

In addition to this effect of axial diffusion for decreasing flow-rates, there is a further effect that may need to be considered in systems where the electrode occupies the full width of the channel. This is the effect that of the walls, where the velocity of the solution is zero due to viscosity forces. This effect causes the diffusion layer thickness to grow in that region, as shown in figure 4.
In order to quantify such effect a 3D model of different channel widths for a 73μm of height were simulated. In all these cases the length of the microband was 20μm.
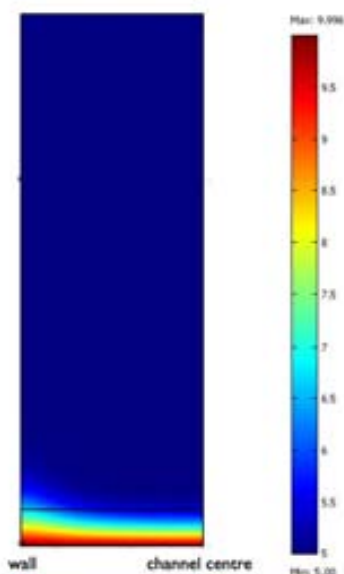
Figure 4.- Section of the concentration profile at the microband electrode. The image comes from a 3D model where wall effects are also accounted for.

Figure 5 shows the current density measured at different points over the microband width (*d*) for 3D and 2D models at channels 50μm and 200μm wide. In order to compare the results from both geometries the current density from the 3D model is normalized to match the 2D current value. The approximation in the 2D model is that the current density has the same value across the whole microband width. As we expected, the effect of the walls is more important as channel width decreases (Figure 5 B). There are more differences between the centre of the channel (d=0μm) and the wall (d=25μm)

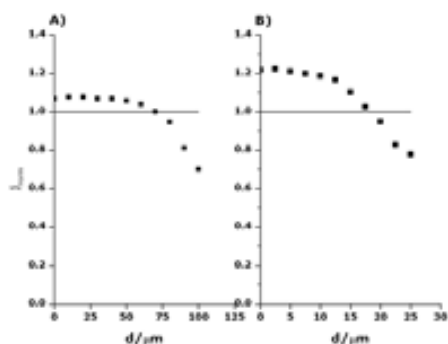**Figure 5 A) Current density at different points of a channel of 200μm of width: 3D model (■) and 2D model (solid line), d=0μm means the centre of the**

channel and d=100 m the wall. B) Current density at different points of a channel of 50μm of width: 3D model (■) and 2D model (solid line), d=0μm means the centre of the channel and d=25μm the wall.

The electrochemical current measured by the microband electrode is computed for a different channel width for 3D and 2D models at $1.7 \cdot 10^{-11}$ $m^3 s^{-1}$. The objective is to compare both current values and determine when the channel features do not influence the calculated current. Figure 6 shows the electrochemical current measured for 50μm, 73μm, 100μm and 200μm channel width. They are normalized to the channel width in order to compare the values for different widths.
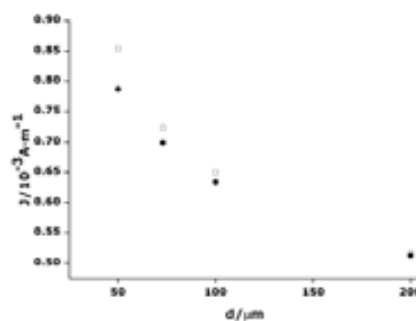

Figure 6 Current normalized to the width of the channel (d). The current is measured by the 3D model (□) and by the 2D model(●)

For 100μm of witdh and 73μm of height the difference between the electrochemical currents measured in 3D and 2D is about 2.5%. Therefore, at the modelled flow rate value for a channel witdh larger than 100μm, it is not strictly necessary to solve a more time consuming full 3D model to get sufficiently close estimates of current. While solving a 3D model may take several hours of computing time, it only takes several minutes to solve an analogous 2D problem.

It is interesting to point out that the relation between the width/height ratio at which the wall effects become significant depends heavily on flow rate. Thus, as flow rate increases, the effect of axial diffusion decreases, but "seeing" the channel walls becomes more likely. In any case, one must be extremely cautious when

interpreting empirical microfluidic data according to Levich's equation.

4. Conclusions

This work has shown the ability of COMSOL Multiphysics to successfully model the response of a microband electrode in a microchannel of square section, both in 2D and 3D.

Although ideally one should center the electrodes inside the channel and make the latter wider than the length of the electrodes in order to avoid *wall effects*, this approach may not be practical when the channels are already a few microns wide because the resulting currents may be too low. In such cases, the best way to increase the current is to make electrodes that span over the full channel width, even though wall effects may become significant at seemingly low flow rates. Simulation enables to determine whether such wall effects contribute significantly to the current, and hence use 3D modelling or if, on the other hand, a simpler 2D model will suffice.

2D models can predict the effect of axial diffusion on the overall current for a given volumetric flow, but they can not account for wall effects because they use a flow velocity profile based on an average linear velocity given the channel section. In other words, generally speaking, the velocity profiles obtained in 2D models are only approximations of the real velocity profile developing in the real system. 3D models, on the other hand, can cope with both kinds of effects and reflect the real situation more accurately but are extremely time consuming. In spite of this, we have shown that in are many cases, the information afforded by 2D models can be safely used to describe a real system. Therefore we advise the combined use of 3D and 2D models to ensure that the working conditions enable the use of the far less consuming 2D simulations.

5. References

1. L. Nyholm, Electrochemical techniques for lab-on-a-chip applications, *Analyst*, **130**,599 (2005).
2. R. G. Compton, A. C. Fisher, R. G. Wellington, P. J. Dobson, and P. A. Leigh, Hydrodynamic Voltammetry with Microelectrodes - Channel Microband Electrodes - Theory and Experiment, *Journal of Physical Chemistry*, **97**,10410 (1993).
3. V. G. Levich, Physicochemical Hydrodynamics, Prentice-Hall, Inc, Englewood Cliffs, N. J., 1962.
4. I. Henley and A. Fisher, Computational electrochemistry: A model to studying ohmic distortion of voltammetry in multiple working electrode, microfluidic devices, an adaptive FEM approach, *Electroanalysis*, **17**,255 (2005).
5. C. Amatore, in Phyical Electrochemistry. Principles, methods and applications (I. Rubinstein, ed.), Marcel Dekker, Inc.
6. S. M. Matthews, G. Q. Du, and A. C. Fisher, Microfluidic voltammetry: simulation of the chronoamperometric response of microband electrodes sited within microreactors, *Journal of Solid State Electrochemistry*, **10**,817 (2006).
7. L. R. F. Allen J. Bard, ELECTROCHEMICAL METHODS. Fundamentals and Applications, John Wiley & sons, New York, 2001.
8. J. A. Alden and R. G. Compton, Hydrodynamic voltammetry with channel microband electrodes: Axial diffusion effects, *Journal of Electroanalytical Chemistry*, **404**,27 (1996).

6. Acknowledgements

ANNEX 3:

Estimation of flow rate from experimental data

The simulation section of the article: On-Chip Electric Field Driven Electrochemical Detection Using a Poly(dimethylsiloxane) Microchannel with Gold Microband Electrodes, Olga Ordeig, Neus Godino, Javier del Campo, Francesc Xavier Muñoz, Fredrik Nikolajeff and Leif Nyholm. *Anal. Chem. 2008, 80, 3622–3632* was perfomed using the simulations of a channel microband electrode described in Chapter 4. In this article, such simulation was used to calculate the effect of leaks to flow rate.

On-Chip Electric Field Driven Electrochemical Detection Using a Poly(dimethylsiloxane) Microchannel with Gold Microband Electrodes

Olga Ordeig,[†,‡] Neus Godino,[†] Javier del Campo,[†] Francesc Xavier Muñoz,[†] Fredrik Nikolajeff,[§] and Leif Nyholm*,[‖]

Centro Nacional de Microelectrónica, IMB-CNM, CSIC, Campus de la Universidad, Autónoma de Barcelona, Esfera UAB, Bellaterra-08193, Spain, Department of Engineering Sciences, The Ångström Laboratory, Uppsala University, Box 534, SE-751 21 Uppsala, Sweden, and Department of Materials Chemistry, The Ångström Laboratory, Uppsala University, Box 538, SE-751 21 Uppsala, Sweden

An external electric field driven in-channel detection technique for on-chip electrochemical detection in micro fabricated devices is described based on a microfluidic system containing an array of 20 microband electrodes. It is shown that an external electric field induces a potential difference between two gold microband electrodes in a poly(dimethylsiloxane) (PDMS) microchannel, and that this enables the electrochemical detection of electroactive species such as ascorbic acid and $Fe(CN)_6^{4-}$. The results, which are supported by simulations of the behavior of the microband electrodes in the microfluidic system, show that the induced potential difference between the electrodes can be controlled by altering the external electric field or by using different microbands in the microband array. As the obtained currents depend on the concentrations of electroactive species in the flowing solution and the detection can be carried out anywhere within the channel without interference of the external electric field, the present approach significantly facilitates electrochemical detection in capillary electrophoresis. This approach consequently holds great promise for application in inexpensive portable chip-based capillary electrophoresis (CE) devices.

Microfluidics provides a way to miniaturize chemical analysis systems and can therefore enable rapid, low cost analyses that generate little chemical waste. Much effort has therefore been made to develop analytical devices based on microfluidic systems. Miniaturized electrophoresis devices have, up to now and by far, been the most widely developed devices due to their scalability and compatibility with the substrates available for device construction.[1,2] Electrophoresis has been used on-chip not only as a separation technique but also for fluid transport and mixing.

A significant advantage of using electrokinetically driven flow is that valves and macroscopic pumps become redundant when injecting and moving liquid samples.[3] Although capillary electrophoresis (CE) is frequently used in conjunction with absorbance and fluorescence detection,[4] electrochemical detection methods are receiving increasing attention for on-chip capillary electrophoresis applications due to their relatively low cost, high sensitivity, and portability.[5] Among electrochemical techniques, amperometric detection has been the most widely employed method in on-chip applications, since first described in 1987 by Wallingford and Ewing.[6] The main problems of using electrochemical detection in (conventional as well as on-chip) CE are caused by interferences due to the presence of the CE electric field[7] and uncertainties in the positioning of the electrodes with respect to the capillary, which may affect the reproducibility of the measurements.[8,9] The latter problem can, however, be minimized by the use of microfabricated systems in which the positions of the electrodes are fixed during the microfabrication process.[10–14] Reviews on the microfabrication of devices and/or applications involving electrochemical detection in on-chip capillary electrophoresis have also been published.[8,9,15,16]

* Corresponding author. E-mail: Leif.Nyholm@mkem.uu.se. Phone: +46 18 4713742.
† Campus de la Universidad, Autónoma de Barcelona.
‡ Present address: MIC-Department of Micro and Nanotechnology, DTU-Building 345east, DK-2800 Kongens Lyngby, Denmark.
§ Department of Engineering Sciences, The Ångström Laboratory, Uppsala University.
‖ Department of Materials Chemistry, The Ångström Laboratory, Uppsala University.

(1) Effenhauser, C. S.; Bruin, G. J. M.; Paulus, A. *Electrophoresis* **1997**, *18*, 2203–2213.
(2) Lacher, N. A.; Garrison, K. E.; Martin, R. S.; Lunte, S. M. *Electrophoresis* **2001**, *22*, 2526–2536.
(3) Stone, H. A.; Stroock, A. D.; Ajdari, A. *Annu. Rev. Fluid Mech.* **2004**, *36*, 381–411.
(4) Dolnik, V.; Liu, S. R.; Jovanovich, S. *Electrophoresis* **2000**, *21*, 41–54.
(5) Wang, J. *Talanta* **2002**, *56*, 223–231.
(6) Wallingford, R. A.; Ewing, A. G. *Anal. Chem.* **1987**, *59*, 1762–1766.
(7) Wang, K.; He, F. Y.; Liu, A. L.; Xu, J. J.; Chen, H. Y.; Xia, X. H. *Langmuir* **2006**, *22*, 7052–7058.
(8) Nyholm, L. *Analyst* **2005**, *130*, 599–605.
(9) Xu, J.-J.; Wang, A.-J.; Chen, H.-Y. *Trends Anal. Chem.* **2007**, *26*, 125–132.
(10) Dossi, N.; Toniolo, R.; Pizzariello, A.; Susmel, S.; Perennes, F.; Bontempelli, G. *J. Electroanal. Chem.* **2007**, *601*, 1–7.
(11) Yao, X.; Wang, J.; Zhang, L. Y.; Yang, P. Y.; Chen, G. *Talanta* **2006**, *69*, 1285–1291.
(12) Tsai, D.-M.; Lin, K.-W.; Zen, J.-M.; Chen, H.-Y.; Hong, R.-H. *Electrophoresis* **2005**, *26*, 3007–3012.
(13) Tsai, D.-M.; Tai, K.-W.; Shih, P.-R.; Chang, R.-L.; Wu, H.; Conte, E.-D.; Zen, J.-M. *Electroanalysis* **2005**, *17*, 1991–1994.
(14) Castano-Alvarez, M.; Fernandez-Abedul, M. T.; Costa-Garcia, A. *J. Chromatogr., A* **2006**, *1109*, 291–299.
(15) Pumera, M.; Merkoci, A.; Alegret, S. *Trends Anal. Chem.* **2006**, *25*, 219–235.

In general, the influence of the CE high voltage on electrochemical measurements results in high levels of noise and shifts in the detection potentials. To avoid or minimize these effects, either decouplers[17–20] or end-column detection[13,21–24] is currently used. In the first case, a new pathway for the CE current to ground is generated while the second approach is based on the fact that the potential drop at the end of narrow capillaries is small enough to allow amperometric detection. Although the end-column detection approach generally is the preferred decoupling method in conjunction with on-chip devices due to its less complicated implementation,[8] the use of palladium based decouplers has also been described.[19,20]

With the end-column detection approach, several techniques have been described to reduce the magnitude of the shift in the detection potential introduced by the separation electric field. One approach is based on the fact that the shift is decreased if the conductivity of the solution immediately outside the separation channel is increased.[8] Another possibility is to increase the distance between the working electrode and the end of the channel.[8,25,26] This, however, gives rise to increased band broadening. To enable electrochemical detection in the presence of the separation electric field, a floating high-voltage separation power supply[27] or an isolated potentiostat[10,28] can be employed. It should, however, be pointed out that this does not eliminate the shift in the potential between the working and the reference electrode induced by the separation electric field. Klett et al.[29] have, on the other hand, shown that the shift can be eliminated if the working and reference electrode are positioned in such a way that both electrodes are exposed to the same separation electric field induced potential. It was also shown[29] that the shift in the working electrode potential can be determined merely by measuring the potential difference between the working and reference electrode in the presence and absence of the separation electric field. A similar technique was employed by Forry et al.,[30] who used the shift in cyclic voltammetry peak potentials to determine the potential needed to compensate for the influence of the electric field when employing electrochemical detection in an electrophoresis channel.

While many reports have been devoted to the elimination of the influence of the CE separation electric field on electrochemical detection, a few groups have instead made use of the separation electric field in novel detection techniques.[31–34] Manz and co-workers[31] thus described a wireless electrochemiluminescence detector based on potential differences induced by a CE separation electric field while Klett and Nyholm[33] described a potentiostatless amperometric detection technique based on the use of the potential induced between microband electrodes positioned at different locations within the separation electric field. A technique analogous to the latter approach was subsequently used by Xu et al.[34] to determine electroinactive species based on the amperometric response of the oxygen dissolved in the solution. The presence of the CE separation electric field can also be used for conductivity detection as was demonstrated by Girault and co-workers.[32] A significant advantage of the separation electric field driven detection techniques is that this type of detection can be carried out anywhere within the separation channel. In the amperometric mode, which generally constitutes a very sensitive electrochemical detection technique, it would also be possible to alter the detection potential merely by selecting different pairs of electrodes with different locations within the channel. The use of many pairs of electrodes should also allow simultaneous detection at a number of different potentials. As Klett and Nyholm[33] merely used microband electrodes positioned at the end of a fused silica capillary to demonstrate electric field driven amperometric detection, further studies are, however, required to investigate the possibilities of the latter approach for on-chip detection within a microfabricated channel.

In this article, we describe an example of on-chip separation electric field driven amperometric detection. It is based on the use of a microfabricated flow system containing an array of 20 gold microband electrodes. The microband electrodes were characterized using cyclic voltammetry at different flow rates, and the obtained results were compared with simulations based on a two-dimensional model. In the presence of an external electric field, the potential difference between two microbands is shown to depend on the distance between the microbands and the electric field strength. The presence of this potential difference enables in-channel amperometric detection to be carried out in the absence of a potentiostat as is demonstrated for the oxidation of ascorbic acid and $Fe(CN)_6^{4-}$.

EXPERIMENTAL SECTION

Chemicals. Potassium hexacyanoferrate(II) (K_4FeCN_6), potassium hexacyanoferrate(III) (K_3FeCN_6), and ascorbic acid were supplied by Merck. Potassium nitrate was purchased from VWR (Prolabo). Sulfuric acid and 2-propanol (>99%) were obtained from Sigma-Aldrich. All chemicals were of analytical reagent grade, and all aqueous solutions were prepared using ultrapure deionized water (DI) (18 MΩ cm).

The microchannel substrates were produced by casting a mixture of poly(dimethyl siloxane) (PDMS) monomer and curing agent from Wacker-Chemie GmbH (München, Germany) on resist

(16) Wang, J. *Electroanalysis* **2005**, *17*, 1133–1140.
(17) Vickers, J. A.; Henry, C. S. *Electrophoresis* **2005**, *26*, 4641–4647.
(18) Kim, J. H.; Kang, C. J.; Jeon, D.; Kim, Y. S. *Microelectron. Eng.* **2005**, *78–79*, 563–570.
(19) Dawoud, A. A.; Kawaguchi, T.; Jankowiak, R. *Anal. Bioanal. Chem.* **2007**, *388*, 245–252.
(20) Mecker, L. C.; Martin, R. S. *Electrophoresis* **2006**, *27*, 5032–5042.
(21) Woods, L. A.; Ewing, A. G. *ChemPhysChem* **2003**, *4*, 207–211.
(22) Wang, J.; Chen, G.; Chatrathi, M. P.; Fujishima, A.; Tryk, D. A.; Shin, D. *Anal. Chem.* **2003**, *75*, 935–939.
(23) Wang, J.; Pumera, M.; Chatrathia, M. P.; Rodriguez, A.; Spillman, S.; Martin, R. S.; Lunte, S. M. *Electroanalysis* **2002**, *14*, 1251–1255.
(24) Wang, J.; Chen, G.; Chatrathi, M. P.; Musameh, M. *Anal. Chem.* **2004**, *76*, 298–302.
(25) Wallenborg, S. R.; Nyholm, L.; Lunte, C. E. *Anal. Chem.* **1999**, *71*, 544–549.
(26) Matysik, F.-M. *J. Chromatogr., A* **1996**, *742*, 229–234.
(27) Hebert, N. E.; Kuhr, W. G.; Brazill, S. A. *Anal. Chem.* **2003**, *75*, 3301–3307.
(28) Martin, R. S.; Ratzlaff, K. L.; Huynh, B. H.; Lunte, S. M. *Anal. Chem.* **2002**, *74*, 1136–1143.
(29) Klett, O.; Björefors, F.; Nyholm, L. *Anal. Chem.* **2001**, *73*, 1909–1915.
(30) Forry, S. P.; Murray, J. R.; Heien, M.; Locascio, L. E.; Wightman, R. M. *Anal. Chem.* **2004**, *76*, 4945–4950.
(31) Arora, A.; Eijkel, J. C. T.; Morf, W. E.; Manz, A. *Anal. Chem.* **2001**, *73*, 3282–3288.
(32) Bai, X. X.; Wu, Z. Y.; Josserand, J.; Jensen, H.; Schafer, H.; Girault, H. H. *Anal. Chem.* **2004**, *76*, 3126–3131.
(33) Klett, O.; Nyholm, L. *Anal. Chem.* **2003**, *75*, 1245–1250.
(34) Xu, J. J.; Bao, N.; Xia, X. H.; Peng, Y.; Chen, H. Y. *Anal. Chem.* **2004**, *76*, 6902–6907.

structured silicon wafers. SU-8 50 resist for master structuring was purchased from MicroChem (Newton). The conductive epoxy used to provide electric contact between the chip and the electrode connectors was supplied by Circuit Works (Lake Bluff).

Instrumentation. The cyclic voltammetric experiments were carried out with an Autolab (Eco-Chemie, Utrect, The Netherlands) system interfaced to a PC using the GPES (version 4.9) software for Windows. A PHD2000 infusion syringe pump (Harvard Apparatus, Holliston) and silicon tubing with an inner diameter of 0.56 mm (from Elfa, Järfälla, Sweden) were used to obtain a flow of solution through the microfluidic channel. The volumetric flow rates used in this work ranged from 1 to 10 μL min^{-1}. In the flow electrochemical measurements, a three electrode cell configuration was used with two microbands acting as working and counter electrodes and an additional microband as a quasi-reference electrode. The counter and reference electrodes were located downstream with respect to the working electrode to avoid interferences due to the counter electrode reactions.[35] Prior to the experiments, the gold microband electrodes were electrochemically activated by cycling the potential from −0.2 to +0.8 V (vs Au quasi-reference electrode) in a solution containing 0.050 M H_2SO_4 and 0.5 M KNO_3.

In the external electric field experiments, the potential difference and current between two gold microband electrodes were recorded using a Keithley 197A voltmeter and a Keithley 485 picoamperemeter (Keithley Instruments, Cleveland), respectively. The external electric field was obtained with a dc power supply by applying a potential difference of up to 50 V between two steel needles placed inside the silicon tubing at the inlet and the outlet of the microfluidic cell. All external electric field experiments were performed under laminar flow conditions employing a flow rate of 5 μL min^{-1}.

Microfabrication Procedures. The microfluidic device was manufactured through the assembly of two separate parts, an upper PDMS part containing the microfluidic channel and reservoir elements and a lower part containing the microband gold electrodes patterned on a Pyrex substrate. Schematic top and side-views of the devices are shown in Figure 1.

The SU-8 master utilized in the manufacturing of the microfluidic channel was fabricated on a 4 in. standard silicon wafer using soft-lithography. The first step of the fabrication process consisted of a careful cleaning of the wafer (using Standard Clean One (SC-1, $NH_4OH/H_2O_2/H_2O$, 65 °C) and Standard Clean Two (SC-2, HCl/H_2O_2, H_2O, 65 °C)) to guarantee good resist adherence. SU-8 50 resist was then spun on the wafer followed by prebaking, exposure to UV light through a CAD-designed chrome mask, and postbaking according to the supplier's recipe. The resist-coated wafer was developed and hard-baked for 30 min at 150 °C. The height and width of the resist pattern were found to be 77 and 95 μm, respectively, when measured with an optical profiler (Vecco, Woodbury). The inverse image of the SU-8 resist pattern was produced by casting PDMS polymer on the structured masters. PDMS prepolymer and curing agent were mixed (10:1 w/w). Air bubbles were removed by letting the PDMS mixture rest for an hour at −20 °C. The polymer mixture was poured over the masters and cured for 1 h at 70 °C in a furnace. After the structures were allowed to cool down, to avoid deformations, the polymer was
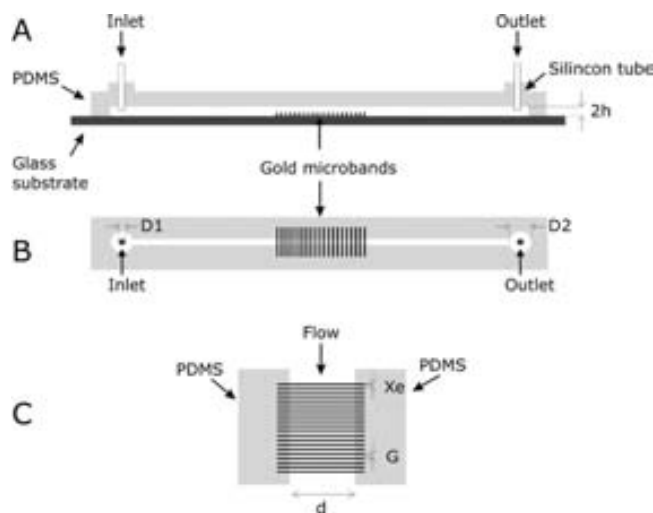
(35) Wang, J. *Analytical Electrochemistry*; Wiley-VCH: New York, 2001.

Figure 1. (A) Lateral and (B) top views of the microfluidic devices used in this work. (C) View of microband electrodes (Xe = 20 μm, G = 50 or 250 μm, d = 95 μm) in the microchannel (2h = 77 μm, d = 95 μm).

peeled off from the masters. Reservoir cavities were then punched in the substrate containing the channels. Small dice of cured PDMS containing a hole with a diameter of 0.56 mm were then bonded over the reservoirs by corona discharge. These dice facilitated the connection of silicon tubing to the microfluidic devices.

The lower Pyrex part of the microfluidic containing 20 parallel gold band electrodes each with a width of 20 μm and separated from their closest neighbor by either 50 or 250 μm was manufactured by lithographic and lift-off techniques. The electrode pattern was defined by a chrome optical mask replicated by lithography into a thin S-1813 photoresist layer spin coated on the Pyrex wafer. A 20 nm adhesion layer of Ti and a 100 nm layer of Au were then evaporated over the developed resist pattern. Once the desired metals had been deposited, the underlying resist was stripped in acetone. Unwanted metallic parts were lifted off, leaving the desired electrode pattern on the wafer. The chips were individually cut from the wafer using a diamond saw.

The PDMS microchannel part and the microelectrode array part were finally bonded together. Prior to this step, the surfaces of both parts were carefully cleaned with 2-propanol and deionized water to increase their hydrophobicity. After the surfaces were dried, the PDMS piece was exposed to corona discharge for about 25 s using a Tesla coil (ETP, Chicago, IL). The PDMS part was then placed perpendicularly over the set of parallel microbands on the Pyrex substrate. The closed structure was next kept at 70 °C during 1 h to produce irreversible bonding between the Pyrex and PDMS surfaces.

As is seen in Figure 1C, the effective length of the microband electrodes in the microchannel was defined by the microchannel width. The area of each microband electrode was hence 1.9 × 10^{-5} cm^2. The optical transparency of the PDMS allowed microscopic examinations of the state of the band electrodes during the experiments.

Safety Considerations. To avoid electrical shocks, the power supply should be handled with care.

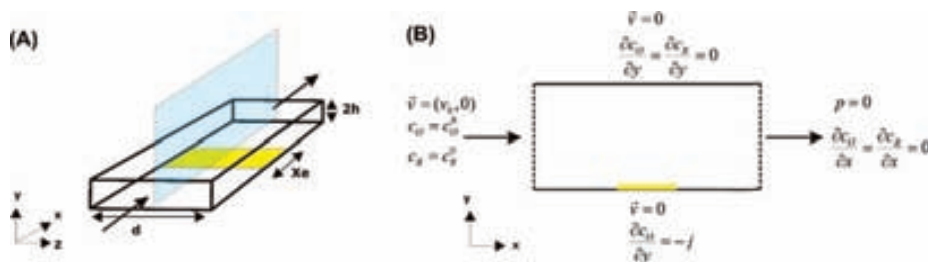**Figure 2.** (A) Three-dimensional view of a band microelectrode placed inside a microchannel, where $2h$ is the height of the channel (77 μm), d is the electrode width (95 μm), and x_e is the length of the band electrode (20 μm). The arrows show the flow direction. (B) Perpendicular plane of the microchannel used for the two-dimensional model simulations. The boundary conditions for the mass transport and fluid movement were defined next to the correspondent surface, where the straight lines represent the walls of the microchannel and the dashed lines the inlet and outlet, respectively.

SIMULATION

In this work, we used finite element techniques to characterize the microfluidic behavior of the device. The aim is to use the current measured at the microelectrodes in the microchannel to calibrate the flow. The presence of tiny leaks is common in this kind of PDMS microfluidic devices, and they are often quite difficult to avoid. The presence of leaks leads to an overestimation of the flow during the measurements. The simulation of microelectrode voltammetric characterization let us estimate the real flow inside the cell. Several authors have used electrochemical measurements or simulations in order to determine a range of fluidic parameters. Amatore et al.[36,37] present a method to reconstruct the velocity profile of a fluid flowing through a rectangular section channel, which is based on electrochemical simulations. Thompson and Compton[38] also studied the effect of the hydrodynamic velocity profile in electrochemical currents. In this case, they focus their work on the hydrodynamic information at the inlet of the channel, where the parabolic velocity profile is not achieved.

The two-dimensional model used in the simulations of the mass transport controlled limiting currents in the microfluidic channel, depicted in Figure 1, is based on mass transport by diffusion and convection. Migration effects were neglected as an excess of supporting electrolyte was used in the experiments. In the present work, we consider a reversible one-electron reduction of species O at the microband electrode:

$$O + e^- \rightleftharpoons R \tag{1}$$

Assuming that the electrode is fast enough to ensure that the current is mass transport limited,[39] then the current is given by the Levich expression.[40] For a microband electrode inside a rectangular section channel, it can be expressed as[41]

$$I = 0.925nFcw(x_e D)^{2/3}\left(\frac{4}{3}\frac{v_{max}}{h}\right)^{1/3} \tag{2}$$

(36) Amatore, C.; Klymenko, O. V.; Svir, I. *ChemPhysChem* **2006**, *7*, 482–487.
(37) Amatore, C.; Oleinick, A.; Klymenko, O. V.; Svir, I. *ChemPhysChem* **2005**, *6*, 1581–1589.
(38) Thompson, M.; Compton, R. G. *Anal. Chem.* **2007**, *79*, 626–631.
(39) Bard, A. J.; Faulkner, L. R. *Electrochemical Methods: Fundamentals and Applications*; Wiley: Chichester, U.K., 2001.
(40) Levich, V. G. *Physicochemical Hydrodynamics*; Prentice Hall: Englewood Cliffs, NJ, 1962.
(41) Compton, R. G.; Fisher, A. C.; Wellington, R. G.; Dobson, P. J.; Leigh, P. A. *J. Phys. Chem.* **1993**, *97*, 10410–10415.

where n is the number of exchanged electrons, F is the Faraday constant, c and D are the concentration and the diffusion coefficient of the electroactive species, h is half-the-height of the channel, x_e and w are the length and the width of the microband electrode and v_{max} is the maximum linear velocity. The latter was derived neglecting the axial diffusion as only axial convection and normal diffusion are relevant in a macroscopic system. In contrast to the Levich equation,[40] our simulations consider both axial and normal diffusion.

The influence of axial diffusion can, however, be significant for microelectrodes at low flow rates. To take this effect into account, the 2D rectangular section of the channel described in the Experimental Section was modeled. Figure 2 is a schematic representation of the two-dimensional channel section used and the boundary conditions assumed in the model used for the simulations. It is important to take in consideration that the electrode should be positioned sufficiently far from the inlet so that a Poiseuille profile is completely developed.[40] In our case the maximum inlet region is around 3 μm for a 10 μL min^{-1} flow rate. Under these conditions, the steady-state mass transport equation of the reactant, O, in the cell is

$$D_O\left(\frac{\partial^2 c_O}{\partial x^2} + \frac{\partial^2 c_O}{\partial y^2}\right) - \left(v_x\frac{\partial c_O}{\partial x} + v_y\frac{\partial c_O}{\partial y}\right) = 0 \tag{3}$$

where c_O is the concentration and D_O is the diffusion coefficient of species O, and (v_x, v_y) are the components of the velocity vector in the channel. To obtain the velocity field, the fluid is considered Newtonian and incompressible, so the steady-state incompressible Navier–Stokes (eq 4) and the continuity equation (eq 5) should be solved:

$$\rho\left(v_x\frac{\partial v_x}{\partial x} + v_y\frac{\partial v_x}{\partial y}\right) - \eta\left(\frac{\partial^2 v_x}{\partial x^2} + \frac{\partial^2 v_x}{\partial y^2}\right) + \frac{\partial p}{\partial x} = 0$$
$$\rho\left(v_x\frac{\partial v_y}{\partial x} + v_y\frac{\partial v_y}{\partial y}\right) - \eta\left(\frac{\partial^2 v_y}{\partial x^2} + \frac{\partial^2 v_y}{\partial y^2}\right) + \frac{\partial p}{\partial y} = 0 \tag{4}$$

$$\frac{\partial v_x}{\partial x} + \frac{\partial v_y}{\partial y} = 0 \tag{5}$$

where ρ and η are the density and the viscosity of the fluid, respectively, and p is the pressure. The boundary condition at the electrode is that the flux through the electrode is controlled by the applied potential, E, via the Butler–Volmer equation:[39]

$$j = j_0 \frac{c_O}{c_O^0} \exp\left[\frac{-\alpha F}{RT}(E - E^{0'})\right] \qquad (6)$$

where j_0 is the exchange current density, α is the symmetry transfer coefficient, $E^{0'}$ is the formal potential, and c_O^0 is the concentration value of species O in the bulk. If the charge transfer at the electrode is mass transport limited, the current can be calculated using Fick's first law.[39]

All the simulations were performed using COMSOL Multiphysics 3.3a (Comsol AB, Sweden) and Matlab 7.0.4 (MathWorks). The two-dimensional microband electrode model consisted of a plane perpendicular to the electrode surface, as it is shown in Figure 2. The values for the diffusion coefficients of ferrocyanide and ferricyanide, D, were both set to 6.5×10^{-10} m^2 s^{-1} [39] while the symmetry transfer coefficient, α, and the temperature were set to 0.5 and 298 K, respectively. The viscosity, η, of the flowing solution was taken as 10^{-3} Pa s while the density, ρ, was set to 10^3 kg m^{-3} (i.e., the viscosity and density of water at 25 °C).

RESULTS AND DISCUSSION

Electrode Characterization and Comparison with Simulations. Since the flow in the present microchannel was laminar, the diffusion layer thickness should be stable and reproducible and steady state voltammograms should be observed. This was also confirmed by the experiment as seen in Figure 3, which shows typical cyclic voltammetric responses of a gold microband electrode obtained with an equimolecular solution containing 5.0 mM ferrocyanide and ferricyanide in 0.5 M KNO$_3$ at different scan rates and a nominal flow rate of 5 μL min^{-1}. All the voltammograms present the expected sigmoidal shape, and it is also seen that the limiting current did not depend on scan rate. In these experiments, one of the gold bands was used as a quasi-reference electrode, and the potential of the latter was found to be -0.147 V vs SCE. The potential of the quasi-reference electrode was found to be stable during the experiments. The stability of the microband used as the working electrode was confirmed by comparing cyclic voltammograms at the same flow rate recorded prior to and after the experiments.

As the results in Figure 3 were obtained using a rather low flow rate (i.e., 5 μL min^{-1}), for which deviations from the Levich behavior could be expected, simulations were performed to investigate the influence of the flow rate on the steady state currents at low flow rates. Figure 4 shows the ratio between the current predicted by our two-dimensional model and the Levich equation (i.e., eq 2) for flow rates between 0 and 5 μL min^{-1}. The channel and electrode dimensions used in these simulations corresponded to those of the experimental device described in Figure 1. Figure 4 shows that the currents predicted by our model and the Levich equation are practically identical at high flow rates but that they become significantly different if the flow rate is decreased sufficiently. This can be explained by the fact that the Levich equation does not take neither edge diffusion at the microband electrodes nor channel wall effects into account. Thus, the limiting current may be underestimated by more than 5% for flow rates lower than 0.3 μL min^{-1} unless edge diffusion is considered. Our results show that radial diffusion at the edge of the microelectrodes needs to be taken into account at flow rates
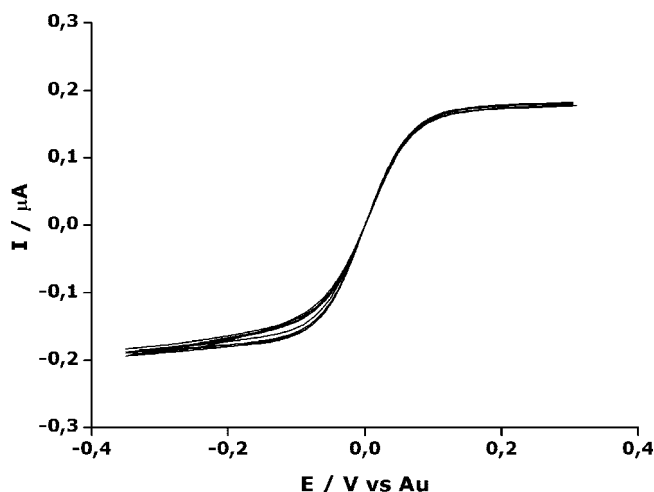

Figure 3. Cyclic voltammograms recorded at a scan rate of 25, 50, 75, and 100 mV s^{-1}, respectively, in a solution of 5.0 mM ferrocyanide, 5.0 mM ferricyanide, and 0.5 M KNO$_3$ at a flow rate of 5 μL min^{-1} with a gold microband as a quasi-reference electrode. The microbands were 20 μm wide, and the interelectrode distance was 50 μm.
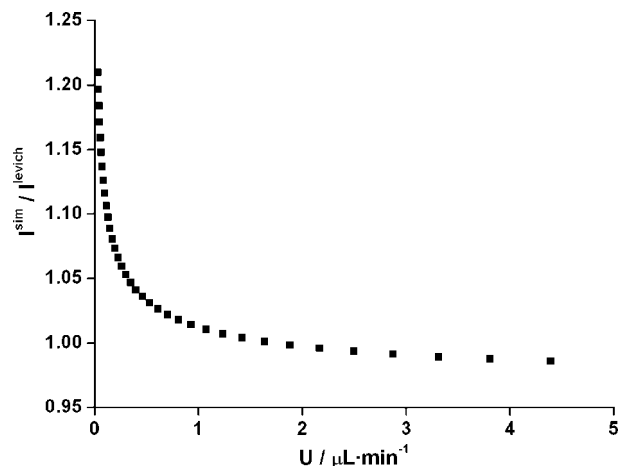

Figure 4. Limiting current ratio between the simulated currents, I^{sim}, and the Levich equation, I^{Levich}, as a function of the volumetric flow rate for a microband electrode ($x_e = 20$ μm, $d = 95$ μm) in a microchannel ($d = 95$ μm, $2h = 77$ μm) containing a solution of 5.0 mM ferrocyanide, 5.0 mM ferricyanide, and 0.5 M KNO$_3$. The flow rate ranged from 0 to 5 μL min^{-1}.

for which the distortion of the diffusion layer due to the convection is lower. The latter effect is illustrated in parts A and B of Figure 5, which depict the diffusion layers for flow rates of 1 and 10 μL min^{-1}, respectively. As the flow rate is increased, the diffusion layer thickness is decreased so that the radial contribution at the "edge" of the electrode becomes negligible. The results of the simulations indicate that this is the case for flow rates higher than about 1 μL min^{-1}, which means that the influence of edge effects should be small for the flow rates (i.e., 1–10 μL min^{-1}) employed in this work.

Figure 6A shows plots of the simulated ($\triangle$) and experimentally ($\blacksquare$) obtained limiting currents, for a scan rate of 100 mV s^{-1}, as a function of the flow rate. The experimental currents were smaller than the simulated ones for all flow rates. As the syringe pump was indeed found to deliver the correct flow rate, we attribute
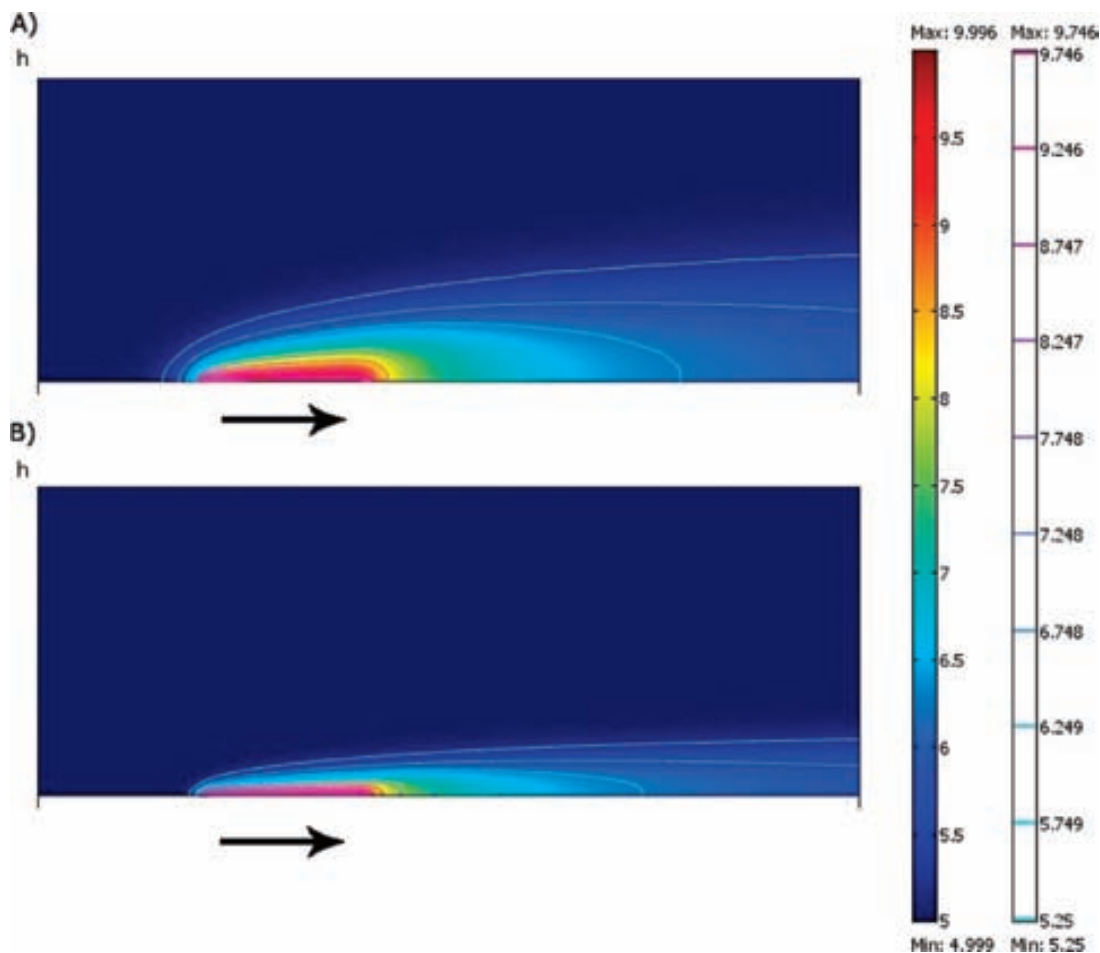
Figure 5. Simulated diffusion layers for a flow rate of (A) 1 and (B) 10 μL min^{-1}, respectively. The flow rates used corresponded to the minimum and the maximum flow rates used in the experiment. The arrows show the flow direction.
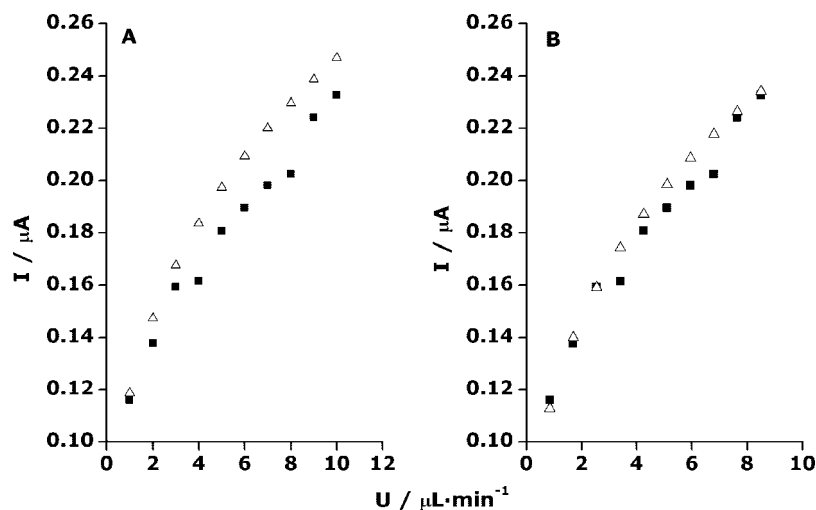

Figure 6. The experimental limiting voltammetric currents (■) and the corresponding simulated currents obtained with the two-dimensional model (△) as a function of the volumetric flow rate (A) before and (B) after correction for the presence of leaks. The uncorrected flow rates in part A ranged from 1 to 10 μL min^{-1} while the estimated real flow rate in part B ranged from 0.85 to 8.5 μL min^{-1}. The solution contained 5.0 mM ferrocyanide, 5.0 mM ferricyanide, and 0.5 M KNO$_3$, and the experimental results were obtained using a three-electrode configuration and a scan rate of 100 mV s^{-1}. The microbands were 20 μm wide, and the interelectrode distance was 50 μm.

these deviations in the current to the presence of tiny leaks at the inlet and outlet of the flow cell, which resulted in slightly lower flow rates. Such leaks are generally very difficult to eliminate completely in the present type of PDMS based microfluidic system. As a result, it is often difficult to predict (and determine) the real flow rate in the flow cells. However, by varying the flow
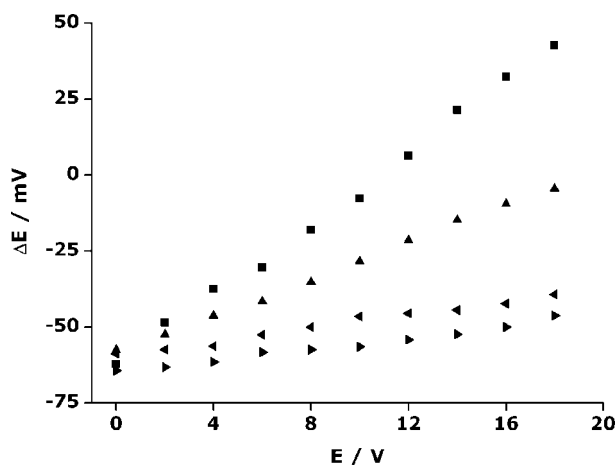
Figure 7. The potential difference between two gold microbands separated by 50 ("solid right triangle"), 120 ("solid left triangle"), 260 (▲), and 400 μm (■) in a solution of 0.5 M KNO$_3$ as a function of the external voltage difference. The corrected flow rate was 4.25 μL min^{-1}.

Figure 8. The potential difference between two gold microbands separated by 50 ("solid right triangle"), 120 ("solid left triangle"), 260 (▲), and 400 μm (■) in a solution of 5.0 mM Fe(CN)$_6^{4-}$, 5.0 mM Fe(CN)$_6^{3-}$, and 0.5 M KNO$_3$ for a corrected flow rate of 4.25 μL min^{-1} as a function of the external voltage difference.

rate used in the simulations and comparing the results of the simulations with the experimental currents, it is possible to estimate the real flow rate in the microfluidic cell. We have consequently used this approach to estimate the real flow rate in our microfluidic cell. As is seen in Figure 6B, the best fit between the experimental (■) and simulated (△) data was found for a flow rate that was about 85% of the nominal flow rate and all flow rates given below have hence been corrected using this correction factor.

Electric Field Induced Microband Potential Differences. As has been described by Klett and Nyholm,[33] the potential difference between two microbands induced by an external electric field can be used for potentiostatless amperometric end-column detection. In the present work, the same approach was used to study electric field induced electrochemical detection using an array of gold microband electrodes positioned within a PDMS microfluidic channel. Figure 7 shows the influence of the external voltage difference (E) on the potential difference (ΔE) between two bands positioned within the channel for different pairs of bands in 0.5 M KNO$_3$ and a flow rate of 4.25 μL min^{-1}. The distance between bands was 50 ("solid right triangle"), 120 ("solid left triangle";), 260 (▲), and 400 μm (■). As is seen in Figure 7, the dependence of ΔE on the applied external voltage difference was practically linear in all four cases. It is also evident that the magnitude of the potential difference between the electrodes increased with the interelectrode distance. The latter is in good agreement with the expectations based on the end-column results previously obtained by Klett and Nyholm.[33] The reproducibility of the results was checked by repeating the experiments at least four times. It was found that the differences between the slopes of the ΔE vs E plots were less than 8% in all cases. The linear dependence of the potential difference between the electrodes on the external voltage difference indicates that the potential difference was controlled merely by the ratio between the solution resistance between the electrodes (which increases with increasing interelectrode distance) and that of the microfluidic system as a whole. This finding also implies that the resistance between the electrodes was independent of the applied voltage difference.
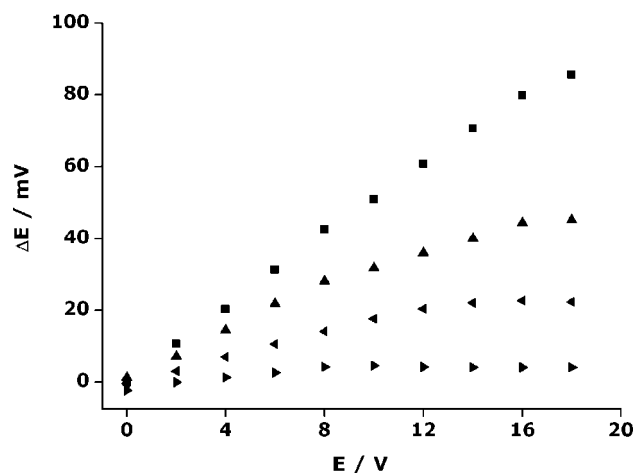
The latter is not unexpected since no species, able to undergo electrochemical reactions at the electrodes for these potential differences between the electrodes, should have been present in this solution.

As is seen in Figure 8, which shows the results obtained with a solution containing 5.0 mM ferrocyanide and 5.0 mM ferricyanide in 0.5 M KNO$_3$, the relationship between the difference in the potential between the microbands and the external voltage difference changed significantly when a redox couple was introduced into the flowing solution. It is seen that for all curves, except that for the largest difference in the distance between the microbands, the potential difference between the microbands reached a practically constant level for sufficiently large external voltage differences, although a linear dependence was seen for smaller external voltage differences. The attainment of the approximately constant potential differences can hence be ascribed to the presence of the ferro/ferricyanide couple which, acting as a depolarizer, modify the potential difference observed between microbands. This finding is in good agreement with previous results obtained by Klett and Nyholm.[33] In the presence of the ferro/ferricyanide redox couple, which can be considered a reversible redox couple, only a small potential difference between the electrodes would be needed to enable oxidation of ferrocyanide at one electrode and reduction of ferricyanide at the other electrode. In the presence of redox reactions, the oxidation current must clearly equal the reduction current and the rate of one of the redox reactions should therefore become rate limiting. The constant potential difference between the electrodes can then be seen as a mixed potential according to the mixed potential theory frequently employed in the discussion of corrosion experiments.[42] On the basis of this theory, the potential plateaus seen in Figure 8 can be explained by the fact that a small potential difference would be sufficient to support a (very small) current through the voltmeter in the presence of a reversible redox couple. It is also evident that the current could not have been mass transfer

(42) Jones, D. A. *Principles and Prevention of Corrosion*, 2nd ed.; Prentice Hall: Englewood Cliffs, NJ, 1996, p 86.

controlled since it should have been too small to induce any significant change in the surface concentrations of $Fe(CN)_6^{4-}$ and $Fe(CN)_6^{3-}$ due to the fact that a voltmeter with a high internal resistance was used in the experiments.

In analogy with Figure 7, the potential difference between the microbands increase with increasing interelectrode distance in Figure 8 as a result of the larger solution resistance between the electrodes. The fact that the value of the mixed potential plateau increased with increasing interelectrode distance can analogously be ascribed to the increased iR drop between the electrodes. The lack of an evident plateau for the largest distance between the electrodes in Figure 8 in fact suggests that the potential difference between these electrodes was controlled by the resistance between the bands (i.e., as in Figure 7) rather than by the solution equilibrium potential (mixed potential) in this case. In the absence of an added redox couple (see Figure 7), a much larger ΔE value would clearly be needed to induce electrochemical reactions (e.g., the oxidation and reduction of water) at the electrodes. This is in good agreement with the linear ΔE vs E relationship in Figure 7 for the same external voltage differences as used in Figure 8.

The results in Figures 7 and 8 clearly demonstrate that the potential difference between the two electrodes increases linearly with the external voltage as long as electrochemical reactions are unable to take place at the electrodes (i.e., as long as the induced potential difference between the electrodes is sufficiently small). In the presence of electroactive species in the solution, the external voltage induced potential differences between the electrodes depend both on the external electric field (ohmic polarization) and the chemical composition of the solution since the electrode potential will be a mixed potential in the presence of redox reactions at the electrodes. As the results in Figures 7 and 8 are in good agreement with the data previously obtained by Klett and Nyholm[33] in end-column experiments, it is clear that it should be possible to use the potential differences induced by an external voltage difference to induce electrochemical reactions on pairs of microband electrodes positioned anywhere within a microfluidic channel. In the presence of an external electric field, the current induced between an appropriately selected pair of microband electrodes could therefore be used for electrochemical detection of electroactive species in the flowing solution, as will be shown in the next section.

Electric Field Induced Microband Currents. In Figure 9, the induced current between pairs of microband electrodes separated by 250, 520, 790, and 1060 μm is shown as a function of the external voltage difference. These experiments, which were performed in a 0.5 M KNO_3 solution, clearly show that an increasingly larger external voltage difference was needed to induce a current as the distance between the microband electrodes was decreased. This can be explained by the fact that the potential difference, and thus the driving force, for the redox reactions at the microband electrodes depends on the interelectrode distance as depicted in Figure 7. For the smallest interelectrode distance of 250 μm, the largest external voltage difference was hence needed to obtain the potential difference required for the onset of redox reactions at the microband electrodes. For a sufficiently low external voltage difference, the induced potential difference between the microbands was hence not large enough to drive the oxidation
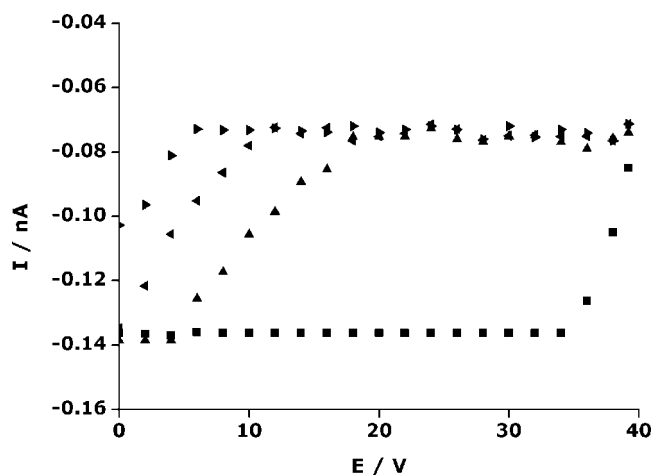

Figure 9. The induced current between two 20 μm wide microbands separated by 250 (■), 520 (▲), 790 ("solid left triangle"), and 1060 μm ("solid right triangle") as a function of the external voltage difference for a solution of 0.5 M KNO_3 at a corrected flow rate of 4.25 μL min^{-1}.

and the reduction reactions and the current was therefore equal to the baseline current given by the picoamperemeter offset current. The current observed for a zero nominal external voltage difference with an interelectrode distance of 1060 μm suggests that a small voltage difference was still present between the electrodes in this case. More importantly, Figure 9 shows that the same limiting current of about 0.06 nA was reached independently of the distance between the microband electrodes. The plots of the current as a function of the external voltage difference for the intermediate interelectrode distances are incidentally very similar to the steady state voltammograms seen in Figure 3. Similar results have likewise been obtained by Klett and Nyholm[33] in the end-column detection mode.

The fact that the same limiting current was found at least for the three largest interelectrode differences in Figure 9 indicates that the current was limited by mass transport of the same redox species in all these cases. Mass transport limitation is further supported by the fact that the total current through the microfluidic cell was found to be 21 μA for an external voltage difference of 40 V. The latter clearly shows that only a very small fraction (i.e., 3×10^{-4}%) of the total current flowed via the electrodes. In the 0.5 M KNO_3 solution, the likely redox reactions include reduction of dissolved oxygen and oxidation of gold, the Ti adhesion layer or impurities in the solution. The oxidation of the adhesion layer was possible since the microfabrication process employed resulted in electrodes for which the Ti adhesion layer was in contact with the electrolyte at the edges of the electrode (see below). Given an electrode area of 1.9×10^{-5} cm^2, the limiting current in Figure 9 corresponds to a current density of about 3 μA/cm^2. As this current density is approximately 1 order of magnitude smaller than the current density expected for mass transport controlled reduction of oxygen in a saturated quiescent solution, the current was most likely limited by the oxidation reaction. This hypothesis was verified by carrying out experiments in the presence of ascorbic acid, as shown in Figure 10. As the oxidation of ascorbic acid is irreversible, the presence of this compound should not affect the reduction process at the microband electrode acting as the
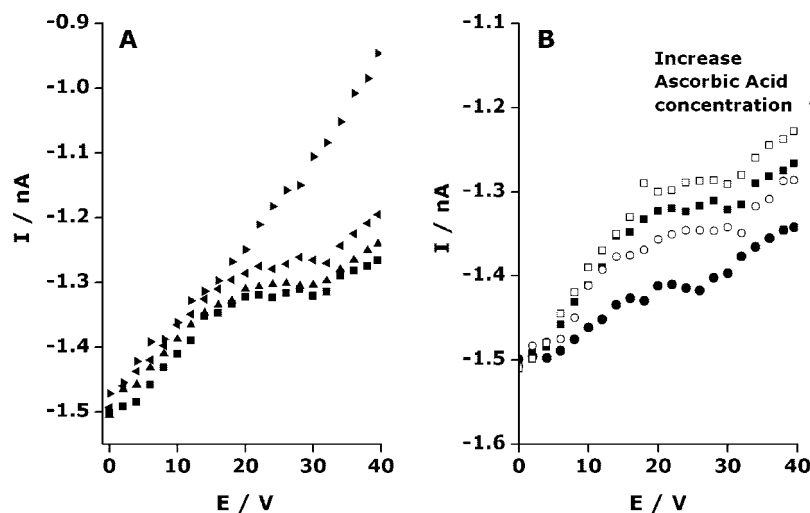
Figure 10. (A) The induced current between two 20 μm wide microbands separated by 50 (■), 120 (▲), 260 ("solid left triangle"), and 400 μm ("solid right triangle") as a function of the external voltage difference for a solution containing 0.5 M KNO$_3$ and 150 μM ascorbic acid. (B) The induced current between two 20 μm wide microbands separated by 50 μm as a function of the external voltage difference for increasing ascorbic acid concentrations from 50 to 200 μM in 0.5 M KNO$_3$. The corrected flow rate was 4.25 μL min^{-1} in both plots.
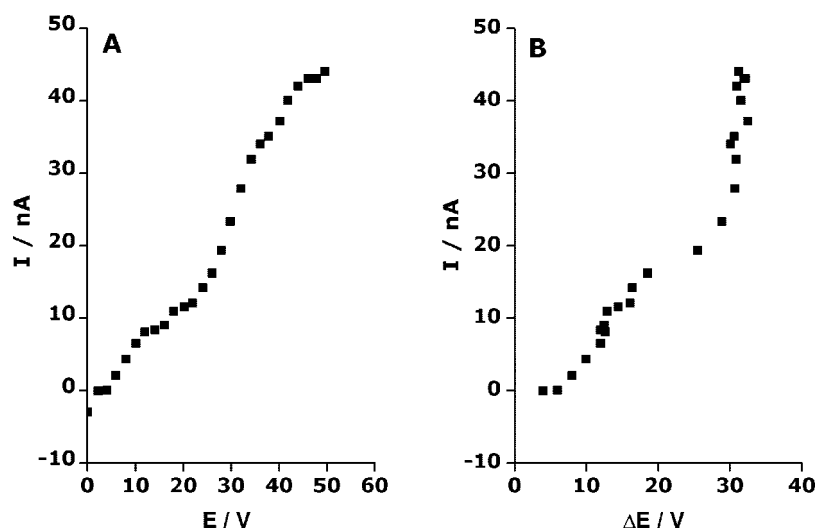

Figure 11. The induced current between two 20 μm wide microbands separated by 50 μm as a function of (A) the external voltage difference and (B) the potential difference between the microbands, respectively, for a solution containing 5.0 mM ferrocyanide, 5.0 mM ferricyanide, and 0.5 M KNO$_3$. The corrected flow rate was 4.25 μL min^{-1}.

cathode. Figure 10A shows that while very similar limiting currents were found for interelectrode distances of 50, 120, and 260 μm, a linear current versus external voltage difference plot was obtained for an interelectrode distance of 400 μm due to the significant influence of the *iR* drop in the latter case. The results for the three smallest distances indicate that well-defined steady state voltammograms with a significantly higher limiting current than in Figure 9 (i.e., about 10 μA/cm^2 compared to 3 μA/cm^2) were obtained when 150 μM ascorbic acid was added to the 0.5 M KNO$_3$ solution. This demonstrates that the current between the microband electrodes was controlled by the concentration of electroactive species in the solution. The exact concentration of ascorbic acid in the flowing solution was, however, difficult to calculate since a significant fraction of the ascorbic acid most likely was oxidized by the oxygen present in the solution. As presented in Figure 10B, experiments were therefore made with increasing ascorbic acid concentrations

from 50 to 200 μM by successively adding ascorbic acid to the solution for an interelectrode distance of 50 μm. It is clearly seen that the limiting current increased as a result of these additions, which further supports the conclusion that the current was limited by the oxidation at the microband serving as the anode.

In Figure 11, it is seen that even larger limiting currents could be obtained when a solution containing a mixture of 5.0 mM Fe(CN)$_6^{4-}$ and 5.0 mM Fe(CN)$_6^{3-}$ was used with the same interelectrode distance (i.e., 50 μm) as in Figure 10. In parts A and B of Figure 11, the current is plotted as a function of the external voltage difference and the measured potential difference between the electrodes, respectively. In Figure 11A, it is seen that a limiting current of about 10 nA, corresponding to a current density of about 0.5 mA/cm^2, was obtained for an external voltage difference of about 15 V. As is seen in Figure

11B, this external voltage difference corresponded to a potential of about 15 mV between the electrodes. The attainment of this current density for such a small potential difference is in good agreement with the fact that a reversible redox couple was present in the solution. An addition of 5.0 mM $Fe(CN)_6^{4-}$ and $Fe(CN)_6^{3-}$ to the solution thus resulted in an increase in the current density by almost 2 orders of magnitude compared to that obtained in 0.5 M KNO_3 in Figure 9. This clearly shows that the current between the electrodes is limited by the redox reactions at the electrodes and that the induced current between two microband electrodes can be used for analytical purposes. After the experiments in the $Fe(CN)_6^{3-}/Fe(CN)_6^{4-}$ solution described above, it was, however, found that the area of the electrode that had served as the anode had decreased significantly due to a partial detachment of the gold layer. As a result of this loss of the gold layer, the electrodes were severely damaged already after a few experiments. We attribute this effect to an oxidation of the Ti adhesion layer resulting in a partial loss of the gold layer as described by Nilsson et al.,[43] who found that oxidation of titanium adhesion layers can take place via pinholes and cracks in the gold layer. The corresponding reaction should in the present case have been facilitated by the fact that the edges of the adhesion layer were in direct contact with the electrolyte. In Figure 11B, it is therefore possible that this reaction was involved in the rapid increase in the current for potential differences between the electrodes larger than about 25 mV in Figure 11B. These results clearly show that the stability of the microband electrodes is an important issue and that care must be taken to ensure that the adhesion layer is not in contact with the electrolyte during the measurements. On the basis of the present results, it is thus very difficult to provide a relevant estimation of the reproducibility and long-time stability of the electrode responses for any of the analytes used in the present work. As will be shown elsewhere,[44] the electrode stability problem can, however, be circumvented by modifying the microfabrication procedure used in the manufacturing of the microband electrode. It should also be mentioned that the need for electrode long-time stability should be less with the approach described in the present work since a new pair of detection electrodes with the same interelectrode distance in the array could be used.

In the electric field induced current experiments, problems due to the presence of gas bubbles were also sometimes encountered. In these cases, the experiments were stopped and the cell was flushed with water or ethanol to remove the bubbles. According to our experience, the bubbles generally stem from oxygen or hydrogen formed as a result of a too large potential difference between the detection electrodes. One way to minimize this problem is thus either to reduce the distance between the electrodes or to employ lower electric field strengths. In a CE separation, the latter would be less attractive as it would affect the separation time and quality significantly. A better solution hence involves the use of electrode arrays with many electrodes and small interelectrode distances, with which it always would be possible to find two electrodes with

an interelectrode potential large enough to enable the detection but small enough to ensure no formation of oxygen or hydrogen. Oxygen (or hydrogen) bubbles can, naturally, also be formed at the "high-voltage" electrodes used to induce the electric field in the flow channel. As the influence of the latter problem depends on the magnitude of the (CE) current and the current density at the "high-voltage" electrodes, the resistance of the channel (or capillary) and the area of the "high-voltage" electrodes should generally be made as large as possible. More importantly, the present results clearly show that it is possible to carry out electric field driven electrochemical detection anywhere within a microfluidic channel without interferences from the applied electric field.

CONCLUSIONS

It has been shown that electrochemical detection can be carried out within a microfabricated channel containing an appropriately positioned array of gold microband electrodes in the presence of an external electric field. The detection, which is driven by the potential difference induced between two microband electrodes, is consequently not dependent on the use of a decoupler such as those commonly employed in electrochemical detection in capillary electrophoresis at the present time.

The present results, which also include simulations of the flow rate dependence of the current at microliter per minute flow rates, clearly show that potential difference between the two microband electrodes depends on the external electric field strength and the distance between the electrodes in the electric field. This means that the potential difference between two microband electrodes can be adjusted to enable the detection of different electroactive species merely by selecting the appropriate electrode pair in an array of microband electrodes. The resulting current between the microband electrodes has been shown to depend on the concentration of the electroactive species in the solution and by plotting the current as a function of the external voltage difference, steady state voltammograms, analogous to those obtained in conventional potentiostatic measurements, can in fact be obtained. Oxidative detection is facilitated by the fact that the solution contains dissolved oxygen which can support the required reduction at the microband serving as the cathode.

To ensure long-term detection stability, care must be taken to eliminate oxidation of the adhesion layers of the microband electrodes by making sure that there is no contact between the adhesion layers and the electrolyte. This can be obtained by making sure that the edges of the adhesion layer are covered by an appropriate insulating layer during the microfabrication step.

The results of the 2D simulations demonstrate that edge diffusion effects can be neglected for flow rates higher than about $1~\mu L~min^{-1}$ (i.e., linear flow rates larger than $0.23~cm~s^{-1}$) and that comparisons between the experimental and simulated results can be used to detect the presence of tiny leaks that otherwise may be difficult to spot.

As standard microfabrication procedures can be used to produce microband array electrodes with excellent control of the electrode dimensions, positions, and interelectrode distances, the present electrochemical detection approach is well-suited for use

(43) Nilsson, S.; Klett, O.; Svedberg, M.; Amirkhani, A.; Nyholm, L. *Rapid Commun. Mass Spectrom.* **2003**, *17*, 1535–1540.
(44) Karlsson, M.; Ordeig, O.; Nikolajeff, F.; Nyholm, L. In preparation.

in electrochemical chip based systems. Although this development clearly is facilitated by the ease by which flow channels of PDMS can be manufactured, it would also be possible to employ microfluidic channels of other materials. We therefore believe that the present electric field driven electrochemical detection technique can contribute to the development of new inexpensive and portable devices for the analysis of species based on, for example, capillary electrophoresis.

ANNEX 4: Papers included in this thesis

Continuous measurement of acute toxicity in water using a solid state microrespirometer

Fco. Javier Del Campo [a],*, Olga Ordeig [b], Nuria Vigués [c], Neus Godino [b],
Jordi Mas [c], Francesc Xavier Muñoz [b]

[a] *Institut de Biotecnologia i Biomedicina (IBB-UAB), Universitat Autònoma de Barcelona, Barcelona 08193, Spain*
[b] *Instituto de Microelectrónica de Barcelona (IMB-CNM), CSIC (Esfera UAB),*
Campus Universitat Autònoma de Barcelona, Barcelona 08193, Spain
[c] *Departamento de Genética y Microbiología, Universitat Autònoma de Barcelona, Barcelona 08193, Spain*

Abstract

This work presents the first true solid-state microrespirometer. It consists on a naturally developed biofilm of *Pseudomonas aeruginosa* over a Nafion modified array of gold microdisc electrodes. Such a device can be used to monitor acute toxicity in water streams based on the oxygen reduction current recorded at the microelectrode array. When a healthy biofilm is exposed to a toxic stream the bacteria conforming stop breathing which results in an immediate increase of the oxygen supply reaching the microelectrode array.

The fabrication and use of such a microrespirometer is described, and a possible operation mode for a real application is presented. Given that different waters may contain toxic compounds of diverse nature, the respirometer presented here provides qualitative information only.
© 2007 Elsevier B.V. All rights reserved.

Keywords: Microrespirometry; Ultramicroelectrode arrays; Oxygen reduction; Linear sweep voltammetry; Biofilm

1. Introduction

This work presents the development of a new solid-state microrespirometer for the continuous monitoring of acute toxicity in drinking water supply lines. Toxicity of drinking water may be determined by different means. Amongst these, the use of assays based on the response of fish [1], algae [2], or even bacteria is commonplace. Such assays diagnose toxicity through the observation of alterations in the physiology of the subject organisms [3].

Biofilms are aggregates of bacteria, which spontaneously associate on top of surfaces in order to improve their survival rate in certain environments [4,5]. In this work, stable biofilms were grown from a culture broth on top of the electrode system. The growth process takes between 10 and 15 days, after which biofilms remain stable. Because the oxygen consumption of biofilms is heavily influenced by environmental parameters, par-

ticularly by the presence of nutrients and toxics, their respiration rate may be used as an indicator of medium toxicity.

The method described here has its foundations in the amperometric monitoring of oxygen [6]. The idea of monitoring biofilm respiration using oxygen electrodes is not new [2]. Individual microelectrodes have been used in the past to study oxygen concentration profiles within a biofilm [7]. The novel of our approach is that a biofilm is allowed to grow spontaneously on top of an array of ultramicroelectrodes and measuring the oxygen flux through it, thus achieving a true solid-state microrespirometer. This is in contrast to past micro-respirometry work where cells have been trapped inside a filter membrane which is later placed in the vicinity or in close contact with a Clark oxygen electrode [7,8].

This work shows how a biofilm based micro-respirometer device enables the semi-continuous monitoring of acute water toxicity. All measurements involving biofilms were performed in a carbon source free environment. Thus, in the absence of nutrients, a biofilm behaves purely as a diffusion barrier because the biofilm does not require a significant amount of oxygen for its survival. However, as soon as nutrients are available, oxygen

---

* Corresponding author. Tel.: +34 93 594 77 00x1313; fax: +34 93 580 14 96.
E-mail address: Franciscojavier.delcampo@cnm.es (Fco.J. Del Campo).

Measuring acute toxicity using a solid-state microrespirometer
Part II. A theoretical framework for the elucidation of metabolic parameters

Neus Godino [a], Diana Dávila [b], Nuria Vigués [b], Olga Ordeig [a,1],
F. Javier del Campo [a,*], Jordi Mas [b], F. Xavier Muñoz [a]

[a] Instituto de Microelectrónica de Barcelona, IMB- CNM (CSIC). Esfera UAB, Campus Universidad Autónoma de Barcelona, Bellaterra 08193, Barcelona, Spain
[b] Departamento de Microbiología y Genética, Universidad Autónoma de Barcelona, 08193-Bellaterra, Barcelona, Spain

ARTICLE INFO

ABSTRACT

This work presents the construction of a numerical model that is able to show the behaviour of a biofilm-based microrespirometer. The model uses finite element methods to solve the mass transport equations for oxygen as it travels from the bulk of the solution towards the microelectrode array through the biofilm and a protective Nafion® layer, whose main purpose is to avoid electrode fouling. The paper describes some of the issues related to the mass transport at arrays of slightly recessed microelectrodes. It provides further evidence of the validity of the diffusion domain approach as a key resource to model microelectrode arrays. The model is used to interpret amperometric data and provide metabolic rate constants that agree reasonably well with measurements performed in bacterial suspensions under similar experimental conditions.

© 2008 Elsevier B.V. All rights reserved.

1. Introduction

Respirometry consists in monitoring the metabolic activity of living organisms. In the present case, we use respirometry to determine the toxicity of a certain environment. In a previous work, we presented a new solid-state microrespirometer based on the amperometric reduction of oxygen going through a biofilm grown over a Nafion® modified array of gold microelectrodes [1]. As the metabolic activity of the biofilm increases in the presence of nutrients and oxygen consumption occurs, a drop in the oxygen reduction current occurs, and changes in the measured current can be interpreted in terms of bacterial metabolic activity.

This work presents a theoretical framework describing the basic operation of such a microelectrode array-based microrespirometer. The model is built using data obtained electrochemically and optically from a series of controlled experiments. It provides a better understanding of some of the physico-chemical processes involved

in the detection. This will in turn lead to the optimization of the device at the design stage.

Ultra-microelectrode arrays are used to enhance sensitivity, and a Nafion® coating avoids electrode passivation arising from the deposition of macroscopic debris as well as unwanted organic material over the electrode surface. Other materials different from Nafion® could also be used for these purposes. However, due to the overall negative charge of its polymer backbone, Nafion® offers the additional advantage of preventing certain electroactive species (such as the hypochlorite commonly used as disinfectant in drinking waters) from reaching the electrode and causing erroneous respiration readings. This is particularly important because the final application is the monitoring of acute toxicity in drinking water supply lines.

The experimental functioning of this device was described in a previous work [1] but, broadly speaking, the detection method consists in exposing our microrespirometer to a test sample containing nutrients. If toxic substances are present in the sample, the bacteria forming the biofilm are inactivated, respiration ceases and a higher concentration of oxygen reaches the electrode surface, thus resulting in a higher current reading. Although the method is unselective and the analyst can never know the nature of the substances present, it can be used to predict whether a sample is toxic or not, and to what extent.

* Corresponding author. Tel.: +93 594 77 00x1306; fax: +93 580 14 96.
E-mail addresses: Olga.Sala@nanotech.dtu.dk (O. Ordeig),
Franciscojavier.delcampo@cnm.es, fjcampo@cnm.es (F.J. del Campo).
1 Present adress: DTU Nanotech - Departmenet of Micro and Nanotechnology, DTU - Building 345 east, DK-2800 Kongens Lyngby, Denmark.

Mass Transport to Nanoelectrode Arrays and Limitations of the Diffusion Domain Approach: Theory and Experiment

Neus Godino,[†] Xavier Borrisé,[†,‡] Francesc Xavier Muñoz,[†] Francisco Javier del Campo,*,[†] and Richard G. Compton[§]

Instituto de Microelectrónica de Barcelona, IMB-CNM-CSIC, and Institut Català de Nanotecnologia, ICN-CIN2, Esfera UAB, Campus Universitat Autónoma de Barcelona, 08193-Bellaterra, Barcelona, Spain, and Department of Chemistry, Physical and Theoretical Chemistry Laboratory, University of Oxford, South Parks Road, OX1 3QZ Oxford, United Kingdom

The diffusion domain approach is a general framework for the understanding, interpretation, and prediction of the response of microelectrode arrays. This work exposes some of its limitations, particularly when dealing with nanoelectrode arrays of a few micrometers in size. This article also provides an overview of the principles and assumptions underpinning the diffusion domain approach, and then applies it to the study to approach, which is then applied to the study of nanoelectrode arrays. The apparent disagreement between theory and experimental data, due to the importance of radial diffusion to nanoelectrode arrays compared to microelectrode arrays, is explained by using simulations and experiments. The principle that an array of micro- or nanoelectrodes eventually behaves as if the entire array were a single electrode of the size of the array, with its corresponding properties, always applies. However, while microelectrode arrays tend to behave as macroelectrodes, nanoelectrode arrays on the other hand may behave as microelectrodes. For the case of arrays of small numbers of electrodes, or array sizes of micrometers or less, this compromises one of the key assumptions of the diffusion domain approach, namely that inner electrodes in an array are equivalent, which may lead the unaware to erroneous conclusions.

1. Introduction

Nanoelectrodes and nanoelectrode arrays are the natural next step in electrode miniaturization after microelectrodes and their arrays. However, only recent advances in nanofabrication techniques and metrology have enabled the controlled fabrication of such devices. This, together with the fact that such techniques are very costly and not so widely available, has limited the number of publications to date in this field. Early reports date back to the late 1990s, but the field did not seem to boom until 15 years later with the works of Arrigan et al.,[1−3] White,[4,5] and Murray,[6] who reported on the mass transport properties of nanoelectrodes of various geometries and their arrays.

One common and intriguing feature of the results presented in these works is the sigmoidal shape of the voltammograms recorded at nanoelectrode arrays even at moderate and low scan rates. This may seem striking if we draw an analogy between the mass transport behavior of nanoelectrode arrays and microelectrode arrays. Compton et al. have pointed to four main regimes of behavior affecting diffusional transport to microelectrode arrays. According to the relationship between size of the individual diffusion layer thicknesses, δ, microelectrode size described by their radius, r, and the intercenter distance between microelectrodes, d,[7,8] and with increasing diffusion layer thickness, these four regimes are as follows: (i) planar diffusion to each microelectrode as $\delta \ll r$, (ii) radial diffusion to each microelectrode as $\delta = r < d$, (iii) a transition zone when $r < \delta$ $\leq d$, and (iv) planar diffusion to the microelectrode array when $\delta \gg d$. Regime ii is the optimum one and it corresponds to the case when the response of the whole array is equivalent to that of a single microdisk, times the number of microelectrodes integrating the array. Regime iv, on the other hand, consists of a complete overlap of individual diffusion layers that results in the array behaving as an electrode of the size of the entire micro- or nanoelectrode array. Hence for most microelectrode arrays steady state currents are observed in regime ii, and then as the diffusion layer grows the current tails off in regime iv. However, nanoelectrode arrays are a special case because their size is typically a few micrometers, so they show steady state currents corresponding to microelectrode behavior, regardless of the extent of overlap between adjacent diffusion layers.

This motivated us to study diffusion at nanoelectrode arrays in more detail, combining simulations and experiments with nanoelectrode arrays fabricated by using electron-beam lithography.[9] We first attempted to simulate the behavior of nanoelectrode arrays by using the diffusion domain approach that has been so helpful in the study of microelectrode arrays. However, the results cast by this approach conflicted with the empirical observations reported in the past and, as we will show here, also with our own experimental data.

Models of nanoelectrode arrays were built based on three-dimensional domains and the results compared with those from two-dimensional models and the available experimental data. The three-dimensional simulations were in agreement with the experimental results, and showed that nanoelectrode arrays working under regime iv behave as single microelectrodes under most conditions.

The main reason why a two-dimensional approach fails to correctly model the behavior of such nanoelectrode arrays is

* To whom correspondence should be addressed. Email: franciscojavier.delcampo@imb-cnm.csic.es. Phone: +34-935-947-700. Fax: +34-935-801-496.
† Instituto de Microelectrónica de Barcelona.
‡ Institut Català de Nanotecnologia.
§ University of Oxford.

RESEARCH PAPER

Construction and characterisation of a modular microfluidic system: coupling magnetic capture and electrochemical detection

**Neus Godino · Detlef Snakenborg · Jörg P. Kutter ·
Jenny Emnéus · Mikkel Fougt Hansen ·
F. Xavier Muñoz · F. Javier del Campo**

Abstract This work presents the fabrication and characterisation of a versatile lab-on-a-chip system that combines magnetic capture and electrochemical detection. The system comprises a silicon chip featuring a series of micro-band electrodes, a PDMS gasket that incorporates the microfluidic channels, and a polycarbonate base where permanent magnets are hosted; these parts are designed to fit so that wire bonding and encapsulation are avoided. This system can perform bioassays over the surface of magnetic beads and uses only 50 μL of bead suspension per assay. Following detection, captured beads are released simply by sliding a thin iron plate between the magnets and the chip. Particles are captured upstream from the detector and we demonstrate how to take further advantage of the system fluidics to determine enzyme activities or concentrations, as flow velocity can be adjusted to the rate of the reactions under study. We used magnetic particles containing β-galactosidase and monitored the enzyme activity amperometrically by the oxidation of 4-aminophenol,

N. Godino · F. X. Muñoz · F. Javier del Campo (✉)
Instituto de Microelectrónica de Barcelona, IMB-CNM (CSIC),
Esfera UAB, Campus Universitat Autónoma de Barcelona,
08193 Bellaterra, Barcelona, Spain
e-mail: FranciscoJavier.delCampo@imb-cnm.csic.es

D. Snakenborg · J. P. Kutter · J. Emnéus · M. F. Hansen
Department of Micro and Nanotechnology, DTU Nanotech,
Technical University of Denmark (DTU),
Oersteds Plads, Building 345 east, room no. 254,
2800 Kongens Lyngby, Denmark

D. Snakenborg
e-mail: Detlef.Snakenborg@nanotech.dtu.dk

enzymatically produced from 4-aminophenyl-β-D-galacto-pyranoside. The system is able to detect the presence of enzyme down to approximately 50 ng mL^{-1}.

1 Introduction

Magnetic particles and amperometry have been combined in the past for (bio)electroanalytical purposes (Choi et al. 2002; Do and Ahn 2008; Farrell et al. 2004; Gabig-Ciminska et al. 2004; Goral et al. 2006; Llopis et al. 2009) and several literature reports describe systems where particles are directly immobilised on a channel wall opposite the electrodes (Choi et al. 2002; Do and Ahn 2008). Choi et al. used interdigitated microelectrode structures operated under generator-collector mode in an example close to our approach (Choi et al. 2002). More recently, a system was reported where the magnetic particles are elegantly immobilised by means of an array of NiFe permalloy blocks (Do and Ahn 2008). However, we believe that the overall performance of those systems may improve if the magnetic particles are captured upstream from the electrodes and not opposite them. This modification would take full advantage of the system microfluidics, which provides controlled and well-defined mass transport conditions leading to higher steady-state currents. Amperometry is a relatively simple, but very important, detection technique in lab-on-a-chip devices because currents recorded in channel electrodes (Alden et al. 1998; Morland and Compton 1999) under laminar flow are directly proportional to analyte concentration (Amatore et al. 2008; Cooper and Compton 1998;

Integration of a PDMS rotary switch valve in a miniaturised electroanalytical system.

Neus Godino[a], F. Javier del Campo[a], F. Xavier Muñoz[a], Mikkel Fougt Hansen[b], Jörg P. Kutter[b] and Detlef Snakenborg*[b]

This work features the design, fabrication and characterisation of a miniaturised electroanalytical
lab on a chip that allows the performance of a complete bioassay, from the capture of magnetic
10 particles through their functionalisation and sample incubation to the detection of electroactive
reaction products. The system is built using mainly polymeric materials such as PMMA and PDMS
and fast prototyping techniques such as milling and moulding. The system also includes a set of
microelectrodes, photo-lithographed on a silicon chip. The novelty lies in the design of the rotary
microvalve, which contains a microreactor so that various reaction and incubation steps can be
15 carried out in isolation from the detection event with zero dead volume. This avoids contamination
and fouling of the electrodes by proteins or other organic matter, and extends the useful lifetime of
the detector. The system operation is demonstrated by a model example, consisting in the
functionalisation of streptavidin-coated magnetic particles with biotinylated β-galactosidase over
periods ranging from 5 to 15 minutes, when the particles saturate. Although the system is intended
20 for the development of enzyme-based electrochemical bioassays, the concept of its rotary
microreactor can be applied more broadly.

Introduction

Miniaturised analytical systems represent an emerging and
25 exciting field for multidisciplinary research [1, 2], as the
development of these systems needs the confluence of
expertise from the physical sciences [3, 4], typically biology or
chemistry, and mechanical and electronics engineering, and
their coordination is a challenge of its own. But in spite of the
30 difficulties, blistering progress has been achieved over the
past couple of years due to the appearance and refinement of
new polymeric materials as well as to the adaptation of key
fabrication techniques [5-7].

This article focuses on the use of two of those materials,
35 namely poly(methyl-metacrylate), PMMA, and
polydimethylsiloxane, PDMS, to develop a versatile
miniaturised analytical system devised for the performance of
electrochemical bioassays. This system builds on the
architecture of a previous system, adding a rotary valve to it.
40 The fact that the rotary valve also integrates a reaction
chamber where magnetic particles can be captured represents
a fabrication challenge particularly from the point of view of
sealing moving parts.

Our previous work [8] presented a versatile electroanalytical
45 microsystem, easy to fabricate, use and re-configure. That
system allowed the performance of a broad range of enzyme-
based bioassays. The microsystem permitted the capture of
enzyme labelled magnetic beads, and their incubation with a
relevant substrate, upstream from an electrochemical detector.
50 After the reaction took place, the flow was restored and a

current peak corresponding to the products was easily
detected as in any other plug-flow system.

However, the simplicity in its design was both the main
strength and the main pitfall of the system. The fact that there
55 was a single channel means that all the solutions used in the
different operations – bead capture, sample and substrate
injection, product detection and washing - had to flow over
the electrodes. The consequence was that part of the
biological materials passing through the system adsorbed on
60 the electrodes and caused gradual losses of sensitivity and
reproducibility.

To preserve the electrodes longer, we want to minimize the
contact of solutions containing biological material with them.
Our approach consists in the integration of a microvalve in the
65 flow path between the biochemical reaction chamber and the
detector. This way we ensure that only the reaction products
flow over the electrodes, while any other potentially fouling
solutions are diverted through an alternative waste channel.

We have been able to integrate a microvalve in our original
70 system due to its flexible architecture based on flexible
building blocks [8]. Despite its small dimensions, the different
parts are sufficiently tolerant to accommodate new
functionalities.

We developed an externally-actuated rotary valve, made in the
75 same materials as the rest of the device. An important
advantage of this new feature is that it minimises the dead
volume between the reaction chamber and the detector, so the
configuration also reduces peak broadening due to
smearing/diffusion of detectable products inside the detector